POWER-LAW CREEP BEHAVIOUR IN MAGNESIUM AND ITS ALLOYS

A thesis
submitted in partial fulfillment
of the requirements for the Degree of

DOCTOR OF PHILOSOPHY IN MECHANICAL ENGINEERING
IN THE
UNIVERSITY OF CANTERBURY

BY

TAKANORI SATO

University of Canterbury

2008

Preface

This thesis is submitted as a partial requirement for the degree of Doctor of Philosophy in Mechanical Engineering in the University of Canterbury. This research was conducted under the supervision of Associate Professor Milo V. Kral in the Mechanical Engineering Department, University of Canterbury, between March 2003 and March 2008.

Acknowledgements

I would like to acknowledge the following people and organizations that have made this research work possible:

- Associate Professor Milo V. Kral for supervision of this thesis and for his technical and personal support throughout the entire research program;
- Foundation for Research Science & Technology, New Zealand for the provision of The Technology for the Industry Fellowships funding;
- Mark Nave from HKL Technology Ltd., for technical assistance in the EBSD systems;
- Members of the University of Canterbury Materials Engineering Group (MEG): Dr. John Smaill, Dr. Mark Staiger, Emeritus Professor Les Erasmus, Emeritus Professor Frank Fahy, Mike Flaws, and Kevin Stobbs; MEG visitors, Dr. George Spanos, and Dr. Chris Hutchinson; as well as fellow MEG students, for all their help, questions, comments, and critique;
- Administrative and technical staffs of Mechanical Engineering Department, Margot Beck, Scott Amies, Ken Brown, Paul Wells, Paul Southward, Julian Philips, Julian Murphy, for all their kind assistance.

Abstract

Creep is a time-dependent deformation of materials under stress at elevated temperatures. The phenomenon of creep allows materials to plastically deform gradually over time, even at stress levels below its yield point or below its transformation temperature. The issues involving creep are especially significant for magnesium alloys, since they are susceptible to creep deformation from temperatures as low as 100 ºC, which inhibits their potential application in areas such as automotive engines.

The University of Canterbury has developed a significant level of experience and infrastructure in the field of Electron Backscatter Diffraction (EBSD). EBSD allows microstructures to be characterized by imaging the crystal structure and its crystallographic orientation at a given point on a specimen surface, whereby the process can be automated to construct a crystallographic "orientation map" of a specimen surface. In light of this, the creep of magnesium and its alloys was studied using a novel technique, in which a conventional tensile creep test was interrupted at periodic intervals, and the EBSD was used to acquire the crystallographic orientation maps repeatedly on a same surface location at each interruption stages. This technique allows simultaneous measurement of the rate of creep deformation and the evolution of the specimen microstructure at various stages of creep, bringing further insight into the deformation mechanisms involved.

This thesis summarizes the study of the microstructural and crystallographic texture evolution during creep of pure magnesium and a creep resistant magnesium alloy Mg-8.5Al-1Ca-0.3Sr. Pure magnesium exhibit a conventional "power-law" type creep, and although its creep properties are well established in the past literatures, there has been little in terms of reconciliation between the observed creep rates and the underlying deformation

mechanisms. The alloy Mg-8.5Al-1Ca-0.3Sr, on the other hand, is a modern die casting alloy used in the automotive industry for engine and gearbox applications, and despite its superior creep resistance, little is known about the microstructural contributions to its creep properties.

This research was conducted to provide a link between the creep properties, observed microstructures, and theories of creep deformation by the use of advanced microscopy techniques. For the first time, the detailed, sequential microstructural development of magnesium and its alloys during creep has been revealed.

Table of contents

1. **T, Sato, B.L. Mordike, J-F. Nie, and M.V. Kral,** *An Electron Microscope Study of Intermetallic Phases in AZ91 Alloy Variants*, Magnesium Technology 2005, Ed. N.R. Neelmeggham, H.I. Kaplan, and B.R. Powell, TMS, pp. 435 - 440 (2005).

2. **T. Sato, M.V. Kral,** *Electron Backscatter Diffraction Mapping of Microstructural Evolution of Pure Magnesium during Creep*, Metall. Mat. Trans. A, Vol. 39, pp. 688 – 695 (2008).

3. **T. Sato, M.V. Kral,** *Electron Backscatter Diffraction Mapping of Microstructural Evolution of Mg-Al-Ca-Sr alloy during Creep*, Mat. Sci. Eng. A (manuscript accepted, awaiting publication).

Table of figures

CHAPTER 1 - INTRODUCTION

This research was initially sponsored by the automotive die-cast component manufacturer (ION Automotive Ltd., New Zealand) to investigate the potential uses for magnesium alloys.

The research direction was narrowed to the study of creep deformation in magnesium and its alloys, rather than fatigue or corrosion. This was because the study of fatigue life in diecast alloys was primarily governed by macroscopic casting defects (porosity, shrinkage), resulting typically in statistical observations with little academic interest. Similarly in the study of corrosion, the majority of the advanced work was in the field of electrochemistry or surface treatment, which departed from the intended research direction in study of microstructures using the advanced facilities such as EBSD. In this respect, the study of creep was found to be the area with the most academic interest in recent progress in light metals in terms of both academic and industrial significance.

The phenomenon of creep in magnesium was of direct interest to the automotive industries since one of the recent ambitions for this industry is to use magnesium alloys to replace aluminum as a material for the primary engine block die-cast. The rewards in cost and weight reduction can be enormous, but one of the largest limiting factors is the creep induced fatigue failure, at the operating temperatures of up to 250 ºC.

Creep is a time-dependent deformation phenomenon of materials under stress at elevated temperatures. The phenomenon of creep allows materials to plastically deform gradually over time, even at well below its yield point or its transformation temperature. It has a highly important technological significance, since many of applications of modern

materials for advanced engineering designs are limited by susceptibility to creep, such as in automotive engines, aerospace components, or in heavy industries such as power generation plants. The issues of creep are especially significant for magnesium alloys, which have some of the lowest creep activation temperatures of all the modern engineering metals.

However, the study of creep in polycrystalline metals still relies heavily on traditional empirical rate equation models, collection of large volumes of creep test data, and microstructural studies of materials only after catastrophic failure has taken place.

The University of Canterbury has developed a significant level of experience and infrastructure in the area of Electron Backscatter Diffraction (EBSD). EBSD allows microstructures to be characterized by showing the relative crystallographic orientation at an array of points on a specimen surface.

In light of this, an opportunity to study creep phenomena by a novel technique was identified, which will be referred to here "sequential creep/EBSD analysis". The technique involves performing a tensile creep test on a specimen, but interrupting the process at periodic intervals, at which EBSD was used to acquire crystallographic orientation maps repeatedly on a same surface location at each interruption. This technique allows simultaneous measurement of creep rate and observation of creep microstructure, bringing further insight into the understanding of the actual mechanisms of creep deformation.

This thesis summarizes the application of the newly developed sequential creep/EBSD analysis technique on pure magnesium and a creep resistant magnesium alloy, and the insights that were gained. For the first time, the detailed, sequential microstructural development of magnesium during creep has been revealed.

1.1 RESEARCH ACHIEVEMENTS

This research program has generated several academic contributions as listed below. The papers that have been published to date are included in the appendix of this thesis.

- **T, Sato, B.L. Mordike, J-F. Nie, and M.V. Kral,** *An Electron Microscope Study of Intermetallic Phases in AZ91 Alloy Variants*, presented at Magnesium Technology 2005: Creep Resistant Magnesium Alloys and Welding-Joining, TMS 134th Annual Meeting & Exhibition, San Francisco, 2005. Manuscript published in Magnesium Technology 2005, Ed. N.R. Neelmeggham, H.I. Kaplan, and B.R. Powell, TMS, pp. 435 - 440 (2005).

- **T, Sato, B.L. Mordike, J-F. Nie, and M.V. Kral,** *Microstructure Study of Magnesium Alloys at Various Stages of Creep using EBSD*, presented at Magnesium Technology 2006: Microstructure and Properties I, TMS 135th Annual Meeting & Exhibition, San Francisco, 2006.

- **T, Sato, B.L. Mordike, J-F. Nie, and M.V. Kral,** *Microstructure Study of Pure Mg and Mg-Al at Various Stages of Creep using EBSD*, presented at Magnesium Technology 2007: Microstructure and Properties, TMS 136th Annual Meeting & Exhibition, Orlando, 2007.

- **T. Sato, M.V. Kral,** *Electron Backscatter Diffraction Mapping of Microstructural Evolution of Pure Magnesium during Creep*, Metall. Mat. Trans. A, Vol. 39, pp. 688 – 695 (2008).

- **T. Sato, M.V. Kral,** *Electron Backscatter Diffraction Mapping of Microstructural Evolution of Mg-Al-Ca-Sr alloy during Creep*, Mat. Sci. Eng. A, (awaiting publication).

1.2 RESEARCH OVERVIEW

A progress chart of the overall research program is outlined in Figure 1.1. This section explains the chronological development of this project, which experienced a major change in scope at an early stage.

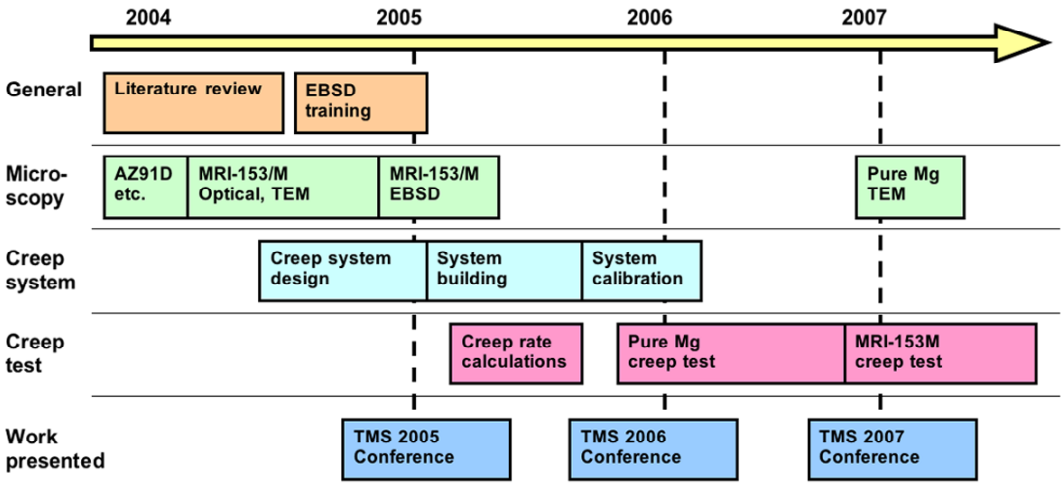

Figure 1.1. Progress chart of the overall research program

1.2.1 Preliminary project scoping

This project was originally sponsored by an automotive component manufacturer (ION Automotive Ltd., New Zealand). ION's Director of Research, Dr. Darius Singh[*], was primarily interested in the fatigue behavior of common magnesium alloys that could potentially replace their current aluminum alloy casting components. Several examples of commercial automotive magnesium casting components were acquired for analysis under

[*] Now Head of Department, Mechanical Engineering at Auckland University of Technology.

optical and electron microscopy. At this stage, it was realized that the general problems attributed to fatigue failure were not as simple as it was initially anticipated, but were in fact a multi-faceted phenomenon caused by compound effects of common sources of defects, (e.g., casting defects and environmental corrosion of the alloy) that create stress concentrations where fatigue cracks originate. Therefore, the observed fatigue life of these alloy specimens were in fact manifestations of macroscopic phenomena and relatively uninteresting from a basic research standpoint.

At this point in time, collaboration was evolving between the University of Canterbury and Monash University. As a result of this collaboration, the project scope was significantly altered to focus on basic research into the creep behavior of magnesium and its alloys. High-pressure diecast samples of creep resistant Mg-Al-Ca-Sr alloy MRI-153M were provided by a visitor to Monash at the time, Prof. B. Mordike from TU Clausthal - Germany, with an objective to further investigate the unique microstructural features of this alloy, supplemented by its predecessors, MRI-153 and MRI-230. The problem of creep in magnesium alloys for use in automotive applications is at least as significant as fatigue, and creep is less subject to defects due to production variables. The project was fortunate to have the flexibility to accomplish this change in scope without any difficulty.

The current study at the University of Canterbury was also envisioned as complementary to the creep studies of the alloy MRI-153 carried out by Prof. J.F. Nie and Dr. S.M. Zhu at Monash University in Melbourne, Australia. The studies carried out by the group at Monash University yielded general microstructure analysis and an array of creep test data at various load-temperatures in order to evaluate the creep life and power-law factor for this alloy [1, 2]. Creep tests require a relatively long time to collect a sufficient quantity of data, since each creep specimen may endure up to several weeks or months before eventual

failure. Therefore, this joint effort by the two universities taking separate paths in research methodology was envisioned to accelerate the gathering of knowledge on these modern alloys.

1.2.2 Characterization of MRI Alloys

The study of phase characterization in MRI alloys was carried out based on the following academic interests:

- Detailed identification of the precipitate phases was not yet reported in this particular alloy or in other similar composition alloys
- Clarification was necessary on the dominant eutectic phase structure when both high calcium and aluminum was present, which are both strong eutectic formers on magnesium.
- Significance of strontium addition in high calcium alloy system was not yet well understood
- Application of EBSD on phase characterization in light metals was new at the time, and was growing in both academic and industrial interest

The studies identified that the unstable eutectic β-phase ($Al_{12}Mg_{17}$), which is known to be detrimental to creep, was completely suppressed in this alloy. Furthermore, the combined use of TEM and EBSD enabled the identification of strontium as a substitutional element in the grain boundary phase $(Mg,Al)_2(Ca,Sr)$. These observations were presented at the TMS 134th Annual Meeting, and the manuscript was subsequently published in the conference proceedings [1].

1.2.3 Study of creep in pure magnesium

Almost all common magnesium alloys undergo creep deformation via a mechanism broadly classified as “power-law” creep, characterized by the dependence of creep rate to the applied stress by a power factor *n*.

According to the deformation mechanism maps published by Frost and Ashby [2], the power-law creep regime could be separated into “high temperature” or “low temperature” power-law creep, where a transition in the aforementioned power factor separates the two mechanisms. However these claims were primarily based on statistical correlations with empirical rate equations, and the contrast had never been clearly illustrated in real experimental observations on one particular material.

Furthermore, a literature review showed that information regarding the creep properties and behavior of pure magnesium was significantly lacking. Fundamental studies of creep in pure magnesium have not been published since the 1950~60’s [3, 4]. Meanwhile, there has been an industrial focus on Mg-Al alloy systems, while pure magnesium was yet to be studied using modern advanced techniques. This presented the present project with an opportunity to fill a hole in the technical knowledge of creep in magnesium.

There has always been an interest in observing the sequential development of microstructure to elucidate mechanisms of change, rather than characterizing ‘before and after’ cases. A case in point is the recent real-time synchrotron study of a copper alloy undergoing creep [5]. Electron backscatter diffraction (EBSD) enables the simultaneous observation of surface microstructure and analysis of crystallographic orientations that was previously only possible in transmission electron microscopy (TEM) and high-energy diffraction techniques. There are several significant advantages of EBSD (1) it is a

scanning electron microscopy (SEM) based surface analysis technique that does not require the destructive specimen preparation required by TEM, (2) a relatively large amount of the data on many different grains can be obtained quickly with higher spatial resolution than is presently possible using synchrotron methods.

Therefore, in this research program, a unique attempt was made to track and characterize the contrasting microstructure evolution of pure magnesium during both low temperature and high temperature power-law creep using a sequential EBSD technique, rather than conventional post-failure microstructure study. In this method (as mentioned previously), a selected area of a sample is exposed to fixed creep conditions and the test is interrupted periodically so that the selected area can be characterized using EBSD mapping. This method reveals the sequence of microstructural development to be illustrated by morphological and crystallographic data over a relatively large area.

It must be noted that a surface analysis technique such as EBSD may reveal microstructural development that differs from the (internal) bulk volume of the material. However, in many industrial applications of magnesium, such as sheet or intricate die-cast components, the specimen thickness is relatively small in relation to the grain size and thus the present EBSD analysis should still provide a relevant representation of the overall creep mechanisms. Another concern about interrupted creep tests is that the resultant creep properties many not accurately represent those of uninterrupted, continuous creep deformation, due to various factors such as shock loading and stress relaxation. Reports by Regev on comparison between continuous and interrupted creep tests of AZ91D alloy suggest that such interruptions will inevitably shorten the creep life of the material and possibly accelerate the creep rate to a small degree [6]. However, the proposed sequential creep/EBSD technique will still be an effective tool as long as the underlying mechanisms

of creep are consistent, since this is the primary objective of the research. It must also be noted that a large majority of creep environments in actual industrial applications (e.g. automotive and aerospace) are discontinuous and interrupted.

The main experimental outcome of this research, irrespective of such considerations, was to observe the microstructural (i.e., morphological and crystallographic) development of pure wrought magnesium during creep. Cumulative creep rate curves were compared with continuous creep data from previous studies collected by Frost and Ashby [2] to allay possible doubt about the validity of this technique.

1.2.4 Study of creep in MRI-153M alloy

The sequential creep/EBSD technique was found to be very effective in revealing the underlying deformation mechanisms in pure magnesium. In light of this, the same methodology was then applied to the fundamental study of microstructural evolution during creep of high-pressure die cast alloy MRI-153M. Significance of this study lies in the fact that this alloy and other similar composition Mg-Al-Ca-Sr alloys are one of the most popular creep resistant magnesium alloys used in the automotive industry, yet there has been little studies carried out in understanding the underlying mechanisms of its improved creep properties.

In comparison to the preceding study of pure magnesium, the study of MRI-153M introduced additional complexities that needed to be taken into consideration. In particular, a complex dendritic microstructure of the MRI-153M alloy may behave differently to the predictions based on homogeneous equiaxed grain structure. With dendritic structures, it is critical to distinguish between secondary dendrite arm boundaries and random, high angle grain boundaries between dendrites, since these may affect the creep properties in

different ways. Confusion arises because many of the past studies on the creep of magnesium alloys have simply referred to any dendrite arm boundary with intermetallic particles as grain boundaries, irrespective of their crystallographic misorientation. A further complexity to the present alloy is that intermetallic phases are distributed on both primary and secondary dendrite arm boundaries.

The main purpose of this study was to describe the microstructural evolution of the alloy MRI-153M under a range of creep conditions. Particular interest was held in identifying underlying dominant creep deformation mechanisms, and describing any changes in mechanism that might occur as conditions were changed. As implied earlier, it was also important to account for how the different types of boundaries may affect the creep behavior.

1.3 LAYOUT OF THIS THESIS

Contents of each of the eleven chapters are briefly summarized as follows.

Chapter 2 begins this thesis by introducing the reader to a basic overview of magnesium and its alloys. In particular, some of the key alloying elements are introduced, followed by a brief introduction to the fundamentals of power-law creep. The discussions do not go deeply into fine technical details, since there are many excellent textbooks available in each of these topics [4, 9, 10, 11].

Chapter 3 explains some of the procedural techniques involved in the surface preparation of magnesium alloys for optical and electron microscopy. Special focus was placed on specific techniques for EBSD and TEM specimen preparation. The intention of this chapter was to provide a reference for future work on similar alloys, since magnesium is one of the

most difficult materials to achieve a satisfactory quality of specimen preparation.

Chapter 4 utilizes the techniques discussed in Chapter 3 to perform microstructural studies of magnesium alloys. The work started with a basic study of commercial AZ91D alloy microstructure, followed by more detailed analysis of the MRI series creep resistant magnesium alloys. The latter part of the chapter draws from a conference proceedings article published during the course of this research [1].

Chapter 5 provides a summary of power-law creep models used to predict the creep rate of pure magnesium and MRI-153M alloy, as a preliminary analysis prior to the commencement of the actual sequential creep/EBSD studies carried out on these materials. The model results are compared against the actual creep data obtained from the subsequent chapters.

Chapter 6 presents the sequential creep/EBSD analysis carried out on specimens of pure magnesium. Comparisons of the two contrasting creep specimens and their behavior are discussed in detail. This chapter was drawn from a journal article published during the course of this research [7].

Chapter 7 briefly summarizes the study of post-creep pure magnesium specimens from Chapter 6 using Transmission Electron Microscopy (TEM) to verify and augment the observations made using EBSD.

Chapter 8 describes the application of the sequential creep/EBSD analysis technique to the creep resistant magnesium alloy MRI-153M. Tensile specimens were tested at various stress levels at a single temperature to observe the changes in the creep microstructure.

Chapter 9 provides an overall conclusion to this thesis by pointing out the key academic

achievements.

Chapter 10 briefly discusses some of the potential future directions that may be derived from the outcomes of this research program.

Appendix A summarizes all of the work undertaken on the development of a low cost creep test machine used for the sequential creep/EBSD analysis technique. The initial design concepts and some of the early design methodologies are discussed, followed by the presentation of the resultant test system that was constructed. This chapter also discusses some of the initial calibration procedures carried out on the creep test machine in order to verify its effectiveness and reliability. In particular, the accuracy of the LVDT extensometer and the specimen-heating unit is discussed in detail.

Appendix B explains the specific techniques used in the acquisition of automated EBSD orientation maps used for the sequential creep/EBSD technique. Similar to Chapter 3, this chapter was written as a general guide for potential future work in this field of research.

Appendix C contains a copy of journal papers published during the research

Chapter References

[1] T. Sato, B. L. Mordike, J.-F. Nie, M. V. Kral, Magnesium Technology 2005 (2004) 305.

[2] H. J. Frost, Ashby, M.F., Deformation-Mechanism Maps, Pergamon Press, 1982.

[3] C. S. Roberts, JOM 5 (1953) 1121.

[4] W. J. M. Tegart, Acta Metall. 9 (1961) 614.

[5] A. Pyzalla, B. Camin, T. Buslaps, M. Di Michiel, H. Kaminski, A. Kottar, A. Pernack, W. Reimers, Science 308 (2005) 92.

[6] M. Regev, O. Botstein, M. Bamberger, A. Rosen, Mater. Sci. Eng. A 302 (2001) 51.

[7] T. Sato, M. V. Kral, Metall. Mat. Trans. A 39 A (2008) 688.

CHAPTER 2 - OVERVIEW OF MAGNESIUM AND ITS ALLOYS

2.1 HISTORY AND RECENT DEVELOPMENTS IN MAGNESIUM ALLOY TECHNOLOGY

Basic properties and applications of common magnesium and its various alloys are not discussed in this thesis, since the reader is expected to have sufficient fundamental knowledge in this topic. However, some key facts are outlined below for the sake of completeness. For further details regarding general information on magnesium alloys, a textbook by K.U. Kainer "*Magnesium Alloys and Technology"* [1] is recommended. In this study, when discussing the "common" magnesium alloys, it is assumed to be about the Mg-Al eutectic alloys and their variants. Recent advances in other families of magnesium alloys such as Mg-Li [2, 3, 4, 5], and Mg-Y [6, 7, 8], although very important, are not discussed in this thesis.

Within the scope of this research, it can be said that one of the earliest successful cases of magnesium alloy technology in commercial applications is in sand casting of automotive engine components in the 1930's, followed by the boom of heavy engineering demands leading towards the Second World War. However, due to the severe limitations on their mechanical properties these alloys were only used in specialized low-volume productions outside of critical structural applications for the remaining part of the 20th century [1].

The early examples of magnesium alloys were somewhat primitive and experimental compositions of Mg, Al, Si, Zn and other various alloying elements, which, due to their

low melting temperatures and high castability, could be treated as extensions to the already well established aluminum alloys production facilities and techniques. Popularity of magnesium in consumer market has been deterred by a common myth that the magnesium alloys are flammable and may spontaneously combust during ordinary operation environments. However, this is unlikely to occur unless the alloy is exposed to direct flame at extremely elevated temperatures (~600 ºC) [2].

The primary advantage of selecting magnesium alloys over other metals is due to its high specific strength, meaning that there is a potential for weight-saving benefits by the use of magnesium alloys over conventional steel or aluminum components. Throughout the 1940's to 1950's, magnesium alloys were abundantly used in the then-booming automotive industries for fabrication of large components of relatively simple geometry, such as wheels and transmission casings. On the other hand, aviation industries, now entering the post-war jet engine era, found magnesium alloys suitable for their pursuit for airframe weight reduction that directly relate to fuel savings and more payload [3].

To summarize, on a social level, some of the key advantages of magnesium alloys were twofold:

Potentials for weight reduction

Engineering demands of the recent era placed a significant focus on the engineering of high volume production of high speed, low cost transport options, such as aircraft and private automobiles, compared to the preceding generation that focused on the development of heavy-duty structural metals used for shipbuilding and civil constructions.

This is primarily attributed to the pace of engineering progress in these new commercially oriented industries [4] and economies of scale [5], whereby the old philosophy of

lifetime durability was now redundant, since the new technologies could make the preexisting designs obsolete and undesirable long before the expiry of the actual materials they are fabricated from. What mattered now instead were the performance gains obtained by opting to select materials even though they may potentially have shorter service life compared to the more traditional structural alloys.

Relative ease of production

The early applications of magnesium alloys were primarily in sand castings for two main reasons. First, the aforementioned rapid technological developments now demand shorter design lifecycles with faster adaptation of new design ideas, which is the primary advantage of low-volume sand casting techniques. Second, Mg-Al alloys' low eutectic melting temperatures and relative ease of raw material acquisition allowed low-volume producers to enter new diversifying industries without the need for extensive large scale production facilities, unlike their steel and aluminum counterparts that require strict vertical integration and high volume production plants.

With such advantages over other structural casting alloys, the future of magnesium alloy development appears bright. However, magnesium alloys have inherent disadvantages that severely limit their potential use in critical engineering applications.

2.2 DISADVANTAGES OF MAGNESIUM AND ITS ALLOYS

2.2.1 Introduction

Magnesium alloys do not have a clearly defined finite fatigue limit, and in conjunction with their low proof strengths (~200 MPa), fatigue manifests a significant role in common applications of these alloys [6]. This is further accentuated by the fact that the majority of critical applications of magnesium alloys are in the automotive and aviation industries where vibration loading is commonplace [7].

The explanation for fatigue mechanism of common magnesium alloys cannot be attributed to one single phenomenon alone. The initial crack formation is a compound consequence of localized imperfections, typically at the component surface due to corrosion, casting defects, forming textures, and/or creep voids. In particular, high-cycle fatigue studies of Mg-Al alloys show direct relationship between fatigue life and pre-existing void density [15, 16]. Furthermore, interactions of corrosion-fatigue are of recent academic interest [17, 18, 19]. Once the crack originates, the anisotropic nature of the magnesium hcp lattice leads to the formation of localized stress concentrations. Particularly in Mg-Al alloys, the brittle grain boundary intermetallic phase is reported to provide easy paths for fatigue crack propagation, which is further accelerated by the localized crevice corrosion mechanism [20, 21]. Therefore, it could be said that the study of fatigue in magnesium alloys cannot be a discrete subject in its own right, but merely a consequence of other defect and deformation mechanisms, since it is practically unrealistic to conduct studies on fatigue properties of defect free magnesium alloy specimens.

2.2.2 Corrosion of magnesium alloys

Atmospheric corrosion plays a significant role in the corrosion of magnesium alloys. Magnesium forms MgO, MgH_2 and $MgOH_2$ oxide layer on the surface upon exposure to the atmosphere. However, unlike aluminum that forms a continuous film of relatively inert oxide layer that protects the subsurface layer, magnesium oxide layer is discontinuous and plays a significantly lesser role as a protective film [1, 8]. Therefore, oxidation does not stop at the surface as it does for aluminum, but persists to attack the bulk of the magnesium alloy by pitting and crevice corrosion mechanisms [9]. In Mg-Al alloys, this acts in conjunction with electro-potential differences induced by the intermetallic precipitates such as $Al_{12}Mg_{17}$, resulting in severe intergranular corrosion damage under even moderately corrosive conditions such as a marine environment [10]. There has been some progress in the development of corrosion resistant magnesium alloys, especially due to the improvement in regulating the level of impurities (Fe, Cu, Ni) during the casting processes [1, 11]. A common industrial solution to the corrosion issue is surface modification and coating (e.g. paint), where significant progress has been observed in the recent years [26, 27]. The topic of corrosion was not pursued any further in the course of this research.

2.2.3 Other contributions to the properties of magnesium alloys

Recent advances in computational thermodynamics and fluid flow models on casting mold design have improved the issues associated with castability of magnesium alloys. Similarly, the use of sophisticated diecasting techniques such as thixo-forming, squeeze casting [28, 29], rheo-casting [12] and vibration casting [13] allows further control of the resultant microstructures. However, many other casting process artifacts still act as the major contribution to the industrial issues in magnesium alloys. Study of various casting

defects, such as the effect of void density on the mechanical properties [32, 33], may be an interesting topic for an industrial process optimization research, but this was not part of the current academic research program.

Another contribution to the mechanical properties is the anisotropy and the formation of nonrandom texture in materials processed at high stress levels, such as in extrusion or sheet forming [34, 35]. Such textural properties cannot easily visualized under crude industrial testing facilities, and the consequences of these parameters are not fully appreciated in many situations, compared to the more obvious visual impact of imperfections caused by void formation or corrosion.

2.3 CREEP OF MAGNESIUM AND ITS ALLOYS

2.3.1 Introduction

Creep is a mechanism of deformation in materials that is governed by applied load, time and temperature.

Although it is often easily compared to simple plastic yield of a material, the phenomenon of creep must be treated separately. The critical differences are:

- Creep deformation is a thermally activated phenomenon that can occur at stress levels well below the yield point of the material (i.e. within the elastic limit) at the specific operating temperature

- Creep deformation is a time dependent phenomenon, whereas plastic yield is solely governed by the applied stress within a reasonable range of strain rate.

Within the scope of the current research project, the phenomenon of creep is defined as a behavior of crystalline metals that undergo time dependent plastic deformation at a stress level well below the yield point when exposed to elevated temperatures, as illustrated on Figure 2.1.

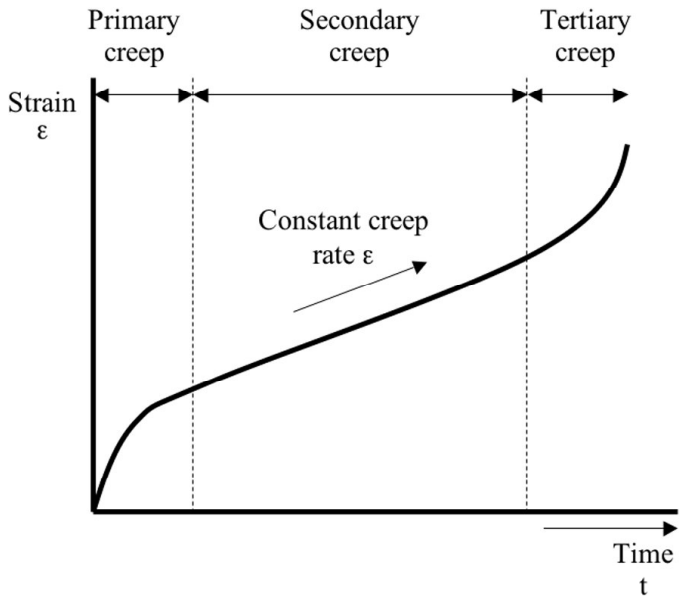

Figure 2.1. A hypothetical time-elongation graph of a typical creep response

In a physical sense, this means that under certain high temperature conditions, a component prone to creep can continue to deform slowly (where strain rate can be as little as 10^{-11}/s, i.e. ~3% per year) and eventually result in catastrophic failure, possibly in a span of months, or even years of service, even though the mechanical design ensured the loading conditions to be well below the material's yield point, and the temperature level is lower than the recrystallization temperature (approximately half the melting temperature).

The underlying mechanisms of creep can vary depending on each material, but the study of creep in magnesium is a popular topic because of its very low melting temperature (650ºC), suggesting that the temperature level to activate creep deformation can be as low as 100 ºC, which is commonly experienced in many practical applications.

A simple example of creep in magnesium can be seen in early efforts to use magnesium castings for automotive engine blocks. Although the blocks were designed considerably below their yield strength, one of the unforeseen problems was that the mounting bolts

screwed into the magnesium engine became loosened over time [14], resulting in the engine unexpectedly detaching from the chassis. This was attributed to the slow creep deformation of highly stressed regions at the bolt interface assisted by the elevated operation temperatures.

2.3.2 Mechanisms of creep in magnesium

The general phenomenon of creep deformation can be attributed to several underlying microstructural and crystallographic characteristics of the subject material. However, since creep deformation can take place in a wide range of conditions from "high temperature - low stress", to "low temperature – high stress" condition, there are a variety of creep mechanism regimes associated within a range of conditions that can be classified into various families.

The experimental basis of creep study is a simple constant-load tensile test carried out at elevated temperatures, to record the time vs. elongation for a given stress and temperature to obtain the "creep rate" of the material, which is effectively a strain rate with the conventional unit of strain per second (/s) as shown on Figure 2.1.

The important point here is that the creep curve can be divided into three separate sections known as primary, secondary, and tertiary creep, as illustrated on Figure 2.1. The initial primary stage of creep is somewhat difficult to analyze, since the nature of the primary stage is the initial release of accumulated dislocations within the material becoming rapidly mobile due to the applied stress and thermal energy. Obviously, this will be influenced by the amount of prior deformation (e.g. cold work) and availability of easy dislocation glide paths, where many of the creep tests conducted in industrial grade alloys result in a large scatter of data [15]. Recent advances in atomic and crystallographic level computer

simulations enable further insight into the primary creep stage, but this is not discussed in this research. Many examples of advanced studies in such fields [38, 39] can be seen in a special feature volume of Metall. Mat. Trans A, Vol. 33, Issue 3 (2002).

The primary creep stage ends once the mobile dislocations are pinned by obstacles and become immobile. The strain rate drops significantly due to this strain-hardening effect, and the creep deformation may not continue beyond this point. However, given sufficient stress and thermal energy, a somewhat equilibrium state of constant strain rate deformation can be achieved. This is identified as the secondary creep stage, which is the focus of interest in majority of creep studies, since this is where a large proportion of deformation takes place. Eventually, localized necking of the deformed region allows plastic collapse to take place, which is manifested by an accelerating creep rate in the stage known as tertiary creep.

In studies of creep, the term "power-law creep" is often used. This does not imply a certain microstructural mechanism or any specific underlying phenomena, but it is simply a term based on the observation from creep tests that indicate a relationship where the secondary creep strain rate fits into a function that is proportional to the *n*-th power of the applied stress. The term "power-law breakdown" is used when the creep data diverts from this power-law behavior due to excess thermal energy approaching the recrystallization temperature of the material. On the other hand, excess creep stress would simply result in conventional yield phenomenon to take place.

Before discussing the theoretical aspects of power-law creep deformation, it is worth noting that the implication of power-law (creep rate proportional to *n*-th power of applied stress) suggest that even a small change in the applied stress can affect the creep rate by

several orders of magnitude, since the effect of applied stress is exponentially magnified by the power factor n (typically around 2~10).

In this research, the primary focus was placed on the behavior of typical power-law creep deformation of magnesium, because although other mechanisms exist at extremes of the load/temperature conditions, their resultant creep rates and lives are unrealistically too short (few minutes), or too long (several decades) to be of significance in practical applications.

The fundamental cause of power-law creep deformation is the activation of recovery mechanisms at elevated temperatures [16-18]. Even below the recrystallization temperature, thermal energy can be sufficient to allow pinned dislocations to become mobile by variety of mechanisms such as dislocation climb, which results in the slow transport of matter allowing for deformation to propagate. This justifies the reason why creep becomes prominent at higher temperature (more thermal energy) and higher applied stress, or due to the amount of prior stress accumulation that increases the dislocation density within the material.

2.3.3 Theories of power-law creep

This section briefly discusses some of the key aspects of power-law creep that are particularly relevant to this research. For further reading, an overview of the general theories of power-law creep mechanisms are explained in "Deformation-Mechanism Maps" by H.J. Frost and M.F. Ashby [17].

As mentioned earlier, the deformation induced in the power-law creep regime is attributed to the activation of alternative paths for pinned dislocations. To simplify the explanation of

this rather diverse topic, it is best to limit the discussion to the theories directly related to magnesium and its alloys. Mobile dislocations are most likely to travel along crystallographic planes that require effort the lowest activation energy, known as glide planes. α-Mg is organized in a hcp (hexagonal close packed) atomic arrangement, in which the conventional Miller indices notation is shown in Figure 2.2a.

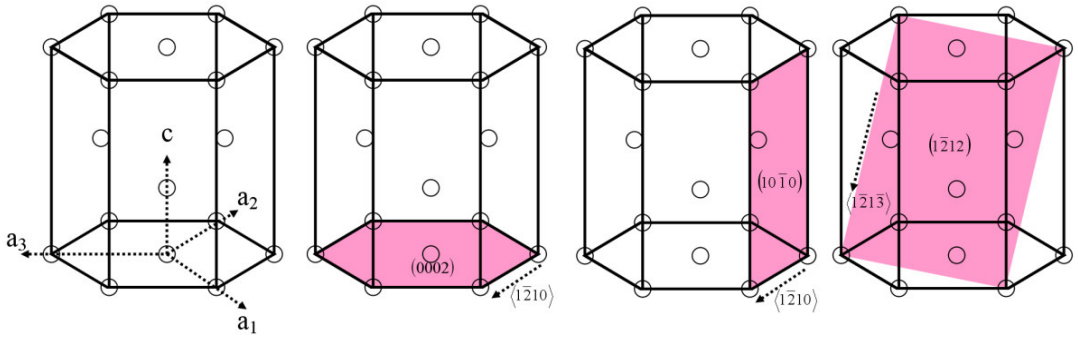

(a) (b) (c) (d)

Figure 2.2. A single hcp lattice with (a) Miller indices notation for the coordinate system, and examples of (b) basal slip, (c) prismatic slip, and (d) pyramidal slip

The most favorable dislocation glide plane for hcp magnesium is its basal plane (0002), along the direction in the "a" axis as illustrated on Figure 2.2b. Since this is the closest packed plane, a defect requires least distance to jump to the adjacent lattice site. Therefore, in an ideal hcp magnesium crystal, the basal slip will act as the easiest path for dislocation glide. However, in polycrystalline magnesium, strain hardening takes place when dislocation gliding on basal planes become pinned at interfaces such as grain boundaries and other obstacles [16]. This dislocation pinning plays a role in slowing down or completely halting the plastic flow process, which is most clearly illustrated by the deceleration of the primary creep stage (Figure 2.1).

When sufficient thermal energy and stress is applied to the material, the lattice will possess

sufficient energy to activate additional deformation mechanisms, such as dislocation "climb" to the adjacent glide planes of lower dislocation density. Furthermore, increase thermal energy and stress allow the material to overcome the critical resolved shear stress (CRSS) to activate slip in the planes other than the primary glide plane. The CRSS required to activate such non-basal slip depends on the ratio of hexagonal base and column lengths (c/a ratio). In particular, the activation of pyramidal slip is of great importance, since this is the only practical mechanism other than twinning that allows deformation in the non-basal direction as illustrated on Figure 2.2d. Studies of the non-basal slip mechanisms in hcp crystals carried out by Barnett [19] shows a relationship between CRSS of various slip modes as illustrated on Figure 2.3. Detailed microstructure studies of various magnesium-based alloys by Agnew [2, 44, 45] further stress the importance of crystallographic texture in plasticity. In hcp crystal structures such as magnesium, these non-basal slip modes are difficult to achieve since the potential glide planes require much larger activation energies compared to the basal slip. However, even a small probability occurrences of these non-basal dislocation motions can offer alternative paths for pinned dislocations to propagate, thus allowing the overall material to overcome the strain hardening effect, although now at a much lesser rate than the primary creep stage. It is also known that the addition of certain alloying elements lowers the CRSS to activate non-basal slip, typically by modifying the c/a ratio of the primary lattice. For example, high elevated-temperature ductility in Mg-Li alloys is attributed to the ease of activation of prismatic slip [20]. This deformation phenomenon, known as creep assisted by dislocation climb, is commonly the dominant deformation mechanism in what is classified as "power-law" creep.

In fact, the deformation mechanism is not as simple as an ideal model as described above,

since it has a more complex nature due to the interaction of various dislocations with each other. For example, an ordered array of parallel dislocations may preferentially form a low angle kink boundary, eventually forming subgrains [16], or opposite dislocation dipoles can cancel each other out or forming sessile loops [18]. Because each of these phenomena occurs in a statistically significant quantity, the prediction and simulation of creep deformation based on the dislocation model continues to be a difficult topic.

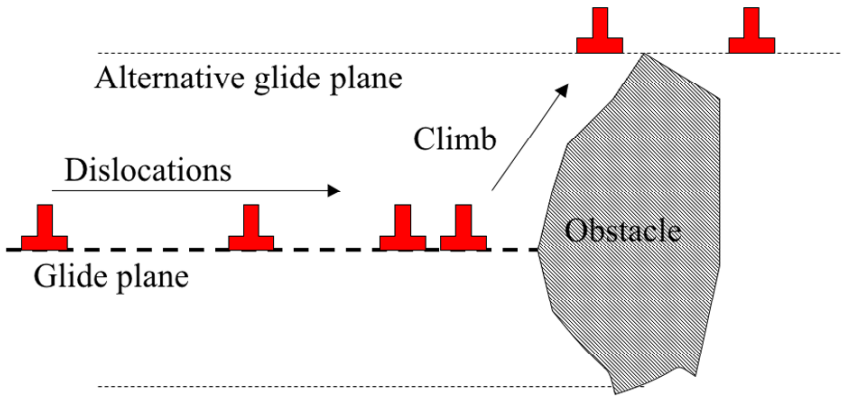

(a)

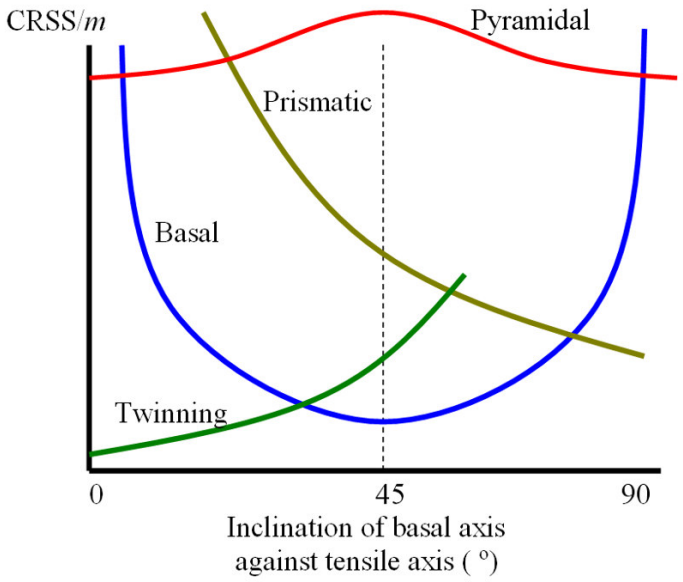

(b)

Figure 2.3. A simple schematic model of (a) dislocation climb and (b) the effect of crystal orientation on the activation of various slip modes

2.3.4 Study of power-law creep in pure magnesium

In power-law creep of pure magnesium, dislocations that are generated or previously pinned by obstacles are now able to migrate within the magnesium lattice by the glide+climb mechanism due to the new thermally activated slip systems. This is the basis for the temperature, stress, and time dependence of deformation during secondary creep. In summary, the rate of secondary creep deformation can be influenced by various factors such as:

- Differences in the CRSS required to activate various slip systems
- Crystallographic texture of the microstructure
- Presence of high angle misorientation boundaries (grain boundaries)
- Presence of low angle misorientation boundaries (subgrain boundaries)
- Initial dislocation density accumulated in pre-creep material.

Unfortunately, fundamental studies of creep in magnesium have been lacking since the 1970's and many of the above theories have been taken for granted without clear experimental evidence upon creep. This is primarily due to the greater interest in alloys such as Mg-Al that are more commonly used in the industry. However, it is not possible to understand the creep mechanisms of complex alloy systems without establishing that the theories of deformation mechanisms do agree with the creep of magnesium. Therefore, this research begins by carrying out extensive study of the deformation mechanisms in pure magnesium under creep. Details of the underlying theories and mechanisms of creep in pure magnesium are discussed further in Chapter 5 and 6.

2.4 CREEP RESISTANT MAGNESIUM ALLOYS

2.4.1 Introduction

Magnesium is one of the most attractive metals for the use in automotive components due to their high strength to weight ratio and high castability. However, inherent creep resistance of pure magnesium is relatively poor, and "High temperature" creep deformation may refer to temperatures as low as 100 ºC, which is frequently experienced in situations not usually considered to be a "high temperature" environment (e.g. automotive and aviation components). Therefore, the studies to improve the creep resistance of magnesium have been of great interest over many decades.

A substantial amount of alloying has historically been carried out to improve the upper threshold of the operating temperature range for magnesium alloys, but this has always been a difficult issue to overcome since many of the alloying elements effective for room temperature properties and castability of magnesium (e.g. aluminum) can in fact be detrimental to the creep properties of the alloy.

Some of the common alloying elements used in magnesium alloys, and their basic contributions are summarized below. However, it must be noted that all alloying elements introduce more than one effect in the overall magnesium alloy systems, for example, improvement in tensile strength may be compromised by an increase in corrosion rate.

Basic alloying elements:

- aluminum, zinc, manganese.

Special alloying elements added to improve creep properties:

- rare earth (RE) (e.g., yttrium, neodymium, mischmetal (MM)),
- alkaline earth (calcium, strontium).

2.4.2 ASTM standard magnesium alloy designations

In magnesium alloys, the ATSM standard designations are commonly used and are relatively easy to follow in comparison to the similar standards on aluminum alloys. Most specialist proprietary alloys developed in the recent years are based around the basic ASTM compositions, with variation in finer details such as the level of impurities or extra additions of rare or exotic alloying elements.

An example of the ASTM designation is AZ91D. The first two of alphabetic characters indicate the major alloying elements as shown on Table 2.1, followed by their nominal compositions in percentage, which in this case is 9% Al, 1% Zn. The last character is a suffix added to define variations on the basic alloy system, such as the upper limit of impurities present. The designation code itself does not indicate the overall composition of the alloy, (i.e. AZ91 does not contain only 9%Al and 1%Zn) but is used as an indication of the general family of alloy systems. The actual composition limits are specified in ASTM standards, such as the examples of AZ91A, AZ91D and AZ91E shown

Table 2.2. In this case, AZ91D is the high purity variant and AZ91E is the corrosion resistant variant of the basic AZ91A standard.

Individual elements can be classified into four broad groups:

- elements to improve mechanical properties,
- elements to improve environmental resistance (creep, corrosion),
- elements to improve castability,
- impurities that must be removed.

Table 2.1. ASTM magnesium alloy element codes

A	Aluminum	M	Manganese
E	Rare Earth	Q	Silver
H	Thorium	S	Silicon
J	Strontium	T	Tin
K	Zirconium	Z	Zinc

Table 2.2. ASTM standard compositions for AZ91D and AZ91E (wt%)

	AZ91A	AZ91D	AZ91E
Al	8.3-9.7%	8.3-9.7%	8.1-9.3%
Mn	> 0.13%	> 0.15%	0.17-0.35%
Zn	0.35-1.0%	0.35-1.0%	0.4-1.0%
Si	< 0.50%	< 0.10%	< 0.20%
Fe	-	< 0.005%	< 0.005%
Cu	< 0.10%	< 0.030%	< 0.015%
Ni	< 0.03%	< 0.002%	< 0.0010%
Other	< 0.30% (total)	< 0.02% (each)	< 0.01% (each) < 0.30% (total)

Detailed descriptions of the common alloying elements and their effects are summarized below. The variety discussed in this section is limited only to those alloying elements and the effects that have direct significance to the current research program. For example, some alloying elements introduce contrasting effects when added in small or large quantity (e.g. zinc) [21]. However, this discussion will only mention the composition range that is relevant to the alloy systems studied in the present research.

2.4.2.1 Aluminum

Aluminum is the most frequently used alloying element in magnesium alloys, and is used in the largest percentage quantity. In fact, when a term “magnesium alloy” is used, it generally refers to Mg-Al alloys of various compositions ranging from 2 to 9 wt%.

Figure 2.4 is a binary phase diagram of magnesium and aluminum. Aluminum has a maximum solid solubility of 12.7 wt% magnesium and forms a eutectic with magnesium

having eutectic composition of Mg - 32 wt% Al. The binary eutectic consists of primary α-Mg and $Mg_{17}Al_{12}$ intermetallic phase commonly referred to as β precipitate phase, arranged in a typical lamellar eutectic distribution as shown on the optical micrograph of AZ91D (Mg-9Al-1Zn) alloy in Figure 2.5.

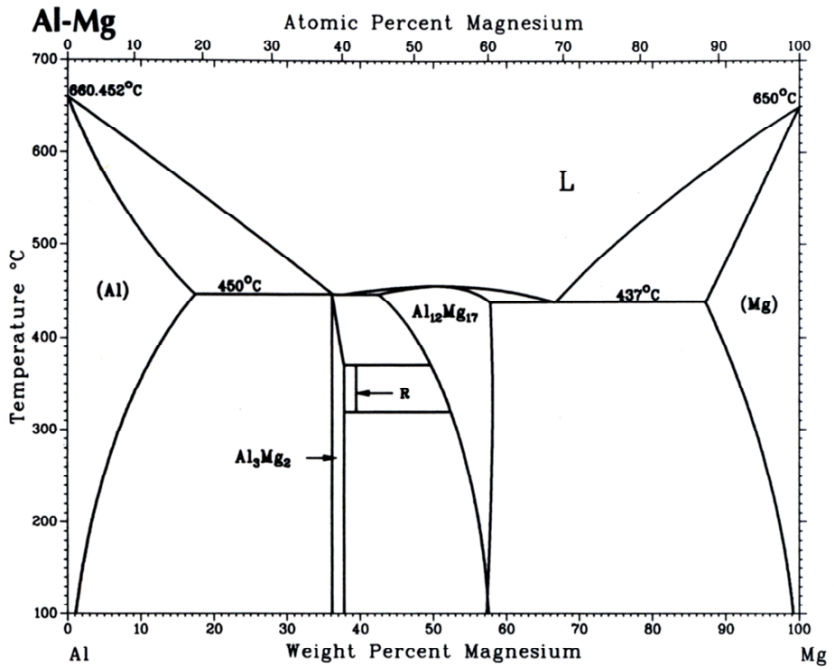

Figure 2.4. Mg-Al phase diagram (ASM Handbook)[22]

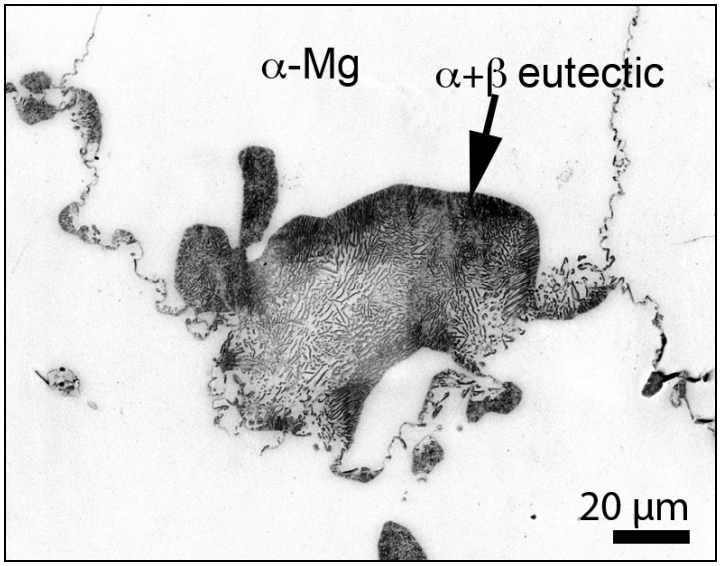

Figure 2.5. Lamellar eutectic structure in AZ91D alloy

Typically 2~9% aluminum is added to the magnesium to providing strengthening via the complex lamellar network and solid solution. The increase in room temperature mechanical properties is significant, as illustrated by the comparison on Table 2.3. However, the addition of aluminum does not typically contribute to improvement in high temperature properties by itself, and in fact exhibits detrimental effects due to its reduction in ductility upon creep deformation. This is attributed to the brittle nature of the lamellar β structure, and the unstable precipitation and age hardening kinetics of the solid solution aluminum in α-Mg [23, 24].

Table 2.3. Comparison of mechanical properties of pure Mg and AZ91D

	Pure Mg	AZ91D
Tensile (MPa)	130	230
Yield (MPa)	100	150
Elongation (%)	8	3

2.4.2.2 Zinc

Zinc forms a solid solution of up to 6.2 wt% in magnesium, heat treatments result in a series of precipitation events from the formation of GP-zones, followed by coherent precipitates, and eventually incoherent precipitates [46, 50, 51] similar to the behavior of Al-Cu alloy systems. Note that the relationship between Al (atomic number (Z) = 13, earth metal) against Cu (Z = 29, metal), is similar to Mg (Z = 12, earth metal) against Zn (Z = 30, metal). Such metastable precipitates provides additional resistance to basal deformation [25]. Zinc is commonly added as a strengthening element due to its low cost and stability, but is limited by the brittleness and poor castability it introduces. In modern advanced alloys, the zinc can be replaced by other stable precipitate formers (e.g. Ca and RE).

2.4.2.3 Manganese

Manganese is added in excess of saturation level in order to trap iron and other impurities within the melt. This is identical in concept to the addition of manganese in aluminum alloys. For magnesium alloys, the level of manganese addition varies depending on the original level of iron contamination of the melt.

The excess manganese forms a discontinuous, stable hard intermetallic compound Al_8Mn_5. Excess addition of manganese is detrimental since the intermetallic compounds decrease ductility and also reduce castability of the material. The amount of manganese is reduced in modern high performance alloys due to the reduction in impurity level of the melt.

2.4.2.4 Zirconium

Zirconium is a special alloying element since it cannot be used in conjunction with aluminum unlike other common alloying elements. Zirconium has an excellent grain refinement effect on primary α-Mg, but becomes ineffective when aluminum is present since the zinc and zirconium form a stable intermetallic compound [26]. Therefore, magnesium alloys containing zirconium are generally only produced in aluminum-free compositions, such as the popular ASTM ZK (zinc-zirconium) series alloys. This research program does not involve the study of this alloy group [21].

2.4.2.5 Rare earth elements

None of the alloying elements described above contribute to the improvement in elevated temperature properties of magnesium alloys. This is because the primary hcp α-Mg structure and many of the intermetallic compounds have inherently low thermal stability [27]. Rare earth elements are the most common additions for improving the temperature

resistance of magnesium alloys [36, 54, 55]. In general, rare earth is added in a "mischmetal" compound consisting of various rare earth elements such as cerium and neodymium. This is because the process of isolating these elements is expensive, yet has no significant benefit on the resultant properties. The RE elements have low solid solubility (< 2wt%), and forms various intermetallic phases with magnesium. The combination of these properties results in a favorable outcome, since:

- Mg-Al-RE alloys have low solidification temperature, and therefore are easy to cast and minimizes the risk of hot cracking.

- Solidification takes place without significant supersaturated solid solution, and therefore avoids subsequent precipitation behavior during creep.

The intermetallic phases such as Mg_3RE and Mg_4RE form a very stable lamellar grain boundary precipitate network that provides resistance against grain boundary defect transfer kinetics during creep [28]. Most RE alloys are designed with upper ceiling in temperature resistance of up to 250 ºC. This limitation is imposed by the thermal stability of the intermetallic phase. Figure 2.6 shows the comparison between the creep properties of conventional AZ92A against Mg-RE-Zn alloy EZ33A [26].

Thorium has a similar effect to the rare earths on improvement in creep resistance [26] for even higher temperatures in excess of 300 ºC, as illustrated on Figure 2.7. In either case, the critical drawback of these creep resistant alloys is the cost of exotic alloying elements, with the mild radioactivity of thorium as further detriment its potential markets. This explains why these highly specialized alloys are so far only used in small-volume military and aviation applications.

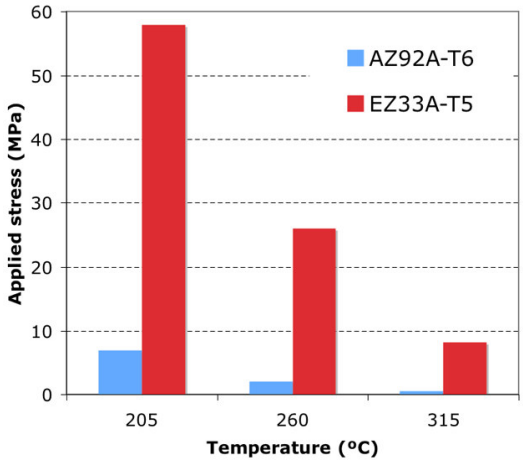

Figure 2.6. Comparison of creep rate in AZ92A and EZ33A. Stress required to undergo creep strain of 0.1% in 1000 hours

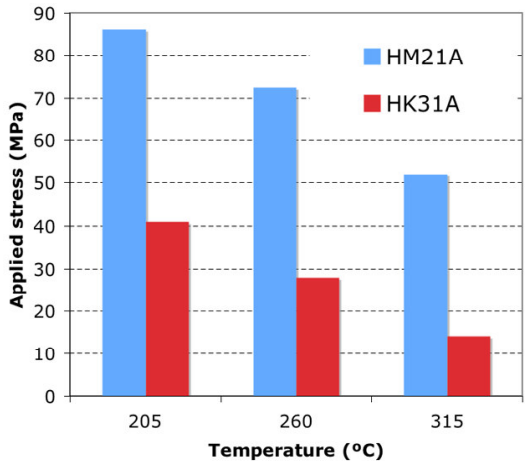

Figure 2.7. Creep properties of HM21A and HM31. Stress required to undergo creep strain of 0.1% in 100 hours

2.4.2.6 Calcium and strontium

Entry of magnesium into mass production market was hindered by the lack of low cost alternatives to the expensive creep resistant alloys. Addition of calcium or strontium was known to provide similar improvement in creep properties to rare earth alloys, but were not commonly used until the last decade due to casting issues such as hot cracking and high

sensitivity to corrosion [14]. However, these problems were overcome in recent times by advances in casting technology, with the introduction of computer-assisted mold design and foundry controls [57, 58, 59] now enabling the production of low defect casting of alloys with poor castability. This is further assisted by the availability of high purity raw materials and improved melt treatments to enable low impurity (Fe, Cu, Ni, heavy metals) content that improves corrosion resistance. It has also been reported that the further additions of zinc restores the castability of high calcium alloys [29].

Typically, calcium and strontium are treated as one group of alloying elements, since both calcium (Z= 20) and strontium (Z=38) are group 2 alkaline earth elements that provide very similar alloying effects to magnesium. Although alloys with calcium and strontium are typically regarded as inferior to Mg-RE alloys, the low cost alloying agents provide strong incentives for industrial mass production such as automotive engine blocks, where requirements for strict process controls are achievable due to economies of scale. The addition of strontium has increased in popularity because of the ready availability of strontium due to its demand as melt modifiers used in aluminum foundries.

2.4.3 Examples of identified phases reported in various Mg-Al-(Ca, Sr, Zn, Mn) alloy systems

Recent growth of interest in calcium and strontium additions has lead to a large number of publications in the study of precipitate phases in these alloys. Magnesium is an alkaline earth with small atomic size, readily forming various compound structures with other elements. Thus, the precipitation mechanisms are not simple relationships based purely on binary compositions, but are interrelated with other accompanying alloying elements. Table 2.4 summarizes a selection of various phases reported in Mg-Al-(Ca, Sr, Zn, Mn) alloys in publications after 2000. The table illustrates the vague nature of the phase

identification in these alloy systems, where a wide range of possible stable intermetallic compositions result in many uncertainties and assumptions upon characterization. In particular, phase identification with EDS/XRD alone was found to be very unreliable because magnesium, aluminum and other alloying elements such as calcium and strontium tend to cluster in the overlapping energy levels and difficult to quantify their compositions accurately.

Table 2.4. Various Mg-Al-(Ca, Sr, Zn, Mn) phases identified in recent literatures

	Material	Phases identified	Techniques
Vogel, Kraft, Starton, Clemens, Rauh, Arzt [30]	Mg - 5Al - 8Zn – (0.3, 0.9)Ca	Al_2(Ca, Zn) $Mg_{32}(Al,Zn)_{49}$ Tau phase $Mg_{32}(Al,Zn)_{49}$ Mg_{32}(Al, Zn, Ca)$_{49}$	SEM, TEM/EDS, SANS
Vogel, Kraft, Arzt [31]	ZA85 Mg – 5Al – 8Zn	$Mg_{32}(Al,Zn)_{49}$ Tau phase $Mg_{32}(Al,Zn)_{49}$	TEM
Ozturk, Zhong, Luo, Liu (General Motors) [32]	GM-B Mg – 4.5Al – 1.9Ca GM-C Mg – 4.5Al – 3.0Ca	Al_2Ca (FCC) [only after annealing] (Mg, Al)$_2$Ca (hcp) [as-cast, partial peaks in XRD]	
Zhang, Couture [33]	Mg – (1.73-6.17)Al – (7.67-14.30)Zn – (0.12-0.40)Mn – (0.47, 0.53)Ca or (0.69, 0.77)Sr	Mg-Zn-Al (variants of Mg_{32}(Al, Zn)$_{49}$) “Complex” Mg-Zn-Al-Ca “Complex” Mg-Zn-Al-Sr	SEM/EDS/XRD
Pekguleryuz (Noranda Magnesium Inc.) (Corporate report)	Mg – 5Al – (1.8-2.2)Sr Mg – 5Al – (1.2-1.7)Sr	$Al_{17}Mg_5Sr_3$(on high Sr) $Al_2Mg_{1-x}Sr_x$(on high Sr) $Al_{12-y}Mg_{17-x}Sr_{x+y}$ (on low Sr) $Al_{10}Mg_{13}Sr$ (on low Sr)	FEG-SEM, STEM, TEM (mentioned but no micrographs shown)
Pekguleryuz (Noranda Magnesium Inc.) [27]	Mg – (2-6)Al – (0-0.25)Mn – (0.1-0.8)Ca Mg – (4.5-10)Al – (0.2-1)Mn – (1-3)RE – (0.1-3)Ca	Al_2Ca Al_2RE	
Pekguleryuz, Renaud (Noranda Magnesium Inc.) [34]	AX508, AX506, AX51 Mg – (4.1-8.9)Al – (0.20-0.29)Mn – (0.6-1.0)Ca	Al_2Ca	SEM/EDS/XRD
Baril, Labelle, Pekguleryuz (Noranda Magnesium Inc.) [35]	AJ62LX Mg – 5Al – 2Sr AJ62X Mg – 6Al – 2.4Sr	Al_4Sr (eutectic with α-Mg) $Al_3Mg_{13}Sr$ $Mg_{17}Al_{12}$	FEG-SEM/XRD, TEM/EDX

2.4.4 Deficiencies of the modern creep resistant alloy development and studies

Based on the brief overview of magnesium alloys in this chapter, it is apparent that the study of microstructural contribution creep in commercial creep resistant Mg-Al-(Ca, Sr) alloys was of great academic and commercial interest. It must be mentioned that in many cases, development of new commercial alloy systems are not necessarily derived from microstructural studies or underlying theories of material science. In fact, the reverse is more customary, whereby the alloy systems that were found to be effective under mechanical testing may be commercialized, which is only later examined in detail for academic interests. This is especially true for commercial applications of light metals, but less so in critical alloy development for defense and aerospace applications. This had resulted in an issue especially in the light metals industry where the producers continue to use basic outdated alloy systems due to their conservatism and lack of knowledge in advanced material science, or conversely, are using new alloys that are tested to show improved performance only under certain test conditions, without any solid scientific reasoning. The gap between alloy development and material science has narrowed in the recent years due to the tighter integration between the commercial industries and academic researches, but are still limited by the following reasons.

- Light alloys, being easy to cast, enable rapid product cycles and adaptation of existing process facilities to new alloys. This lowers the risks involved in small adjustments the alloying or casting processes, and therefore requires less technical risk assessment unlike large scale steel industries.

- In many small-scale foundries, the limitation imposed on mechanical properties is due to the presence of macroscopic defects and poor casting mould designs. Therefore, the microstructural contributions are of lesser importance in perspective, compared to the case of high volume wrought sheet metals that have controlled microstructures.

- Many modern light alloy producers are privately operated and are unlikely to invest significant capital in long term research and development programs. The only exceptions are the large national scale producers such as Noranda (Canada), Norske Skog (Norway), Dead Sea (Israel) and GM (USA), who regularly maintain contributions toward academic publications on light metals research.

These reasons are not to suggest that the light alloy industries are in demise, but to point out that there are large opportunities for academic research contribution to provide further understanding of the material science of vast array of modern alloys. For this reason, a typical example of modern commercial Mg-Al-(Ca,Sr) alloy, namely MRI series Mg-Al-Zn-Ca-Sr alloy system was chosen for detailed phase characterization study.

2.5 MRI SERIES CREEP RESISTANT ALLOYS

This section provides a brief overview of the significance of MRI series of creep resistant magnesium alloys, their compositions and their creep characteristics. Detailed microstructural studies of these alloys are discussed in Chapter 4.

The primary objective of this research program was to relate the contribution of microscopic and crystallographic factors to the creep properties of magnesium and its alloys. For this reason, batches of high quality high pressure diecast specimens of pure magnesium and specialized creep resistant magnesium alloys were acquired as the test subjects to study the underlying creep mechanisms in these alloys.

2.5.1 Basic description of the MRI alloys

An Israeli company, Dead Sea Magnesium Ltd. is one of the global leaders of primary magnesium and alloy ingot production, founded on the abundant magnesium-rich mineral supplies of the Dead Sea (a salt lake situated between Israel and Jordan, famous for its extremely high saline composition).

One of the key operations of Dead Sea Magnesium is the production of patented specialist magnesium alloys with high creep resistance ideal for use in automotive industries, designated MRI (Magnesium Research Institute) series. These alloys are analyzed and studied in collaboration with academic institutes in Israel and abroad, and are one of the most popular family of creep resistant alloys used in the European automotive industries, such as BMW and Volkswagen. Its direct competitors are ASTM AE and AJ series magnesium alloys that are popular in the USA automotive industries [36, 55]. Mechanical

properties of the other MRI series alloys are published by Aghion et al. [36], and exhibit room temperature strength and ductility comparable to the conventional AZ91D alloy.

This research program focused on an alloy designated MRI-153M, which was recently introduced in the line of MRI family of alloys [37]. This alloy was developed within the last decade, and their basic mechanical properties were published in 2003 [38] and are summarized in Table 2.5. The table shows that the alloy MRI-153M has similar room temperature mechanical properties as the conventional AZ91D alloy, but has a superior creep resistance.

Table 2.5. Room temperature mechanical properties and minimum creep rate of die cast MRI-153M along with pure magnesium (rolled and annealed) and AZ91D (die cast) as a comparison [36]

Properties	MRI-153M	Pure Mg	AZ91D
Tensile yield strength (MPa)	170	100	160
Ultimate tensile strength (MPa)	250	170	260
Elongation (%)	6	7	6
Minimum creep rate at 200°C 50MPa (/s)	5×10^{-9}	$> 10^{-4}$	1×10^{-7} [39]

2.5.2 Compositions of the alloys MRI-153 and MRI-153M

Since the MRI family of alloys was developed commercially, their general nominal compositions and the process parameters are not readily available, and will not be discussed further in this report. However, the key alloy compositions of the batch of high-pressure diecast alloys used in this research program are summarized in Table 2.6. These data were provided by the research group that produced these die-cast specimens at TU Clausthal, Germany [40], and therefore further details of their alloying process is unknown, except by confirmation with the EDS data in the subsequent microscopy.

The compositions illustrate that the primary constituents are similar to the conventional AZ series alloys, but with a substantial addition of 1% calcium in both cases. The major difference between the two alloys MRI-153 and MRI-153M is that the high zinc, low strontium content in the MRI-153 alloy is replaced by low zinc, high strontium content in MRI-153M alloy.

By knowing that the MRI-153M alloy was introduced later than the MRI-153, it is reasonable to speculate that the development of these alloys was conducted in a two stage sequence, where:

- Earlier development of MRI-153 was based around the conventional AZ91 composition for aluminum and zinc ratio, with the addition of calcium and a small addition of strontium to improve its creep properties.

- The later development of MRI-153M (most likely named as MRI-153"Modified") was to do away with the zinc addition and increase the strontium content, which adds further creep resistance but at the cost of difficulty in casting and increase in price. The improved process also reduced the level of detrimental copper impurity by an order of magnitude.

Traditionally, zinc is added for improved castability on alloys that are prone to hot cracking such as those involving calcium. Furthermore, excess zinc consumes the residual aluminum to form thermally stable intermetallic Mg-Al-Zn compounds (e.g. $Mg_{32}(Al,Zn)_{49}$) instead of the detrimental $Al_{12}Mg_{17}$ precipitates [29]. The combination of calcium and zinc is also reported to form $Al_2(Ca, Zn)$ precipitation [30].

With recent advances in casting technologies, the risk of hot cracking was reduced, and the

role of $Al_{12}Mg_{17}$ suppression appears to be now transferred to the more thermally stable Ca and Sr-rich precipitation mechanisms at higher temperatures in which the excessive age-hardening behavior of the Mg-Zn system is now detrimental. However, additions of strontium to AZ91 is also reported to reduce its room temperature fracture toughness due to the more angular grain boundary precipitate phases [41].

Table 2.6. Compositions of MRI-153 and MRI-153M alloys (%)

Element	MRI-153	MRI-153M
Mg	89	91
Al	8.6	8.4
Si	< 0.01	< 0.01
Fe	< 0.0005	< 0.0005
Cu	0.01	0.001
Ca	0.94	0.99
Mn	0.29	0.28
Ni	0.0006	0.001
Zn	0.63	0.01
Sr	0.1	0.27

2.5.3 Significance of the study of the MRI alloys

MRI series creep resistant magnesium alloys were selected as a test subject for this research program since these alloys were considered representative of modern, advanced low-cost creep resistant magnesium alloys that are already in commercial application. Several creep test studies on the alloy MRI-153 have already been carried out by the other researchers and in particular by the team at Monash University [42]. Basic mechanical and creep properties of the alloy MRI-153M is published by the producer Dead Sea Magnesium Ltd., but little is known about its microstructures and the reasons behind its superior creep properties. In particular, some of the significant interests in the study of this

alloy are as follows:

- The effect of additional strontium on the MRI-153M microstructure is unclear.
- The presence of $Al_{12}Mg_{17}$ β-phase is known to be detrimental to creep. Roles and effects of this and the other precipitates present on the MRI alloys must be evaluated.
- The secondary creep rates of the MRI-153 were found to agree with the basic power-law model [42]. However, whether the underlying deformation mechanisms correspond to the power-law creep is unclear.
- The use of power-law creep models based on deformation mechanisms proposed by Frost and Ashby [17] have not been attempted on this type of alloy systems.
- In conjunction with the model predictions, the corresponding textural evolutions upon creep can be studied using advanced microscopy techniques such as EBSD (electron backscatter diffraction).

2.6 CONCLUSION

The potentials for the use of magnesium alloys for many industrial applications are compromised by their susceptibility to creep. The phenomenon of creep deformation can take place due to a variety of mechanisms. In magnesium, this is primarily attributed to the mechanism of climb-assisted dislocation glide, and exhibits time and temperature dependent deformation that is classified as “power-law” creep. The study of creep involves the observation of underlying diffusion process of such defects, and it is influenced by the crystallographic texture of the material and various alloying elements that may result in accelerating or retarding the motion of dislocations.

In this research, the effects of the underlying microstructural features on creep were studied in detail on pure magnesium, followed by the MRI series of Mg-Al-Ca-Sr alloys. Pure magnesium was used since its relatively simple microstructures allow for direct comparison between theory and observation, whereas the MRI alloy was chosen because it is representative of a modern, low cost creep resistant die cast alloy, yet little is known about the reasons behind their superior creep resistance and the microstructure evolution during creep.

Chapter References

[1] K. U. Kainer, Magnesium Alloys and Technology, Wiley-VCH, 2003.

[2] N. V. R. Kumar, J. J. Blandin, M. Suery, E. Grosjean, Scripta Mater. 49 (2003) 225.

[3] H. Furuya, N. Kogiso, S. Matunaga, K. Senda, Mat. Sci. Forum 350 (2000) 341.

[4] G. Dunlop, Magnesium Technology 2002 (2002) 233.

[5] S. Das, JOM 55 (2003) 22.

[6] J. D. Bryant, D. R. White, Aluminum and Magnesium for Automotive Applications, TMS, Warrendale, Pennsylvania, 1995.

[7] H. J. Ertelt, Some fatigue properties of magnesium alloys, in: European Space Agency, (Special Publication) ESA SP, 1999, p. 263.

[8] B. A. Shaw (Ed.) ASM Handbook: Corrosion, 2003, p.

[9] E. Ghali, Mat. Sci. Forum 350 (2000) 261.

[10] R. Ambat, N. N. Aung, W. Zhou, Corrosion Science 42 (2000) 1433.

[11] W. A. Ferrando, Jnl. Mater. Eng. 11 (1989) 299.

[12] S. Ji, M. Qian, Z. Fan, Mater. Sci. Eng. A 434 (2006) 7.

[13] A. Maltais, M. Fiset, D. Dube, Grain refinement of magnesium alloy AZ91D cast in permanent mold using mechanical vibrations, in: Thermec 2003, vol 426, Trans Tech Publications Ltd, Madrid, Spain, 2003, p. 527.

[14] P. Labelle, M. O. Pekguleryuz, Heat Resistant Magnesium Alloys for Power-Train Applications, Noranda Inc., Montreal, 2001.

[15] K. Pettersen, P. Bakke, D. Albright, Magnesium Technology 2002 (2002) 241.

[16] R. W. K. Honeycombe, The Plastic Deformation of Metals, Edward Arnold Publishers, 1984.

[17] H. J. Frost, Ashby, M.F., Deformation-Mechanism Maps, Pergamon Press, 1982.

[18] A. J. Kennedy, Process of Creep and Fatigue in Metals, Oliver and Boyd Ltd., Edinburgh, 1962.

[19] M. R. Barnett, Z. Keshavarz, X. Ma, Metall. Mat. Trans. A 37A (2006) 2283.

[20] D. M. Schwartz, J. B. Mitchell, J. E. Dorn, Acta Metall. 15 (1967) 485.

[21] I. J. Polmear, Light Alloys - Metallurgy of the Light Metals, 1989.

[22] H. Baker, ASM Handbook, Vol.3: Alloy Phase Diagrams, ASM International, Ohio, 1992.

[23] C. S. Roberts, JOM 5 (1953) 1121.

[24] G. V. Raynor, The Physical Metallurgy of Magnesium and Its Alloys, Pergamon Press, Oxford, 1959.

[25] J. Koike, Y. Kawamura, K. Hayashi, M. Suzuki, K. Maruyama, A. Inoue, Mat. Sci. Forum 350 (2000) 105.

[26] S. Housh, B. Mikucki, A. Stevenson, ASM Handbook 2 (1990) 455.

[27] M. O. Pekguleryuz, Mat. Sci. Forum 350 (2000) 131.

[28] B. Smola, I. Stulikova, J. Pelcova, B. L. Mordike, Jnl. Alloys and Compounds 378 (2004) 196.

[29] I. A. Anyanwu, S. Kamado, T. Honda, Y. Kojima, S. Takeda, T. Ishida, Mat. Sci. Forum 350 (2000) 73.

[30] M. Vogel, O. Kraft, P. Staron, H. Clemens, R. Rauh, E. Arzt, Zeitschrift fuer Metallkunde 94 (2003) 564.

[31] M. Vogel, O. Kraft, E. Arzt, Scripta Mater. 48 (2003) 985.

[32] K. Ozturk, Y. Zhong, A. A. Luo, Z.-K. Liu, JOM 55 (2003) 40.

[33] Z. Zhang, A. Couture, Scripta Mater. 39 (1998) 45.

[34] M. O. Pekguleryuz, J. Renaud, Magnesium Technology 2000 (2000) 279.

[35] E. Baril, P. Labelle, M. O. Pekguleryuz, JOM 55 (2003) 34.

[36] E. Aghion, B. Bronfin, Mat. Sci. Forum 350 (2000) 19.

[37] E. Aghion, B. Bronfin, F. Von Buch, S. Schumann, H. Friedrich, JOM 55 (2003) 30.

[38] P. Bakke, K. Pettersen, H. Westengen, JOM 55 (2003) 46.

[39] V. Sklenicka, M. Pahutova, K. Kucharova, M. Svoboda, T. G. Langdon, Metall. Mat. Trans. A 33 (2002) 883.

[40] B. Mordike, T.U. Clausthal, Germany, in: 2003.

[41] S. Lee, S. H. Lee, D. H. Kim, Metall. Mat. Trans. A 29A (1998) 1221.

[42] S. M. Zhu, B. L. Mordike, J. F. Nie, Magnesium Technology 2005 (2005) 429.

CHAPTER 3 - SPECIMEN PREPARATION TECHNIQUES FOR OPTICAL MICROSCOPY, EBSD AND TEM

3.1 INTRODUCTION

Objectives of the use of EBSD in this research were twofold. The first stage of the research involving the study of MRI series magnesium alloys utilized the EBSD system to identify the precipitate phases present in the microstructure. At this stage, EBSD was used in conjunction with the EDS and TEM as a supplementary tool to identifying the phases. During the second half of the research, EBSD system was used extensively to obtain the crystallographic orientation texture maps of the surface microstructure. This technique was unique only to the EBSD system and was not possible with any other analysis tool currently available.

3.2 SURFACE PREPARATION

For magnesium alloys, the final polishing is the most critical step in the specimen preparation for EBSD analysis. A problem arises when the standard polishing procedures for optical microscopy does not necessarily result in a satisfactory surface quality for EBSD. On many occasions, a magnesium alloy specimen was polished to what appears to be a good surface finish when observed under optical microscopy or SEM, yet somehow failed to provide a useful EBSD pattern. When such a situation occurred, the only solution was to remove the specimen from the SEM vacuum chamber and re-polish the surface

again in hope that the next attempt would be successful. One occurrence of such occasion generally consumes up to three hours of labor, therefore consistently achieving a successful surface preparation was possibly the most timesaving factor in this research program. This section summarizes the key steps involved in a typical surface preparation procedure, with special attention paid to achieving a satisfactory surface quality for EBSD analysis. There were several factors that could be attributed to a poor EBSD pattern. In many cases, these factors were both compounding and contradictory, hence multiple factors may be present at any occasion and trying to eliminate one factor could result in worsening of another factor. These are explained in detail in the subsequent sections of this chapter.

3.2.1 Coarse grind and polish

The specimen was progressively ground with coarse silicon carbide sandpaper (240, 400, and 1200 grit) in wet condition. This stage was critical to obtaining a flat, defect free specimen surface. Each step was performed for at least 1 minute at 100 rpm to remove the prior surface deformation layer generated by the previous grinding step. Manual polishing was then performed with 9µm and then with 3µm diamond paste at 100~150 rpm for at least 2 minutes for each stage. One important technique used was to perform counter-rotating polish for the first 1 minute 30 seconds, followed by several turns of static polishing by placing the specimen at one spot on the rotating polishing pad. By performing this static polishing step, a scratch free, flat surface was ensured if the scratches were all marked in same direction, whereas if they were not, then that would indicate that the specimen is either not flat or still carries scratches from the prior stage. At this stage, use of water was permitted for washing the specimens without being concerned about the surface oxidation.

3.2.2 Final polish

Final polish was the most critical step in the entire process. Fortunately, since magnesium is relatively soft, any mistakes caused in the final step generally did not require the process to go back to the previous steps. Typically, the final polishing of microscopy specimens were performed with 0.1µm grade alumina or 0.05µm colloidal silica in fluid suspension on synthetic felt pad. In this research, three final polishing solutions were used along with four polishing pads. Observations made from experimentation with every combination of the polishing solutions and pads are summarized in Table 3.1. These observations are purely based on trials for magnesium alloys only, and are not related to the recommendations suggested by the manufacturer.

Table 3.1. Various final polishing solutions and pads used for magnesium

Polishing solutions	
Buehler Mastermet (colloidal silica, thin blue)	Fast polish, reactive with ethanol, slightly corrosive to the sample
Buehler Masterprep (alumina, viscous white)	Slow polish, pitting, etching effect, can be diluted with ethanol
Buehler Masterpolish (mixed oxide, thin white)	Fast polish, flat finish but produces scratches
Polishing pads	
Buehler Nanocloth (blue, short nap/fibre)	Slow polish, very flat finish but produce scratches
Buehler Chemomet (black, short nap/fibre)	Moderately fast polish, moderately flat finish
Buehler Microcloth (brown, long nap/fibre)	Fast polish, uneven, easily become contaminated
Buehler Mastertex (white, long nap/fibre)	Fast polish, scratch easily, difficult to wash off residue

*All product names are registered trademarks of Buehler Ltd., Illinois.

For general optical microscopy, Buehler Masterprep on Mastertex pad provided best results. For EBSD analysis, Buehler Mastermet on Chemomet pad provided best results.

Automatic polishing was not used in any of the steps because of three reasons. Firstly because magnesium alloys polish very quickly due to their softness, therefore the time and effort-saving aspects of the automated method are unimportant. Secondly, because many of the specimens were of irregular shape (e.g., tensile test specimen), conventional automated polishing specimen holders could not be used. Thirdly, the surfaces of magnesium alloy specimens corrode very quickly when exposed to water and most polishing suspensions while polishing is not taking place. Therefore the specimen had to be washed with alcohol immediately after the polishing process (typically within 1 second) hence the time consumed in attaching and removing the automatic polishing equipment resulted in negative effects for the final polishing outcome.

3.2.3 Effects of various final polish techniques

In general, the combination of thick slurry suspension and soft textured pad results in a very slow polishing process for most metals such as steels. However, this was preferable in case of magnesium alloys because they are typically very easy to polish. Soft, long nap pads generally results in uneven polishing process in which the soft phases of the specimen become polished away quickly, leaving behind the hard phases such as intermetallic precipitates, thereby resulting in an etched appearance that is suitable for optical microscopy. On the other hand, choosing a harder synthetic polishing pad results in a very even and flat surface finish due to their greater contact surface, but are typically more prone to surface scratching. The scratching occurs more frequently on harder pads probably because any foreign particles introduced during the polishing procedure would

be more likely to roll around and be in contact with the specimen frequently compared to a soft pad in which the foreign particles would be embedded and difficult to move around. The difference in appearance of the surface finish after various final polish techniques is illustrated on Figure 3.1.

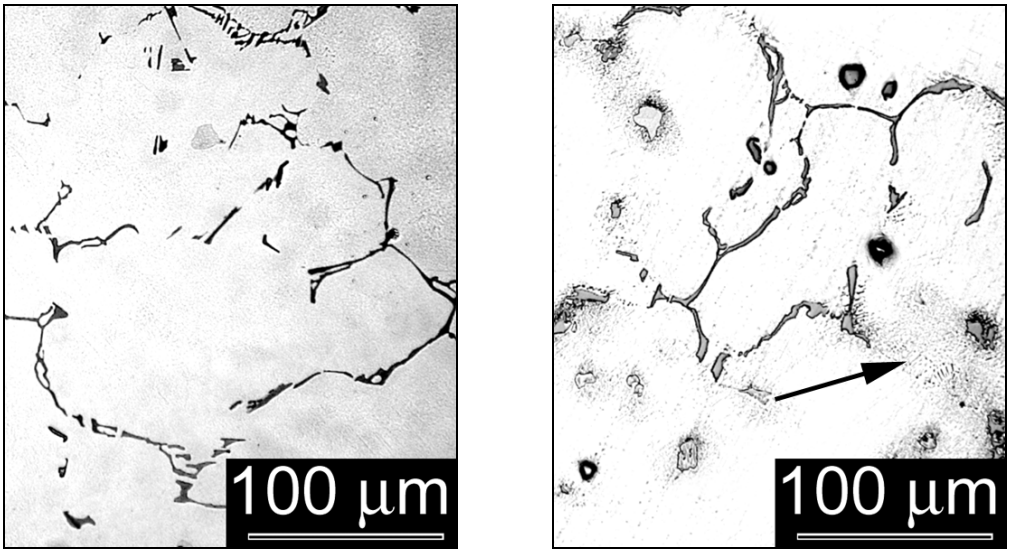

(a) (b)

Figure 3.1. Comparison of unetched micrographs of MRI-153M after (a) Mastermet-Chemomet and (b) Masterpolish-Microcloth, with preferential etching of Al-rich areas (arrow)

The polishing procedure described above for optical microscopy was not suitable for EBSD analysis. This was primarily because the uneven surface polishing effect of the soft pad was not appropriate for EBSD system that requires the surface to have a constant geometric relationship with the detector. Therefore, Buehler Chemomet (harder, short nap synthetic pad) was more appropriate for achieving a very flat surface finish. Although this pad created more large scratches compared to Mastertex, these occasional scratches could be ignored if they did not interfere with the EBSD target region.

The Masterprep and Masterpolish solutions did not produce a satisfactory surface finish for EBSD analysis. This was because although these polishing suspensions provided

excellent phase contrast in optical and SEM examination, it also created many fine surface scratches that deteriorated the EBSD pattern acquisition quality. After several trials, Buehler Mastermet 0.05µm colloidal silica solution was found to be best suited for surface preparation for EBSD analysis.

However, the use of Buehler Mastermet colloidal silica solutions was not without its own set of problems. Since the suspension is a water-based solution, the magnesium surface corrodes rapidly if the polishing action was halted. Therefore, the specimen surface had to be washed immediately after the polish (within a few seconds). This was hindered by another serious problem, whereby the Buehler Mastermet is chemically reactive with alcohol and solidifies into white viscous glue-like substance that becomes adhered to the specimen surface.

On the other hand, the Masterprep and Masterpolish fluids did not react with alcohol, therefore these fluids could be immediately washed off by spraying with ethanol after the polishing procedure, or alternatively, the polishing solution could be diluted with ethanol to adjust their rate of polish. Unfortunately these alcohol compatible polishing solutions did not give adequate surface quality for EBSD analysis.

3.2.4 Best polishing technique for EBSD analysis of magnesium and its alloys

The primary problem was that the Buehler Mastermet was the only polishing solution that produced satisfactory surface quality for EBSD, yet was reactive to ethanol, and could not be washed off easily. Having even a slight film of silica residue on the surface, as illustrated on Figure 3.2 typically results in strong charging of electron beam and poor EBSD contrast.

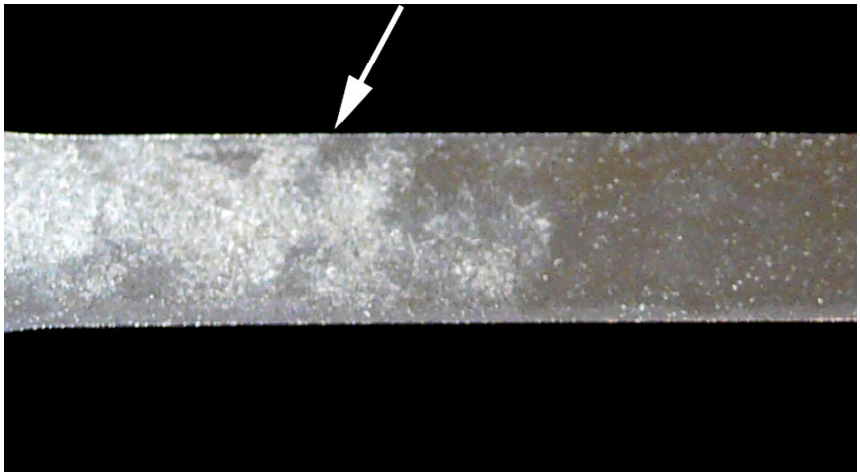

Figure 3.2. Typical surface damage caused by a film of colloidal silica residue

The solution to this problem was reached by following the procedure outlined as follows: When the final polishing was finished, the polishing pad was quickly scrubbed with water until no silica residue was visible. This was followed by a very short polish of the specimen with waster (up to 5 seconds) to wash off the Mastermet residue on the specimen surface but applying very high pressure to avoid the formation of oxidation film. The surface was then immediately sprayed with ethanol to remove any water residue and surface was checked to see if corrosion had taken place, which is characterized by white,

dull appearance. From this stage, the specimen was only handled with laboratory gloves to prevent contamination. This was followed by ultrasonic cleaning of the specimen in ethanol for up to 20 seconds to remove any excess Mastermet residue still embedded on the specimen. Any longer exposure to ultrasonic cleaning was not beneficial, since ethanol inevitably contains some water content and therefore causes corrosion. In addition, excess ultrasonic cleaning has the risk of causing precipitates to fall out.

Failure to perform the above workflow properly usually resulted in poor specimen preparation, either by surface oxidation or colloidal silica residue, in both cases causing excessive charging of the specimen surface under SEM.

3.2.5 Specific precautions for EBSD surface preparation for sequential/EBSD creep test specimens

In the second half of the research, several sequential creep/EBSD experiments were carried out. A detailed explanation of this experimental technique is provided in Chapter 6. To summarize the key points, interrupted creep experiments involve stopping the tensile creep test at fixed time intervals during creep deformation and the specimen surface microstructure is recorded by EBSD at these intervals to observe the changes in crystallographic orientation texture at various stages of creep. Therefore, this technique requires the specimen surface to be polished to EBSD quality for each of these interruptions, since the surface becomes corroded by the atmospheric exposure during the creep test. The fundamental assumption of this technique is such that the polishing does not remove a significant thickness of the specimen to alter the basic microstructure, so the identical surface area could be observed at every interruption stages. This assumption was made based on the fact that only the final 0.05μm polishing process was carried out for

each interruption step, simply to "clean off" any surface oxidation layer, thereby only removing up to 5 μm of surface layer per polishing step.

Knowing that up to 5 μm of surface layer could be removed during each polishing process, the problem arises due to the aforementioned fact that not every polishing process results in a satisfactory EBSD surface quality. This added another limitation to the polishing process whereby an unsatisfactory polishing process could not be tolerated and all processes had to be carried out in as few attempts as possible. In all of the sequential creep/EBSD experiments carried out in this research, the required polishing process was typically one or two attempts, and no more than three attempts were required in all cases.

3.2.6 Determination of the removed thickness

It was mentioned above that the maximum surface layer removed at a typical 0.05 μm final polishing procedure was 5 μm. This was evaluated using a method described as follows:

A 100-gf microhardness test diamond indent was placed on a polished magnesium alloy surface, and the dimensions of the indent were recorded. The specimen was polished once again with 0.1μm final polishing procedures, and the same diamond indent dimensions were recorded again. Based on the difference in dimensions and the profile of the diamond indenter, the effective surface removal depth could be evaluated. The appearance of diamond indent mark after various polishing cycles is shown on Figure 3.3.

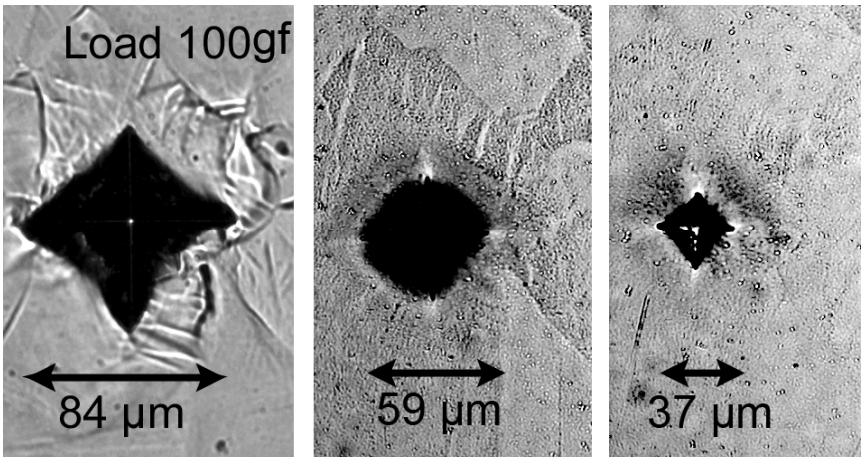

Figure 3.3. Microhardness indent used to measure the removed surface thickness, at (a) no polish, (b) one polish, and (c) two polish passes

3.3 TEM DUAL JET ELECTROPOLISHING OF MAGNESIUM ALLOYS

3.3.1 Introduction

In this research, all TEM specimen foils were produced by dual jet electropolishing method. According to the textbook "Transmission Electron Microscopy" by Williams and Carter, electropolishing is a "*black art*", in which the " *…correct conditions of temperature, electrolyte solution chemistry, stirring rate, applied voltage, polishing current, etc., can only be achieved through trial and error."* [1]. Historically, many variations of the electropolishing techniques were devised for particular alloy systems [2], but there is yet to be one single procedure that is equally effective for a wide range of materials.

Electropolishing of magnesium alloys is especially difficult compared to other metals due to the extremely corrosive nature of magnesium, where the foil may disintegrate in less

than one second if the applied polishing condition was incorrect. As a benefit, the polishing process can be completed very quickly (typically 1~2 minutes) compared to other metals (e.g. some steels can take up to 10 minutes). Therefore the approach in experimentation was to fabricate as many foils as possible, and attempt a wide range of polishing parameters to narrow down the most suitable procedure.

It must also be noted that the corrosive nature of magnesium means that the fabricated foils cannot typically be stored, and should be analyzed directly after the polishing procedure to achieve maximum effect. Therefore, the general process involved in the TEM analysis performed in this research was to experiment with various parameters until a suitable foil was fabricated, then the process was immediately followed by the analysis of the foil under the TEM, and subsequent foil making was halted. Optimal TEM foil making procedure

After several trial and error experiments, optimal TEM foil polishing procedure and effects of various critical parameters was determined as described in the subsequent sections.

3.3.1.1 Cutting and thinning

A block of specimen was cut into thin ribbon strips. The width must be at least 3 mm since the final dimension of the TEM foil is a disc of 3 mm diameter. The ribbon was made as thin as possible, but the amount of surface deformation and heating had to be minimized so that the original microstructure is retained for analysis. This is particularly the case for diecast magnesium alloys, since the grain size is fairly large (>100μm) with respect to the foil dimensions, and the phase transformation temperature can be as low as 200 ºC. Therefore, use of high speed abrasive saw, wire cutting or laser cutting was avoided. The best results were obtained by using a low speed circular diamond saw with an oil lubricant to provide cooling.

The low speed diamond saw was set up to cut the magnesium alloy block into 300µm thickness sections at blade feed rate of approximately 1 m/s. Since the amount of surface microstructure damage was difficult to evaluate, the limitation of the minimum thickness was chosen to prevent the ribbon from curling upon cutting.

The 300µm ribbon strips were then manually thinned further using 1600 grit sandpaper until the strips were thin enough to be punched into 3 mm discs without cracking or significant distortion. Once the foils were punched into 3 mm discs, they were further thinned to 100 µm with 1600 grit sandpaper using a special fixture. This final thinning stage determines the effectiveness of the electropolishing stage, so extra care was taken to measure and ensure all discs lie within 100 ± 20 µm thickness. Any over-thinned discs were discarded since these may cause uncertainties in determining the optimal parameters during the polishing trial and error stage.

3.3.1.2 Electropolishing

Electropolishing was performed using Fischione dual jet electropolishing system. Three different electropolishing solutions gave reasonable results.

Solution 1

585 ml methanol
355 ml n-butyl alcohol
60 ml perchloric acid

Solution 2

750 ml methanol
150 ml butoxyethanol
17 g magnesium perchlorate
8 g lithium chloride

Solution 3

750 ml methanol
250 ml nitric acid

In all three cases, the primary objective was to achieve a desired rate of electropolishing without severe pitting or chemical reaction. Other than these fundamental factors, it is desirable to store the solution without degradation, and must not be too hazardous to handle, since the process of electropolishing can be the most time consuming aspect of the TEM analysis, and therefore any sources of unexpected problems must be avoided. For this reason, although solution 3 provided reasonable polishing results, it was omitted from the final selection due to the high concentration (25%) of nitric acid, which is difficult to dispose of, and cannot be stored along with other conventional etching solutions. At the same time, the effect of inaccurate composition becomes significant, when the methanol evaporates and the concentration of nitric acid increases. For example, the methanol plus nitric acid is commonly found in literatures in various compositions and polishing parameters, in which each of the researchers would have obtained their own particular compositions based on trial and error. Some of the examples are shown below:

- Methanol + 30% nitric acid, -20ºC, 15V [3]
- Methanol + 25% nitric acid, -15ºC, 15V [4]
- Methanol + 33% nitric acid, -15ºC, 12V [5]

One critical factor in making the polishing solution was the quality of dilution alcohol such as methanol or ethanol. Lower quality ethanol (~99.7% purity) contains a high level of water that corrodes the magnesium specimens rapidly. This can be observed by immersing a freshly polished magnesium foil specimen in a beaker of low quality alcohol, in which

case the foil generates bubbles and the surface turns dull. In worst case, the surface becomes black due to reactions with other chemical elements present in the low quality alcohol. Having mentioned this fact, it does not mean that using high quality (>99.97%) ethyl alcohol always guarantees satisfactory results since it is hydrophilic. Therefore, extreme care was taken never to use any old, pre-opened bottled alcohol of unknown origin, and all alcohol was tested by the specimen immersion test prior to formulating the polishing solution. Since the surface of magnesium alloys are typically dull in appearance compared to aluminum, it is difficult to determine whether the surface is in fact compromised by observation. However, it becomes evident that the electropolishing reaction slows down dramatically when the specimen is heavily corroded during the process.

3.3.1.3 Jet speed

On the Fischione dual jet electropolishing machine, jet speed is controlled by a knob with numerical range of 0 ~ 10. The purpose of jet speed adjustment is to constantly feed fresh polishing solution to the polishing area, normalize the temperature, and wash away the surface deposits so that pitting does not occur.

In all cases, the primary concern with electropolishing of magnesium alloys is that the material is very soft and weak, so that the excessive jet speed will tear the thin area once it is penetrated. This problem is also complicated by the fact that the jet speed is not necessarily consistent even with a same knob position, since the flow rate depends on the operating temperature and the polishing solution used.

To minimize this issue, a standard procedure was established to determine the initial jet speed. Firstly the jet is set to speed 5 to obtain a steady strong flow and calibration is

performed to align the jet nozzles for the dual jet to meet at a central point. Once the calibration is completed, the jet speed is reduced until the two jets are flowing down by gravity and are almost not touching each other. By keeping the jet flow at this strength, a continuous flow of fresh polishing solution is fed to the foil surface without applying strong forces that may tear the foil surface.

This slow jet speed procedure is the starting point of the jet speed determination. Once several foils are polished, if the foils are tearing, then the polishing speed is decreased slightly. If the foils are pitted (dark, rough appearance) then the jet speed is raised slightly. The worst situation is when multiple small holes are produced on the foil rather than one central large hole with a large thin area at the circumference. This is typically caused by either a misaligned jet nozzle that does not focus the flow to the centre of the foil, or by the presence of large precipitates on the specimen microstructure that are prone to fall out during the electropolishing process. Therefore, some cases of poor outcomes can be remedied by reactive parameter changes, whereas others depend heavily on luck based on the underlying specimen microstructure.

3.3.1.4 Temperature

Temperature plays an important role in the electropolishing process. In general, lowering the temperature results in slower chemical reaction and therefore the polishing process can be regulated more precisely. This is especially the case for magnesium alloys that are chemically very reactive, and the polishing process may finish in less than one minute if temperature is moderate. To regulate the temperature, the polishing solution was surrounded by an insulated bath of alcohol cooled down by liquid nitrogen. The alcohol used as the cooling agent in the bath must be matched to the same alcohol used in the

polishing solution (in this case methanol), although lower quality type can be used for the cooling bath. The cooling temperature was typically chosen in the range of -40 to -20 ºC, depending on the time taken to complete the electropolishing process.

3.3.1.5 Electropolishing voltage and current

Increasing the polishing current across the specimen accelerates the electropolishing process. The adjustment of electrical parameters for the electropolishing process is to regulate the feed voltage to obtain the desired current across the specimen. This is because the current is a function of applied voltage divided by the overall resistance of the electropolishing circuit. Because the electropolishing machine is fabricated from electrical insulator material (plastics), the charge is carried across the specimen by the jet of electropolishing solution and passes through the specimen to the ground via a platinum wire. Therefore, assuming the resistance of the jet is fixed for a particular polishing solution, flow rate and temperature, the most variable factor in electropolishing process is the electrical resistance of the specimen itself.

The resistance of metallic specimen changes with the level of oxidation. This implies that a freshly polishing specimen free of oxidation film buildup on the surface will require less polishing voltage to achieve a desired polishing current, whereas a poor specimen that oxidized during the polishing process will be identified by gradual fall in the charge current across the specimen even at a constant voltage.

Typically the voltage was adjusted to obtain the current of 10~15 mA across the specimen. Depending on the specimen, the corresponding applied voltage can vary in the range of as much as 10~60V.

It was mentioned in the discussion of the jet speed and temperature controls that the speed of electropolishing must be sufficiently slowed down to prevent the foil from tearing or polishing too quickly. Therefore, it may be suggested that the polishing current should be reduced to achieve the effect of slowing down the polishing process. However, this approach did not yield satisfactory results. This was because the electropolishing current plays the most important role in determining the borderline between the mechanism of polishing against simple corrosion by immersion, where too little applied current results in preferential etching of certain regions of the specimen (e.g. grain boundaries, precipitates), resulting in disintegration of the foil. On the other hand, too high of an applied current results in accelerated polishing and aggressive pitting of the foil, resulting in multiple small pinholes without creating any desired thin areas. Therefore, the rate of polishing should be regulated by adjusting the polishing temperature, whereas the current should be regulated to achieve the desired polishing outcomes at that given rate of polishing. Williams and Carter [1] summarizes this observation with a graph relating voltage, current, and polishing outcome as shown on Figure 3.4.

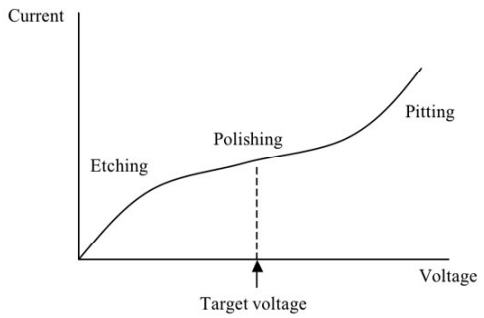

Figure 3.4. Relationship between current, voltage and polishing outcome

3.3.1.6 Summary

Figure 3.5 illustrates some of the outcomes of the electropolishing procedure on pure magnesium. A satisfactory electropolish such as those shown on Figure 3.5a, b can only be achieved when all of the control parameters are experimentally determined to the optimal condition. Failure to meet such a condition in any of the parameters would result in outcomes such as severe corrosion or pitting as shown on Figure 3.5c, d.

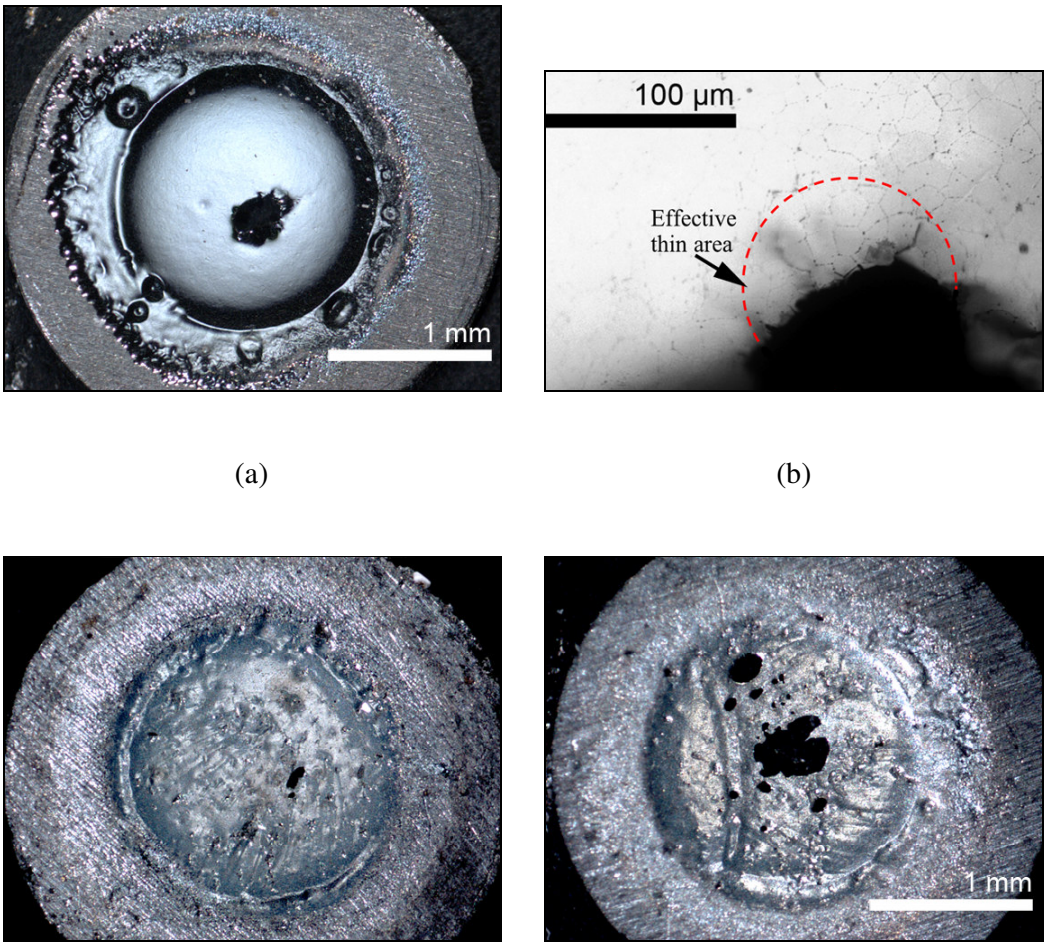

Figure 3.5. Examples of TEM foil specimens after electropolishing – (a) good polish, (b) higher magnification image of (a), (c) heavily corroded foil, and (d) heavily pitted foil

3.4 CONCLUSION

Typically the topic of specimen preparation for microscopy is not discussed in detail due to its trivial nature and the presence of already well-established techniques. However, preparation of magnesium alloys for EBSD and TEM required additional efforts due to their soft and highly reactive nature.

Surface preparation for EBSD required specific procedures in order to achieve satisfactory signal strength. TEM foil fabrication was also encountered with numerous issues due to their fragility. For example, personal experiences with the TEM foil fabrication of other materials (Ti, Al alloys) resulted in success rate of over 70%, compared to magnesium at less than 30%.

The specialized specimen preparation techniques developed in this chapter were applied extensively in the subsequent chapters involving the microscopy analysis of magnesium and its alloys.

Chapter References

[1] D. B. Williams, C. B. Carter, Transmission Electron Microscopy, Plenum, New York, 1996.

[2] G. Christiansen, Brown, J.R., Lindbo, J., Materials Characterization 49 (2003) 331.

[3] P. C. Bai, T. T. Zhou, P. Y. Liu, Y. G. Zhang, C. Q. Chen, Materials Letters 58 (2004) 3084.

[4] M. C. Carroll, P. I. Gouma, M. J. Mills, G. S. Daehn, B. R. Dunbar, Scripta Mater. 42 (2000) 335.

[5] R. E. Lee, W. J. D. Jones, Jnl. Mater. Sci. 9 (1974) 469.

CHAPTER 4 - MICROSCOPY OF MRI-153 AND MRI-153M

4.1 OVERVIEW

This chapter summarizes the study of microstructures of three magnesium alloys MRI-153 and MRI-153M, using a wide range of techniques involving optical microscopy, SEM, EDS, TEM, and most importantly, the use of EBSD for phase identification. The chapter also briefly discusses the microstructures of a conventional die cast alloy AZ91D as a comparison to the modern creep resistant MRI alloys. The analysis of the MRI series alloys was of a particular academic importance, since this had never been carried out to such an extensive level in the past. Part of the work on the MRI-153M alloy presented in this chapter was published in Magnesium Technology 2005 [1], and was presented at the Light Metals symposium at the TMS Annual Conference 2005.

4.2 MICROSCOPY OF A COMMERCIAL DIE CAST MAGNESIUM ALLOY AZ91D

4.2.1 Introduction

This section briefly discusses the microstructure study of a conventional automotive die cast alloy AZ91D (Mg-9Al-1Zn). The alloy specimen was acquired from an ex-service automotive wheel (model "Magnesio", O.Z Racing S.p.A, Italy) that was recently decommissioned prior to the onset of alloy's susceptibility to fatigue failure [2]. It is evident from historical development that conventional Mg-Al alloys such as the AZ91 is not appropriate for high temperature applications, and exhibit poor creep properties [3]. To illustrate this point, the alloy was subject to a simple annealing experiment in order to observe the changes in the microstructure.

Microscopy specimens were cut out from the core section of the wheel as illustrated on Figure 4.1, and were polished and etched (10 seconds in 3% HNO_3 + ethanol). For the annealed specimen, a block of the alloy was heated to 240 ± 3 ºC and held for 24 hours in a resistance furnace.

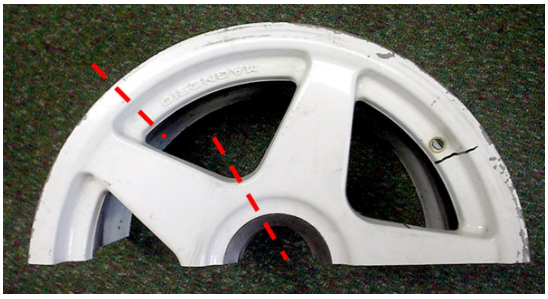

Figure 4.1. Magnesium wheel in as-received condition

4.2.2 Microstructures of the alloy AZ91D

Due to the high cooling rate of the high-pressure die cast process, the overall microstructure of the alloy is primarily large grains of primary α-Mg supersaturated with Al as shown on Figure 4.2, with a small amount of discontinuous grain boundary precipitation of lamellar eutectic $Al_{12}Mg_{17}$ β-phase shown in a higher magnification on Figure 4.3. The average sizes of the primary grains were found to be 330 μm using linear intercept method. Typical AZ91D alloy contains up to 0.15% Mn to suppress iron contamination, and the excess Mn forms blocky intragranular Al-Mn intermetallic phase such as Al_2Mn as indicated on Figure 4.2. A large amount of mechanical twins were observed near the casting surface as shown on Figure 4.4, illustrating the susceptibility of α-Mg to undergo deformation by twinning.

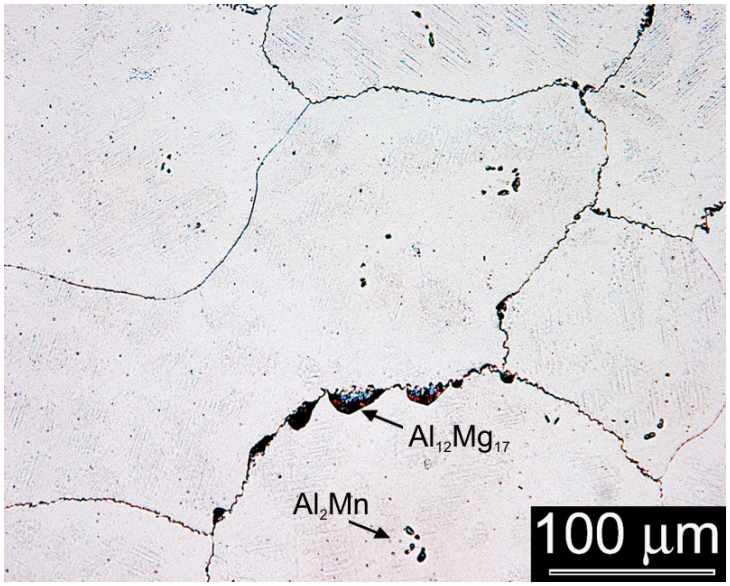

Figure 4.2. Optical micrograph of as-cast AZ91D wheel

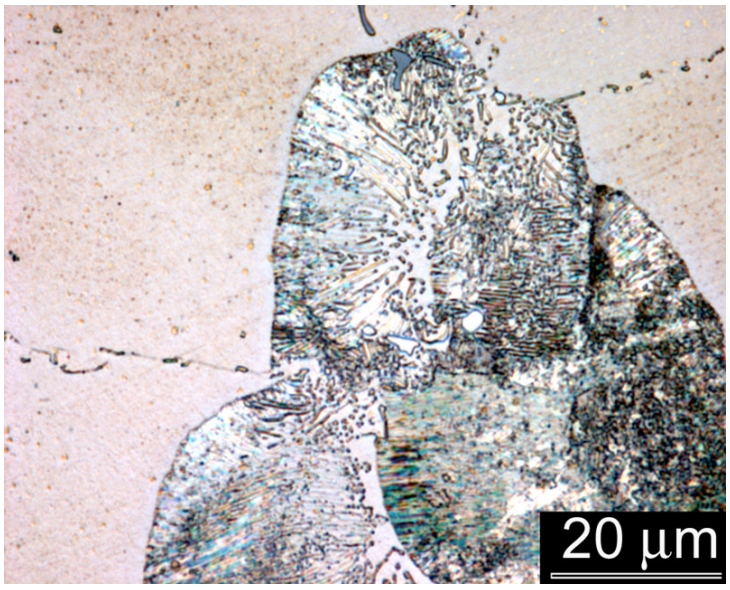

Figure 4.3. Lamellar eutectic β-phase cluster

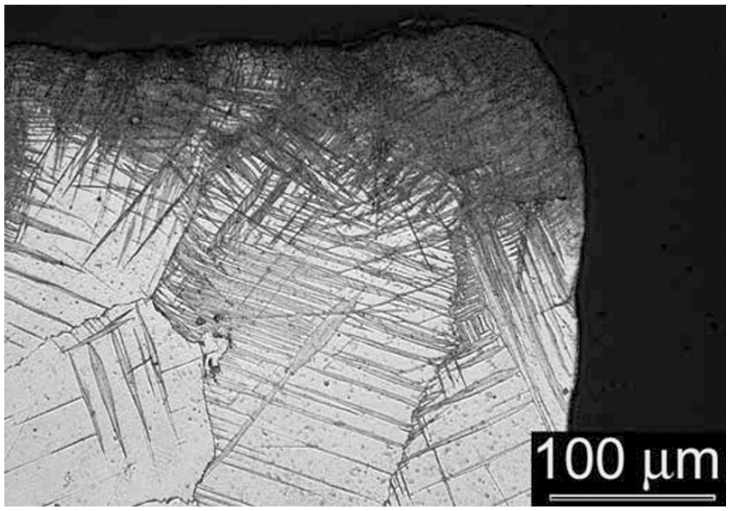

Figure 4.4. Mechanical twins present near the casting surface

Figure 4.5 shows the optical micrograph of the AZ91D alloy after annealing at 240 ºC for 24 hours, which exhibits growth of both the intergranular and intragranular lamellar eutectic β-phase precipitates. Although aluminum supersaturation contributes to the room temperature mechanical properties of Mg-Al alloys, it is apparent that when the alloy is exposed to elevated temperatures, thermal energy allows the precipitation to take place, either by thickening the intergranular lamellar regions, or forming large clusters of eutectic

lamellae within the grains. As discussed in Chapter 2, dynamic precipitation of the β-phase during the course of the creep deformation process contributes to the weakening of the material and general unpredictable nature of creep life in Mg-Al alloys.

Based on the observations made on the annealed microstructures of the conventional die casting Mg-Al alloy AZ91D, it is clear that such alloys do not provide stable microstructures at elevated temperatures, and although these alloys can be annealed prior to service in order to minimize the detrimental dynamic precipitation during service, it is generally impractical due to the reduction of mechanical properties and the additional process costs involved. The preliminary studies of the AZ91D alloy reinforced the Importance of the development and study of alternative creep resistant magnesium alloys such as the MRI series of alloys discussed in the subsequent sections.

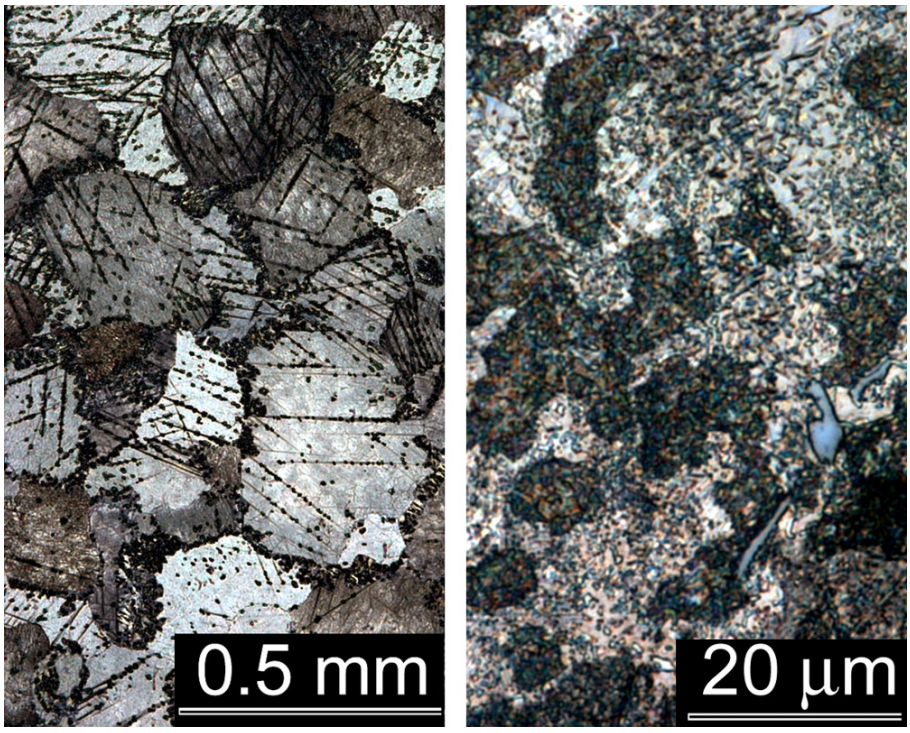

Figure 4.5. Optical micrographs of AZ91D annealed at 240°C for 24 hours

4.3 MICROSCOPY OF CREEP RESISTANT MAGNESIUM ALLOYS MRI-153 AND MRI-153M

4.3.1 Introduction

The conventional die casting alloy AZ91D has a relatively high susceptibility to creep failure. It has been suggested that this is primarily due to the discontinuous precipitation of thermally unstable α-Mg + $Al_{12}Mg_{17}$ eutectic [4, 5]. Although the $Al_{12}Mg_{17}$ precipitates are stable up to 260 °C and provide positive influence on the moderate-temperature mechanical properties by dispersion strengthening [4], Dargusch concludes that the deterioration of creep rate is attributed to the precipitation at grain boundaries during creep promoting grain boundary sliding [6].

High-pressure die casting can achieve faster solidification rates than conventional casting, thus supersaturating aluminum in the α-Mg matrix, achieving a finer grain structure [7] and reducing shrinkage voids during solidification [8]. However, for any magnesium alloys with aluminum supersaturated in the primary Mg matrix, precipitation of $Al_{12}Mg_{17}$ phase is unavoidable upon aging at elevated temperatures [9], resulting in the rapid deterioration of creep resistance.

Since a reduction of aluminum content would reduce castability and room temperature strength, it is of great interest to suppress the formation of $Al_{12}Mg_{17}$ phase while maintaining an appropriate aluminum content under solid solution.

Modern creep resistant alloys rely on the formation of other aluminum-rich precipitates that are stable at elevated temperatures, in order to reduce the formation of $Al_{12}Mg_{17}$, and

to act as stable barriers against dislocation motion [4]. In recent developments, such precipitates are typically binary compounds of (Mg, Al) and (rare earths, Ca, Sr). Modern creep resistant alloys containing up to 2 wt% rare earths (RE) or strontium achieved dramatic improvements in mechanical properties up to 250°C due to a fine distribution of Al_4RE or Al_4Sr precipitates, but problems with poor castability, hot tearing and high oxidation rate, along with the significant cost of the alloying elements are also of concern [4, 5].

Recently, addition of up to 3% calcium has gained attention, in which the formation of thermally stable Al_2Ca precipitate achieved similar creep resistance compared to rare earth alloys at significantly lower cost [10]. Calcium additions may introduce problems with castability and hot tearing although these effects can be mitigated with proper casting conditions and additions of zinc to similar levels as AZ91D [10, 11]. As the creep resistance of some magnesium alloys has reached the levels comparable to some aluminum alloys [11], some interests in current developments lie in the areas of reducing alloying costs (e.g., reducing the use of expensive elements such as RE and Th) and improving castability (reducing process control costs).

Two patented high-pressure die cast alloys, designated MRI-153 and MRI-153M (Dead Sea Magnesium Ltd.), were studied in the present work. These are modified AZ91D type magnesium alloys, designed to improve high temperature properties with less expensive alloying elements, based on a combination of alloying with Ca and Zn for MRI-153 and Ca and Sr for MRI-153M. Room temperature mechanical properties and minimum creep rate of the MRI-153M alloy is summarized on Table 2.6 and can be found elsewhere [12, 13].

The purpose of the present work was to reveal the major phases present, their

morphologies and distributions in order to provide more information regarding the reasons behind their improved high-temperature properties. One of the key objectives for carrying out this experiment was to evaluate the effectiveness of EBSD in identifying the phase and orientation information from magnesium alloys, by comparing the results obtained from EBSD to the more accurate and established TEM method.

The EBSD system acquires a unique crystallographic diffraction pattern known as "Kikuchi pattern" generated by the SEM beam spot on a specimen surface area of interest, and identifies its phase and orientation by matching this with a simulated Kikuchi pattern generated from the crystal database. The EBSD software tolerates up to a specified angle of mismatch between the real and simulated patterns, and this determines the accuracy of the phase and orientation identification. For the phase identification carried out in this chapter, the patterns were ensured to have a mismatch of less than 1.5°.

4.3.2 Experimental Procedures

The specimens prepared for this study were high-pressure die cast patented Mg-Al-Ca-Sr alloys MR-153 and MRI-153M, provided by Prof. B. Mordike of T.U. Clausthal, Germany. The specimens were fabricated in rods 20 mm diameter and 200 mm length to high quality laboratory analysis specifications, with minimum microstructure disparities and macroscopic casting defects. The specimens were also provided in rectangular sections of extruded ingots, approximately 100 × 20 × 200 mm dimension. The relative compositions of each alloy are shown in Table 2.5. Rods of high-pressure die cast specimens 180 mm length, 20 mm diameter, were obtained in the as cast condition.

The alloys were received in as-cast/extruded condition without any homogenization or

annealing processes. The microscopy analysis was initially carried out in this as-received state unless otherwise stated. One of the potential issues with such specimens is the lack of chemical homogeneity between the surface and the core region of the casting due to the segregation. Furthermore, extruded specimens may have a nonrandom crystallographic texture[14]. Therefore, samples of MRI-153 and MRI-153M alloys from the same ingots were also annealed at 200 ºC for 24 hours. The purpose of this annealing process was to provide a direct comparison against the prior study of annealed AZ91D alloy earlier in this chapter.

Specimens for optical microscopy and SEM/EDS were mounted in a conductive copper/diallyl phthalate mixture and polished to 0.01 μm alumina suspension. Details of the standard polishing procedure are discussed further in Chapter 3. Some optical microscopy specimens were etched in 2% picric acid in ethanol solution but most were studied in as-polished unetched condition. Specimens for electron backscatter diffraction analysis (EBSD) were not etched.

For transmission electron microscopy (TEM) studies, the same alloy ingots from the optical analysis were sliced into 0.3 mm thickness ribbons using a low speed diamond saw. 3 mm diameter discs were punched from these and then ground to approximately 0.1-mm thickness. Some specimens were thinned using a Fischione twin jet electropolishing unit in solution of 7% magnesium perchlorate, 3% lithium chloride, 75% methanol, 15% butoxyethanol at nominal condition of –45°C, 12 mA. Optimal TEM specimen fabrication techniques and polishing parameters was reached after a series of trial-and-error experiments, which is discussed in Chapter 3. Some foil specimens of MRI-153 were prepared using a Gatan Model 656 Dimple Grinder and a Model 691 Precision Ion Polishing System.

SEM-EBSD observations were carried out on JEOL JSM-6100 equipped with HKL Nordlys II with HKL Channel 5 acquisition software and an Oxford eXL EDS system. The database for identification of possible phases was comprised of all compounds listed in Pearson's Handbook [15] containing combinations of Mg or Al with Ca, Mn, Zn, and Sr. Details of the EBSD system configuration is discussed in Appendix B. TEM observations were carried out on a Hitachi H-600 operated at 100kV and a Philips CM20 operated at 160kV and 200kV.

The analysis on the Philips CM20 TEM was conducted by Assoc. Prof. Milo V. Kral (research supervisor) to supplement the analysis data using the equipment at Monash University, Melbourne, Australia.

4.3.3 Results

4.3.3.1 MRI-153

The optical micrograph in Figure 4.6a shows the typical appearance of the MRI-153 alloy in the as-cast condition. The main feature is the interconnected grain boundary network of intermetallic phases. Compared to typical micrographs of AZ91 alloys shown in Figure 4.2 and found elsewhere [16], the grain boundary phases appear more continuous and primary α-Mg grains generally larger and dendritic, although with large variations in grain size.

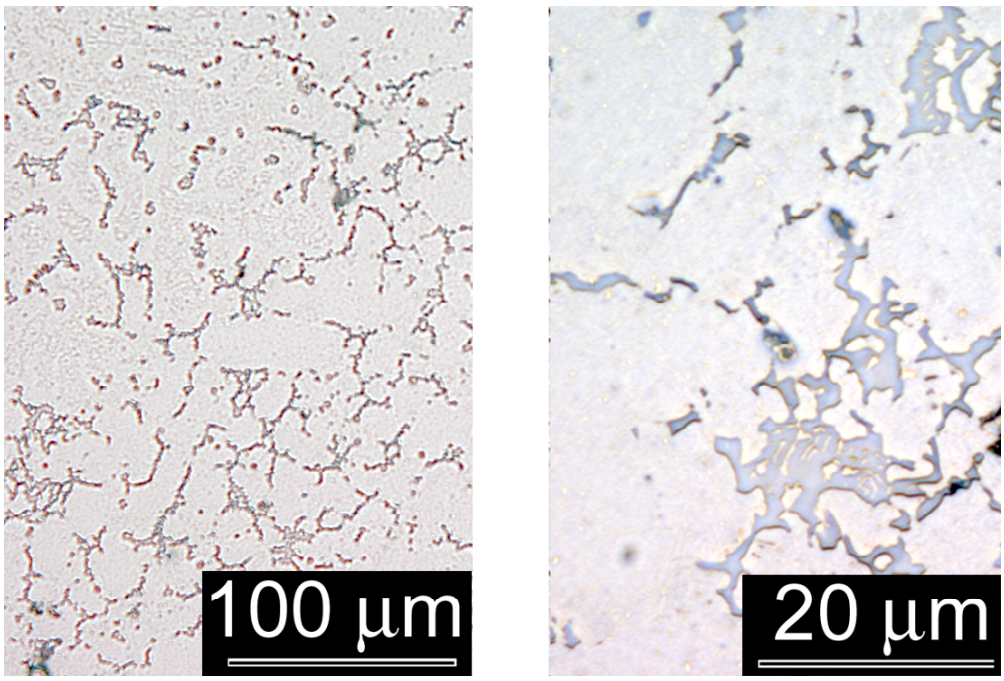

Figure 4.6. Optical micrograph of as-cast MRI-153 showing intergranular phases surrounding the primary α-Mg grains (unetched)

Observation of the MRI-153 microstructure revealed two distinct precipitate phases as shown in Figure 4.6. The most abundant was the nearly continuous lamellar intergranular phase as shown in Figure 4.7a and c. This phase was identified as hexagonal Mg_2Ca [17] by EBSD and SAD (Figure 4.7 b and d). EDS spectra at various locations in the Mg_2Ca phase revealed the presence of varying amounts of aluminum within each precipitates as shown on Figure 4.8. Although the exact local compositions of aluminum could not be determined due to the contribution of the surrounding α-Mg grains on the EDS spectra, the aluminum appear to be incorporated into the hexagonal Mg_2Ca phase, forming a ternary intermetallic phase $(Mg, Al)_2Ca$. This phase was also reported by Luo et al. on similar composition alloys [18]. It must be noted that the cubic Al_2Ca phase [19] was not observed in the present work, which is in agreement with a report by Ozturk et al. [9] that the formation of cubic Al_2Ca phase was suppressed in high-pressure die cast materials due to their relatively rapid solidification rate.

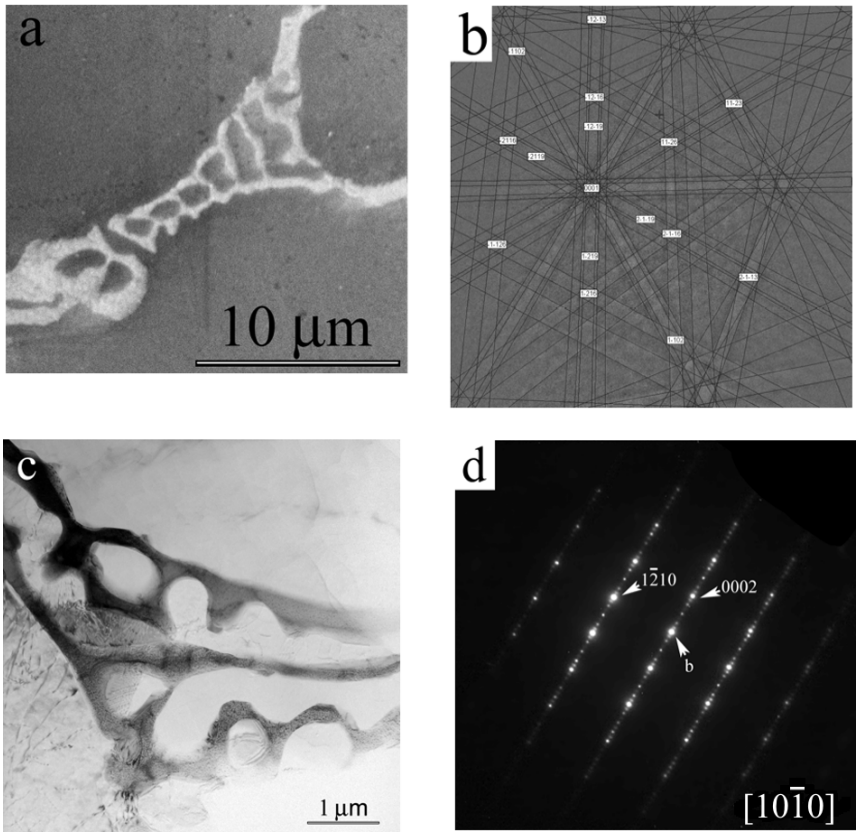

Figure 4.7. Intergranular $(Mg, Al)_2Ca$ phase seen in (a) SEM and identified by (b) an indexed EBSD pattern; also shown by (c) bright field TEM and (d) SAD pattern from the particle in (c)

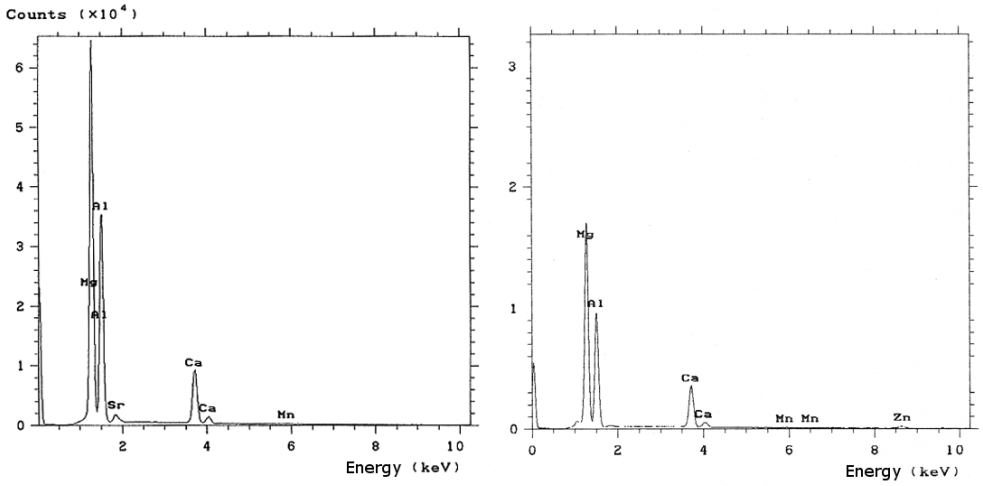

Figure 4.8. EDS spectra of $(Mg, Al)_2Ca$ phase showing various compositions of Al

The $Al_{12}Mg_{17}$ phase [20] was also observed to a lesser extent, as shown in Figure 4.9, typically surrounded by the more abundant $(Mg, Al)_2Ca$ intergranular phase. Although this phase is easily distinguished in optical microscopy, there is very little difference in contrast in the SEM, either in SE or BSE mode. The only way to be certain of identification of this phase was to employ EBSD in the SEM (Figure 4.9b) or CBED/SAD in TEM analysis.

A bulky and faceted, comparatively minor phase containing aluminum and manganese was identified by EBSD as Al_8Mn_5 [21] as shown on Figure 4.10. This identification was confirmed by selected area diffraction in TEM. It is reported that manganese is often added to suppress the formation of detrimental Fe-containing intermetallic phases [22] and excess Mn will form large blocky precipitates in the alloy.

Occasional instances of $Al_{46}Ca_{25}Mn_4$ [23] were identified in this alloy in both EBSD and TEM/SAD, in which the relatively large lattice parameter of this phase (a=0.5723 and c=1.826 nm) was observed.

Although the MRI-153 alloy contains 0.63% zinc, there were no observations of zinc rich precipitates such as $Mg_{32}(Al, Zn)_{49}$ that are reported elsewhere [24]. Isolated examples of $Al_6Mg_{11}Zn_{11}$ were found in very small quantity but most of the zinc was contained as solid solution in the α-Mg matrix [25].

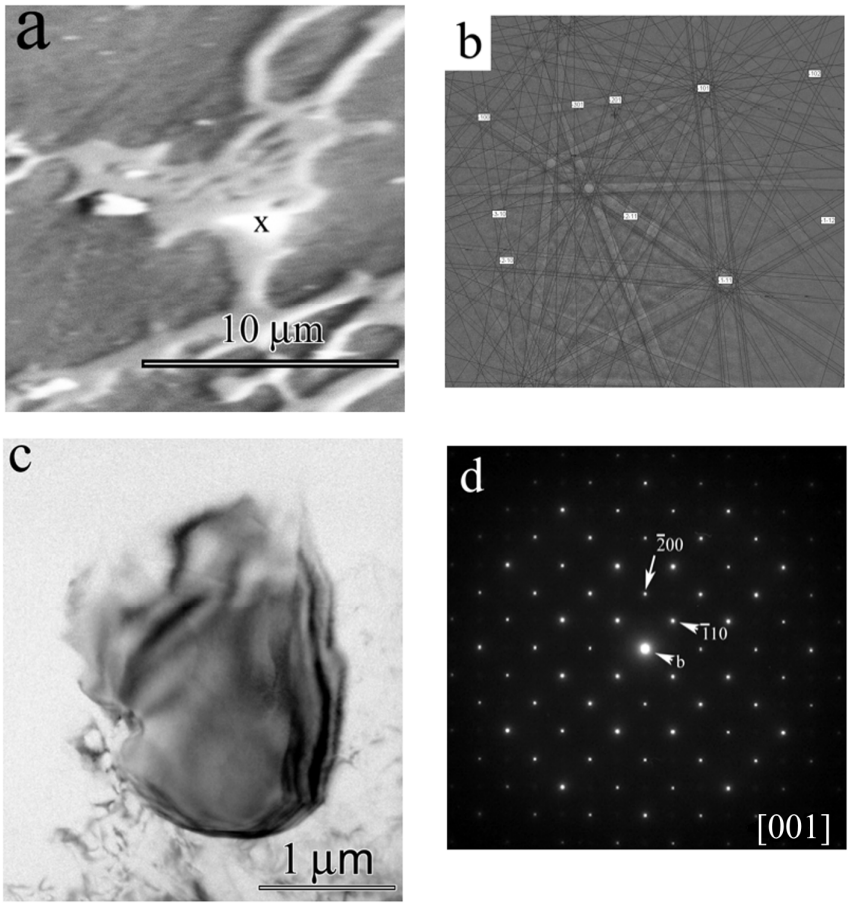

Figure 4.9. $Al_{12}Mg_{17}$ precipitate (a) surrounded in $(Al\ Mg)_2Ca$, shown in SEM and identified by (b) an indexed EBSD pattern of the same particle; shown in (c) bright field TEM and identified by (d) am indexed SAD pattern from the same particle in (c)

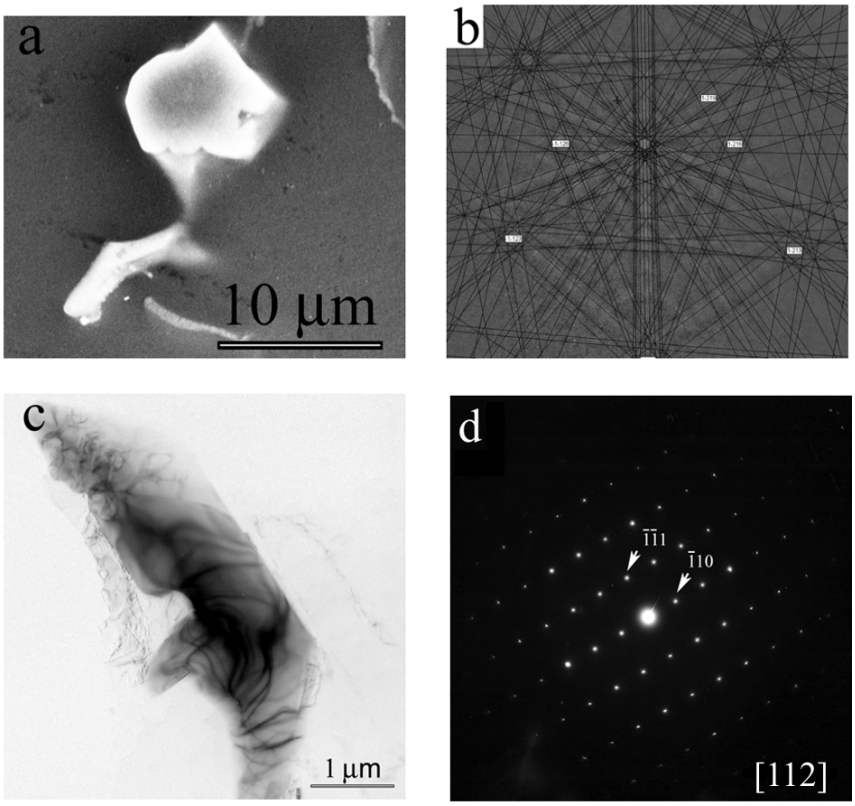

Figure 4.10. Al_8Mn_5 shown in (a) SEM and identified by (b) an indexed EBSD pattern; also shown by (c) bright field TEM and (d) SAD pattern from the particle in (c)

4.3.3.2 MRI-153M

Optical microscopy of MRI-153M such as the typical region represented in Figure 4.11a revealed a basic microstructure of primary α-Mg surrounded by intergranular precipitates. The grain boundary phases appear to be coarser and less interconnected in comparison to the MRI-153 alloy shown in Figure 4.6. Although the overall as-cast microstructures of MRI-153 and MRI-153M appear similar, the phases present in the grain boundary network are different. As in MRI-153, the majority of the intermetallic phase was $(Mg, Al)_2Ca$, indicated as '1' in Figure 4.11b .SEM and TEM observations of this phase are summarized in Figure 4.12.

Another abundant intermetallic phase, indicated as '2' in Figure 4.11b, was identified by EDS to contain significant amounts of Sr. These Sr-rich precipitates were typically found at grain boundaries, especially at grain corners, surrounded by, or possibly interconnected to the $(Mg, Al)_2Ca$ precipitates. EDS results exhibited inconsistent, variable proportions of Mg, Al and Ca, and EBSD patterns (Figure 4.13) were indexed as hexagonal Mg_2Sr [26], suggesting that this phase is in fact most accurately described as hexagonal $(Mg, Al)_2(Ca,Sr)$.

Other Sr-rich phases, such as the orthorhombic Al_2Sr or tetragonal Al_4Sr phases that have been reported elsewhere in earlier studies [27], were not observed in this alloy. Unlike MRI-153, only one small example of the $Al_{12}Mg_{17}$ phase was ever identified in MRI-153M.

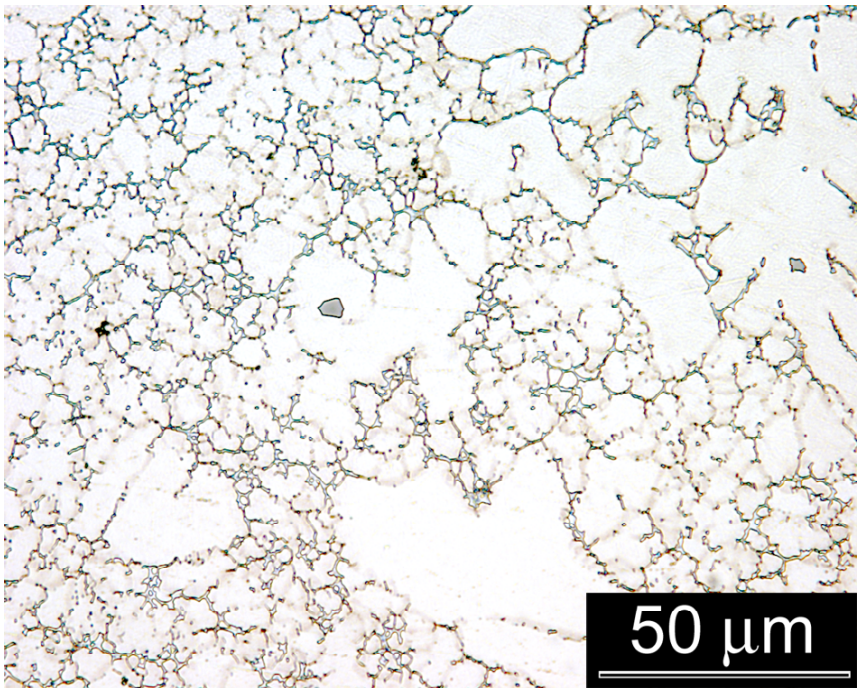

(a)

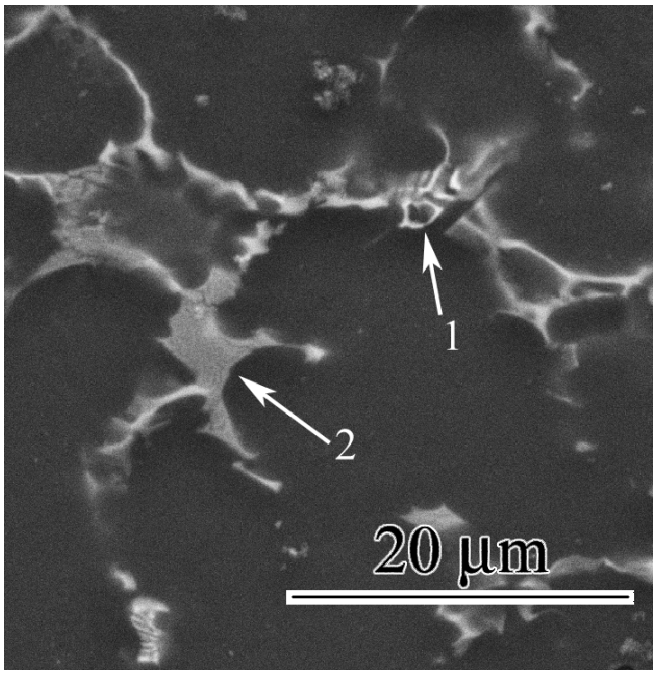

(b)

Figure 4.11. (a) Optical micrograph of as-cast MRI-153M showing grain boundary phases surrounding primary α-Mg grains (unetched) and (b) backscatter electron image with arrows indicating the (1) Ca-rich and (2) Sr-rich phases

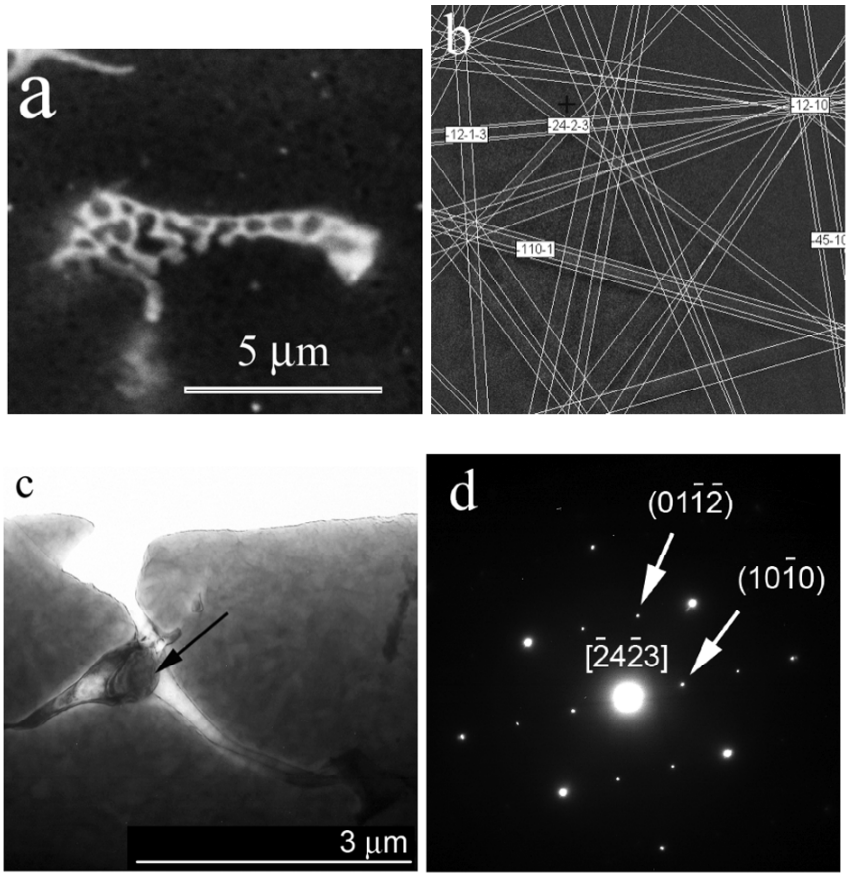

Figure 4.12. Intergranular (Mg, Al)$_2$Ca phase shown in SEM and identified by (b) an indexed EBSD pattern; also shown in (c) bright field TEM and identified by (d) SAD pattern from the particle in (c)

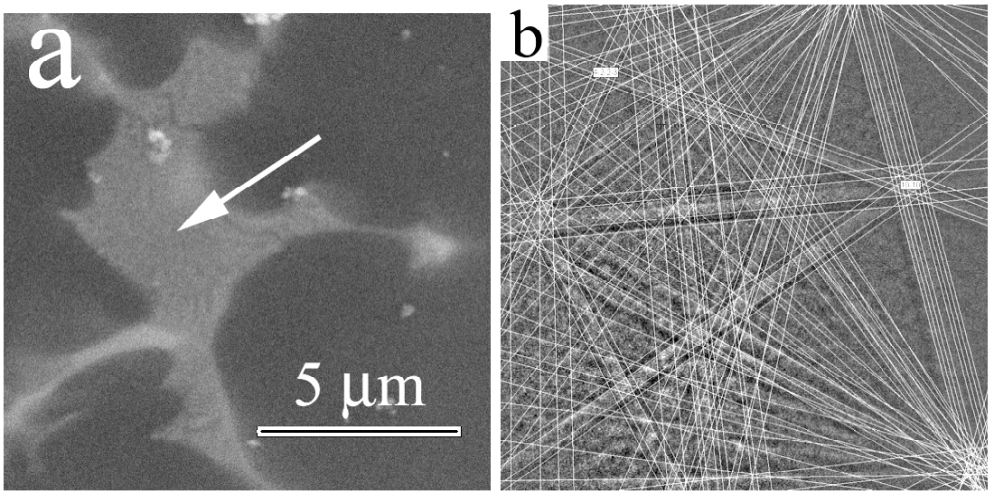

Figure 4.13. Intergranular (Mg, Al)$_2$(Ca, Sr) phase, shown by (a) SEM and identified by (b) an indexed EBSD pattern

4.3.4 Annealed microstructures

Figure 4.14a and b, respectively, show the microstructures of MRI-153 and MRI-153M specimens after annealing at 200°C for 48 hours. The most obvious microstructural change in the alloys after the annealing treatment was the development of a fine distribution of sub-micron sized aluminum-rich precipitates in the vicinity of the coarse grain boundary phases. Examples of such precipitates shown in Figure 4.15b were identified as $Al_{12}Mg_{17}$ using EBSD on MRI-153 alloy. However, these precipitates did not occur in sufficient quantity to be observed in the MRI-153M alloy.

Examination of the annealed MRI-153 alloy using TEM identified a relatively infrequent occurrence of a different type of intragranular precipitate in the primary α-Mg matrix that was previously not found in the as-cast specimens. This phase, shown in Figure 4.15a as elongated plates or rods, may be the orthorhombic $Mg_{21}(Zn,Al)_{17}$ phase reported by other groups [25] but was not crystallographically identified in the present effort due to its relatively small size and limitations of the equipment currently available.

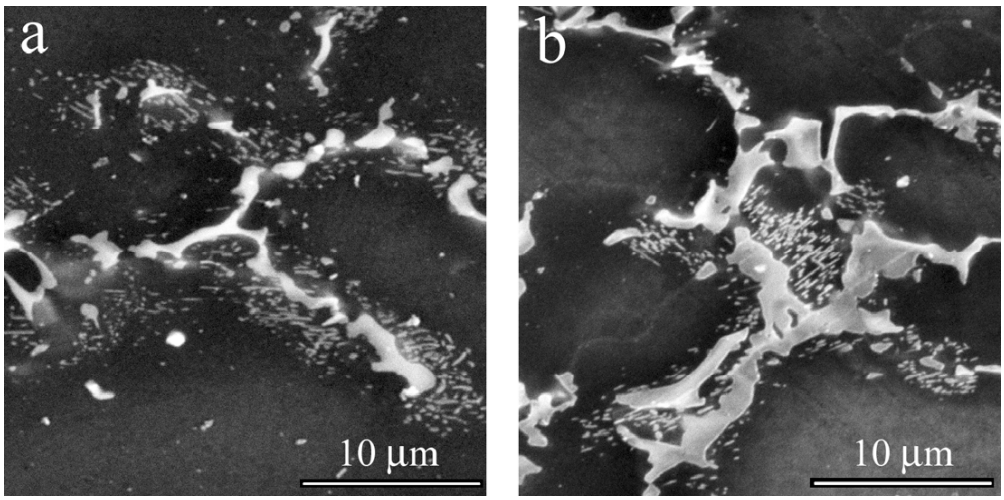

Figure 4.14. SEM images of (a) MRI-153, and (b) MRI-153M alloy annealed at 200 ºC for 48 hours, showing the formation of $Al_{12}Mg_{17}$ precipitates in the α-Mg matrix near grain boundary regions

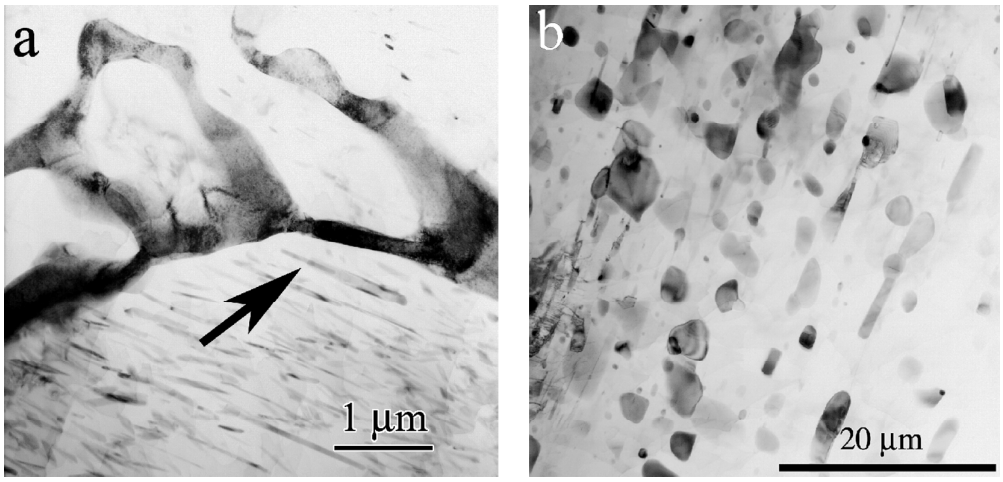

Figure 4.15. Bright field TEM images showing (a) fine intragranular precipitates and (b) relatively coarse $Al_{12}Mg_{17}$ precipitates in annealed MRI-153 alloy

4.3.5 Discussion

One interesting feature of the MRI-153M alloy system was the identification of the complex nature of the grain boundary precipitate phase designated $(Mg,Al)_2(Ca,Sr)$. The formation of other Mg-Sr compounds were not identified in this study, where phases such as $Mg_{17}Sr_2$ are reported in similar alloys with higher strontium content (< 1%) [28].

The nature of this substitutional behavior between calcium and strontium can be explained by the similarity of the lattice parameters of the hexagonal Mg_2Ca and Mg_2Sr phases. Both phases have the same space group (194), and the lattice parameters are within approximately 3% (Mg_2Sr: a=0.6426, c=1.0473 nm; Mg_2Ca: a=0.6225, c=1.018 nm). The automated pattern matching failed to distinguish between the two phases within its limit of resolution. Furthermore, the issue was further complicated by the fact that the precipitate phase $(Mg, Al)_2(Ca, Sr)$ had almost exactly twice the lattice parameter of hcp magnesium (Mg: a=0.321, c=0.521 nm), therefore EBSD frequently misindexed the phases due to the coincidence of the higher order diffractions, that effectively resembles a pattern of identical geometry. Therefore, a reliable identification of the precipitate phases was achieved only through the combination of EBSD and EDS. This technique showed that the Sr-rich areas of the precipitate phase were concentrated particularly at grain corners, resulting in somewhat more bulky appearance compared to the rest of the Mg_2Ca network.

The $Al_{12}Mg_{17}$ β-phase was identified infrequently in as-cast MRI-153 alloy specimen, but was not found at all in MRI-153M specimen. This may be attributed to the presence of strontium in MRI-153M alloy altering the Mg-Al-Ca ternary phase diagram, where studies by Suzuki et al. [28] shows that the addition of strontium increases the solubility of aluminum in the α-Mg. The suppression of $Al_{12}Mg_{17}$ in MRI-153M would have a positive

influence upon creep resistance of this alloy, since current theory of creep resistance in similar alloys attributes poor creep performance to the formation of $Al_{12}Mg_{17}$ [25].

Although the bulky $Al_{12}Mg_{17}$ β-phase was suppressed to low levels in both MRI alloys, annealed specimens exhibited formation of very small (~ 1 μm) spherical $Al_{12}Mg_{17}$ precipitates near grain boundaries. However, the evolution of this phase may in fact influence the creep performance in positive ways. This is because unlike the coarse lamellar $Al_{12}Mg_{17}$ precipitates found in AZ91D, precipitation such as that observed in Figure 4.15b is reported to lead to improvement in creep properties due to a dispersion strengthening mechanism [29] without introducing significant defect concentrations that lead to acceleration in creep. However, thermal instabilities in a microstructure are also reported to be unfavorable for interrupted creep conditions that more closely represent the real-life service conditions, in which case, pre-aging the alloys may be favorable for some applications [30]. In any case, these fine $Al_{12}Mg_{17}$ only appeared in limited quantity specifically at matrix grain corners.

4.3.6 Conclusion

The microstructures of MRI-153 and MRI-153M high-pressure die cast alloys were investigated in as-cast and annealed conditions. The microstructures of both alloys contained calcium-rich grain boundary intermetallic phase described as $(Mg,Al)_2Ca$. Compared to AZ91D, the presence of $Al_{12}Mg_{17}$ was reduced in the MRI-153 alloy and appeared to be nearly completely suppressed in the MRI-153M alloy. The MRI-153M phase contained a hexagonal strontium-rich phase described here as $(Mg,Al)_2(Ca,Sr)$. Upon annealing, both alloys exhibited a distribution of fine intragranular $Al_{12}Mg_{17}$ precipitates in the vicinity of the grain boundary intermetallic phase network.

4.4 DEEP ETCHED MICROSTRUCTURE ANALYSIS OF MRI-153 AND MRI-153M ALLOY

4.4.1 Introduction

Previous attempts to determine the compositions of various precipitates present in MRI-153 and MRI-153M creep resistant alloys were faced with an issue where the precipitates were so small and thin that the SEM electron beam could not obtain an isolated EDS signal from the precipitate phase alone. The EDS spectra were influenced by the surrounding primary magnesium grains, and the EBSD patterns were ill-defined due to the formation of overlaid "double" pattern of precipitate and the matrix. To overcome this issue, deep etching was performed on thin foils of the alloys in order to selectively remove the primary α-Mg phase and isolate the precipitates of interest to be analyzed by SEM/EDS.

4.4.2 Experimental procedure

High-pressure die cast MRI-153 and MRI-153M magnesium alloys were fabricated into thin foil (≈ 0.3 mm) strips similar to those produced for TEM foil making. Specimens were taken from the same alloy ingot as the previous optical and SEM studies.

These foil specimens were placed on conductive carbon adhesive tape and immersed in a large volume of 2 % nital solution for four hours. By performing this immersion etching process, the primary α-Mg phase was completely dissolved away, leaving the precipitate phases behind. The actual α-Mg removal process was completed in a period much shorter than four hours, but the etching duration of four hours was chosen to make sure that the

precipitate phases were not affected even under prolonged exposure to the etching solution. A schematic diagram of this process is illustrated on Figure 4.16.

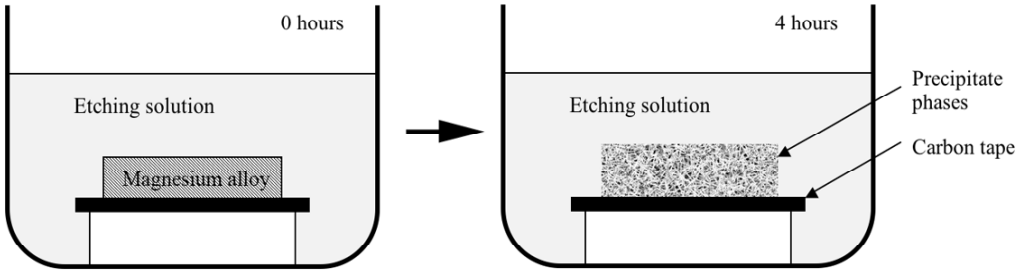

Figure 4.16. Schematic diagram of the deep etching process

After the deep etching process, the specimens were then carefully immersed in ethanol, dried and placed in JEOL JSM-6100 SEM for imaging and EDS analysis. Conductive carbon adhesive tape was appropriate for this process since it was unaffected by the nital etching solution or alcohol, and retained its adhesive properties to trap the precipitate phases even after the immersion and drying process.

4.4.3 Results and discussion

4.4.3.1 Precipitate phases in MRI-153 alloy

The deep etching was successful in isolating the precipitate phases for SEM/EDS analysis. Figure 4.17 shows the general overview of the deep etched microstructure of the MRI-153 alloy. The deep etching process revealed that the grain boundary precipitates are in fact interconnected in a complex network surrounding the primary α-Mg grains, and their scaffolding network structure was retained without breaking down even after the deep etching process. The level of interconnectivity of the grain boundary precipitates was unknown in a standard 2-dimensional surface optical microscopy, but the deep etching

process makes it apparent that the majority of the grain boundary precipitates are fully connected to the adjacent precipitates.

The previous EDS analysis identified these grain intergranular precipitates to contain small traces of aluminum and calcium, but their precise composition was unknown. The EDS spectrum collected from the deep etched specimen shown in Figure 4.17 (b) identifies the presence of Mg within the precipitate without the contribution of background α-Mg grains. This agrees with the phase identification by EBSD as hexagonal $(Mg, Al)_2Ca$, with substitutional Mg and Al composition.

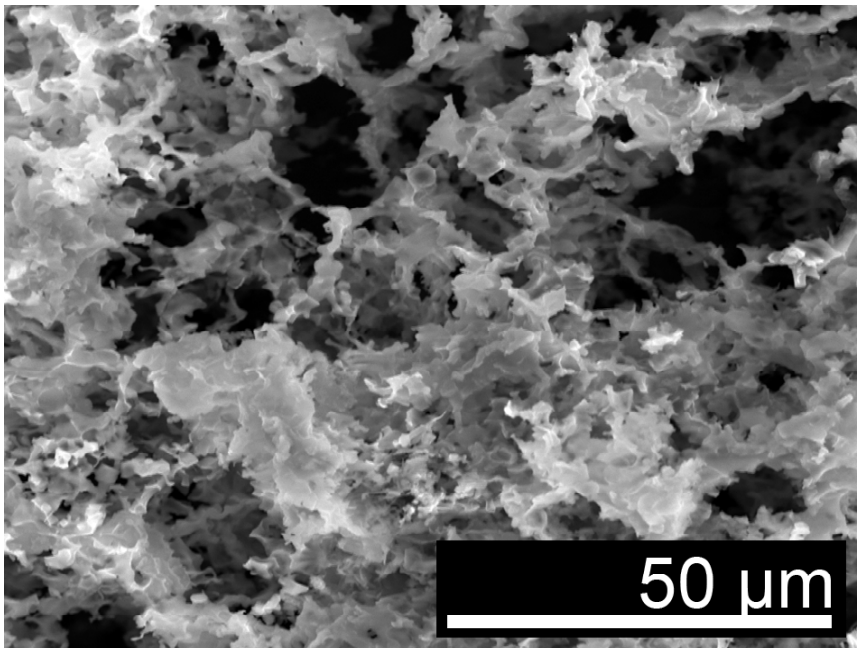

(a)

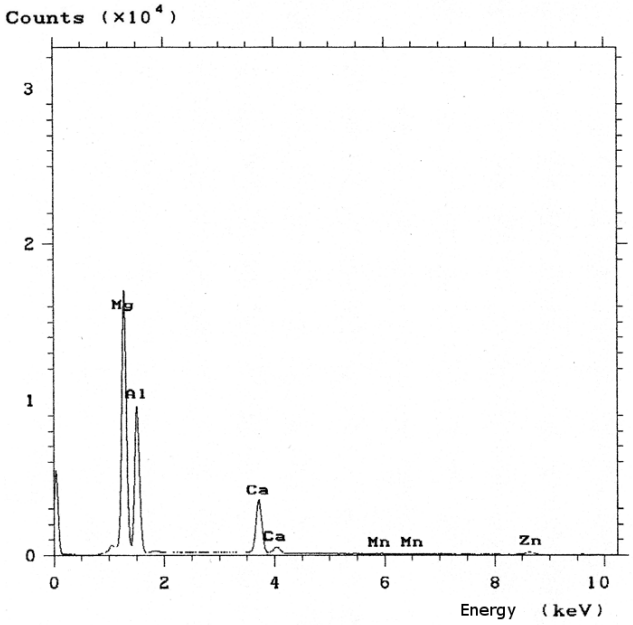

(b)

Figure 4.17. (a) Grain boundary network Mg-Al-Ca precipitate and (b) its EDS spectrum

In some regions of the specimen, small quantities of calcium-free precipitates were observed. These isolated precipitates were bulky and vastly different in appearance compared to the two aforementioned precipitate types, as shown on Figure 4.18a. The EDS spectrum on Figure 4.18b shows Mg-Al composition that is typical of $Mg_{17}Al_{12}$ "β" precipitates commonly present in AZ series Mg-Al alloys.

As discussed in Chapter 2, these β precipitates are known to be one of the primary causes of poor creep resistance in conventional AZ series magnesium alloys, and therefore the presence of β precipitates in this MRI-153 alloy indicates its susceptibility to creep under the same mechanism as the AZ series. However, it is apparent from this deep etching experiment that the intent to suppress the formation of detrimental β precipitates was successful, since the majority of β precipitates was substituted by the presence of intergranular $(Mg, Al)_2Ca$ network. In addition to the Mg-Al-Ca precipitates, small quantities of manganese-rich precipitates were also identified, as shown on Figure 4.19a. These Mn-rich precipitates were always spherical, and correspond to the intragranular Mn-rich particles identified in the previous SEM analysis at some grain centers. They are most likely the excess Mn from the Fe suppression treatment during the melting process. The excess Mn forms Mn-Al compound as shown on the EDS spectrum on Figure 4.19b (typically Al_8Mn_5) that act as inoculant for nucleation of α-Mg grain formation upon solidification.

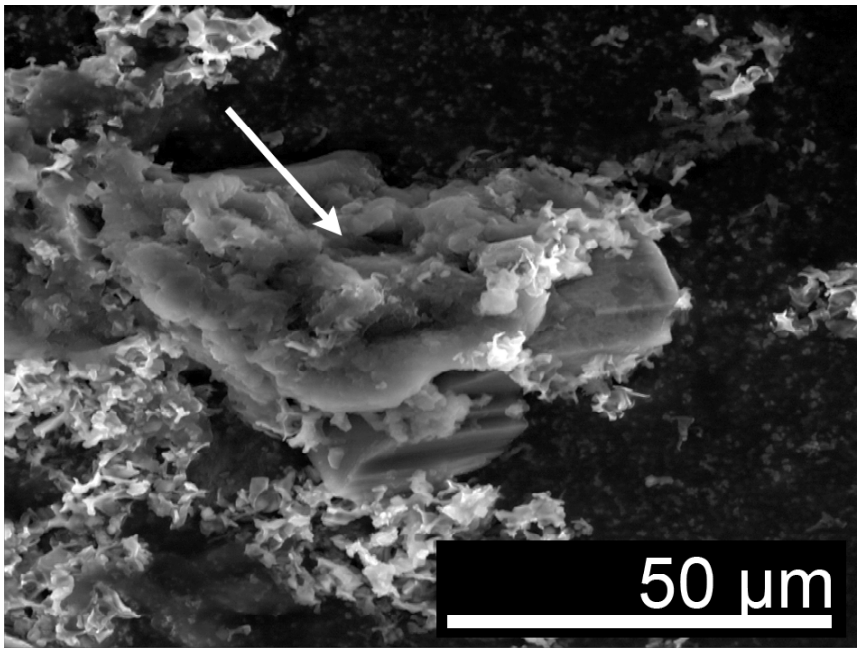

(a)

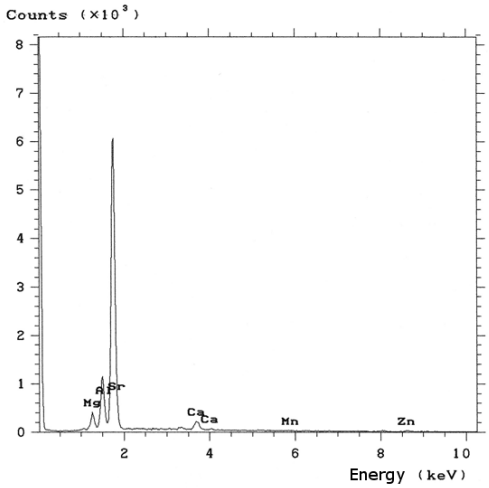

(b)

Figure 4.18. (a) Bulky Mg-Al precipitate surrounded by the Mg-Al-Ca precipitate and (b) EDS spectrum of the Mg-Al precipitate

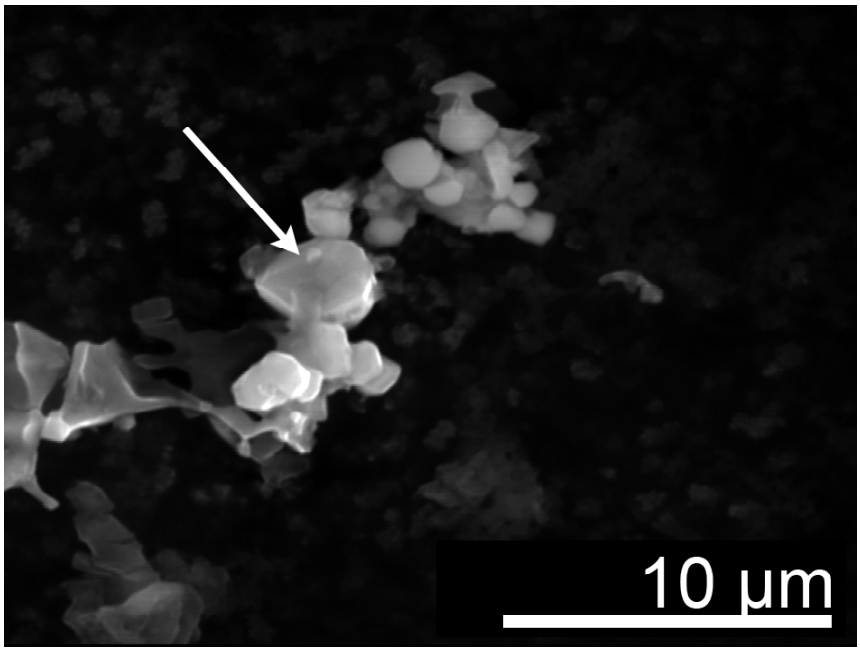

(a)

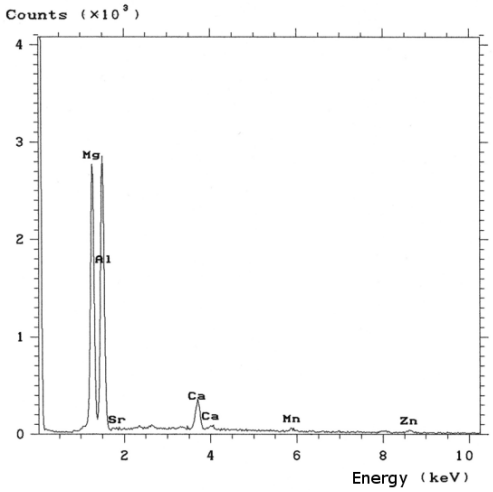

(b)

Figure 4.19. (a) Small spherical Al-Mn precipitates, (b) same precipitates at higher magnification, and (c) its EDS spectrum

4.4.3.2 Precipitate phases in MRI-153M alloy

The same deep etching experiment was also carried out on the alloy MRI-153M. The two alloys showed no difference in their appearance or the rate of etching. Figure 4.20 shows the overall appearance of the deep etched microstructure, and the appearance is very similar to the MRI-153 alloy. Closer examination of the deep etched microstructure on Figure 4.21 identified the areas with high strontium concentration within the (Mg, $Al)_2Ca$ phase network. These strontium-rich regions were found at areas that correspond to corners of the primary α-Mg grains. This suggests that the precipitation of the grain boundary phase initially begins with the formation of strontium-rich hexagonal $(Mg,Al)_2Sr$ phase at α-Mg grain corners, followed by the transition to the $(Mg,Al)_2Ca$ phase composition as the strontium is depleted.

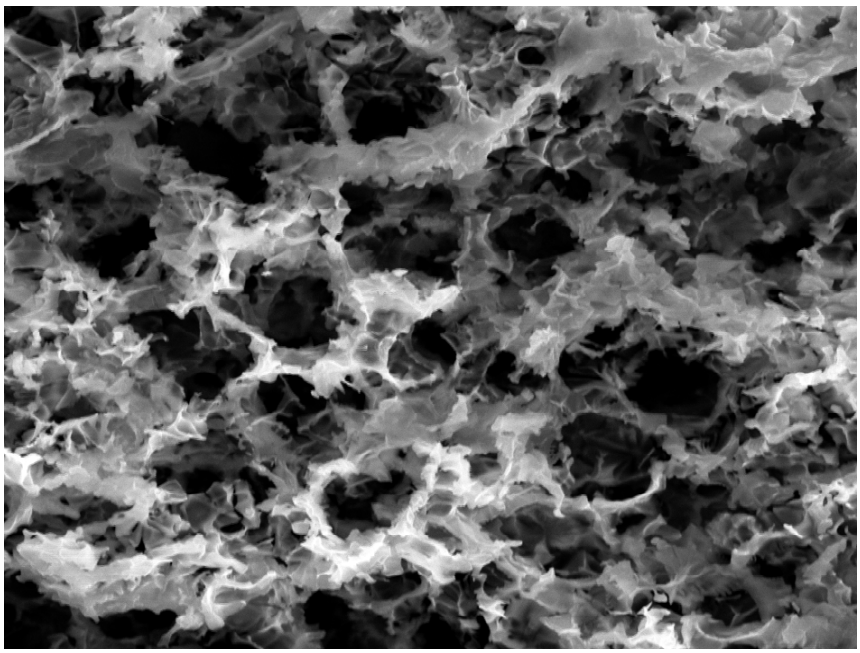

Figure 4.20. General appearance of the Mg-Ca network

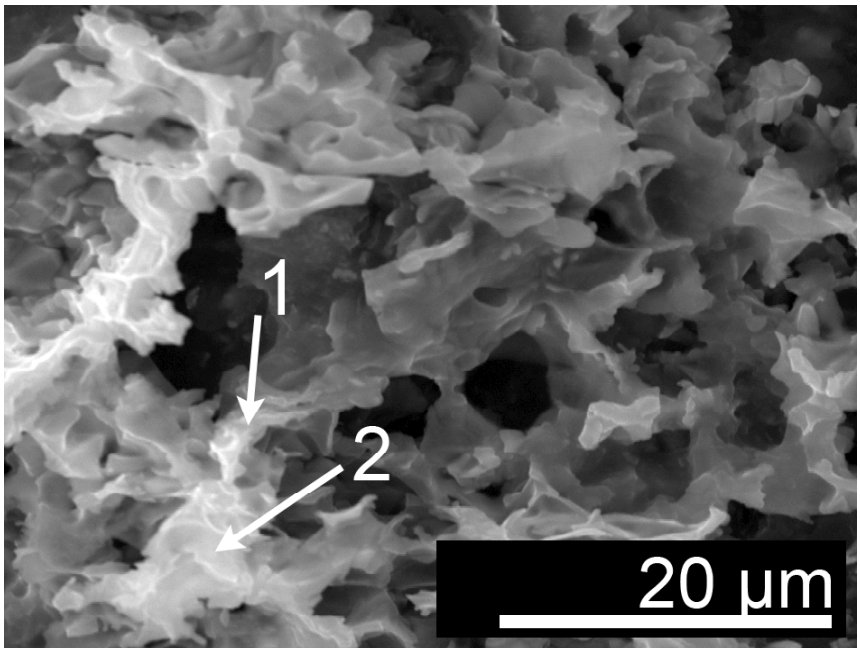

(a)

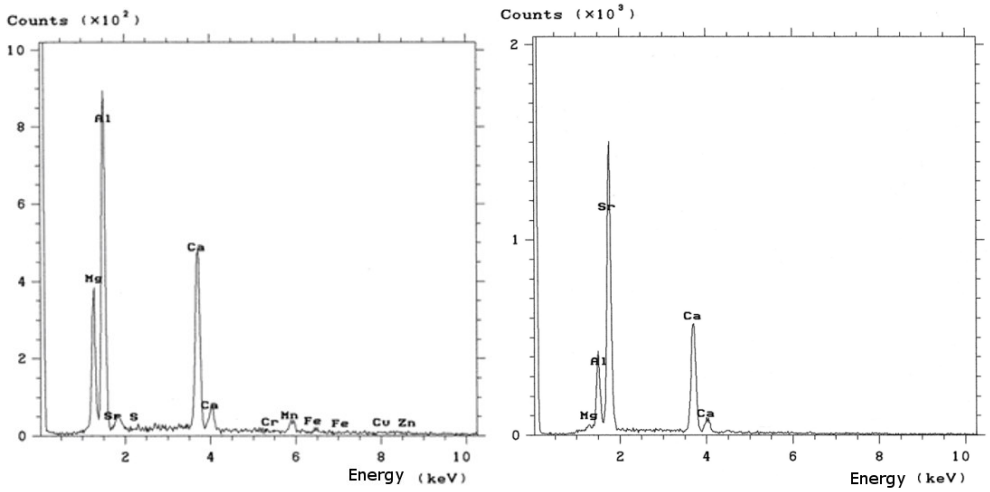

(b) (c)

Figure 4.21. (a) Grain boundary network of Mg-Al-(Ca, Sr) phase and EDS spectrum at (b) point 1 and (c) point 2

4.4.3.3 Other inclusions and infrequently occurring phases

Other than the main precipitate phases identified in the two alloys, there were several phases that were only observed in one or two occasions in the entire deep etched specimens. One of the most notable of these was the presence of large angular particles shown on Figure 4.22, which the EDS spectrum identified as pure strontium. This particle was observed only rarely (one on MRI-153 and two on MRI-153M). In addition, the deep etching process was able to locate pure aluminum (Figure 4.23), a flake shaped iron-rich inclusion (Figure 4.24), and a spherical sulfur-rich inclusion (Figure 4.25). These observations, although microstructurally less important, provides an indication that the deep etching technique may be useful for applications in the study of casting defects and inclusions.

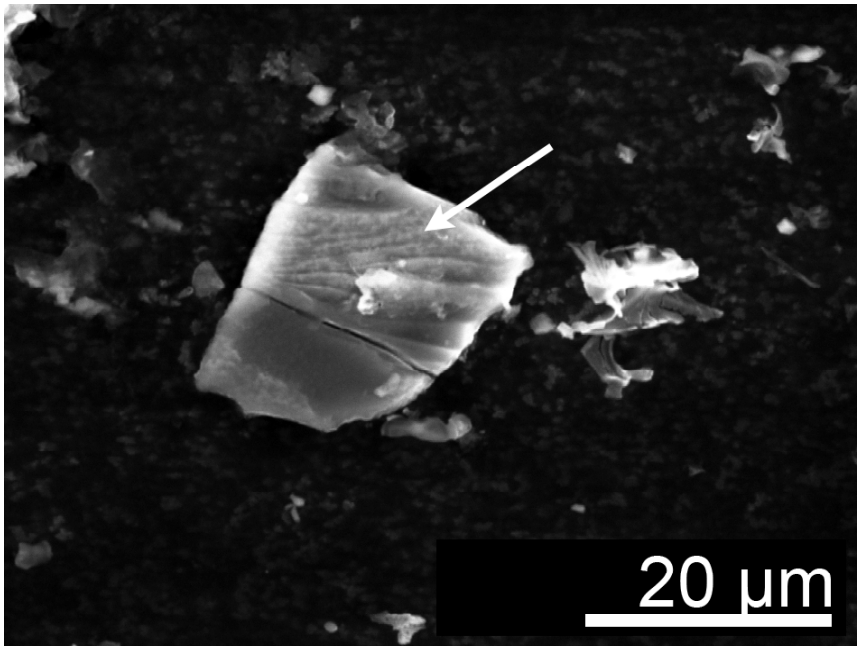

(a)

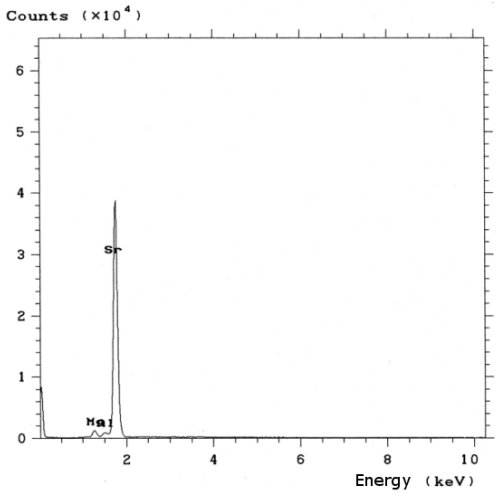

(b)

Figure 4.22. (a) Large pure Sr particle and (b) its EDS spectrum

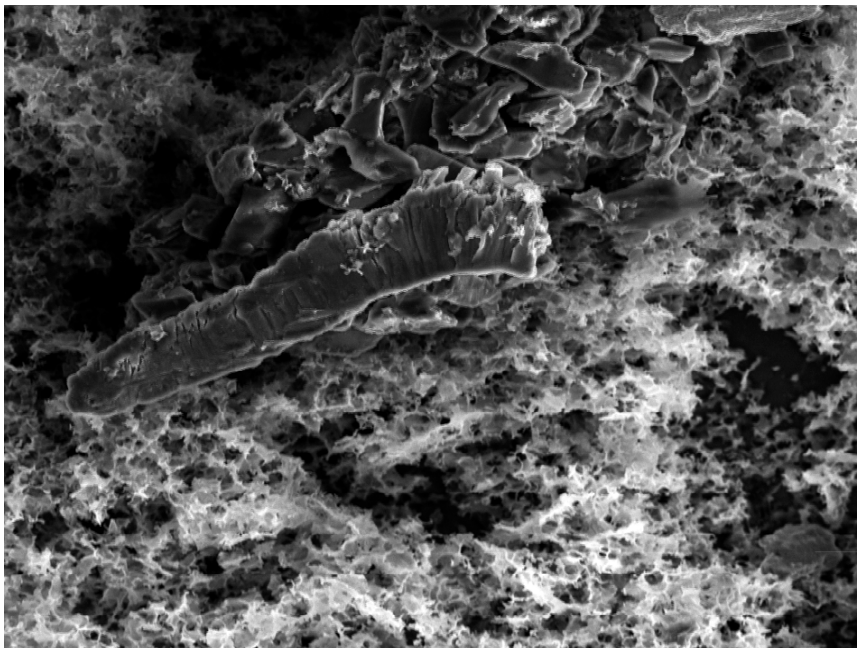

(a)

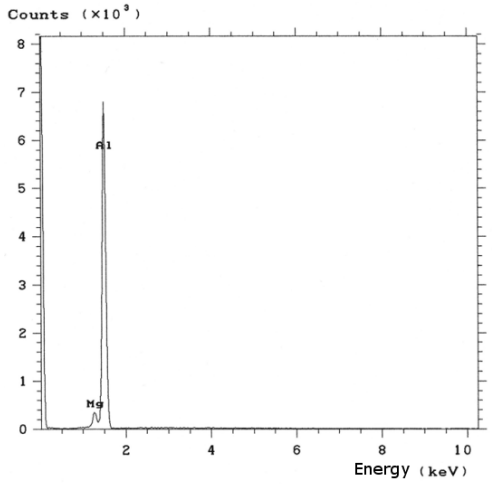

(b)

Figure 4.23. (a) Al-rich phase and (b) its EDS spectrum

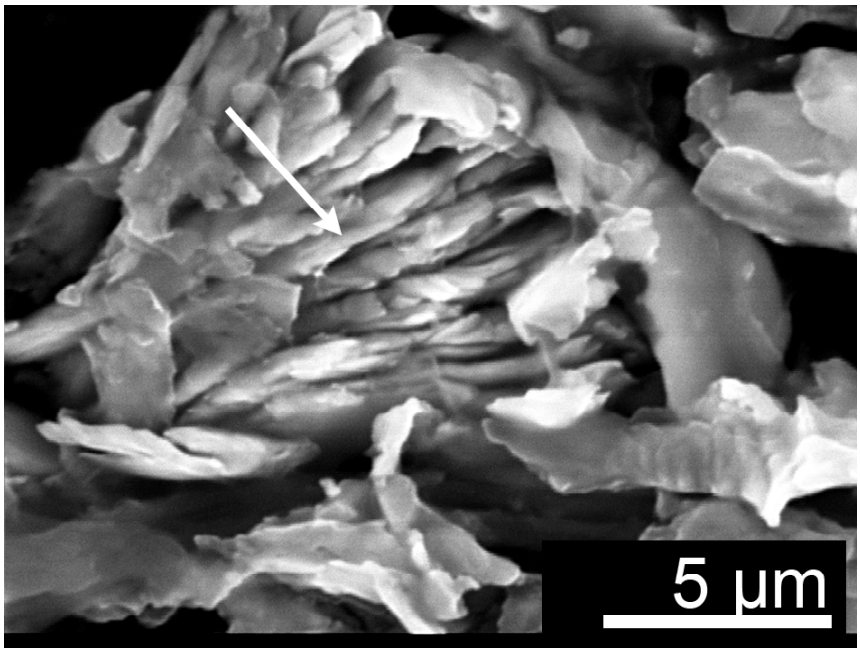

(a)

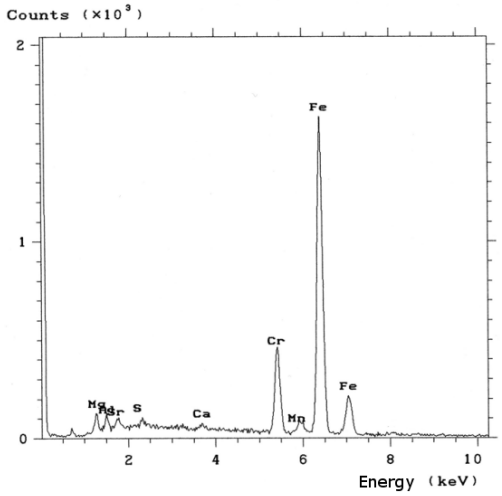

(b)

Figure 4.24. (a) Fe-rich inclusion and (b) its EDS spectrum

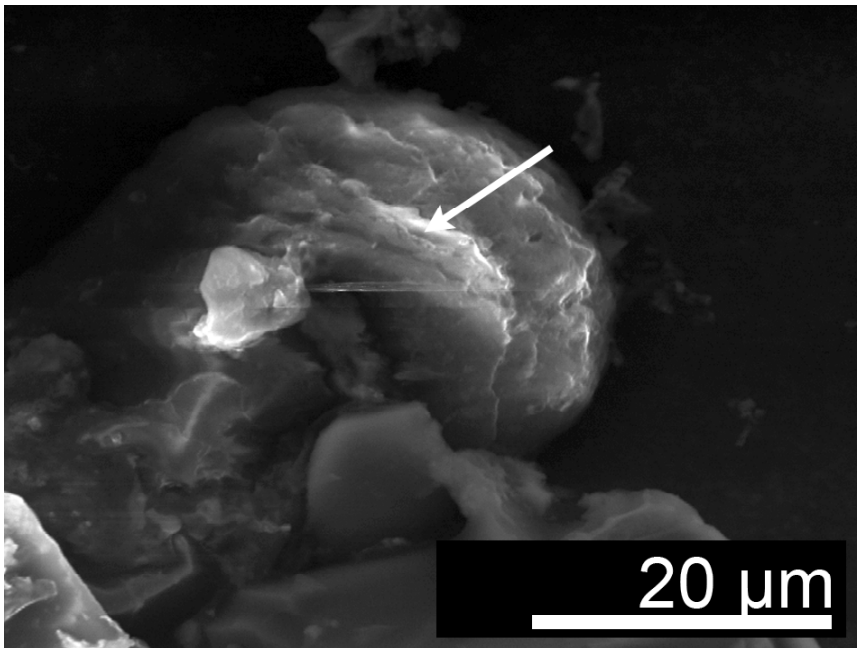

(a)

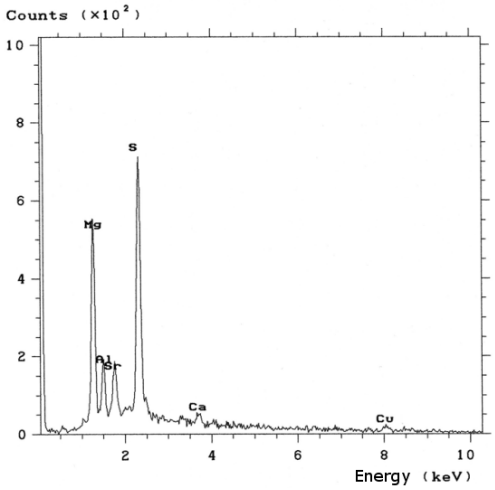

(b)

Figure 4.25. (a) S-rich inclusion and (b) its EDS spectrum

4.4.4 Conclusion

Deep etching was successful in isolating the precipitate phases from various magnesium alloys by selectively removing the primary α-Mg grains. The $(Mg,Al)_2(Ca,Sr)$ intergranular phase was retained and exhibited its 3D interconnected network structure after the deep etching process. Furthermore, to back up the prior 2-dimensional EDS/EBSD analysis, the detrimental $Mg_{17}Al_{12}$ β-phase was observed in very small amounts in the MRI-153 alloy, and seems to be completely suppressed in MRI-153M alloy. This may explain the reason behind the MRI-153M's superior creep resistance compared to MRI-153.

Chapter References

[1] T. Sato, B. L. Mordike, J.-F. Nie, M. V. Kral, Magnesium Technology 2005 (2004) 305.

[2] J. Stearns, et. al, Mater. Sci. Eng. A A366 (2004) 262.

[3] B. R. Powell, JOM 54 (2002) 49.

[4] K. U. Kainer, Magnesium Alloys and Technology, Wiley-VCH, 2003.

[5] M. O. Pekguleryuz, Mat. Sci. Forum 350 (2000) 131.

[6] M. S. Dargusch, K. Pettersen, G. L. Dunlop, Proc. North American Die Casting Association (1997) 131.

[7] E. Cerri, S. Barbagallo, M. Cabibbo, E. Evangelista, Magnesium Technology 2002 (2002) 221.

[8] S. Kleiner, O. Beffort, P. J. Uggowitzer, Scripta Mater. 51 (2004) 405.

[9] K. Ozturk, Y. Zhong, A. A. Luo, Z.-K. Liu, JOM 55 (2003) 40.

[10] R. Ninomiya, T. Ojiro, K. Kubota, Acta Metall. Mater. 43 (1995) 669.

[11] E. Baril, P. Labelle, M. O. Pekguleryuz, JOM 55 (2003) 34.

[12] E. Aghion, B. Bronfin, F. Von Buch, S. Schumann, H. Friedrich, JOM 55 (2003) 30.

[13] E. Aghion, B. Bronfin, Mat. Sci. Forum 350 (2000) 19.

[14] R. W. K. Honeycombe, The Plastic Deformation of Metals, Edward Arnold Publishers, 1984.

[15] P. Villars, L. D. Calvert, Pearson's handbook of crystallographic data for intermetallic phases, ASM International, Materials Park, OH, 1991.

[16] A. Maltais, D. Dube, M. Fiset, G. Laroche, S. Turgeon, Materials Characterization 52 (2004) 103.

[17] H. Nowotny, Zeitschrift fuer Metallkunde 37 (1946) 31.

[18] A. A. Luo, M. P. Balogh, B. R. Powell, Metall. Mat. Trans. A 33A (2002) 567.

[19] A. Iandelli, Jnl. Less-Common Metals 135 (1987) 195.

[20] P. Schobinger-Papamantellos, P. Fischer, Naturwissenschaften 57 (1970) 128.

[21] K. Schubert, S. Bhan, W. Burkhardt, R. Gohle, H. G. Meissner, M. Potzschke, E. Stolz, Naturwissenschaften 47 (1960) 303.

[22] E. Ghali, Mat. Sci. Forum 350 (2000) 261.

[23] E. Czech, G. Cordier, H. Schafer, Jnl. Less-Common Metals 90 (1983) 109.

[24] M. Vogel, O. Kraft, E. Arzt, Scripta Mater. 48 (2003) 985.

[25] L. Bourgeois, B. C. Muddle, J. F. Nie, Acta Mater. 49 (2001) 2701.

[26] M. M. Makhumudov, O. I. Bodak, A. V. Vakhobov, T. D. Dzhurayev, Russian Metallurgy 6 (1981) 209.

[27] A. Prince, N. I. Nikitina, Aluminum-Magnesium-Strontium, in: G. Petzow, G. Effenberg (Eds.), Ternary Alloys, vol 16, John Wiley & Sons Inc, Hoboken, NJ, 1999, pp. 413-425.

[28] A. Suzuki, N. D. Saddock, L. Riester, E. Lara-Curzio, J. W. Jones, T. M. Pollock, Metall. Mat. Trans. A 38 (2007) 420.

[29] W. Blum, B. Watzinger, P. Zhang, Adv. Eng. Mat. 2 (2000) 349.

[30] M. Regev, O. Botstein, M. Bamberger, A. Rosen, Mater. Sci. Eng. A 302 (2001) 51.

CHAPTER 5 - MODELING CREEP OF PURE MAGNESIUM AND MRI-153M

5.1 INTRODUCTION

This chapter discusses the application of a simple creep rate prediction model based on the traditional diffusion-based rate equation models. A simple model was initially constructed for creep of pure magnesium, followed by the introduction of further corrections to model the creep behavior of the alloy MRI-153M. These models were used to assist the prediction of creep rates anticipated in the subsequent interrupted creep experiments. The predicted creep rates were then compared against the actual secondary creep rates evaluated from the interrupted creep experiments of pure magnesium (Chapter 6) and MRI-153M alloy (Chapter 8).

At the point of writing, there is no single model that can satisfactorily predict the overall response of polycrystalline metals in power-law creep. This is because the phenomenon of power-law creep deformation occurs in a series of three distinct stages known as primary, secondary, and tertiary creep as illustrated on Figure 5.1, each requiring a detailed understanding of the complex material-specific mechanisms of deformation. Primary and tertiary creep stages are also known as “transient” creep since they do not exhibit constant creep rates. The scope of this research is restricted to the secondary creep stage, in which the majority of the creep deformation under power-law creep takes place.

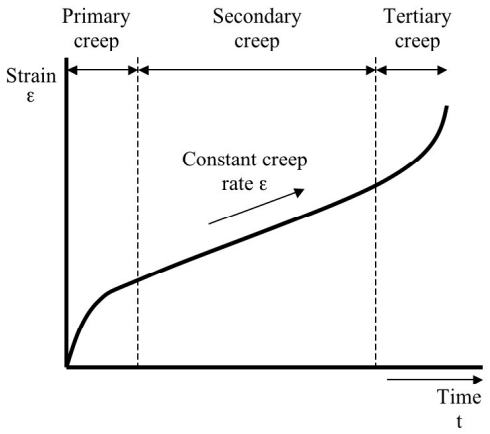

Figure 5.1. A hypothetical creep curve of a typical crystalline metal

Prior to the emergence of computer simulations and high resolution TEMs, a wide variety of theories were proposed in order to correlate the fundamental material science theories to the experimentally observed creep data. Links between creep rate and dislocation densities [1], subgrain formation [2], and experimental verification and modifications of the Dorn equation based models [3, 4, 5] were independently evaluated during the 1960~70's. This eventually led to the greater understanding of the phenomenon of creep in the early 1980's by the establishment of what is now known as the basic "power-law" creep model [3], which generated many positive responses from the researchers in this field [4, 5]. Such dislocation-based models were further complemented by the studies such as by Taylor [6] on the crystallographic dependence of deformation, in order to take into account the variation in deformation of non-random textures.

It can be said that the recent advances in the understanding of the creep behavior of materials are largely due to the attempt to reconcile these early experimental and theoretical models by the use of modern computational and experimentation techniques in order to simulate a more complex phenomenological interactions. In publications since the 1980's, modeling techniques on creep behavior of crystalline metals have diversified into

four fields of interest:

1. Modifications of the simplified rate equations for specific use in a particular alloy system of interest [7, 8]

2. Traditional modeling based on the contribution of activation energies required to initiate various deformation mechanisms [9]

3. Local dislocation theories and crystallographic models of various dislocation modes in an ideal lattice [13, 14, 15]

4. Finite element based lattice or atomic structure models based on fundamental elasticity theories [16, 17, 18]

In broad terms under the above grouping, modeling types 1 and 2 attempts to predict the secondary creep rate, whereas types 3 and 4 generally attempt to predict more detailed sub-microstructural development, especially in the transient region of creep.

5.2 PRIMARY TRANSIENT CREEP

Rapid strain of a material during the initial transient period of creep is primarily attributed to the consumption of easily accessible glide paths and the migration of pre-existing dislocations until such options are exhausted. This rate of strain hardening is the critical factor in the magnitude and decay of the transient primary creep, and therefore dependent on the initial dislocation density and the available easy glide planes along the applied shear stress. Therefore, the primary interest in modeling the behavior in the transient primary creep is the contribution of simple glide of the available dislocations, plus additional corrections based on the alternative dislocation motions, such as in the interactions of edge

or screw pairs, partials [7, 10], or the resultant formations of complex jogs and sessile dislocations [14, 20, 21, 22]. These alternative mechanisms become statistically significant factors in the primary transient creep stage, when the dislocation density is already very high, particularly in heavily worked materials.

A general difference of opinion lies in whether to ignore the study of transient behavior since it is assumed to be an inherently unpredictable phenomenon dependent on prior defect concentration, or a statistically systematic process that can be explained by extension of the basic theories of secondary creep. Nabarro [11] provided a short summary and reviewed references to various conceptual models.

5.3 TERTIARY TRANSIENT CREEP

Tertiary creep is attributed to the catastrophic failure of a material due to the accumulation of creep-induced defects weakening the material to the level resulting in plastic collapse. The activation of tertiary creep is a dominant factor in understanding the maximum service life under creep. A ductile, homogeneous material that can tolerate substantial plasticity will have a delay in the onset of tertiary creep stage. On the other hand, a material that is brittle or exhibits uneven localized plasticity will be more prone to early emergence of tertiary creep stage due to formation of high stress concentration areas, which is more pronounced in hcp materials such as magnesium due to anisotropic deformation behavior [12]. However, the study of tertiary creep is a niche area in both academic [13] and industrial interests since the total duration of the tertiary creep stage is typically very short compared to the secondary creep stage, hence the attempt to control and possibly regulate the tertiary creep “rate” is a questionable approach for improving the creep resistance of a material.

5.4 SECONDARY CREEP

The secondary creep stage is commonly referred to as the "power-law" creep stage, in which the creep rate (which is typically known as the "minimum" creep rate) can be modeled by a function to the *n*-th power of the applied stress. In 1984, Frost and Ashby published a book "*Deformation-Mechanism Maps*" [14], which is effectively a large database of the secondary creep rates determined by past studies carried out by other researchers in various metallic materials. The gathered data were summarized in comprehensive graphs known as deformation mechanism maps, which classify the range of applied temperature and load conditions to different contributing mechanisms of creep based on fitting various rate equation models that agree with the past experimental observations. An example of a deformation mechanism map for pure magnesium is shown on Figure 5.2. The figure also highlights the two creep test specimens used in Chapter 6, illustrating how the two specimens can achieve an identical creep rate at different stress-temperature combinations, at different creep mechanism regimes.

Since this research was primarily focused on the "power-law" creep phenomenon, the fundamental definition of power-law was applied to modeling creep in pure magnesium and the MRI-153M alloy. To simplify the matter and make this chapter concise, a worked example is outlined in the following section for one particular creep test condition. In reality, the creep rate models were calculated for a wide range of test conditions using computation techniques. Some of these results are illustrated in various graphs in the following sections.

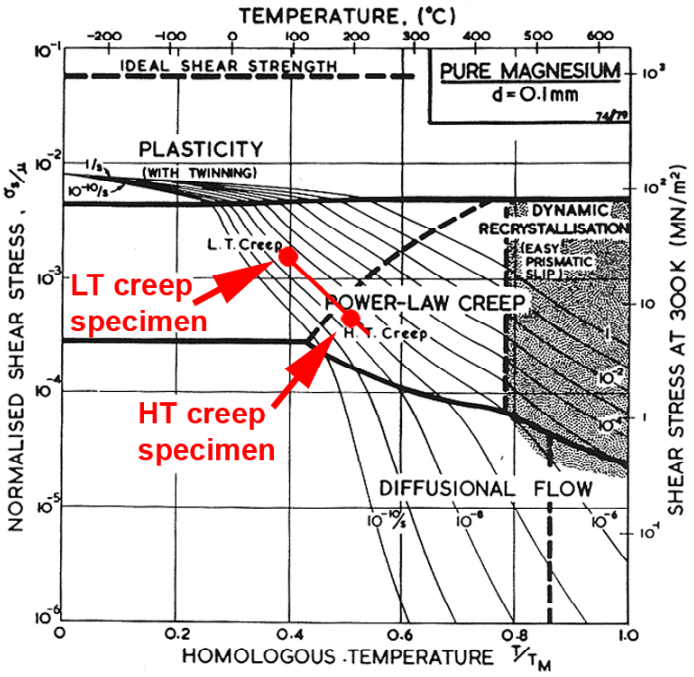

Pure magnesium with a grain size of 0·1 mm.

Figure 5.2. Creep rate prediction via deformation mechanism map

5.5 WORKED EXAMPLE FOR THE SIMULATED TESTING CONDITIONS USED IN HT-LS SPECIMEN

In Chapter 8, interrupted creep test of pure magnesium specimen designated HT-LS (high temperature – low stress) was performed at 200 ºC, 17.7 MPa. Shown below is a worked example of power-law creep rate model based on the contributions from lattice and core diffusion activation energies. According to Frost and Ashby, the power-law creep rate under shear stress can be modeled by Equation 5.1.

$$\dot{\gamma}_{PL} = \frac{A_2 D_{eff} \mu b}{kT}\left(\frac{\sigma_s}{\mu}\right)^n \tag{5.1}$$

The following constants were tabulated for hcp Mg by Frost and Ashby:

$b = 3.21\times10^{-10} m$	Burgers vector for basal deformation hcp Mg
$n = 5$	Power-law creep constant
$A = 1.2\times10^{6}$	Dorn constant for Mg
$\mu_0 = 16.6\times10^{9} Pa$	Shear modulus for Mg at room temperature, 1atm
$\frac{T_m d\mu}{\mu_0 dT} = -0.49$	Shear modulus temperature correction factor for Mg
$k = 1.381\times10^{-23}\ m^2 kg\ s^{-2} K^{-1}$	Boltzmann constant
$D_{0v} = 10^{-4} m^2/s$	Lattice diffusion pre-exponential for Mg
$Q_v = 135000 J/K$	Lattice diffusion activation energy for Mg

$a_c D_{0c} = 3 \times 10^{-23} m^4 / s$ Core diffusion pre-exponential for Mg

$Q_c = 92000 J / K$ Core diffusion activation energy for Mg

The power-law creep equation illustrates that the creep rate is a function of effective diffusivity (D_{eff}) of the material and the n-th power of the normalized shear stress. It may be questioned why the creep rate equation is a reciprocal function of temperature, even though an increase in temperature should result in an increase in creep rate. This can be explained by the fact that the effective diffusivity D_{eff} is also controlled by an Arrhenius equation, hence the rate equation is exponentially related to temperature as illustrated on Figure 5.3. Other necessary parameters of the power-law creep equation are calculated using Equations 5.2 to 5.4.

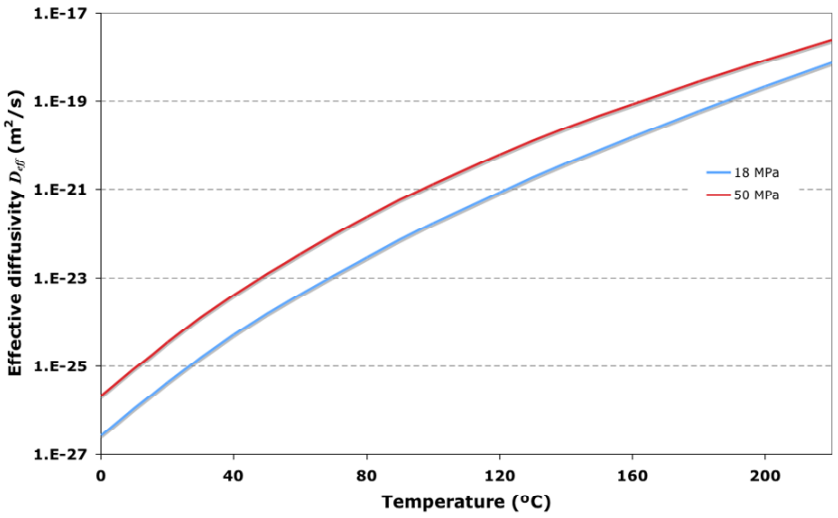

Figure 5.3. Effective diffusivity against temperature for pure magnesium

The average isotropic shear stress is calculated from the applied tensile stress of 17.7MPa:

$$\begin{aligned}\sigma_s &= \frac{\sigma_T}{\sqrt{3}} = \frac{17.7\times10^6}{\sqrt{3}} \\ &= 10.22\times10^6\,Pa\end{aligned} \tag{5.2}$$

The shear modulus for pure magnesium is corrected for the creep test temperature:

$$\begin{aligned}\mu &= \mu_0\left[1+\left(\frac{T-300}{T_m}\right)\left(\frac{T_m d\mu}{\mu_0 dT}\right)\right] \\ &= 16.6\times10^9\left[1+\left(\frac{473-300}{923}\right)(-0.49)\right] \\ &= 15.08\times10^9\,Pa\end{aligned} \tag{5.3}$$

The Dorn constant must also be corrected for power law creep factor *n*:

$$\begin{aligned}A_2 &= A\left(\sqrt{3}\right)^{n+1} \\ &= 1.2\times10^6\left(\sqrt{3}\right)^6 \\ &= 3.24\times10^7\end{aligned} \tag{5.4}$$

5.5.1 Calculation of diffusivity components

The total effective diffusivity D_{eff} for power-law creep is a compound value derived from the two active modes of transport, lattice diffusivity D_v and core diffusivity D_c. The difference between lattice and core diffusion mechanisms is explained in Chapter 2. In order to evaluate the effective diffusivity, the two contributing diffusivity values must be determined for the test temperature of 200 ºC.

Lattice diffusivity corrected for the creep test temperature:

$$D_v = D_{0v}\exp\left(-\frac{Q_v}{RT}\right) = 10^{-4}\exp\left(-\frac{135000}{8.314\times 473}\right) = 1.23\times 10^{-19} m^2/s \tag{5.5}$$

Core diffusivity corrected for the creep test temperature:

$$a_c D_c = a_c D_{0c}\exp\left(-\frac{Q_c}{RT}\right) = 3\times 10^{-23}\exp\left(-\frac{92000}{8.314\times 473}\right) = 2.07\times 10^{-33} m^2/s \tag{5.6}$$

Total effective diffusivity D_{eff}:

$$D_{eff} = D_v f_v + D_c f_c = \left[D_v + \frac{10 a_c D_c}{b^2}\left(\frac{\sigma_s}{\mu}\right)^2\right] = 1.23\times 10^{-19} + \frac{10\times 2.07\times 10^{-33}}{\left(3.21\times 10^{-10}\right)^2}\left(\frac{10.22\times 10^6}{15.08\times 10^9}\right)^2 = 2.16\times 10^{-19}\ \mathrm{m^2/s} \tag{5.7}$$

5.5.2 Relative contributions of lattice diffusion and core diffusion creep mechanisms

As calculated in Equation 5.7, the effective total diffusivity D_{eff} under the power-law creep mechanism is treated simply as a sum of diffusivities for the two complimentary mechanisms of dislocation motion, lattice diffusion D_v (climb + glide within lattice) and core diffusion D_c (formation of localized dislocation cells).

The values for the HT-LS (high temperature – low stress) specimen in this work calculated in Equation 5.5 and 5.6 are:

$$D_{eff} = 2.16 \times 10^{-19} \text{ m}^2/\text{s} \text{ (Effective total diffusivity)}$$

and $$D_v = 1.23 \times 10^{-19} \text{ m}^2/\text{s} \text{ (Lattice diffusion component of diffusivity).}$$

Therefore we can make a simple observation in which the relative contributions of lattice and core diffusion components to the total power law creep deformation can be visualized by the fraction:

$$f_{lattice} = \frac{1.23 \times 10^{-19}}{2.16 \times 10^{-19}} = 0.57 \tag{5.8}$$

In other words, at 200 ºC and 17.7 MPa, the total power law creep deformation would be attributed to approximately 57% lattice diffusion, 43% core diffusion mechanism. A similar analysis on the LT-HS specimen at 100 ºC and 50.2 MPa from Chapter 6 results in 1% lattice diffusion, 99% core diffusion mechanism. The simulated ratio of lattice and core diffusion mechanisms within the expected temperature range for power-law creep is illustrated on Figure 5.4.

One may question why an interrupted creep experiment on LT-HS specimen was carried out in 99% core diffusion condition, but the HT-LS specimen was only carried out in 57% lattice diffusion condition, instead of trying to achieve 100% lattice diffusion. This can be explained by the equation for D_{eff}, which shows that the lattice diffusion component is always present, and the core diffusion component is added to this as a function of applied stress. Therefore when creep deformation is assisted by tensile stress, it is unreasonable to achieve fully lattice diffusion controlled creep under power-law creep regime, unless we are dealing with recrystallization at elevated temperatures without any application of external stresses.

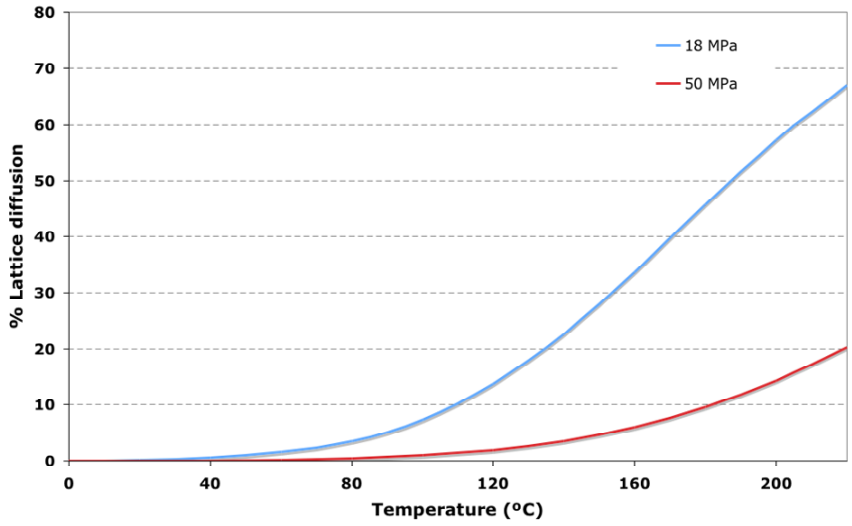

Figure 5.4. Simulated ratio of lattice diffusion and core diffusion mechanism in creep of pure magnesium

5.5.3 Calculation of predicted creep rate for HT-LS specimen

Finally, Equation 5.9 evaluates the secondary creep rate for the HT-LS specimen using the parameters obtained so far.

$$\begin{aligned}\dot{\gamma}_{PL} &= \frac{A_2 D_{eff} \mu b}{kT}\left(\frac{\sigma_s}{\mu}\right)^n \\ &= \frac{(3.24\times10^{7})(2.16\times10^{-16})(1.51\times10^{10})(3.21\times10^{-10})}{(1.381\times10^{-23})(473)}\left(\frac{10.22\times10^{6}}{1.51\times10^{10}}\right)^5 \\ &= 7.37\times10^{-7}/s\end{aligned} \tag{5.9}$$

The equivalent creep rate for an isotropic tensile stress is:

$$\dot{\varepsilon}_{PL} = \frac{7.37\times10^{-7}}{\sqrt{3}} = 4.26\times10^{-7}/s$$

This basic power-law creep model based on the activation energies required for core diffusion and lattice diffusion predicted the secondary creep rate of 4.26×10^{-7} /s for the pure magnesium HT-LS Specimen (200 ºC, 17.7 MPa).

5.5.4 Correction for grain size

The rate equation described in Equation 5.9 was calculated based on the constants evaluated by Frost and Ashby from past literatures. One of the differences between the current research specimens and those tabulated by Frost and Ashby is the average grain size, which is 40.4 μm in the current research, compared to 100 μm stated by Frost and Ashby. Since their work was essentially a compilation of data gathered from past studies in creep of magnesium, it is doubtful whether the claimed 100 μm has any real significance. A reduction in grain size is generally considered to be detrimental to creep resistance, since

grain boundaries offer easy pathways to assist dislocation transport. Therefore, the creep rate calculated with Equation 5.9 is possibly an underestimate compared to the actual experimental results. However, to compensate for the smaller grain size of the specimen, one may take into account the diffusional flow at grain boundaries. Frost and Ashby summarizes the model devised by Gibbs [15], and Raj and Ashby [16] as follows:

$$\dot{\gamma}_{GB} = \frac{42\sigma_s \Omega}{kTd^2} D_{eff} \qquad where\ D_{eff} = D_v + \frac{\pi\delta}{d} D_b \tag{5.10}$$

The effective diffusivity D_{eff} illustrate that the boundary diffusion component D_b will become more dominant if the average grain size d is small (i.e. more boundaries).

An example calculation for the effect of grain boundary diffusion in total creep rate for the measured average grain size of the test specimen (40 μm) is shown below:

$d = 4 \times 10^{-5} m$ Average grain size

$\Omega = 2.33 \times 10^{-28} m^3$ Atomic volume for magnesium

$Q_b = 92000 J/mol$ Boundary diffusion activation energy

$\delta D_{0b} = 5 \times 10^{-12} m^2/s$ Boundary diffusivity constant

(All other constants are same as in the power-law creep case)

Boundary diffusivity for the test temperature of 200 ºC is:

$$\begin{aligned} \delta D_b &= \delta D_{0b} \exp\left(-\frac{Q_b}{RT}\right) = 5 \times 10^{-12} \exp\left(-\frac{92000}{8.314 \times 473}\right) \\ &= 3.46 \times 10^{-22} m^2/s \end{aligned} \tag{5.11}$$

The effective diffusivity is:

$$D_{eff} = D_v + \frac{\pi\delta}{d} D_b = 1.23\times10^{-19} + \frac{3.14\times3.46\times10^{-22}}{4\times10^{-5}} \\ = 2.73\times10^{-17} m^2/s \tag{5.12}$$

The creep rate under shear for the HT-LS specimen due to grain boundary diffusivity is:

$$\dot{\gamma}_{GB} = \frac{42\sigma_s\Omega}{kTd^2} D_{eff} = \frac{42\left(10.22\times10^{6}\right)\left(2.33\times10^{-28}\right)\left(2.73\times10^{-17}\right)}{\left(1.38\times10^{-23}\right)473\left(4\times10^{-5}\right)^2} \\ = 2.61\times10^{-7}/s \tag{5.13}$$

The equivalent creep rate for an isotropic tensile stress is:

$$\dot{\varepsilon}_{GB} = \frac{2.61\times10^{-7}}{\sqrt{3}} = 1.51\times10^{-7}/s$$

Comparing this result to the earlier prediction based on power-law creep at 4.26×10^{-7} /s, it becomes apparent that the contribution from the grain boundary component is significant. By combining these two creep rates, one can predict a total creep rate of:

$$\dot{\varepsilon} = 4.26\times10^{-7} + 1.51\times10^{-7} \\ = 5.77\times10^{-7}/s$$

For the creep of pure magnesium, this will become the total secondary creep rate anticipated from the subsequent experiment on HT-LS Specimen (200 ºC, 17.7 MPa). As a comparison, a similar calculation on LT-HS Specimen (100 ºC, 50.2 MPa) predicts the secondary creep rate of 4.67×10^{-7} /s.

5.5.5 Significance of grain size variation on the total creep rate

To investigate the effect of grain size variation on the total creep rate, the same creep test conditions of both HT-LS and LT-HS specimens were simulated at various grain sizes from 1 to 100 µm. The results illustrated on Figure 5.5 shows that the effect of grain size becomes prominent below a threshold grain size of approximately 50 µm. It is also apparent that the low temperature creep is not greatly influenced by the grain size until the grains become much smaller than in any of the present experiments (~ 5µm).

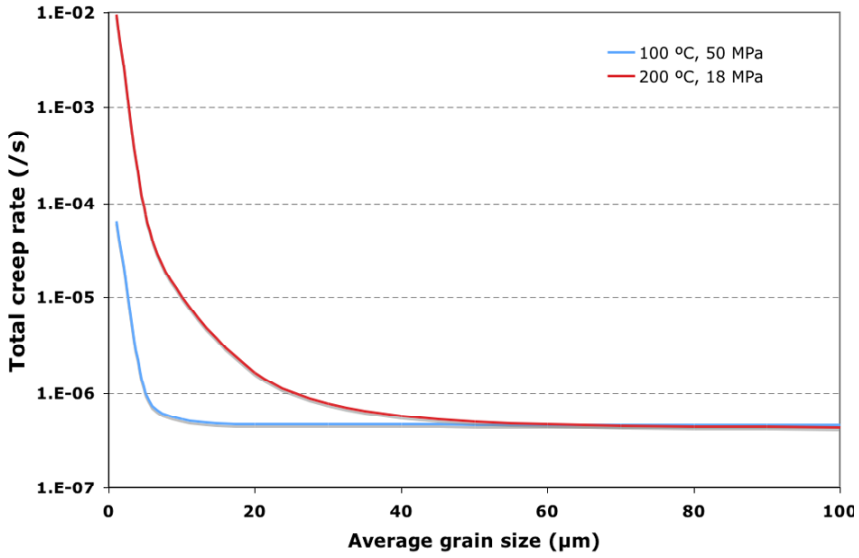

Figure 5.5. Effect of grain size variation on HT-LS and LT-HS specimens of pure magnesium

5.5.6 Conclusion

As shown in Table 5.1, the predicted creep rates for pure magnesium agree exceptionally well with the actual experimental creep rates obtained from Chapter 6.

Table 5.1. Comparison of predicted creep rate against experimental results for pure magnesium

	Experimental	Model prediction
LT-HS specimen	5.31×10^{-7} /s	4.67×10^{-7} /s
HT-LS specimen	5.26×10^{-7} /s	5.79×10^{-7} /s

Since the experimental creep rates were obtained from the interrupted creep tests, the predicted creep model also confirms that the periodic interruptions in the creep tests did not affect the creep properties to a significant degree. The correlation between theory and experiment was anticipated since the creep behavior of pure magnesium is essentially very straightforward, and the only significant external factor was the variation in grain size and crystallographic texture of the specimen. Macroscopic defects in the material typically do not affect the secondary creep rate, but shorten the creep life or accelerate either of the transient creep stages. It must be noted that the creep rate can vary by several orders of magnitude with even a small change in applied load or temperature, as illustrated on Figure 5.3. In the following section, the same power-law creep model was further expanded to model the creep rate of the creep resistant alloy MRI-153M.

5.6 ADAPTATION OF POWER-LAW CREEP MODEL TO THE MRI-153M ALLOY

The effect of alloying on the overall creep rate is a very difficult matter to evaluate, and there is yet to be a satisfactory model to handle this issue generically. This is due to the introduction of additional competing mechanisms accelerating or inhibiting the creep rate, further complicating the already crowded and ambiguous creep model of Equation 5.9. The magnesium alloy MRI-153M is in fact a very difficult material to model, since three separate mechanisms can take place within the typical creep temperatures of up to 200 ºC:

- Solid solution aluminum and zinc will act to introduce resistance to glide-controlled creep within the primary grains.
- The grain boundary intermetallic phase Mg_2Ca will act to retard grain boundary dislocation motion. Properties of this grain boundary phase is further complicated since it is in fact a substitutional heterogeneous $(Mg, Al)_2(Ca, Sr)$ structure in MRI-153M.
- The precipitation of supersaturated aluminum in a fine dispersion of $Al_{12}Mg_{17}$ β-phase, which may act to pin the lattice dislocations. This is a dynamic process taking place during creep, hence would require kinetic correction factors.

To understand the relative contributions in its simplest form, the contributions are separated into two independent effects that act as correction to the original creep rate equations:

- Effect of alloying on dislocation diffusivity within grains (lattice diffusion)
- Effect of alloying on dislocation diffusivity at grain boundaries (boundary flow)

In this section an example calculation was carried out for the MRI-153M alloy Specimen E, at 200 ºC and 50 MPa. Results of creep rate models for other MRI-153M specimens are summarized in Table 5.3 at the end of this chapter.

5.6.1 Effect of alloying on diffusivity within grains

For a climb-controlled (power-law) creep in a two-component system such as Mg-Al, Frost and Ashby [14] suggest the treatment of diffusivity correction as a rule of mixtures, where x_{Mg} and x_{Al} are the composition fractions.

$$\overline{D}_v = \frac{D_{Mg} D_{Al}}{D_{Mg} x_{Al} + D_{Al} x_{Mg}} \tag{5.14}$$

The lattice diffusivity of pure magnesium was calculated previously:

$$D_{Mg} = 1.23 \times 10^{-19} \text{ m}^2/\text{s}$$

The lattice diffusivity of aluminum can be determined from the values tabulated by Frost and Ashby:

$D_{0v} = 1.7 \times 10^{-4} m^2/s$ Lattice diffusion pre-exponential for aluminum

$Q_v = 142000 J/K$ Lattice diffusion activation energy for aluminum

$$D_{Al} = D_{0v} \exp\left(-\frac{Q_v}{RT}\right) = 1.7 \times 10^{-4} \exp\left(-\frac{142000}{8.314 \times 473}\right)$$
$$= 3.54 \times 10^{-20} m^2/s$$

Assuming full supersaturation of aluminum in MRI-153M alloy (x_{Al} = 8.4%), since this will give the maximum creep resistance:

$$\overline{D}_v = \frac{D_{Mg} D_{Al}}{x_{Al} D_{Mg} + x_{Mg} D_{Al}} = \frac{\left(1.23\times10^{-19}\right)\left(3.54\times10^{-20}\right)}{0.084\left(1.23\times10^{-19}\right)+0.916\left(3.54\times10^{-20}\right)} \qquad (5.16)$$
$$= 1.02\times10^{-19} m^2 / s$$

This is followed by a correction in the overall power-law creep rate by the introduction of a periodic array of obstacles, which in this case would give an increase in lattice resistance due to the solid solution Al and Zn. The model proposed by Frost and Ashby modifies the creep shear strain rate $\dot{\gamma}$ by the following equation:

$$\dot{\gamma}_T = \dot{\gamma} \exp\left[-\frac{\Delta F}{kT}\left(1-\frac{\sigma_s}{\hat{\tau}}\right)\right] \qquad (5.17)$$

Where:

ΔF	Activation energy to overcome the obstacle without aid from external stress
$\hat{\tau}$	Flow strength of the solid at 0 K, i.e. without aid from thermal energy

The parameters ΔF and $\hat{\tau}$ are characterized by the type of obstacles the precipitates may introduce, and are classified by their effective "obstacle strength", as shown on Table 5.2 [14].

Table 5.2. Characteristics of obstacles

Obstacle Strength	ΔF	$\hat{\tau}$	Example
Strong	$0.2\mu b^3$	$> \frac{\mu b}{l}$	Dispersions; large or strong precipitates (spacing *l*)
Medium	$0.2 - 1.0\mu b^3$	$\approx \frac{\mu b}{l}$	Forest dislocations, radiation damage; small or weak precipitates (spacing *l*)
Weak	$< 0.2\mu b^3$	$<< \frac{\mu b}{l}$	Lattice resistance; solution hardening (solute spacing *l*)

Based on correlation with the experimental results, these factors were found to agree with $\Delta F = 0.14\mu b^3$ and $\hat{\tau} \approx= \frac{\mu b}{l}$, which agrees with the "weak" obstacle strength for the ΔF (i.e. solution hardening), but approaching towards the "medium" obstacle strength for $\hat{\tau}$ that suggests a small influence of strengthening by the presence of precipitates. With these factors, the creep rate correction at the test condition for Specimen E (200ºC and 50MPa) becomes:

$$\begin{aligned} \dot{\gamma}_{adj} &= \dot{\gamma} \exp\left[-\frac{0.14\mu b^3}{kT}\left(1 - \frac{l\sigma_s}{\mu b}\right)\right] \\ &= \dot{\gamma}_{adj} = \left(2.4 \times 10^{-5}\right)\dot{\gamma} \end{aligned} \tag{5.18}$$

An approximate solute spacing of $l = 10^{-9}$ was used for Equation 5.18. However, a reasonable variation (100-fold) in the solute spacing produced negligible impact on the overall function.

Doubt arises here since the values for ΔF and τ can be very arbitrary, heavily relying on

agreement with the experimental observations. This is understandable since the contribution of the solute will be strongly affected by their crystallographic lattice occupation and their relative atomic size factors. These parameters can be modeled by ideal lattice simulations, but were not pursued within this research program. What the equation does tell us is that the overall creep rate due to lattice diffusion may be reduced by up to the order of 10^{-5} by the presence of an idealized solute. It must be stressed that many parameters such as ΔF and τ are material specific and may not be directly applied to another alloy system.

5.6.2 Effect of alloying on diffusivity at grain boundaries

Effects at grain boundaries is even more ambiguous in a bulk model analysis, since it is not the actual second phase precipitate itself that affects the creep rate (unless the phase is unstable), but it is due to the drag effect it causes on the surrounding grains by pinning the grain boundary dislocation motion. Therefore, a simple model would treat the grain boundary precipitate as stiff inert phase that acts as impermeable wall against dislocation motion. Frost and Ashby suggest a model [9, 14] for diffusional flow with limited mobility:

$$\dot{\gamma}_{GB} = \frac{\left(\frac{42\sigma_s \Omega D_{eff}}{kTd^2}\right)}{\left(1 + \frac{21\Omega D_{eff}}{kTd\rho_b b_b^2 M}\right)} \qquad \text{where} \quad M = \frac{D_s \Omega}{\beta kT b_b^2 C_0} \tag{5.19}$$

It can be seen that the numerator of the fraction is equivalent to the standard boundary diffusional flow model. Therefore, if the denominator of the fraction approaches unity, then there would be no apparent effect of boundary drag on the overall creep rate. If the

denominator of the fraction becomes greater than one, this suggests that the grain boundary precipitation phase has a beneficial effect of retarding the grain boundary mobility, and vice versa.

The Burgers vector for boundary diffusion, b_b, is the magnitude of Burgers' vector of dislocations that are constrained to travel along the boundary planes. The magnitude of b_b is smaller than those required for lattice diffusion, and can be approximated as 1/3 of the normal lattice Burgers vector, b [14]. The relatively small magnitude of b_b indicates that it is difficult to obstruct in comparison to the lattice diffusion creep, and therefore suggests that the boundary diffusion plays a significant role in alloyed material where lattice diffusion creep is suppressed.

Constants α and β are in the order of 1~20, and C_0 is the atomic fraction of solute aluminum, hence these can be clustered as one constant K in the order of magnitude of unity, to reduce the equation:

$$\dot{\gamma}_{GB} = \frac{\left(\frac{42\sigma_s\Omega}{kTd^2}D_{eff}\right)}{\left(1+K\frac{7\mu b}{dD_b\sigma_s}D_{eff}\right)} \qquad \text{where } K \approx (1\sim20) \qquad (5.20)$$

5.6.3 Definition of grain size

In the creep model for pure magnesium, average grain size was simply calculated as 40.4 μm based on the optical and electron microscopy measurements. However, the definition of the term grain size is not as clear in the modeling of MRI-153M due to the dendritic nature of the microstructure. There is a significant importance in deciding whether to treat the secondary dendrite arm spacing or actual high angle misorientation interface as a grain

boundary. A simple calculation for each case yields average grain size of 58 µm for secondary dendrite arm spacing, compared to 375 µm for high angle grain boundaries (> 15º misorientation) as measured from EBSD orientation maps such as the example illustrated on Figure 5.6.

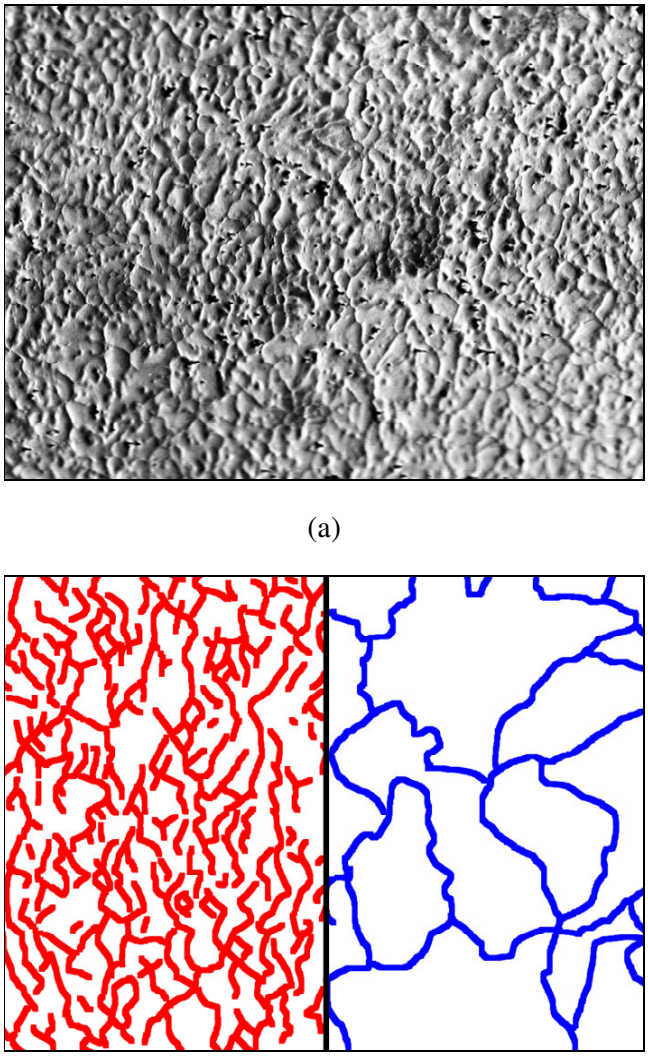

(a)

(b) (c)

Figure 5.6. Grain size interpretation of (a) the MRI-153M microstructure based on (b) dendrite arm boundaries, and (c) high angle (> 15º) misorientation boundaries

Based on the effect of grain size on the creep rate of pure magnesium illustrated on Figure 5.5, the contribution of grain boundary precipitate "drag" may seem redundant since the creep rate derived from grain boundary diffusional flow was very small compared to the overall creep rate due to lattice diffusion. However, this assumption does not hold for the case of MRI-153M alloy, because the lattice and core diffusion that were the dominant creep mechanisms in pure magnesium case are now retarded in the MRI-153M alloy due to the presence of solid solution strengthening. Therefore, the overall contribution of the boundary diffusion component may now become a more dominant factor.

By using the dendrite arm spacing of 58 μm as the grain size *d*, Equation 20 yields a viscous drag controlled boundary creep rate of:

$$\dot{\gamma}_{GB} = \frac{\left(\frac{42\sigma_s\Omega}{kTd^2} D_{eff}\right)}{1+\left(4.6\times10^{-3}\right)K} \qquad \text{where } K \approx (1\sim20)$$

This equation illustrates that the effect of viscous drag at interfaces is very small, contributing to the reduction in the boundary creep rate of 10% at most (if K = 20). Therefore this suggests that the effective contribution of boundary diffusion is less retarded than the lattice diffusion, further reinforcing the significance of the effect of grain size on the overall creep rate of the alloy.

5.6.4 Combined effects and creep rate prediction model for MRI-153M

Combining all of the model corrections leads to the prediction of total creep rate for the alloy MRI-153M. Results of the calculations along with the actual creep data from the interrupted creep tests on Specimens B to F from Chapter 10 are summarized on Table 5.3. The model results are shown for both the grain size of 58 μm (dendrite arm spacing) and 375 μm (high angle grain boundary).

Table 5.3. Predicted creep rates for MRI-153M specimens

		Creep rate (/s)		
Specimen	Condition	Actual	Model d =58μm	Model d =375μm
B	250ºC, 87MPa	4.4×10^{-7}	1.1×10^{-5}	9.4×10^{-6}
C1	200ºC, 60MPa	2.4×10^{-8}	1.8×10^{-7}	1.9×10^{-8}
C2	200ºC, 75MPa	1.7×10^{-7}	2.9×10^{-7}	8.7×10^{-8}
D	200ºC, 75MPa	2.3×10^{-7}	2.9×10^{-7}	8.7×10^{-8}
E	200ºC, 50MPa	5.4×10^{-9}	1.4×10^{-7}	5.9×10^{-9}
F	200ºC, 60MPa	3.5×10^{-8}	1.8×10^{-7}	1.9×10^{-8}

From Table 5.3 it becomes apparent that the approximate prediction differs greatly depending on what grain size value was used in the model. It appears that the model based on dendrite arm spacing overestimates the creep rate, particularly at low stress levels, whereas the model based on high angle grain boundaries results in a general agreement with the predicted model except for Specimen B. By ignoring the only specimen tested at

250 ºC (Specimen B), all the remaining specimens can be plotted on an isothermal graph of stress vs. creep rate at 200 ºC on Figure 5.7, along with the model predictions for the two grain sizes.

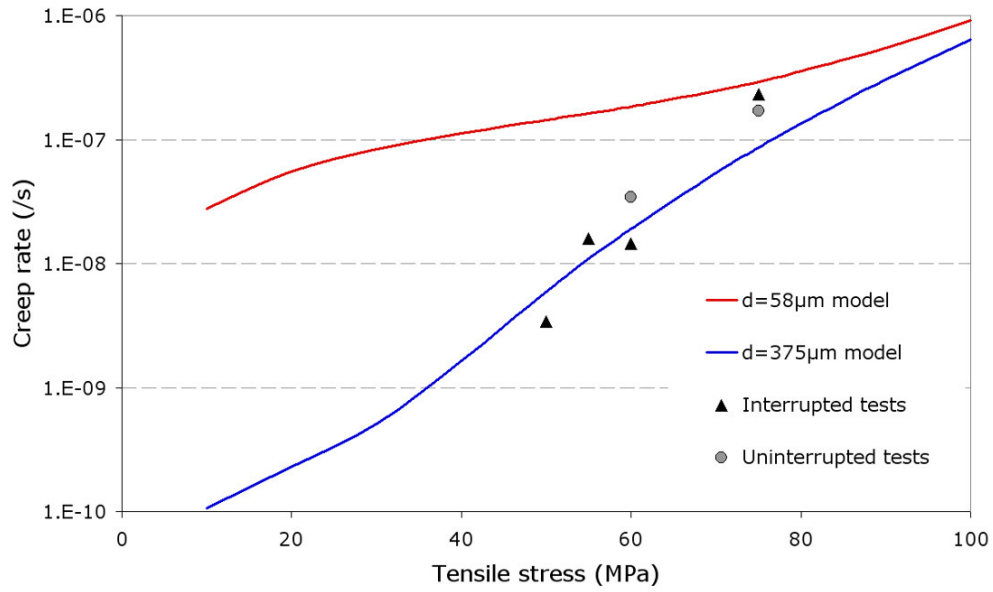

Figure 5.7. Tensile stress vs. creep rate for MRI-153M alloy at 200 ºC

Model verification

The creep rate model for alloy systems involves a large number of variables and many assumptions had to be made. The most significant assumption made in the current mode was the choice of $\hat{\tau} = \frac{\mu b}{l}$ for the boundary diffusion correction. This choice was made to achieve a model of best fit against the actual creep test results.

In order to justify the choice of $\hat{\tau} = \frac{\mu b}{l}$ for the model, a χ^2 (chi-square) distribution of the model was evaluated with a varying factor *X*, where $\hat{\tau} = X\frac{\mu b}{l}$, against the actual creep test results. For the χ^2 analysis the creep rates ($\dot{\varepsilon}$) were converted to $(\log \dot{\varepsilon})^2$ in order to

normalize the creep rates to a same order of magnitude, since χ^2 analysis is ineffective when the data sets differ by orders of magnitude, such as in the case of secondary creep rates (e.g. 10^{-7}~10^{-9} /s). This normalization process affects the magnitudes of the χ^2 values but does not affect the relative comparisons between the data sets. Therefore, the χ^2 test is conducted as follows:

$$\chi^2 = \sum_{i=1}^{k} \frac{\left[\left(\log \dot{\varepsilon}_{model}\right)_i^2 - \left(\log \dot{\varepsilon}_{actual}\right)_i^2\right]^2}{\left(\log \dot{\varepsilon}_{actual}\right)_i^2}$$

Outcomes of the χ^2 analysis are shown on Figure 5.8, in which a high χ^2 value indicates good agreement between the model creep rates and the actual creep test results. Key point of the figure is that the model based on the 375 μm grain size is always in closer agreement with the actual creep test results compared to the 58 μm grain size model. The figure also shows that the $X = 0.2$ has the closest correlation with the actual creep test results (χ^2 = 0.953). However, $X = 1$ was chosen for this study, since this has the closest correlation (χ^2 = 0.883) when the 75 MPa (highest stress) creep test results are excluded. This is because the creep rate at a high stress level (75 MPa) appears to disagree with the trend observed in all other creep test results, as illustrated on Figure 5.7. The reason for this phenomenon is explained further in the study of creep in the MRI-153M on Chapter 8.

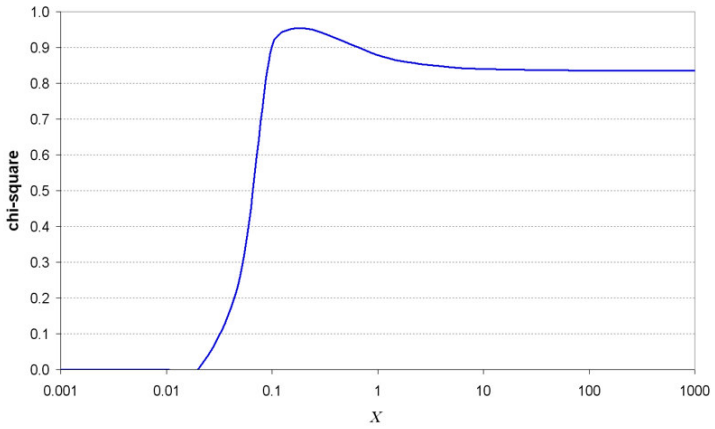

(a)

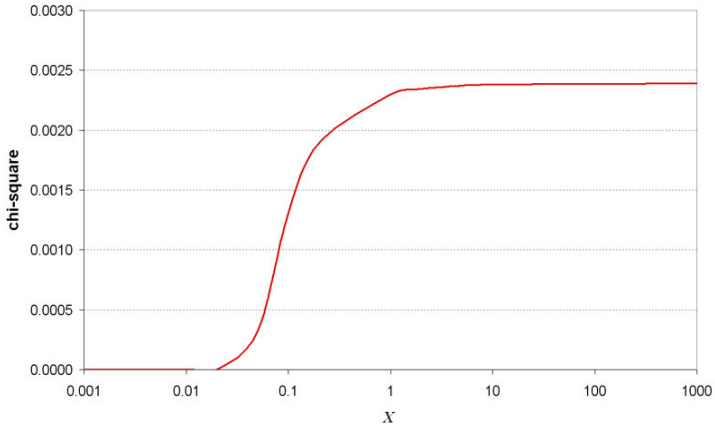

(b)

Figure 5.8. Correlation of the creep rate model against the actual creep test results, represented by χ^2 (chi-squared) under variation in X for (a) 375 μm and (b) 58 μm grain size models

5.6.5 Conclusion

Although the use of high angle grain boundaries in the model yields a close correlation with the actual creep test data, it must be stressed that the model is in no way an accurate representation of the underlying creep mechanisms, and therefore should not be trusted as a robust model for other testing conditions. The issue here is that it was not feasible to collect a sufficient number of creep rate data to produce a convincing open model that

applies to other test conditions, since that was not the objective of the research program. Instead of adjusting the vast number of model parameters to force agreement with what little quantity of experimental data collected, it is best for the model to be left as an open issue for future work, until a sufficient number of creep data is collected in order to accurately model the phenomenon at more wider range of load and temperature conditions.

For example, the results illustrate the effect of creep retardation by the addition of a single alloying element into solid solution (aluminium). However, this does not take into account the difference between various second phase intermetallic precipitates, or the presence of small addition of zinc, which would be treated as insignificant when applied to Equation 5.20, but actually significantly influences mechanical properties.

Admittedly, the above model has a number of assumptions and simplifications. However, it does bring into light three important aspects of creep in MRI-153M alloy:

- The basic diffusion model with standard correction factors does in fact agree very well with the experimental observations without any significant adjustments.

- Reduction in lattice diffusion due to the solid solution strengthening plays an important role in reducing the overall creep rate.

- Closer correlation of the experimental data with the model using the high angle grain boundaries shows that the interdentritic $(Mg,Al)_2(Ca,Sr)$ phase provides high resistance to creep deformation.

Furthermore, the tendency for the experimental data to converge towards the dendrite arm spacing model at higher stress levels indicates the breakdown of reinforcement provided by the $(Mg,Al)_2(Ca,Sr)$ phase. This may suggest that a change in the alloy fabrication

principle is required when designing creep resistant alloys that are subject to the stress levels beyond this breakdown threshold. In particular, the density of high angle misorientation boundaries is no longer the sole factor in determining the creep rate, but the density and distribution of the dendrite arms must also be accounted for in the alloy design in order to minimize the secondary creep rate.

Chapter references

[1] J. B. Bilde-Sorensen, Acta Metall. 21 (1973) 1495.

[2] A. K. Miller, S. L. Robinson, O. D. Sherby, Philosophical Magazine 36 (1977) 757.

[3] A. M. Brown, M. F. Ashby, Scripta Met. 14 (1980) 1297.

[4] B. Walser, O. D. Sherby, Scripta Met. 16 (1982) 213.

[5] P. Gondi, A. Sili, Scripta Met. 21 (1987) 1393.

[6] G. I. Taylor, Jnl. Inst. Metals 62 (1938) 307.

[7] A. J. Kennedy, Process of Creep and Fatigue in Metals, Oliver and Boyd Ltd., Edinburgh, 1962.

[8] B. Wilshire, Metall. Mat. Trans. A 33 (2002) 241.

[9] M. F. Ashby, R. A. Verrall, Acta Metall. 21 (1973) 149.

[10] E. Clouet, Acta Mater. 54 (2006) 3543.

[11] F. R. N. Nabarro, Acta Mater. 54 (2006) 263.

[12] B. Plunkett, R. A. Lebensohn, O. Cazacu, F. Barlat, Acta Mater. 54 (2006) 4159.

[13] Y. Ni, C. Liu, D. Lin, Mater. Sci. Eng. A 423 (2006) 79.

[14] H. J. Frost, Ashby, M.F., Deformation-Mechanism Maps, Pergamon Press, 1982.

[15] G. B. Gibbs, Phil. Mag. 13 (1966) 317.

[16] R. Raj, M. F. Ashby, Met. Trans. 2 (1971) 1113.

CHAPTER 6 - SEQUENTIAL CREEP/EBSD STUDIES OF PURE MAGNESIUM

6.1 INTRODUCTION

6.1.1 Mechanisms of creep

The underlying theories of creep deformation in crystalline metals were briefly discussed in Chapter 2. To go over the key points, in its common operating temperature range of approximately 0 - 200ºC, creep of magnesium is known to fit into the power-law creep regime, governed by the ability for dislocation climb to take place. Within the power-law creep regime, as illustrated by the deformation mechanism map compiled by Frost and Ashby [1], there is an inflection in the iso-strain rate curves as the underlying creep mechanism shifts from "low temperature power-law creep" to "high temperature power-law creep". These theoretical models were also briefly discussed in Chapter 7.

High temperature power-law creep can take place by a lattice diffusion dominant mechanism since there is enough thermal energy to permit significant self-diffusion [1, 2, 3] within the interior of the ordered lattice (i.e. grain). However, the material within the low temperature power-law creep regime, with little thermal energy, would consequently require a higher stress in order to achieve an equivalent creep rate at a lower temperature. A higher applied stress would directly result in increased dislocation density and the material would undergo creep deformation by the formation of subgrain cell structures. This is because the dislocations in the lattice prefer to divert to a nearby high-energy interface, such as grain boundaries [1].

6.1.2 Significance of studying pure magnesium

Although it has little industrial relevance, pure wrought magnesium has the experimental advantage of reduced macroscopic problems such as porosity, segregation, grain size and orientation variations that can be found in cast alloys. Furthermore, comprehensive creep data is readily available for pure magnesium [1], enabling the comparison between the data obtained by past conventional creep tests and the present sequential creep tests.

One of the characteristics of the wrought magnesium is its tendency to form a nonrandom crystallographic texture during extrusion [4, 5, 6, 7]. This is significant because creep deformation of magnesium is primarily dependent on the crystallographic orientation of the grains, since there is limited number of potential slip systems available for the hexagonal close packed (hcp) lattice. In particular, the orientation for the activation of basal slip becomes an important factor [2, 3]. Therefore, in wrought magnesium where the prevailing texture can be oriented in a way to make basal slip difficult, such as in the case of a rolled sheet in tension, the activation of other high energy slip modes such as prismatic, pyramidal or twinning becomes of interest.

Although the pioneering studies of creep by Roberts, Gibbs, Sherby and others [10, 11, 12, 13, 14, 15] provide good understanding of the underlying mechanisms of creep in polycrystalline magnesium as discussed in Chapter 2, there is surprisingly little information available on microstructural development during creep, perhaps due to the greater industrial interest in Mg-Al alloys. Microstructurally, the high temperature, low stress power-law creep is believed to exhibit an ordered arrangement of dislocation substructures resulting in the formation of parallel lines of dislocation that may be observed as slip lines on unpolished surface [3, 11, 16]. On the other hand, low

temperature, high stress creep has been shown to be dominated by more localized clustering of dislocation cells or subgrains [4], which eventually break down into fine grains. Please note that in these experiments, adjacent grain misorientations of 5 – 15º are considered subgrains and misorientations greater than 15º are considered grain boundaries [5].

The relationship between flow stress and subgrain size, and its contribution to the creep rate is summarized by Sherby et al. [6] and remains an area of interest in the study of creep mechanisms [17, 19]. Examples of low-temperature creep microstructures at high stress levels were illustrated in a compilation by Gandhi and Ashby [7]. More recently, a similar microstructure was also exhibited in the work by Liu and Wu [8] on creep of AZ31 at a very fast strain rate. However, these observations are of little relevance, since both the temperature and the strain rates are very high (673~773 K, 10^{-3}~1 /s), which may lead to activation of additional slip systems and dynamic recrystallization beyond the "steady-state" dislocation governed creep mechanisms of interest.

The present series of sequential creep tests on pure magnesium was therefore conducted in order to identify the contrasting creep mechanisms within the power-law creep regime. This study on pure magnesium is by no means a simple precursor to the subsequent studies carried out on MRI series alloys. With very little understanding of the underlying creep in MRI alloys, it would be unreasonable to commence sequential creep experiments without confidence in whether the observations in the interrupted method do represent the conventional creep deformation mechanisms. Therefore, the study on pure magnesium also plays the most important role of validating the effectiveness of the proposed sequential creep/EBSD test technique.

Sequential creep tests were conducted on extruded 99.6% pure magnesium specimens under two basic sets of temperature-stress conditions in order to represent the different power-law creep mechanisms. At each interruption, selected regions were EBSD mapped to track microstructure, texture and intragranular misorientations throughout the creep deformation process. To our knowledge, such a series of experiments has never been conducted previously.

6.2 EXPERIMENTAL PROCEDURES

An extruded ingot of 99.6% high purity magnesium with an average grain diameter of 40 μm was wire-cut into miniature ASTM E8 rectangular tensile test specimen shapes with 3 × 4 mm cross-section and 15 mm gauge length. The specimens were tested as-received, and not annealed prior to creep testing. This decision was made based on the findings after carrying out several annealing experiments:

- Due to the small size of the original high purity magnesium ingots, it was very difficult to achieve a compromise between excessive grain growth due to annealing and strong texturing due to cold working.
- The introduction of microscopic defects such as corrosion pits upon annealing was significant.
- The as-received microstructures produced a fair representation of rolled sheet metal texture with controlled grain size, provided that the heavily textured surface layer was removed.
- The as-received microstructure contained tension twins in the primary magnesium grains, due to the compressive rolling process. The role of such tension twins upon tensile creep deformation was of interest, since this would represent a typical sheet metal microstructure.

The surfaces were polished with 0.05μm colloidal silica and two microhardness indents were placed, 0.5 mm from each sides, as reference markers for EBSD mapping. Details of the polishing procedures are discussed in Chapter 3. The microhardness indents were small enough such that final fracture did not initiate from the indents in any of the creep tests.

Creep tests were conducted in a heated pure silicone oil bath to reduce the temperature fluctuations and surface oxidation. The specimen extension was measured by a linear variable displacement transducer (LVDT) extensometer with a resolution of 1μm.

Two creep tests were conducted, with one LT-HS (Low temperature – High stress) specimen at 373 K and 50.2 MPa, and one HT-LS (High temperature – Low stress) specimen at 473 K and 17.7 MPa. These conditions were selected to achieve a minimum creep strain rate of $2.5 \sim 5 \times 10^{-7}$ /s for both specimens, based on the available data for pure magnesium [1] as illustrated on Figure 7.2.

Furthermore, consideration must be made for the difference in grain size between the specimens used in this experiment (approximately 40 μm using linear intercept method), compared to those used to generate the deformation mechanism maps (100 μm). It has been suggested that the reduction in grain size has an effect of reducing the creep resistance [9], due to the fact that the grain boundaries act as preferential sites for dislocation motion under power law creep. This is in contrast to a simple tensile yield case, in which the reduction in grain size typically has the effect of increasing the yield point by increase in internal energy due to higher defect density. Therefore, for creep deformation, the predicted creep rate based on these maps was corrected based on a boundary diffusion model in Chapter 5.

The samples were removed from the creep test every six hours and the same pre-determined surface locations were repeatedly mapped by EBSD, aided by the microhardness indent markers. The surface was lightly polished prior to each EBSD map with 0.05 µm colloidal silica to remove the oxide layer formed during the creep test. The polishing step removed up to 5 µm of thickness, and therefore the procedure is not strictly non-destructive, but this effect was considered negligible, since the general microstructure showed minimal variations. The automated EBSD maps were constructed on a 560 × 410 µm window with 1 µm step intervals using an HKL Channel5 EBSD system on a JEOL JSM-6100 SEM. A schematic of the specimen geometry is shown in Figure 6.1. Details of the EBSD orientation mapping process are discussed in Appendix B.

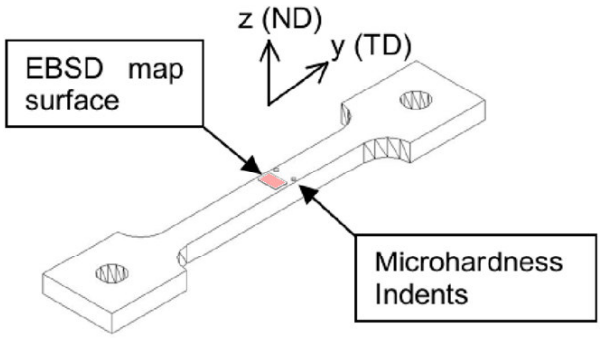

Figure 6.1. Geometry of the creep specimen indicating the tensile direction (TD) and EBSD scan normal direction (ND)

6.3 RESULTS

The general microstructure of the pure magnesium specimen prior to the creep tests is shown on Figure 6.2. The overall microstructure is a reasonably homogenous equiaxed grain structure, unlike the dendritic microstructures of the MRI-153/M alloys observed in Chapter 4. Some of the darker grains contain significant twinning, but the lighter colored grains do not exhibit any twins. The circular black defects are most likely to be pits formed during the etching procedure.

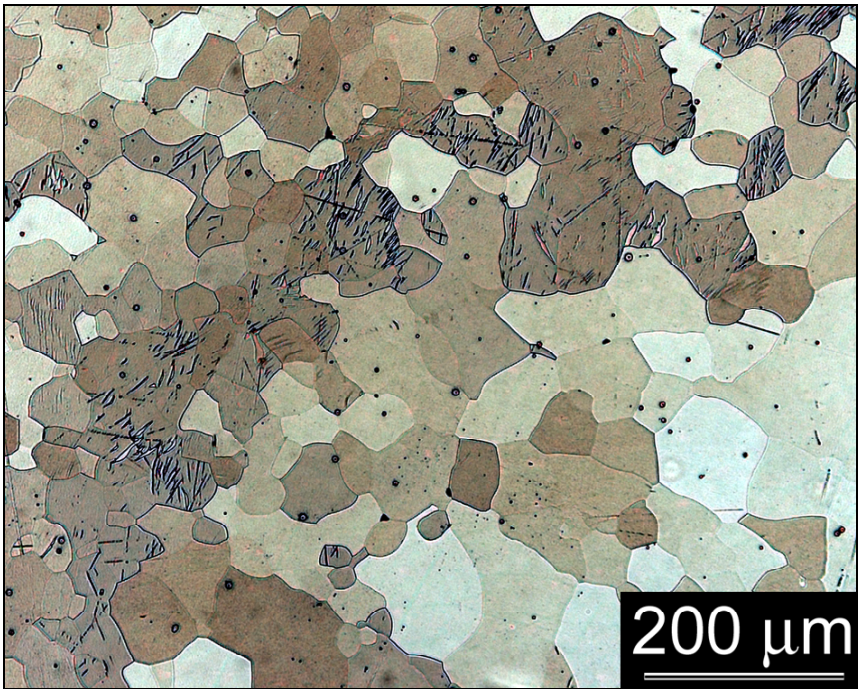

Figure 6.2. Optical micrograph of pure magnesium specimen, etched with 2% picric acid

Figure 6.3 shows a plot of creep strain vs. time for both sequential creep tests. The markers placed at six-hour intervals correspond to each interruption stage. The data exhibits the expected transient region in the first 20 hours, with up to 4% deformation, which is the primary transient creep stage. Following this, secondary creep produced a consistent creep strain rate even after each interruption, which suggests that the periodic removal of the creep specimen did not lead to any significant shock or cyclic loading issues. The secondary creep rates of LT-HS and HT-LS specimens were 5.31×10^{-7} and 5.26×10^{-7} /s respectively. This agrees very well with the creep rate initially predicted ($2.5 \sim 5 \times 10^{-7}$ /s), whilst taking into account that the predicted rates would be a slight underestimate by considering the smaller grain size of the specimens tested.

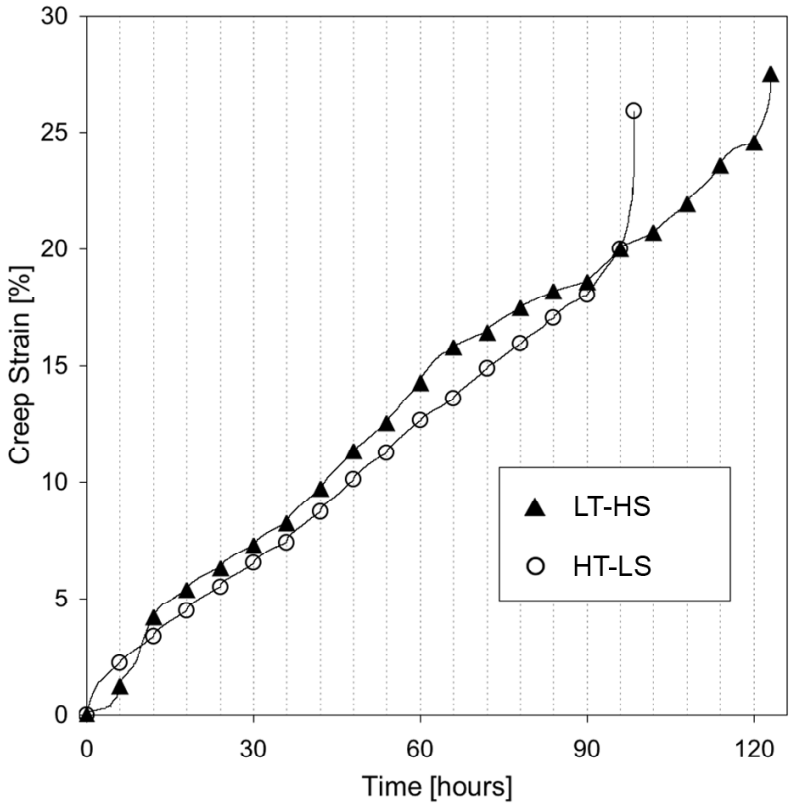

Figure 6.3. Combined creep strain graphs of Specimens 1 and 2. Each marker represents an interruption

Since the texture data was collected at six-hour intervals on the same area, the deformation process is best illustrated as a time sequence animation of pole figures and orientation maps. Since animation is not possible in print, Figure 6.4 offers a compromise by showing selected pole figures from the specimens at much larger time intervals. The axes in Figure 6.4 refer to the coordinate system identified on Figure 6.1, where the z-axis is the specimen surface normal, the y-axis is the tensile axis and the x-axis is the specimen transverse direction. The contour lines are drawn at intervals of 2 multiples of uniform distribution (MUD), which shows the strength of the clustering of poles relative to that of a random distribution.

Initially the specimens were cut in an orientation with a general alignment of the [0001] direction perpendicular to the y-direction. This is characteristic typical of an extruded magnesium, in which the hexagonal basal plane lies parallel to the direction of extrusion [10, 11]. Although the two specimens originated from the same source material, the difference in initial texture between them was unavoidable due to the inhomogeneity in the specimen and the limitation in the size of surface area covered by the EBSD mapping technique.

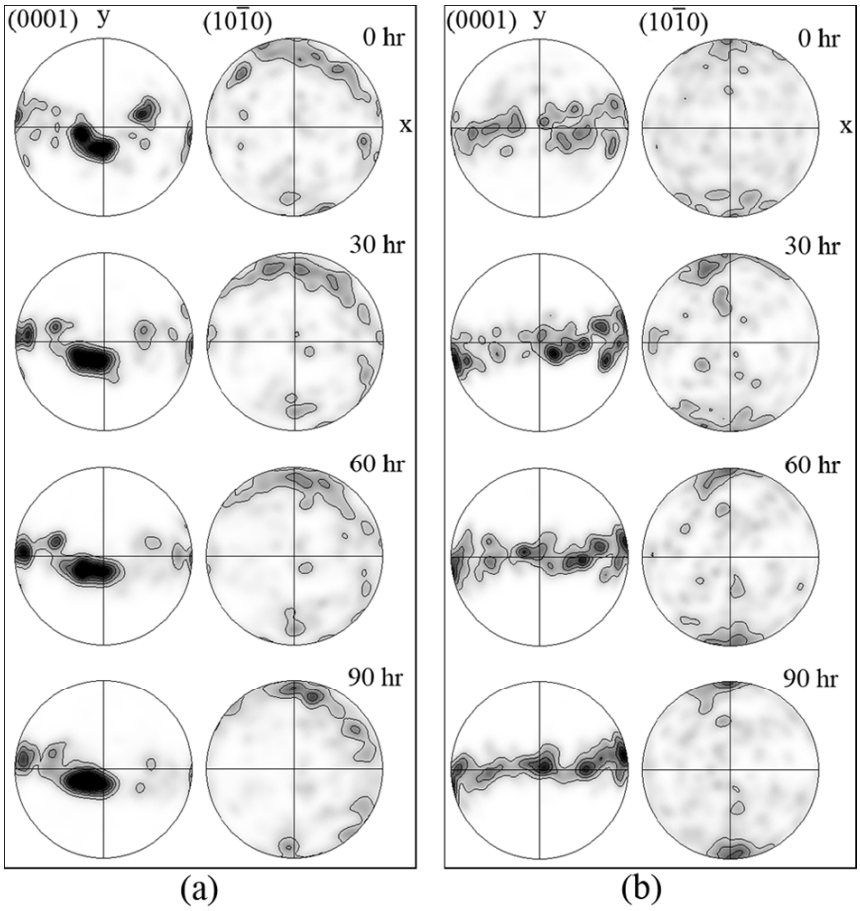

Figure 6.4. Sequence of pole figures for (a) LT-HS specimen and (b) HT-LS specimen before creep, and after 30, 60, and 90 hours of creep. Each contour line is at 2 MUD apart. The z-axis is the specimen surface normal, y-axis is the tensile axis

6.3.1 Texture development during creep

In the early stages of creep, both specimens showed a tendency for the [0002] to rotate perpendicular to the tensile axis [11]. This effect appears subtle in Figure 6.4, but is illustrated clearly by the decrease in y-axis Kearns factor F_y as shown on Figure 6.5. Kearns factor is evaluated by the EBSD system, and quantifies the strength of a particular texture on an EBSD map, represented by a factor for each axis, where $Fx+Fy+Fz = 1$. In this case, the Kearns factor was evaluated for the strength of (0001) on the specimen y-axis, which is the tensile axis. (e.g. If $F_{y,}= 1$ then the entire EBSD map surface will have the [0001] parallel to the tensile axis). In this case, the HT-LS specimen in particular, has a rapid decrease in F_y in the first 12 hours of creep. This behavior is typical of tensile creep in hcp material [12]. Basal slip, with the most easily activated slip system in hcp magnesium, contributes to the specimen strain until all of the basal planes approach being parallel to the tensile axis. Through this process, basal slip gradually becomes less favorable as the resolved shear stress upon the (0001) planes tends toward zero [11].

The data shown in Figure 6.4 appears similar to pole figures that can be generated in X-ray diffraction experiments, but it should be noted that these pole figures were obtained from the exact same local regions on the specimens' surface, after each interruption.

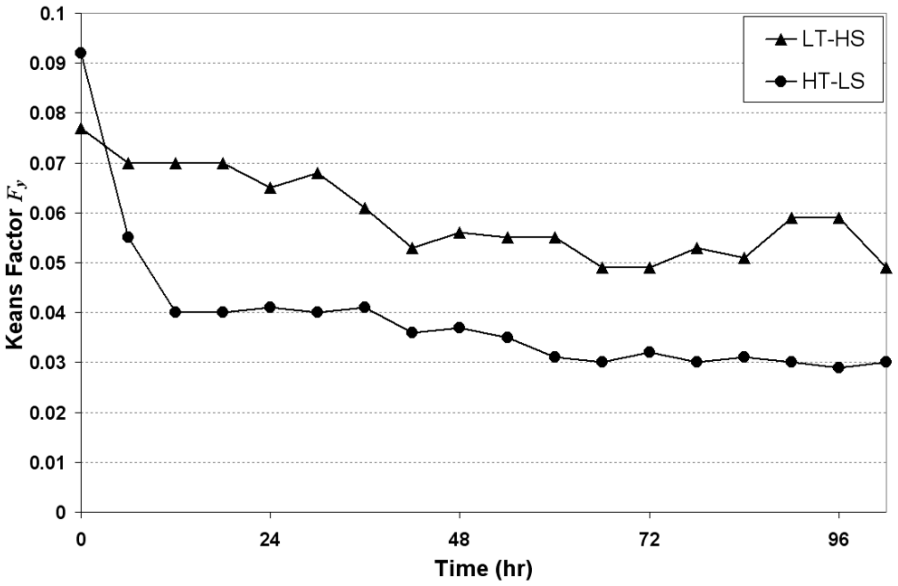

Figure 6.5. Kearns factor F_y for (0001) on y-axis (tensile axis) for the two creep specimens. Markers indicate creep interruptions where data was taken.

Figure 6.6 shows the sequence of EBSD orientation maps obtained from both specimens as creep progressed. These maps were created by contrast based on the crystallographic orientation, where darker areas represent (0001) facing the x-axis, and the lighter areas having (0001) facing towards the z-axis. Grain boundaries have also been superimposed. It must be noted that there is a significant difference in microstructural appearance between the 6 and 30 hour maps. This is attributed to the fact that the actual interruption intervals were in fact 6 hours, hence a significant amount of initial transient creep deformation and up to 25 μm of material was removed by surface polishing during each 30-hour interval. However, the pole figures in Figure 3 suggest that such changes in appearance did not significantly alter the overall texture.

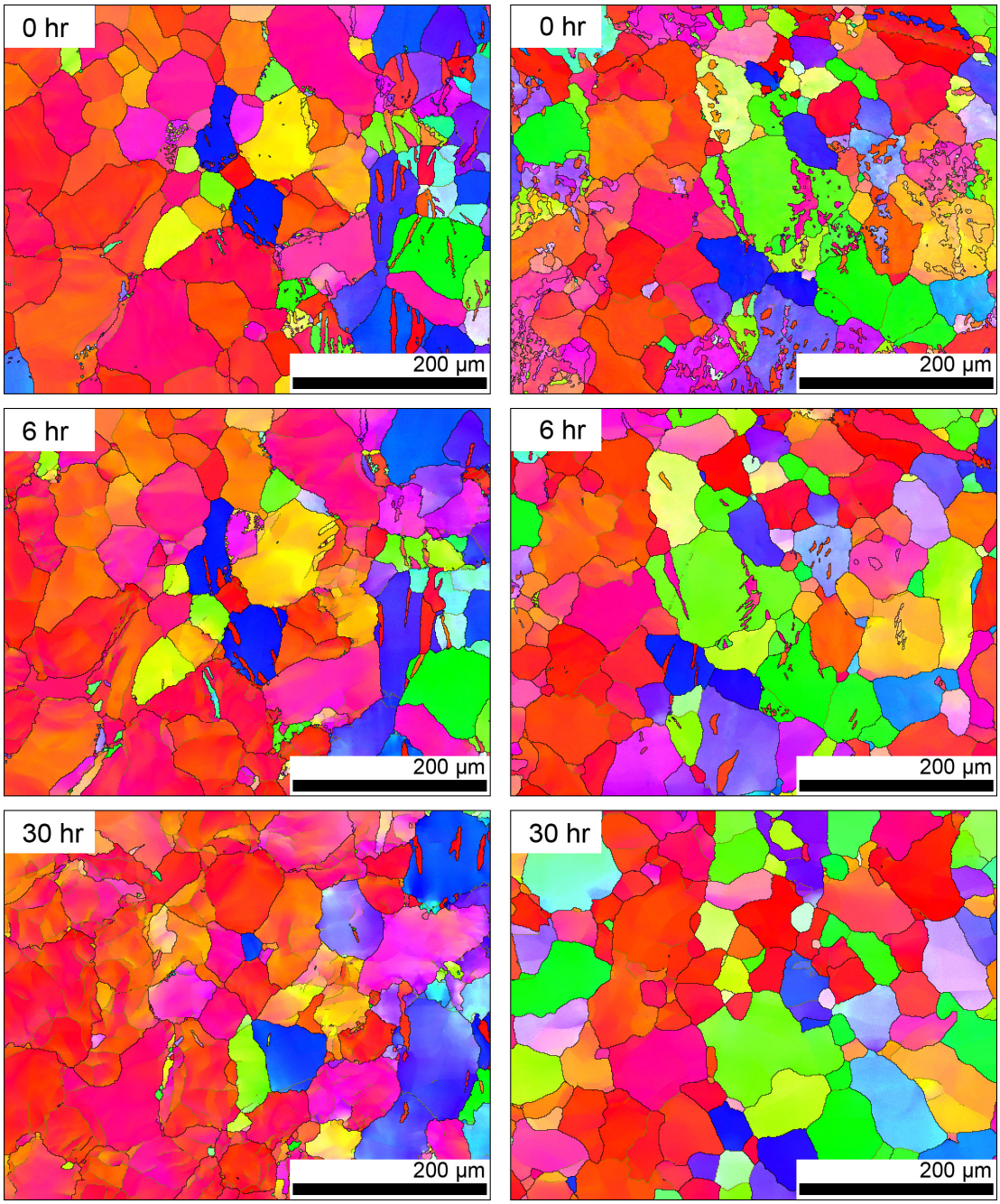
0 hr
200 µm
0 hr
200 µm
6 hr
200 µm
6 hr
200 µm
30 hr
200 µm
30 hr
200 µm

(a) (b)

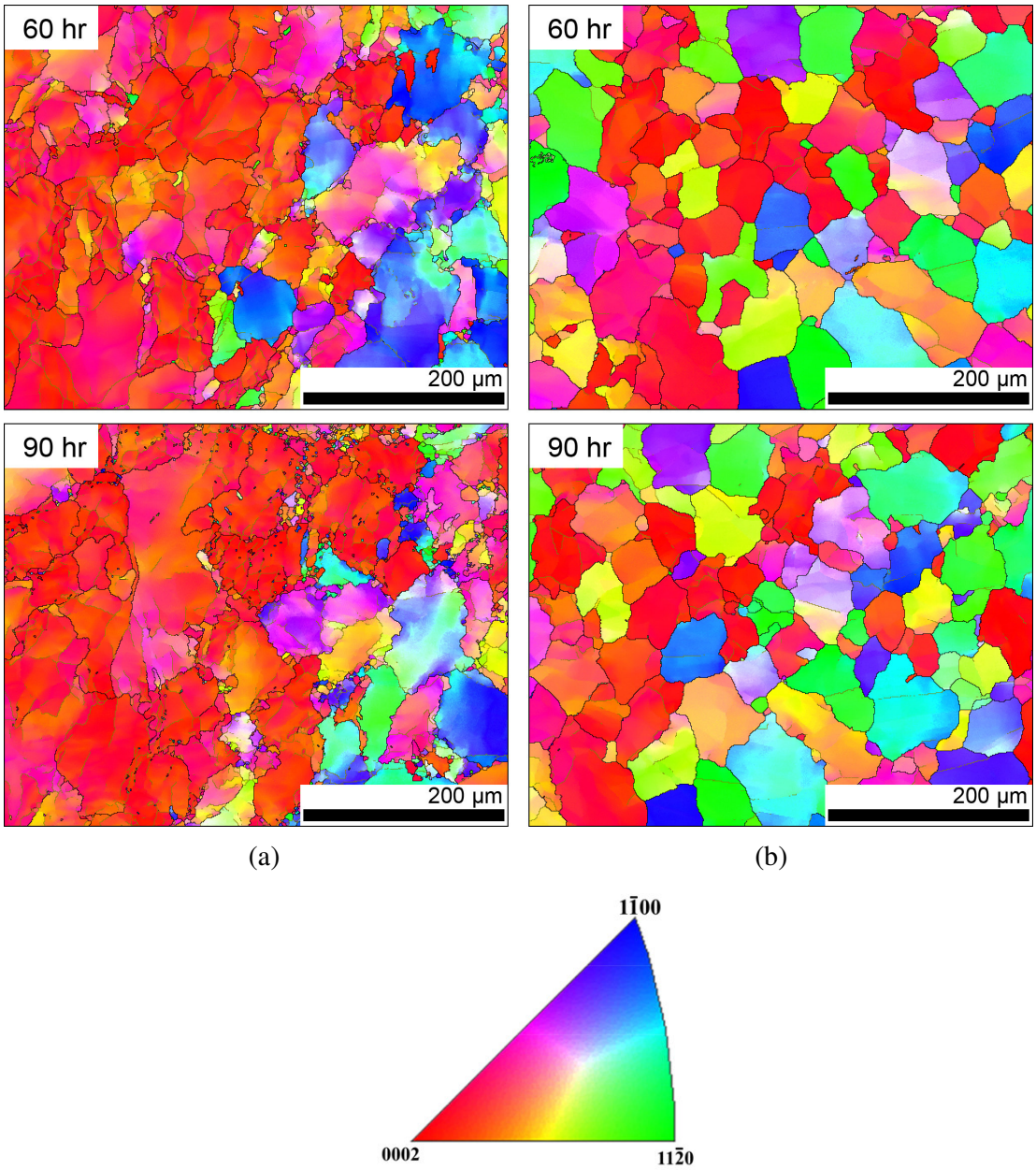

Figure 6.6. EBSD orientation maps of (a) LT-HS specimen and (b) HT-LS specimen as creep progresses. The inverse pole figure represents the surface normal direction.

6.3.2 Tension twins

It can be seen that both specimens exhibit tension twin boundaries created by the extrusion process. A typical twin is shown at higher magnification in Figure 6.7, where the misorientation angle of 86º about $\langle 2\bar{1}\bar{1}0 \rangle$ rotation axis was determined by the EBSD software. In the early stages of creep, both specimens exhibited a reduction in the number of tension twin boundaries. No development of compression twins [27, 28, 29] was observed, which is not surprising since the specimens' texture did not favor the formation of compression twins [13, 14]. After testing commenced, the relative frequency of twins dropped rapidly up until approximately 30 hours of testing and then remained at a steady, relatively low value. This is illustrated on Figure 6.8 but the use of EBSD map showing misorientation boundaries greater than 15º, where the special 86º $\langle 2\bar{1}\bar{1}0 \rangle$ boundaries are highlighted in red.

The degree of twinning in each EBSD map area was quantified by the HKL Channel 5 software. The method used here was to determine the misorientation angles between all adjacent pairs of EBSD patterns comprising the map area, ignoring all misorientation pairs of less than 15º (low angle boundaries), and the relative frequency of the occurrence of 86 ±1º misorientation pairs was recorded for each creep interruption, as shown in Figure 6.9a. As a comparison, the number of twins present in the EBSD maps was manually counted and also displayed on Figure 6.9b for the first 60 hours of creep. The result illustrate that the automated measurement of the 86º interfaces correspond very close to the physical number of twins counted in the microstructure.

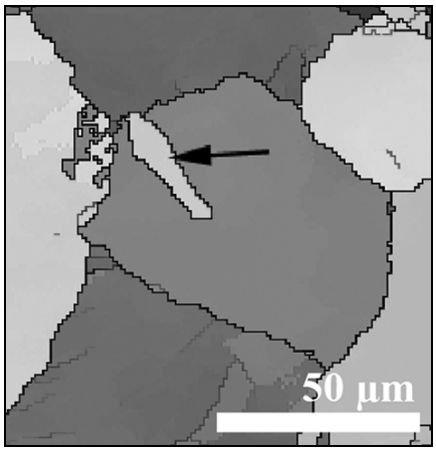

Figure 6.7. A typical twin boundary identified as a 86º misorientation interface on an EBSD map of LT-HS specimen

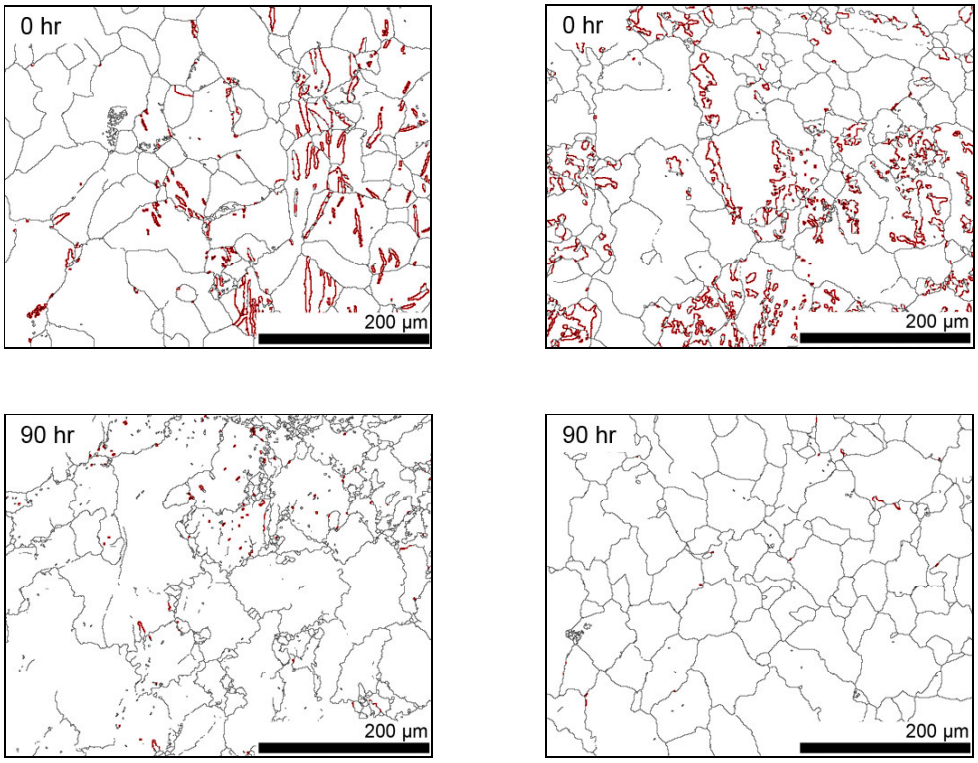

(a) (b)

Figure 6.8. Misorientation boundary maps of (a) LT-HS and (b) HT-LS specimen highlighting the 86º special boundaries

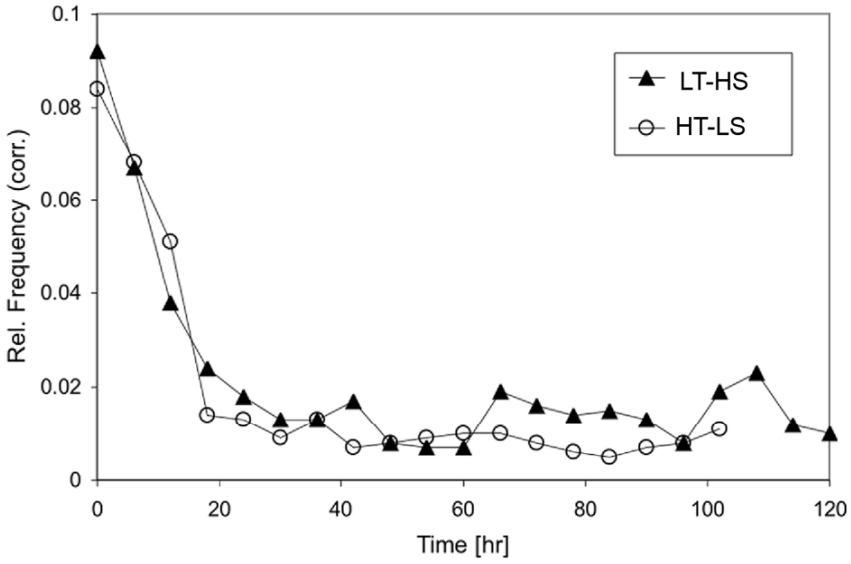

(a)

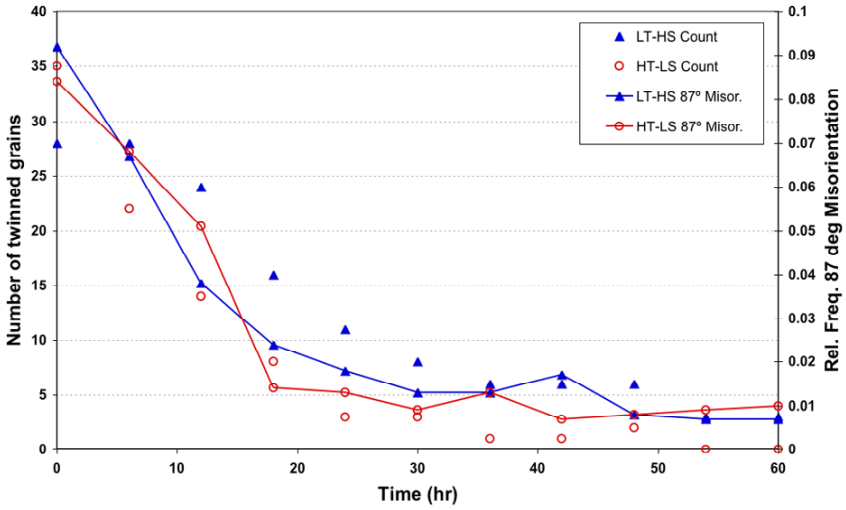

(b)

Figure 6.9. Frequency of 86º misorientation pairs relative to the total number of boundaries with misorientation greater than 3º (b) Number of twinned grains counted vs. 86º misorientation evaluated by EBSD for the first 60 hours

6.3.3 Low angle boundary and subgrain formation

After the initial transient stage, both specimens developed relatively high frequencies of low angle subgrain boundaries. This is quantified in Figure 6.10, which shows the relative frequency of 5º– 15º misorientation boundaries at each creep interruption stage. Boundaries misoriented less than 5º were not displayed in the figures so that the significant (5º– 15º misorientation) low angle boundaries are clearly visible. A high angle grain boundary misorientation was defined as 15º, according to established convention [15, 16]. LT-HS specimen exhibited a rapid development of low angle boundaries during the early stages of creep compared to HT-LS specimen, but after approximately 70 hours both specimens settled to a similar frequency occurrence of low angle boundaries. This is graphically visualized in Figure 6.11, which illustrates the contrast between the two specimens in the formation of misorientation boundaries as creep progressed.

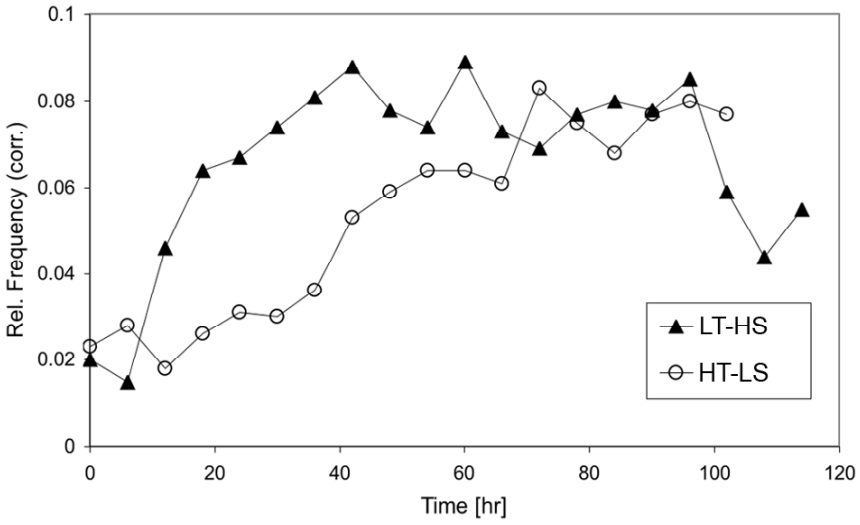

Figure 6.10. Frequency of misorientation pairs with 5º low angle boundary relationships in each EBSD map relative to the total number of boundaries with misorientation greater than 3º

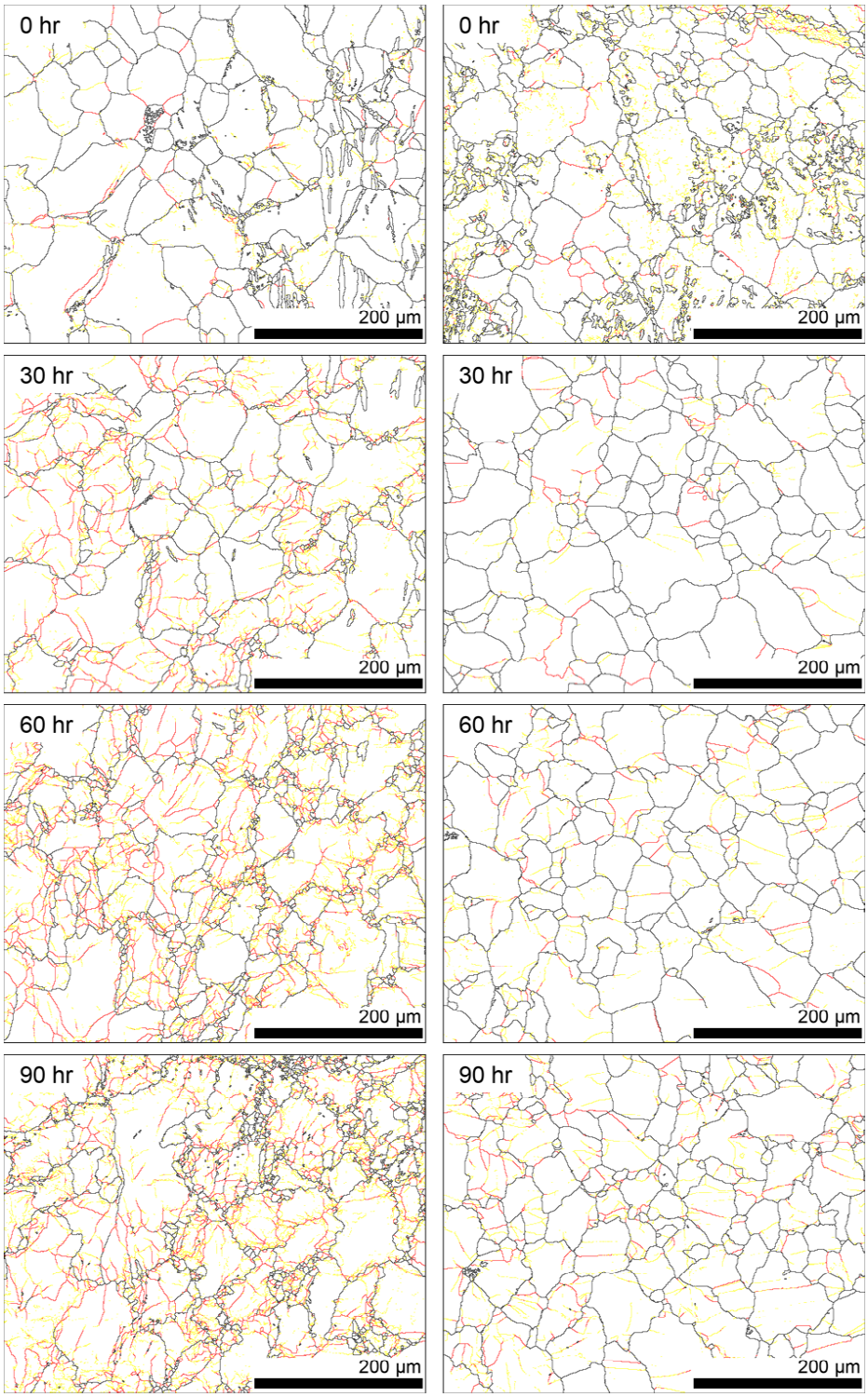

(a) (b)

Figure 6.11. EBSD maps of (a) LT-HS and (b) HT-LS specimen only showing the misorientation boundaries, 2-5º (yellow), 5-15º (red), and >15º (black)

The characteristic difference between the specimens was that LT-HS specimen exhibited a clustering of low angle boundaries near the original high angle boundaries to a point where after approximately 96 hours (16% deformation), subgrains had evolved into a network of fine grains as illustrated in Figure 6.12a. This observation is also quantified in Figure 6.13 which plots the average grain size over time. The grain sizes were measured using the EBSD software by counting the number of pixels enclosed within a misorientation boundary of greater than 15º. One pixel on a map is equal to 1 μm^2, which is the EBSD pattern acquisition step interval used for generating all of the maps. The average grain size of LT-HS specimen increased during the initial transient stage due to the elimination of twins, followed by a reduction in average grain size after 48 hours of creep. There is a large scatter in LT-HS specimen average grain size data beyond 48 hours, since some fine subgrains lie in the borderline range for EBSD grain detection criteria and are also easily affected by the surface polishing process. In contrast, HT-LS specimen formed parallel lines of low angle boundaries in certain grains as shown in Figure 6.12b and, after the transient stage, the grain size of HT-LS specimen maintained a steady value until failure finally occurred.

Figure 6.14 shows the final grain size distributions in both specimens, in terms of both frequency of occurrence and total area for a range of grain size categories. LT-HS specimen had a few very large grains and a relatively large number of small grains after 96 hours of creep. On the other hand, HT-LS specimen shows a near Gaussian distribution of grain size after 96 hours of creep, which is basically unchanged from the original distribution.

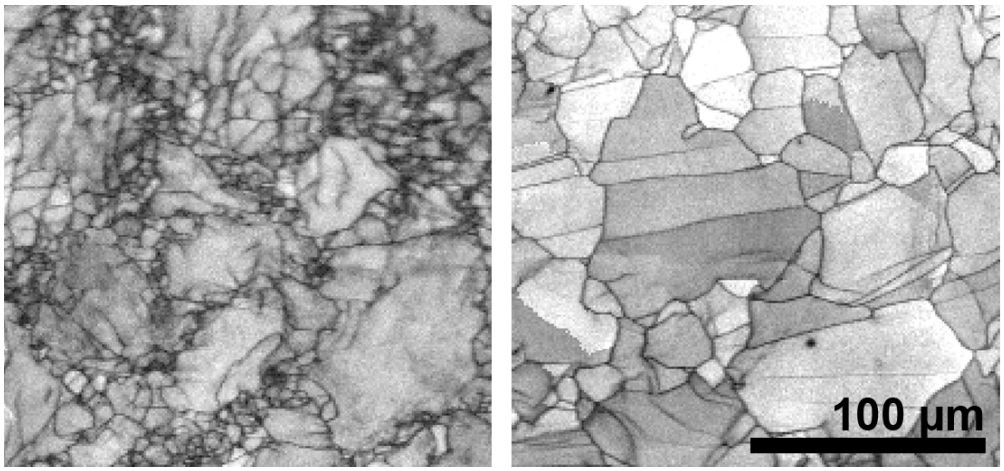

(a) (b)

Figure 6.12. Part of pattern quality maps of (a) LT-HS specimen and (b) HT-LS specimen at 96 hours of creep

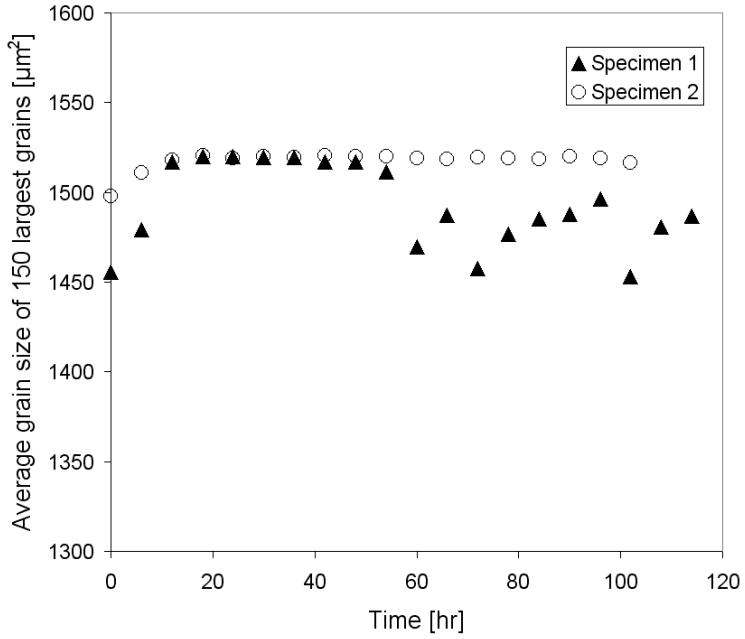

Figure 6.13. Average grain size vs. time

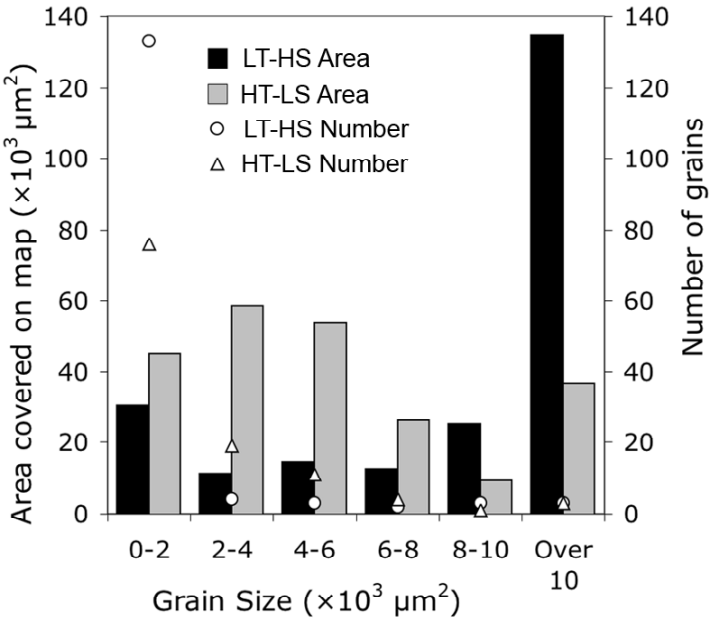

Figure 6.14. Grain size distributions of (a) LT-HS and (b) HT-LS specimen after 96 hours of creep measured automatically via EBSD

6.4 DISCUSSION

The time-sequence crystallographic orientation maps from the sequential EBSD technique provide new insight to the study of creep. The present work showed three important aspects of microstructural development during creep of pure wrought magnesium. The first aspect consists of the statistical reduction of the number of tension twins. Secondly, strain also occurs via a simple hcp a-axis basal slip until the supply of the available "crystallographically soft" grains gradually dwindles, which is illustrated by the rotation of (0001) poles towards the equator in the pole figures of Figure 6.4. The first two aspects of microstructural development are similar in mechanism and magnitude in both the low-temperature and high-temperature power law creep regimes. However, there is a departure in behavior of the two regimes at approximately 60 hours, which is marked by a change in average grain size (see Figure 6.13) for the low temperature power law creep regime.

In the third aspect of microstructural development, which distinguished the two different creep regimes, subgrain boundaries gradually become more evident as illustrated in Figure 6.12. In low temperature power law creep, subgrain cell structures form and subsequently develop into a fine grain networks near the original grain boundaries. This observation suggests a localized movement of dislocations toward the nearest grain boundaries, and is consistent with (1) insufficient thermal energy to activate creep deformation by lattice diffusion alone [17] and (2) an increase in dislocation density due to the relatively high applied stress. In contrast, the high temperature power law creep specimen, although experiencing a similar level of strain, displayed no noticeable fine grain formation near the original grain boundaries. Instead, low angle boundaries aligned into what can be observed as straight parallel lines, as shown on Figure 6.6 and Figure 6.12.

For pure magnesium, the only other microstructural characterization of creep near the current test conditions (to the authors' knowledge) was provided by Roberts [18], who illustrated a combination of both fine grain networks and slip line formation due to ambiguous test conditions. The work performed in the current study intentionally separated the two regimes of microstructural development, by firmly choosing test conditions in low-temperature power-law creep and high-temperature power-law creep for Specimens 1 and 2, respectively.

The pattern quality map in Figure 6.12 reveals low angle boundaries and damaged regions (i.e. poor pattern quality) more clearly than the equivalent Euler orientation maps, but does not provide any information about the orientation and significance of each of the observed boundaries, since both low and high angle boundaries appear as dark regions. One benefit of EBSD mapping is the diverse ways of expressing the map data, which is especially useful in the present case to further illuminate the microstructural evolution of high-temperature power-law creep (HT-LS specimen). Figure 6.15 highlights the significant low angle (5º~15º) boundaries in red, and the grains are colored based on the orientation of [0001] on the specimen x, y and z axis colored green, yellow and blue respectively, as illustrated on the accompanying pole figure.

Figure 6.15b clearly shows that, in HT-LS specimen, ordered parallel lines of low angle boundaries are more frequently observed in green coloured grains that have their [0001] oriented toward the x-axis, whereas blue grains tend to have the low angle grain boundaries in less ordered manner. It is also noted that there are no yellow grains, since there are very little grains with [0001] oriented parallel to the specimen y-axis (tensile axis). In contrast to the observations in high-temperature power-law creep (HT-LS specimen), low-temperature power-law creep (LT-HS specimen) showed little ordered

deformation by lattice diffusion creep alone. Both blue and green grains showed less development of ordered low angle boundaries, and the accumulation of low angle boundaries and breakup near the original grain boundaries is apparent, while the original grain interiors remain relatively undamaged.

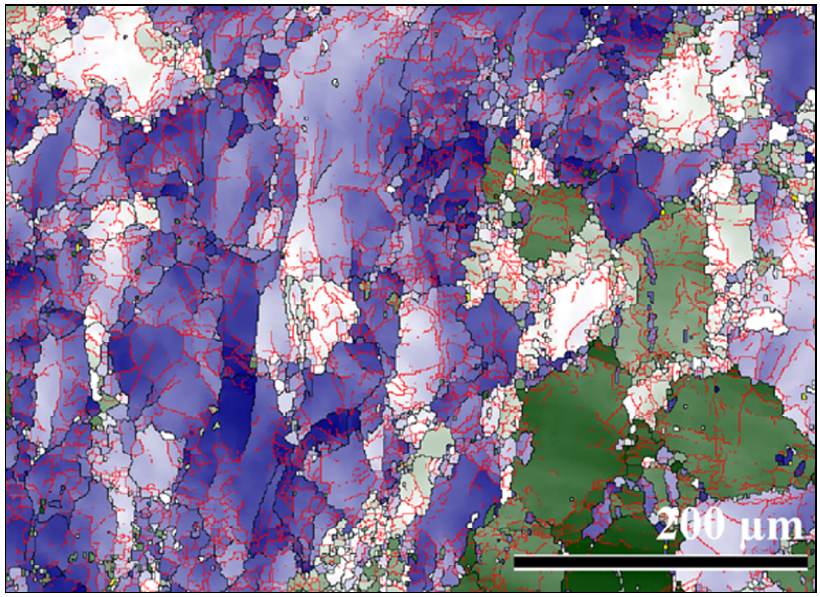

(a)

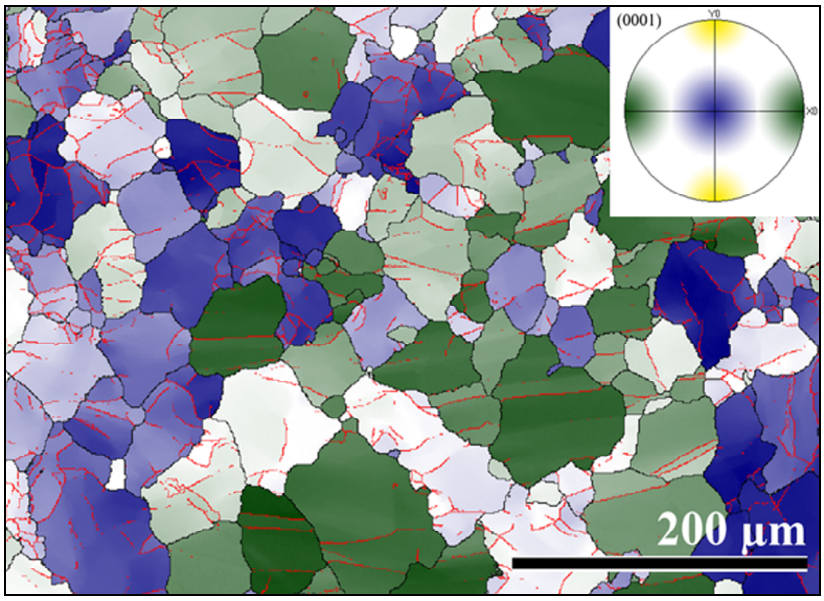

(b)

Figure 6.15. Grain orientation map of (a) LT-HS specimen and (b) HT-LS specimen at 90 hours of creep

Four grains from the HT-LS specimen with clearly defined low angle boundaries are shown in Figure 6.16. The respective pole figures show that these grains have their [0001] almost perpendicular to the tensile axis (y-axis), hence deformation by basal slip is restricted due to the low Schmid factor [13]. As mentioned previously, in such conditions, high temperature may allow the activation of alternative HCP slip systems [13, 19].

The poles figures on Figure 6.16 are acquired from each grains at points indicated by white arrows, and the plane traces on the $\{10\bar{1}0\}$ pole figure shows that the low angle boundaries appear to lie parallel to $\{10\bar{1}0\}$ of each grains. Figure 6.17 shows the contoured pole figures of these four grains generated from all EBSD data points within the grains. These pole figures aim to visualize the variation in texture within the grains due to the crystallographic tilt introduced by the low angle boundaries. The pole figures indicate that the grains "a" and "b", with the [0001] parallel to the specimen x-axis, exhibit subgrain rotation illustrated by the wide scatter in the high intensity pole (red region) on the $\{0001\}$ pole figure about the z-axis. In comparison, the grains "c" and "d", with the [0001] parallel to the specimen z-axis, show little or no scatter in the high intensity pole, but only a subtle scattering of the surrounding low intensity regions (green region), which indicates that the large bulk of the grain retained its integrity with only a minor breakdown in small localized regions.

Further study is required to fully characterize the exact nature of these ordered low angle boundaries. However, the deformations introduced at these boundaries appear to be a significant contribution to the overall creep deformation process.

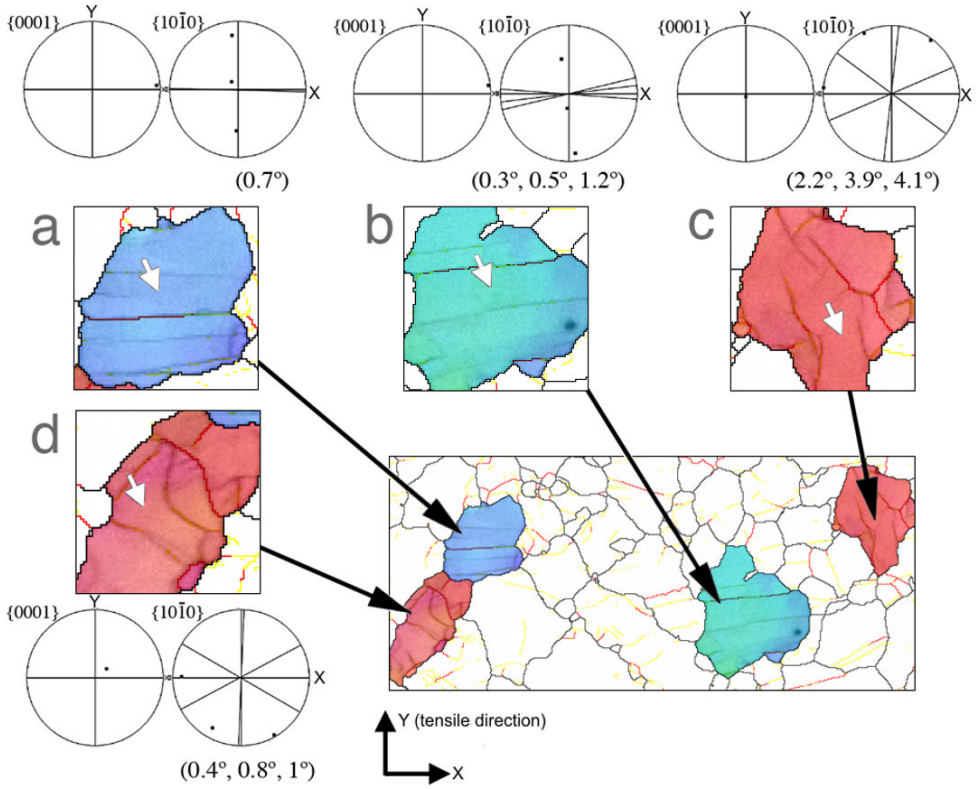

Figure 6.16. EBSD orientation map of HT-LS specimen ay 90 hours of creep, highlighting four grains with distinct low angle boundaries, along with their pole figures at locations indicated by white arrows

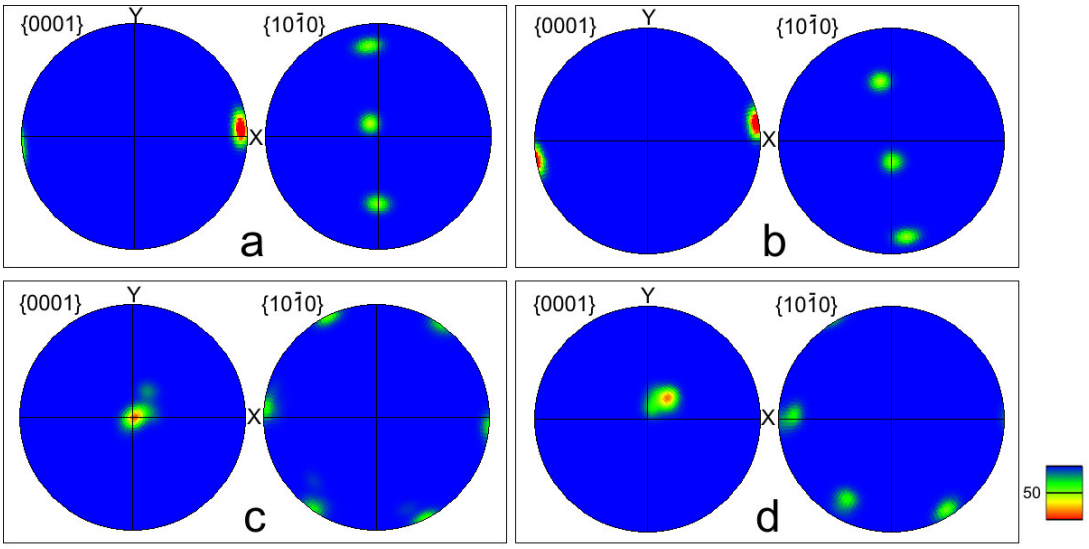

Figure 6.17. Contoured pole figures illustrating the scatter of poles within a grain on the four grains a~d on Figure 6.16 above

The parallel observation of two different creep deformation regimes in sequence has successfully linked classical diffusion-based creep theories with microstructural observations, and holds the potential to provide useful data towards further studies such as deformation modeling and texture simulations. Recent computer-based texture simulation techniques can predict the likely overall texture development of a polycrystalline structure, but have difficulty in modeling the subgrain formation and breakup into high angle boundaries due to the complexity of the transitions in contributing mechanisms. Although transmission electron microscopy (TEM) could provide higher resolution information regarding the activity of individual dislocations in specific grains, sequential EBSD analysis was found to be useful in illustrate the effects of various creep deformation regimes with the advantages of greater statistical robustness, relative ease in specimen preparation while avoiding specimen destruction.

6.5 CONCLUSION

Sequential orientation mapping of creep specimen surfaces successfully implemented to study the evolution of microstructure during creep. In the present experiments in pure magnesium, two creep regimes, low-temperature and high-temperature power law creep, were studied. In each regime, three aspects of microstructural evolution were shown to occur: (1) the elimination of tension twins and (2) the rotation of [0001] in “soft” grains to be perpendicular to the tensile axis (i.e., a hardening process). These first two aspects were shared in both creep regimes.

The regimes differed in the third aspect. Low temperature power law creep exhibited the formation of fine grains (LT-HS specimen) while high temperature power law creep developed little breakup of grains, but the formation of parallel lines of low angle boundaries (HT-LS specimen).

Chapter References

[1] H. J. Frost, Ashby, M.F., Deformation-Mechanism Maps, Pergamon Press, 1982.

[2] K. U. Kainer, Magnesium Alloys and Technology, Wiley-VCH, 2003.

[3] D. J. Bacon, V. Vitek, Metall. Mat. Trans. A 33 (2002) 721.

[4] H. Brehm, G. S. Daehn, Metall. Mat. Trans. A 33 (2002) 363.

[5] F. J. Humphreys, P. S. Bate, Acta Mater. 54 (2006) 817.

[6] O. D. Sherby, R. H. Klundt, A. K. Miller, Met. Trans. A 8A (1977) 843.

[7] C. Gandhi, M. F. Ashby, Acta Metall. 27 (1979) 1565.

[8] Y. Liu, X. Wu, Metall. Mat. Trans. A 37 (2006) 7.

[9] C. R. Barrett, J. L. Lytton, O. D. Sherby, Trans. AIME 239 (1967) 170.

[10] A. Beck, The Technology of Mangnesium and its Alloys, F.A. Hughes & Co. Limited, 1941.

[11] R. W. K. Honeycombe, The Plastic Deformation of Metals, Edward Arnold Publishers, 1984.

[12] G. E. Dieter, Mechanical Metallurgy, McGraw-Hill, 1961.

[13] M. R. Barnett, Z. Keshavarz, X. Ma, Metall. Mat. Trans. A 37A (2006) 2283.

[14] Z. Keshavarz, M. R. Barnett, Scripta Mater. 55 (2006) 915.

[15] V. Randle, The Measurement of Grain Boundary Geometry, Institute of Physics Publishing, 1993.

[16] F. J. Humphreys, Scripta Mater. 51 (2004) 771.

[17] L. Shi, D. O. Northwood, Acta Metall. Mater. 42 (1994) 871.

[18] C. S. Roberts, JOM 5 (1953) 1121.

[19] C. S. Roberts, Magnesium and its Alloys, John Wiley & Sons, Inc., 1960.

CHAPTER 7 - TEM STUDY OF DISLOCATION STRUCTURE IN POST-"SEQUENTIAL CREEP" PURE MAGNESIUM SPECIMENS

7.1 INTRODUCTION

EBSD studies carried out on pure magnesium specimens at various stages of creep (Chapter 6) illustrated that two separate mechanisms take place in the power-law creep regime depending on the applied stress and temperature.

The LT-HS (Low temperature - High stress) specimen (100ºC, 50 MPa) exhibited the formation of subgrain cell structure and breakdown of original grain boundary regions into a finer grain structure, suggesting the dislocations moving to the nearby high-energy boundaries without significant adherence to dominant slip systems within the bulk lattice. On the other hand, the HT-LS (high temperature, low stress) specimen (200 ºC, 18MPa) with nearly identical creep rate underwent creep deformation with the formation of a regular arrangement of straight low angle boundaries, leaving the original grain size distribution relatively unchanged. The two specimens underwent total creep strains of 27.5% (LT-HS) and 25.9% (HT-LS) to failure.

TEM studies were conducted using the post-creep specimens obtained from the sequential EBSD/creep experiments in order to identify and reconfirm the underlying dislocation substructures that led to the deformation mechanisms observed under the EBSD. The greatest limitation of the EBSD analysis is that its resolution is ultimately dependent on the

SEM beam spot size, and therefore is unable to resolve sub-microscopic, atomic lattice level defects such as individual dislocations. TEM analysis makes this possible, but requires destruction of the tensile test piece in order to fabricate a suitable foil specimen. By carrying out the TEM analysis on the post-creep specimens after sequential creep/EBSD test have been completed, the two techniques can complement each other to provide a better overall understanding of the underlying microscopic mechanisms of creep.

7.2 EXPERIMENTAL PROCEDURES

The two post-creep failure specimens of pure magnesium were cut into half thickness sections as illustrated on Figure 7.1 by a low speed rotary diamond saw at blade feed rate of 2m/s in Buehler Isocut fluid.

The test piece sections were reduced to 0.3 mm thickness by manually grinding with dry 1200 grit sandpaper. Details of the subsequent foil-making procedures were described in Chapter 3. In this case, the electropolishing was conducted in magnesium perchlorate + lithium chloride solution, with polishing conditions of -37 ºC, 30V, 3~6mA.

Special care was required in the foil making process since each tensile test piece could only produce up to four 3 mm foil discs. Out of the total of six specimen discs, only one useful HT-LS specimen foil and two LT-HS specimen foils were produced, whereas the remaining discs were ruined during the electropolishing process due to excessive corrosion damage.

The most concerning issue regarding the TEM study of pure magnesium was its highly reactive nature, in which the TEM foil specimen could undergo corrosion within minutes of the foil production. It was found that the foil was practically unusable after overnight

storage in a desiccator. Foils had a prolonged life if left in the TEM column, but this was often impossible due to the requirements of other TEM users.

Another concern was that the energy of the TEM beam at 100 kV could heat up the specimen sufficiently to deform the thin areas and in many cases resulted in visible motion of dislocations due to the induced thermal stresses. In order to minimize this effect, the specimen holder and the TEM vacuum system was constantly cooled down by liquid nitrogen to reduce the heating and contamination during the operation.

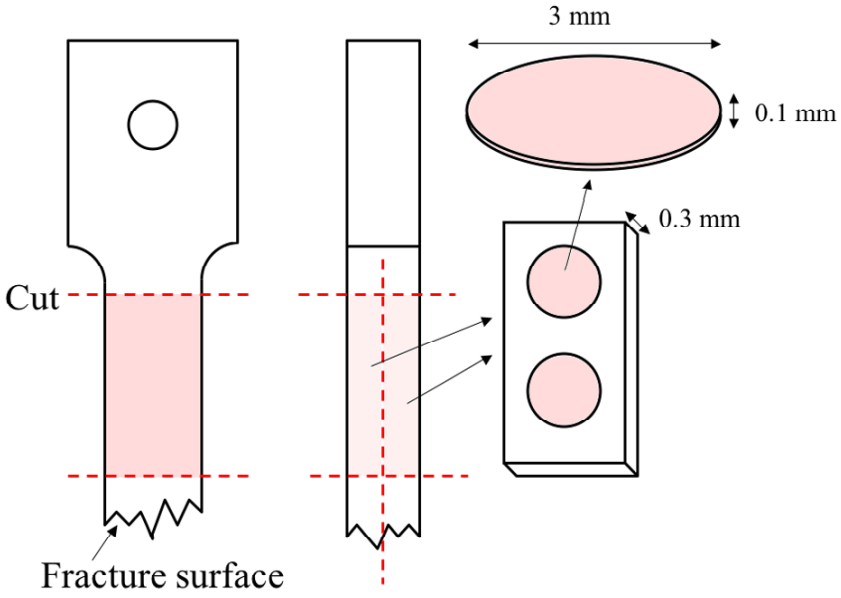

Figure 7.1. Cutting orientation of the post-creep specimens

7.3 RESULTS

The fabrication process produced foils with orientation of the foil normal to correspond with the EBSD map surface, i.e. normal to the tensile axis. For determination of the dislocation vector (*b*), diffraction patterns were acquired at $B = [2\bar{1}\bar{1}0]$ beam direction with excitation of $g = (0002)$ and $g = (01\bar{1}1)$ in two-beam condition in most cases. Alternatively $[\bar{1}2\bar{1}3]$ was used when the specimen tilt was insufficient to achieve $[2\bar{1}\bar{1}0]$ orientation. The corresponding $g \cdot B$ solutions are summarized on Table 7.1.

Table 7.1. g·B solutions for the zone axes used in this experiment. g·B ≠ 0 indicates that the particular dislocation component is visible under a selected zone axis

Beam direction *B*	$[2\bar{1}\bar{1}0]$	$[2\bar{1}\bar{1}0]$	$[\bar{1}2\bar{1}3]$
Diffraction vector *g*	(0002)	$(01\bar{1}1)$	$(10\bar{1}0)$

Zone axis	Component	g·B solutions		
[0002]	<c>	2	1	0
$1/3[11\bar{2}0]$	<a>	0	1	1
$1/3[1\bar{2}10]$	<a>	0	-1	0
$1/3[\bar{2}110]$	<a>	0	0	1
$1/3[11\bar{2}3]$	<c+a>	2	2	1
$1/3[1\bar{2}13]$	<c+a>	2	0	0
$1/3[\bar{2}113]$	<c+a>	2	1	-1
$1/3[11\bar{2}\bar{3}]$	<c+a>	-2	0	1
$1/3[1\bar{2}1\bar{3}]$	<c+a>	-2	-2	0
$1/3[\bar{2}11\bar{3}]$	<c+a>	-2	-1	-1

7.3.1 Low temperature – High stress creep specimen

Under the EBSD, the LT-HS sequential creep specimen (100ºC, 50 MPa) exhibited a deformation process primarily attributed to the breakdown of the original grains into a disordered agglomerate of small, angular grains surrounding the original grain boundaries. TEM analysis of several grains identified that the majority of grain interiors contained no particular ordered arrangement of dislocations, but a large number of grains exhibited a formation of concentrated regions of dislocation accumulation resulting in a localized planar defect at grain corners, as illustrated on Figure 7.2. The two diffraction vectors on Figure 7.2a-b highlighting the dislocations within the grains suggest these to contain a non-basal component. In some rare cases where an ordered arrangement of dislocations was observed, such as those illustrated on another grain on Figure 7.3, these dislocations still accumulated at a grain corner to form a subgrain cell while the central region of the grains remained relatively undeformed.

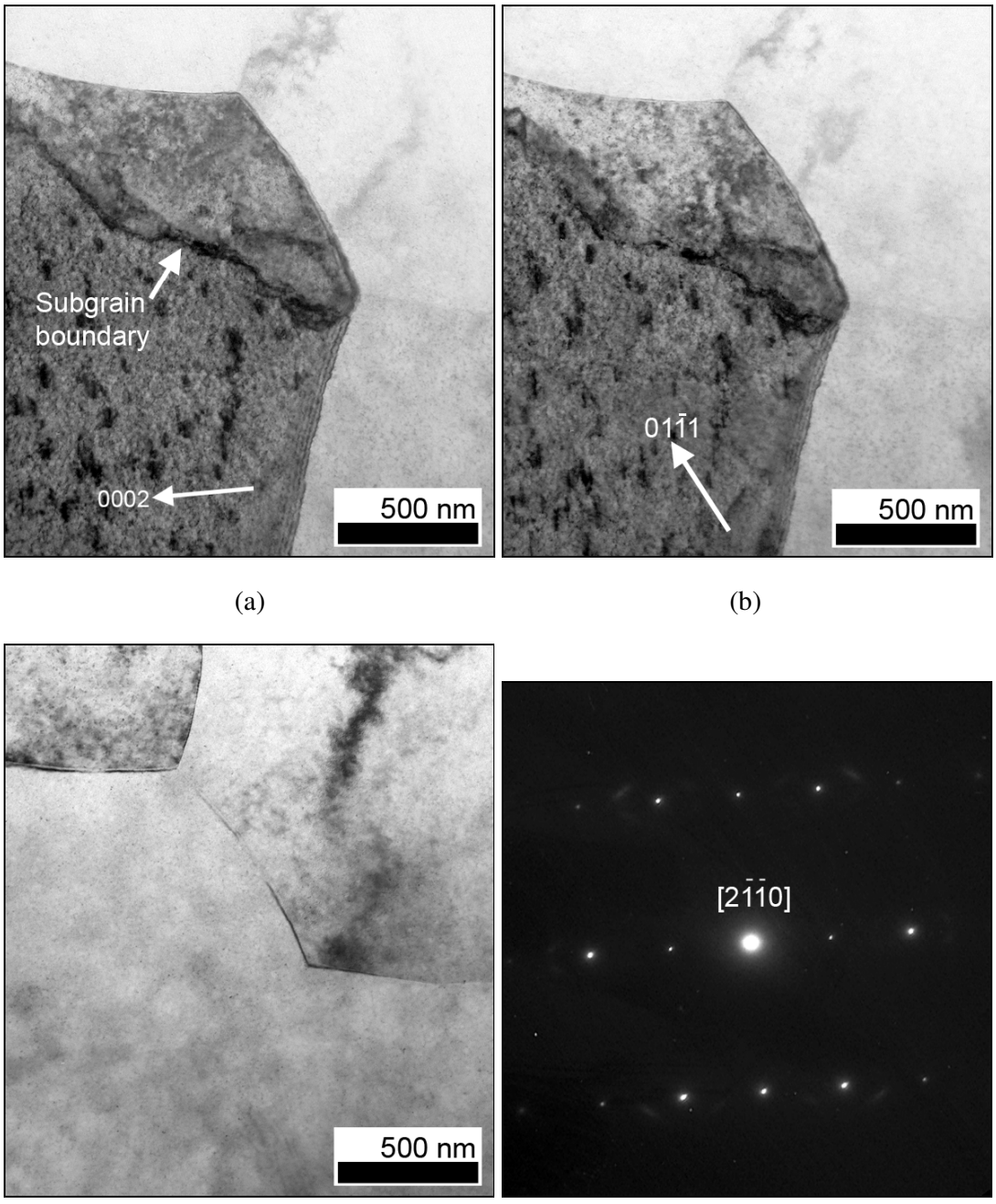

(a) (b)

(c) (d)

Figure 7.2. Formation of local subgrain cell at a grain corner with (a) g = (0002), (b) g = $(01\bar{1}1)$, and (c) no particular diffraction vector on (d) B = $[2\bar{1}\bar{1}0]$ beam direction

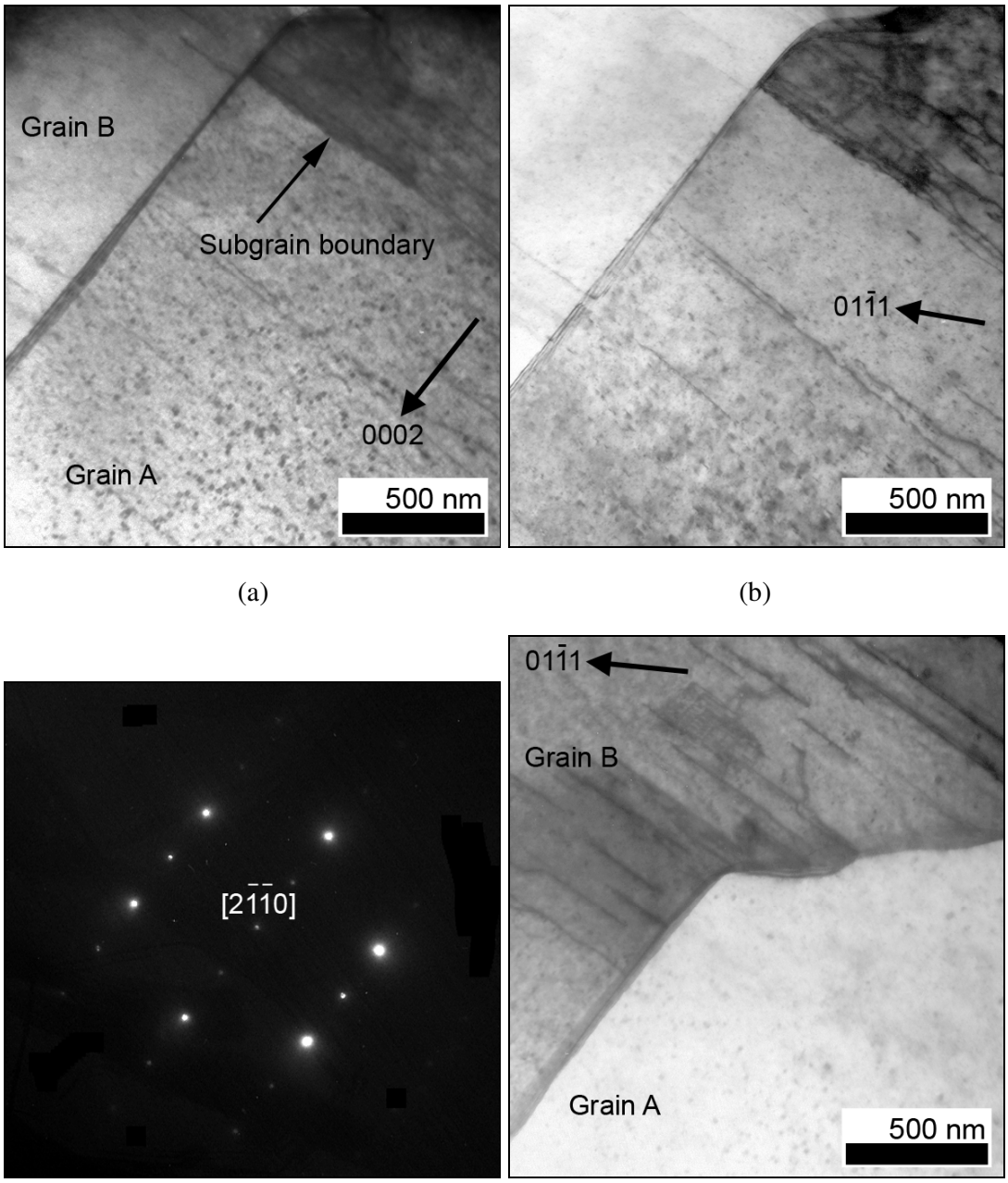

Figure 7.3. LT-HS specimen indicated "Grain A" at (a) g = (0002), (b) g = $(01\bar{1}1)$, with (c) B = $[2\bar{1}\bar{1}0]$ beam direction, and (d) adjacent "Grain B" with g = $(01\bar{1}1)$

7.3.2 High temperature – Low stress creep specimen

Dislocation substructures were much more apparent and well defined in the HT-LS (200 ºC, 18 MPa) sequential creep specimen compared to the LT-HS specimen described above. A typical example is shown in Figure 7.4, where subgrain cells have formed within a grain with clearly defined network of dislocations. Similar case is seen on Figure 7.5, which illustrate a pair of adjacent grains. The upper grain "B" on Figure 7.5a-b exhibits a cellular dislocation structure similar to Figure 7.4, whereas the lower grain "A" on Figure 7.5c-e shows a parallel array of basal dislocations with no apparent cell structure.

In some grains a special feature such as those shown on Figure 7.6 was observed, in which a continuous stepped dislocation line cut across a grain interior.

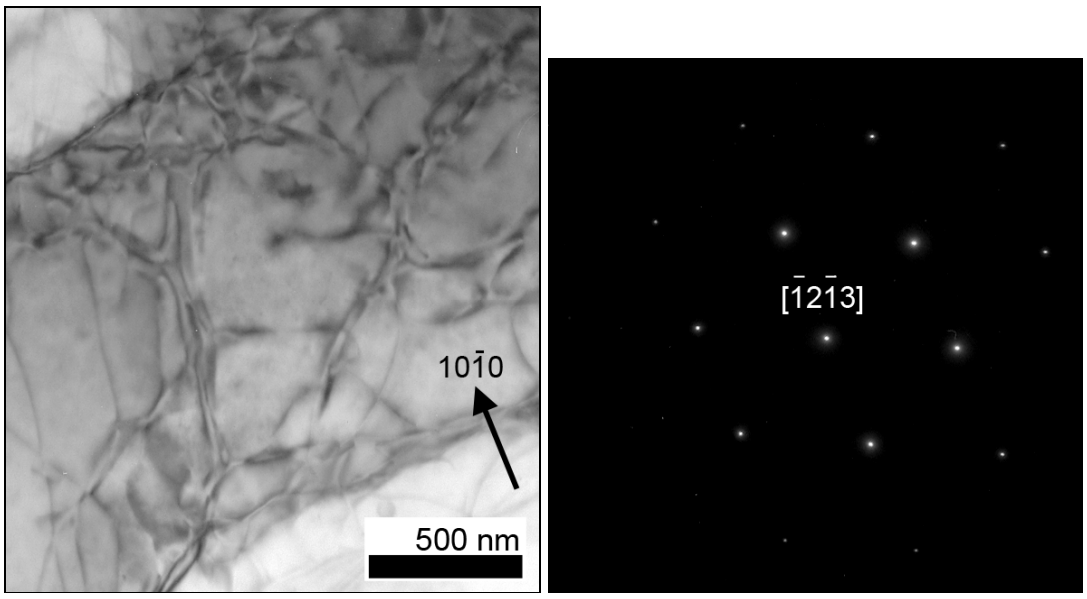

(a) (b)

Figure 7.4. (a) HT-LS specimen with g = $(10\bar{1}0)$ on (b) B = $[\bar{1}2\bar{1}3]$beam direction

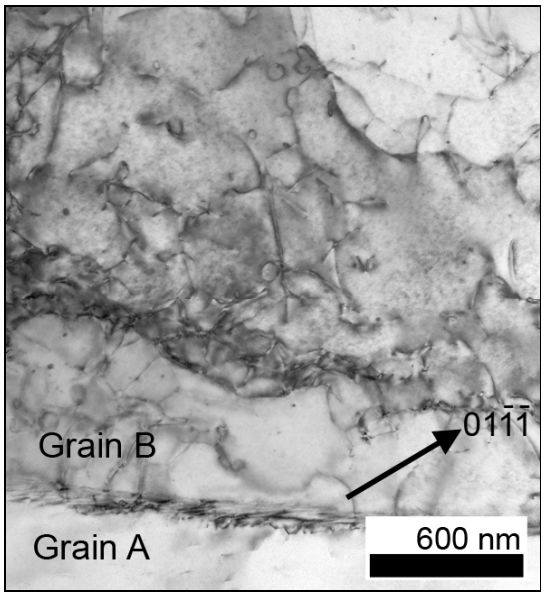
Grain B
$01\bar{1}\bar{1}$
Grain A
600 nm

(a)

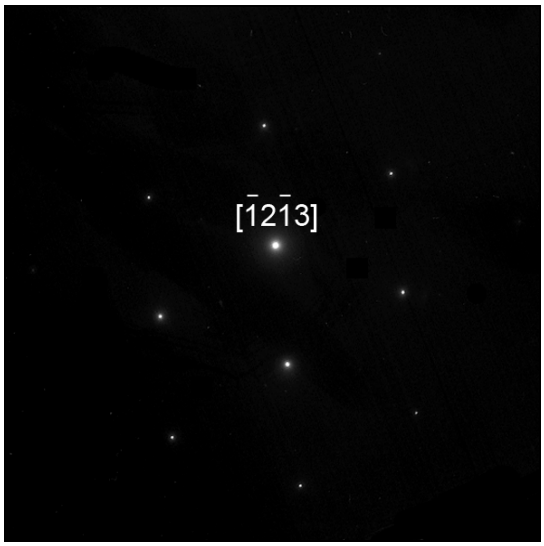
$[\bar{1}2\bar{1}3]$

(b)

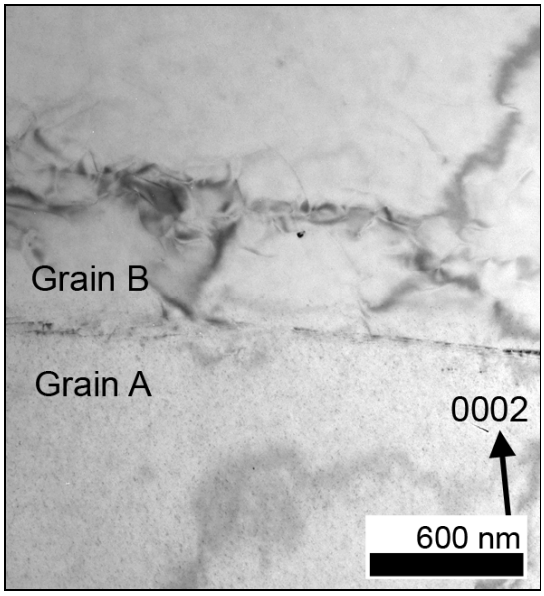
Grain B
Grain A
0002
600 nm

(c)

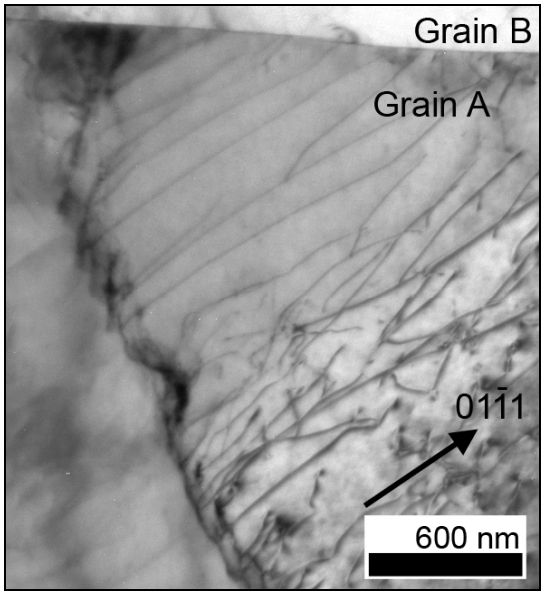
Grain B
Grain A
$01\bar{1}1$
600 nm

(d)

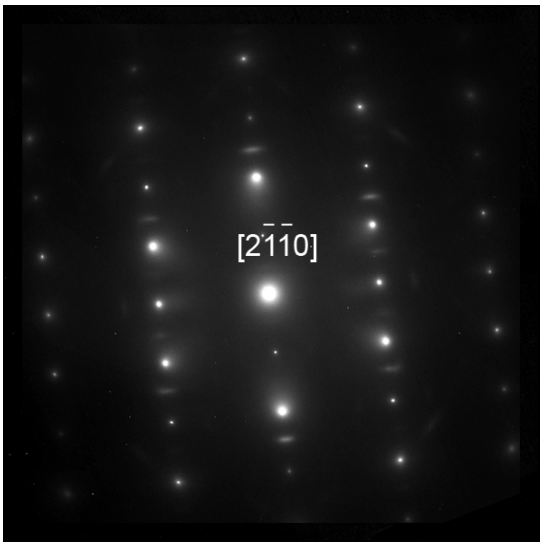

(e)

Figure 7.5. Pair of adjacent grains on HT-LS specimen with upper grain (grain B) with (a) g = $(01\bar{1}1)$ with (b) B = $[\bar{1}2\bar{1}3]$ beam direction, and lower grain (grain A) with (c) g = (0002) and (d) g = $(01\bar{1}1)$ with (e) B = $[2\bar{1}\bar{1}0]$ beam direction

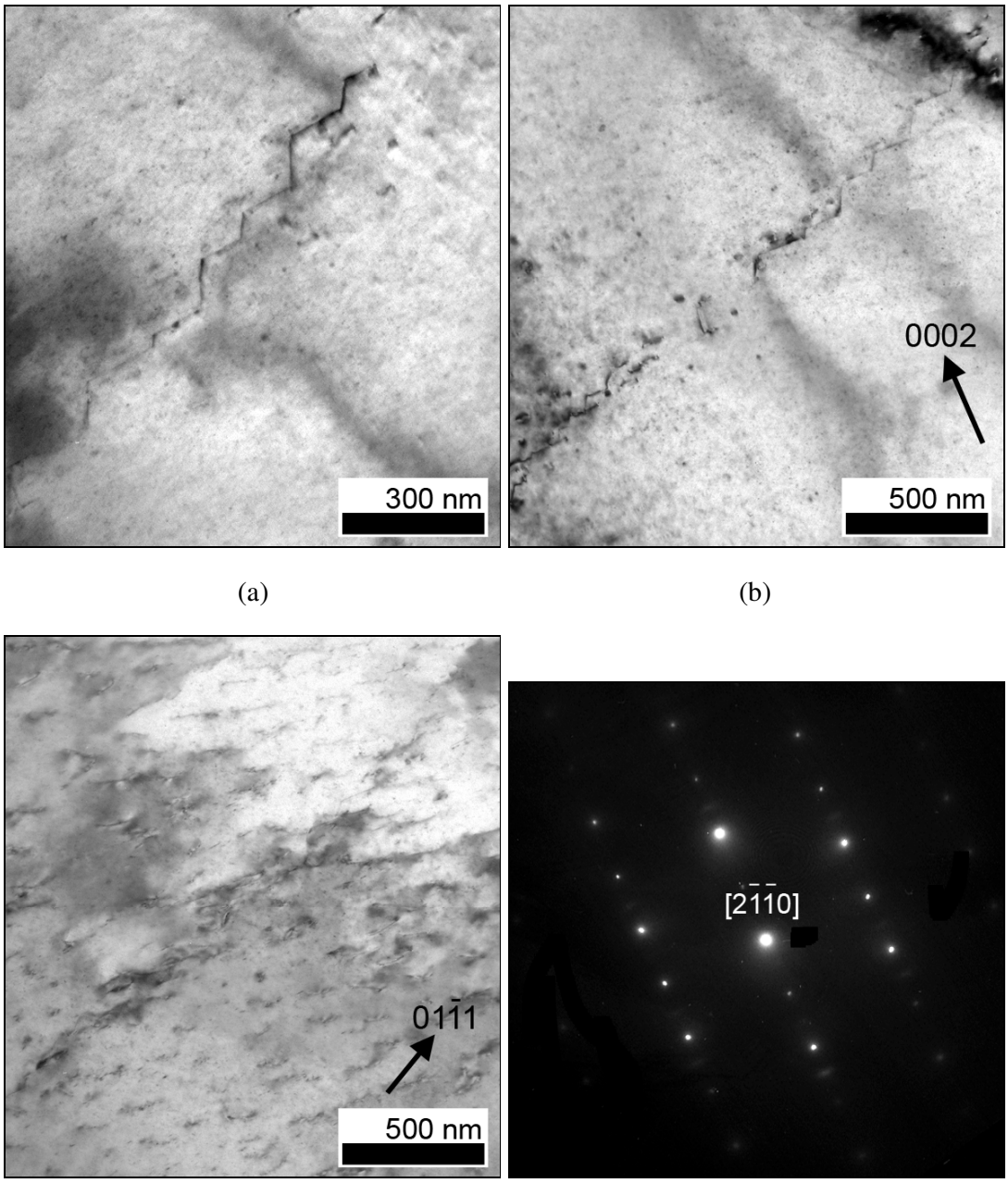

Figure 7.6. A dislocation array (a) with no particular diffraction vector, (b) g = (0002), and (c) g = $(01\bar{1}1)$ with (d) B = $[2\bar{1}\bar{1}0]$ beam direction

7.4 DISCUSSION

7.4.1 Low temperature, high stress (LT-HS) power-law creep specimen (100 ºC, 50.2MPa)

Under the sequential creep/EBSD experiment, the LT-HS specimens exhibited no particular ordered arrangement of low angle boundaries, but underwent decomposition of grain boundary region into fine grain structure, producing what can be described as a viscous layer surrounding the primary grains as illustrated on Figures 6.11a and 6.12a. This agrees with the grains illustrated on Figure 7.2 and Figure 7.3 that both indicate the formation of dislocation accumulation into a closed cell structure at a grain corner, which inevitably will lead to the breakup of the grain with incoherent high angle boundaries adjacent to the original grain boundaries. Under the TEM, this type of incoherent boundary formation was only observed at grain corners with a sharp angle, further illustrating the movement of the accumulated dislocation within the bulk grain into the nearby high-energy interface. This type of grain boundary breakdown typically suggests a "grain boundary sliding" deformation mechanism such as those known as the McLean model [1]. However, the sequential EBSD maps of Figure 6.6a suggest that the majority of the creep strain was attributed to the actual breakdown of the boundaries, since relative translations of the residual large grains are not apparent for the duration of the creep deformation.

7.4.2 High temperature, low stress (HT-LS) power-law creep specimen (200 ºC, 17.7MPa)

In the HT-LS specimens, the dislocation structure was more ordered and abundant in consistently large quantities throughout the grain interiors. It must be reminded that the TEM foil surface is parallel to the EBSD map surface of Figure 6.6b, and the SAD patterns were taken within 10º tilt against the foil normal.

On Figure 7.4 and grain "B" on Figure 7.5a, $[\bar{1}2\bar{1}3]$ beam direction was achieved at almost perpendicular to the foil normal (i.e. 40º from $[2\bar{1}\bar{1}0]$ and 68º from $[0002]$). The two-beam condition highlights a complex arrangement of cellular dislocation network, which was not observed in the prior LT-HS specimen. On the lower adjacent grain "A" on Figure 7.5c-d, the complex dislocation arrays was again observed, but in this case aligned in a parallel manner. Using the $[2\bar{1}\bar{1}0]$ diffraction pattern on Figure 7.5e, images taken at the two diffraction vectors illustrate the dense dislocations consist of purely basal <a> component.

Similarly in Figure 7.6, majority of the dislocations only carries the basal component, highlighted by their abundant presence in Figure 7.6c with g = $(01\bar{1}1)$ two-beam condition. A unique chain of dislocations is visible at the center of the image, with occasional 60º "steps" connecting the basal dislocations, which Figure 7.6b indicates the presence of <c+a> component. This chain may evolve to become a large stacking fault that cut across the grain such as the parallel lines of low angle boundaries observed in the EBSD orientation maps such as those shown on Figures 6.11b and 6.12b.

These ordered intragranular defect arrangements were observed frequently in the HT-LS

specimen, compared to the grain boundary cell structure observed in the LT-HS specimen. This clearly illustrates the contrast between the defect growth and distribution mechanisms between the two creep test conditions.

7.5 CONCLUSION

Observations from the TEM studies confirmed the findings of the EBSD by illustrating a large contrast in development of creep deformation under the LT-HS and HT-LS test conditions on pure magnesium. The LT-HS specimen was characterized by concentrated defect accumulation near grain boundaries, forming low angle cells, particularly at sharp grain corners. In the HT-LS specimen, a high density of basal dislocations was identified in almost all grains. Both EBSD and TEM studies agree that the creep deformation was due to predominantly basal and prismatic slip with very little contribution by non-basal dislocations.

The original purpose of this TEM study was to verify and reconfirm the observations made under the novel sequential creep/EBSD technique. In this regard, a conclusion can be made that the two studies did not contrast in their observations, and by being aware that the amount of time, effort and equipment required in conducting a post-creep TEM studies, this further stresses the effectiveness of the sequential creep/EBSD technique.

Chapter References

[1] A. J. Kennedy, Process of Creep and Fatigue in Metals, Oliver and Boyd Ltd., Edinburgh, 1962.

CHAPTER 8 - SEQUENTIAL CREEP STUDY OF MAGNESIUM ALLOY MRI-153M

8.1 INTRODUCTION

Sequential creep/EBSD study of pure magnesium resulted in successful outcomes, yielding many valuable observations of the textural evolution of the surface microstructure during creep. The same technique was next applied to the study of creep resistant magnesium alloy MRI-153M. The underlying microstructural features of this Mg-Al-Zn-Ca-Sr alloy were studied in detail in Chapter 4, but its creep properties and deformation mechanisms are yet to be determined.

8.1.1 Procedural differences between creep testing of pure magnesium and MRI-153M alloy

Although it may seem straightforward to test the MRI-153M alloy specimens under the same testing conditions as the pure magnesium tests carried out in Chapter 6, there are several critical differences that make the testing of the MRI-153M alloy more challenging compared to pure magnesium.

Firstly, there are little or no past studies conducted on the creep properties of this alloy, let alone their post-creep microstructures. Unlike the pure magnesium, creep rate predictions cannot be based on the deformation mechanism map, since no such map exists for this alloy system.

In general, Ca, Sr, RE based creep resistant alloys such as the current alloy MRI-153M tend to rely on stable precipitation hardening mechanisms, and have very low creep strain to failure [1, 2], since this is the very definition of being "creep resistant". Unlike the pure magnesium that exhibited creep strain in excess of 20%, these magnesium alloys typically only exhibit up to 2~3% strain at failure [1]. Therefore, the observed changes in the microstructure at each interruption stages will be far smaller compared to the dramatic changes in texture observed in pure magnesium.

The reason for such a low creep deformation in MRI-153M alloy is believed to be due to the presence of stable grain boundary intermetallic precipitates and solid solution aluminum in α-Mg, generating high internal stresses within the microstructure to resist deformation. Relative contributions of these two features to the secondary creep rate were briefly illustrated in Chapter 5.

In order to visualize the changes in the surface microstructure during creep such as those achieved in pure magnesium case, both the LVDT extensometer/demodulator system and the EBSD orientation maps must be able to handle greater data resolution than the tests on pure magnesium. A simple anticipation will be that a tenfold reduction in the total strain to failure (from 20% to 2%) would require a tenfold increase in the LVDT and EBSD resolution.

The second concern for the creep testing of MRI-153M is that this alloy is more prone to intergranular corrosion compared to the pure magnesium specimen. The introduction of second phase grain boundary precipitates introduce galvanic reaction cells within the bulk material, resulting in an accelerated preferential corrosion at these interfaces, as illustrated on Figure 8.1. Although pure magnesium does corrode over time, it is primarily only a

formation of surface oxide layer that can easily be polished away.

The third and possibly the most complex issue is that the high-pressure diecast MRI-153M alloys have a complex dendritic microstructure. The problem with the dendritic structure is that two types of "grain" boundaries are exhibited, namely dendrite arm boundaries and high angle misorientation boundaries. Since second phase particles appear on both types boundaries, it is difficult to differentiate them using optical microscopy alone. For example, in Figure 8.2, the conventional SEM image illustrates the dendrite arm boundaries (d = 58 μm), whereas the EBSD orientation map highlights the high angle boundaries (d = 375 μm). The second phase precipitation can be seen in the higher magnification optical microscopy image on Figure 8.2c. Because both types of interfaces can contribute to the overall creep deformation, their relative importance must be evaluated. Changes in the creep rate prediction based on the two different grain size models were discussed in Chapter 5.

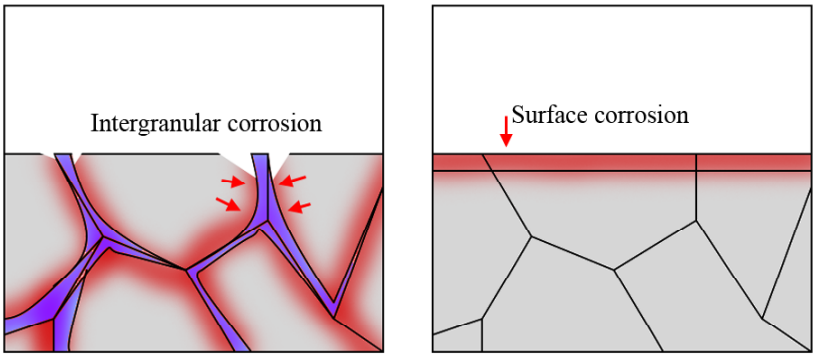

(a) (b)

Figure 8.1. Dominant atmospheric corrosion mechanisms in (a) MRI-153M alloy with $(Mg,Al)_2(Ca,Sr)$ grain boundary precipitate phase and (b) pure magnesium

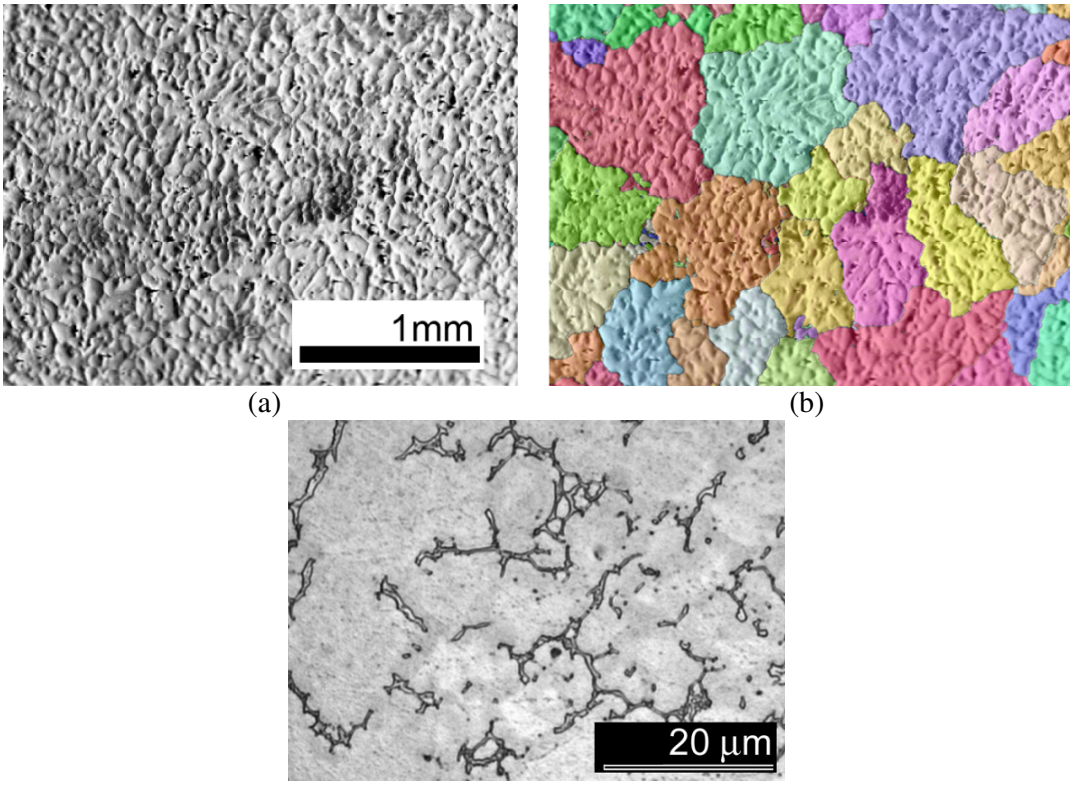

(a) (b)

(c)

Figure 8.2. Comparison between (a) dendrite arm boundaries, (b) high angle (>15º) misorientation boundaries of identical area observed under SEM/EBSD, and (c) optical microscopy image of the same alloy

8.1.2 Determination of the creep test parameters

Temperature and load combinations applied to the tests were evaluated based on the simple rate equation models calculated in Chapter 5. The creep rate prediction was further assisted by previous creep studies carried out by the research program at Monash University on a similar alloy MRI-153 [2, 4], and other similar alloy variants [5, 6, 7]. However, these materials would not exhibit identical creep behavior since they are different alloy composition to MRI-153M, and the casting and tensile test piece fabrication process is also different.

Prior to determining the creep rates of the alloy MRI-153M, an assumption was made that the dominant creep deformation at the test temperature range (< 250 ºC) and load (< 100 MPa) would most likely be power-law creep of some form, since the condition would be insufficient for dynamic recrystallization or catastrophic diffusional flow to take place.

8.2 EXPERIMENTAL PROCEDURE

A laboratory quality high-pressure diecast block (approx. 150 × 100 × 20 mm) of MRI-153M alloy was wire-cut into miniature ASTM E8 rectangular tensile test piece shapes with 3 × 4 mm cross-section and 15 mm gauge length. The test pieces were fabricated from the same batch of alloy block as those used for the optical and electron microscopy in Chapter 4, and the cutting process was ensured to achieve the same test piece orientation for all six test pieces fabricated from one diecast block.

The specimens were tested as-received, and were not annealed prior to the creep tests. This was due to the similar reasoning as for the pure magnesium case, in which the creep tests

were intended to reveal the response of as-cast microstructure under exposure to creep, since this will be a good representation of the actual application in service.

The surfaces were polished with 0.05μm colloidal silica and two microhardness indents were placed as reference markers for EBSD mapping. Details of the polishing procedures are discussed in Chapter 3. The microhardness indents were small enough such that the final fracture did not initiate from these indents in any of the creep tests.

Creep tests were conducted in a heated pure silicone oil bath to reduce the temperature fluctuations and surface oxidation. The specimen extension was measured by a linear variable displacement transducer (LVDT) extensometer. The LVDT demodulator system was improved subsequent to the previous pure magnesium experiments in Chapter 6, and now achieved a linear resolution of approximately 1μm.

Due to the uncertainties in the anticipated creep rate of the MRI-153M alloy, a series of creep experiments was conducted as summarized on Table 8.1. It must be noted that these test conditions were not decided all at once, but were derived from a process of adjusting the load and temperature for each subsequent specimens in order to achieve a satisfactory creep rate.

Table 8.1. Sequential creep tests of MRI-153M

Specimen	Temperature (ºC)	Load (MPa)
A	200	50-
B	250	87
C	200	50
D	200	75
E	200	50
F	200	60

The samples were removed from the creep test at fixed time intervals and the same pre-determined surface location was repeatedly mapped by EBSD, aided by the microhardness indent markers. The surface was lightly polished prior to each EBSD map with 0.05 μm colloidal silica to remove the oxide layer formed during the creep test.

The automated EBSD maps were constructed on a 500 × 370 point window at various magnifications using an HKL Channel5 EBSD system on a JEOL JSM-6100 SEM. The most effective magnification was evaluated during the course of the creep experiments, and therefore is discussed in the results section. Details of the EBSD orientation mapping techniques are summarized in Appendix B.

EBSD phase identification was only carried out on the primary HCP α-Mg grains, and the other precipitate phases were ignored. This was because the size of the precipitates were at the threshold of SEM beam spot size and the EBSD map step intervals (<1 μm) [2], such that an automated attempt to identify these phases would result in overlaid double-pattern of α-Mg grains and the second phase, as discussed in Appendix B. Ignoring the precipitate phases was not considered a significant issue due to the two assumptions made, as follows:

Assumption 1: Practically all of the precipitate phases were identified to be $(Mg,Al)_2(Ca,Sr)$ in the microstructure analysis carried out in Chapter 3. Therefore, it was not necessary to identify these precipitates using the automated EBSD pattern matching.

Assumption 2: Unlike the $Al_{12}Mg_{17}$, the $(Mg,Al)_2(Ca,Sr)$ grain boundary precipitates phase found in this alloy was assumed to be a stable, incoherent, and rigid structure during creep. Therefore, the crystallographic orientation and relationship with the surrounding Mg matrix was assumed to play very little role in the overall creep deformation.

These two assumptions allow the analysis to overcome the technical limitations of the automated EBSD map. However, the fact that the precipitate phases were ignored from the automated EBSD maps does not necessarily mean that their presence remains undetected. A conventional SEM image such as an example shown on Figure 8.3, taken concurrent to the EBSD map, clearly illustrates the presence and locations of the $(Mg,Al)_2(Ca,Sr)$ precipitate network and therefore can be overlaid on top of the EBSD map to supplement the analysis if necessary.

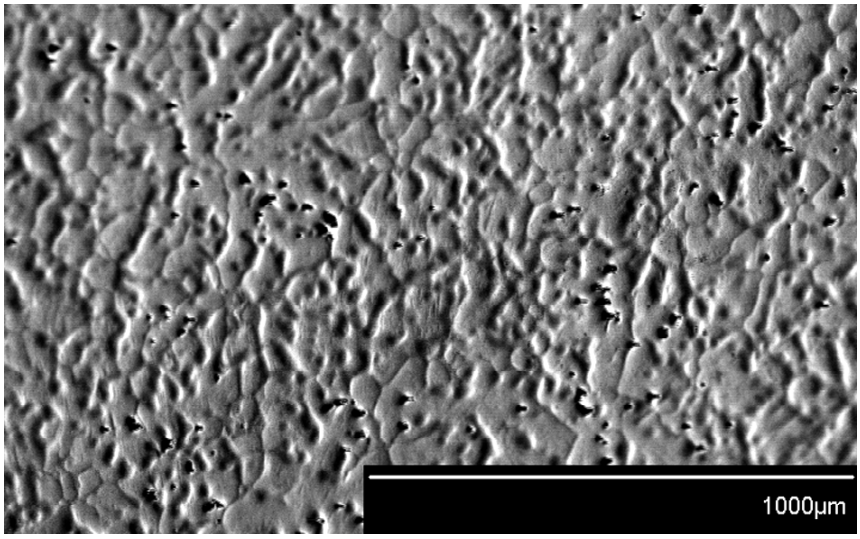

Figure 8.3. SEM image highlighting the grain boundary precipitate phases

8.3 RESULTS

Table 8.2 summarizes the results obtained from all creep test specimens. The secondary creep rates were measured from the compound creep rate graphs from all interruption stages. Details of the results obtained from the individual creep specimens are discussed in the subsequent sections.

Table 8.2. Results of sequential creep of MRI-153M specimens

Specimen	Tempera-ture (ºC)	Load (MPa)	Secondary creep rate (/s)	Strain to failure (%)	Comment
A	200	17.7	-	-	Preliminary trial
B	250	87	4.4×10^{-7}	1.2	Too fast, failed rapidly
C1	200	55	1.6×10^{-8}	-	Silicone oil solidified
C2	200	75	1.7×10^{-7}	2.6*	Continued from C1
D	200	75	2.3×10^{-7}	3.4	Strain rate too fast
E	200	50	5.4×10^{-9}	-	Too slow, did not fail
F	200	60	1.9×10^{-8}	-	Did not fail

*C1 stopped due to silicone oil solidification. Load increased and continued as C2. Strain to failure is for C1+C2

Unlike the creep test on pure magnesium that was interrupted at every six hours, the interruption times on MRI-153M were adjusted for later specimens (E~F) as summarized in Table 8.3. The EBSD orientation map size was also increased to cover a wider area for later specimens. The reason for this decision is discussed in the following section.

Table 8.3. Creep interruption intervals and EBSD mapping parameters for MRI-153M alloy

Specimen	Interruption (hr)	EBSD step (μm)	Map area (μm)	Number of large grains in one EBSD map
A	6	2	1100 × 820	8
B	6	2	1100 × 820	5
C	6	2	1100 × 820	-
D	6	5	2500 × 1850	37
E	24	5	2500 × 1850	41
F	6~48	5	2500 × 1850	40

8.3.1 Specimen C (200 ºC, 55-75 MPa)

The creep test on specimen C was conducted at 200 ºC, 55 MPa, generating a secondary creep rate of 2.4×10^{-8} /s. However, the test was compromised after 24 hours due to the solidifying silicone oil bath issue that is discussed in Appendix A. Being aware that the test was now invalidated, the same specimen was reused after the fresh oil replenishment, with an increased load of 75 MPa. The overall creep curve is shown on Figure 8.4. The decision to increase the load to 75 MPa was made because the original creep rate of 2.4×10^{-8} /s at 55 MPa was found to be too slow. This resulted in an increase in secondary creep rate to 1.7×10^{-7} /s. It was also found that the map size of 1120 x 820 microns at 2 micron step intervals was too fine, and the map could only cover about ten large grains.

Although the test was invalidated, it nonetheless generated meaningful secondary creep rate values, and the findings from this specimen was used as a basis for determining the creep test and EBSD map parameters for the subsequent creep specimens.

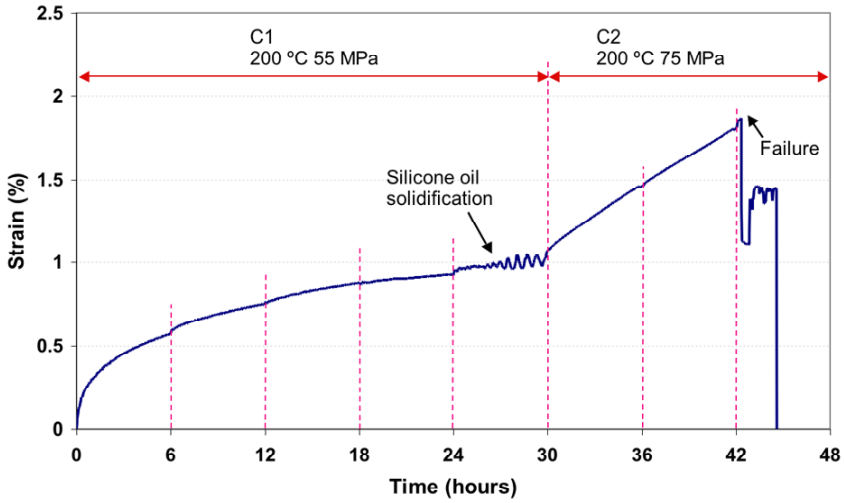

Figure 8.4. Creep curve of Specimen C (200 ºC, 60 MPa) that was interrupted by solidified silicone oil at 25th hour. The test was restarted at 75 MPa from 30th hour

8.3.2 Specimen D (200 ºC, 75 MPa)

Specimen D was tested at 200 ºC, 75MPa, but the EBSD maps were now acquired on a map size of 2500 x 1850 micron at 5 micron step intervals. This map covers over 30 grains and therefore is a more statistically significant representation of the overall microstructure.

The creep strain-time plot of Specimen D is shown on Figure 8.5. Unfortunately, the specimen failed short of the third interruption stage (18 hours), at total strain of 3.4%, suggesting that the applied stress level may have been too high. However, the plot exhibits a smooth secondary creep rate of 2.3×10^{-7} /s. The failure appears to be catastrophic with very little tertiary creep stage. It must be noted that the failure occurred prior to, not during, the interruption process at 18 hours, and therefore any shock induced during the interruption process played no part in the failure process.

The sequential EBSD orientation maps of Specimen D are summarized on Figure 8.6. By pure fortunate coincidence, the specimen exhibited catastrophic failure within the area

targeted by the sequential EBSD maps, and therefore the process of the grain boundary void formation at 6 hours (top right area of the map) to the eventual catastrophic crack path at failure (18 hours) is clearly visible.

The pole figures before creep test and after 12 hours of creep are shown on Figure 8.7. The microstructure does not have any strong nonrandom texture, unlike the pure magnesium specimens. There is very little information obtained from the pole figures due to the small amount of strain experienced by the specimen. Therefore, the pole figures are omitted from the results of the subsequent specimens.

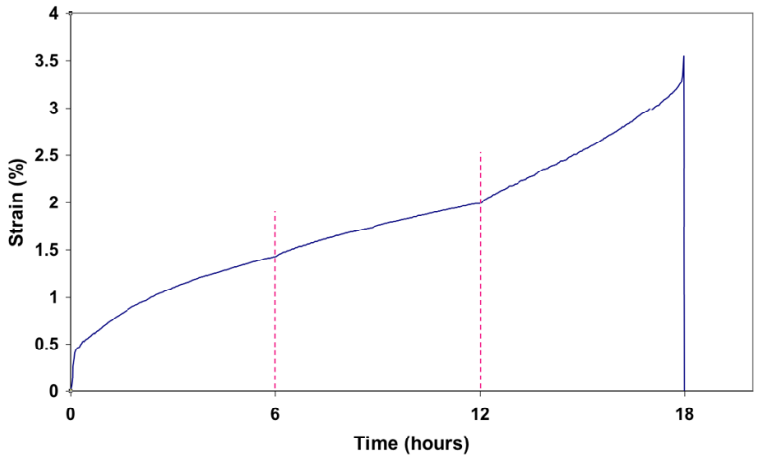

(a)

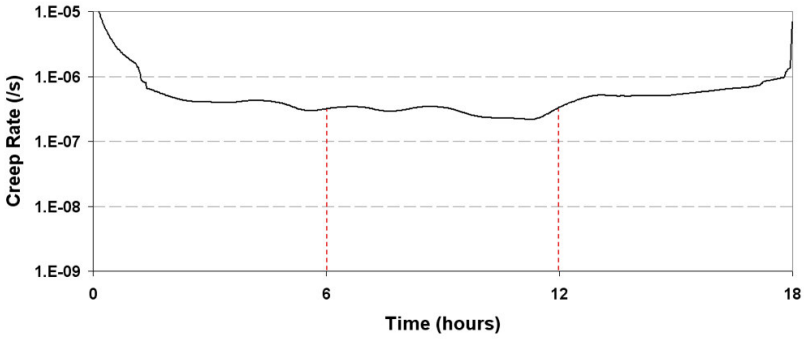

(b)

Figure 8.5. (a) Sequential creep time-strain graph and (b) creep rate graph of Specimen D (200ºC, 75MPa). Red lines indicate the interruption stages

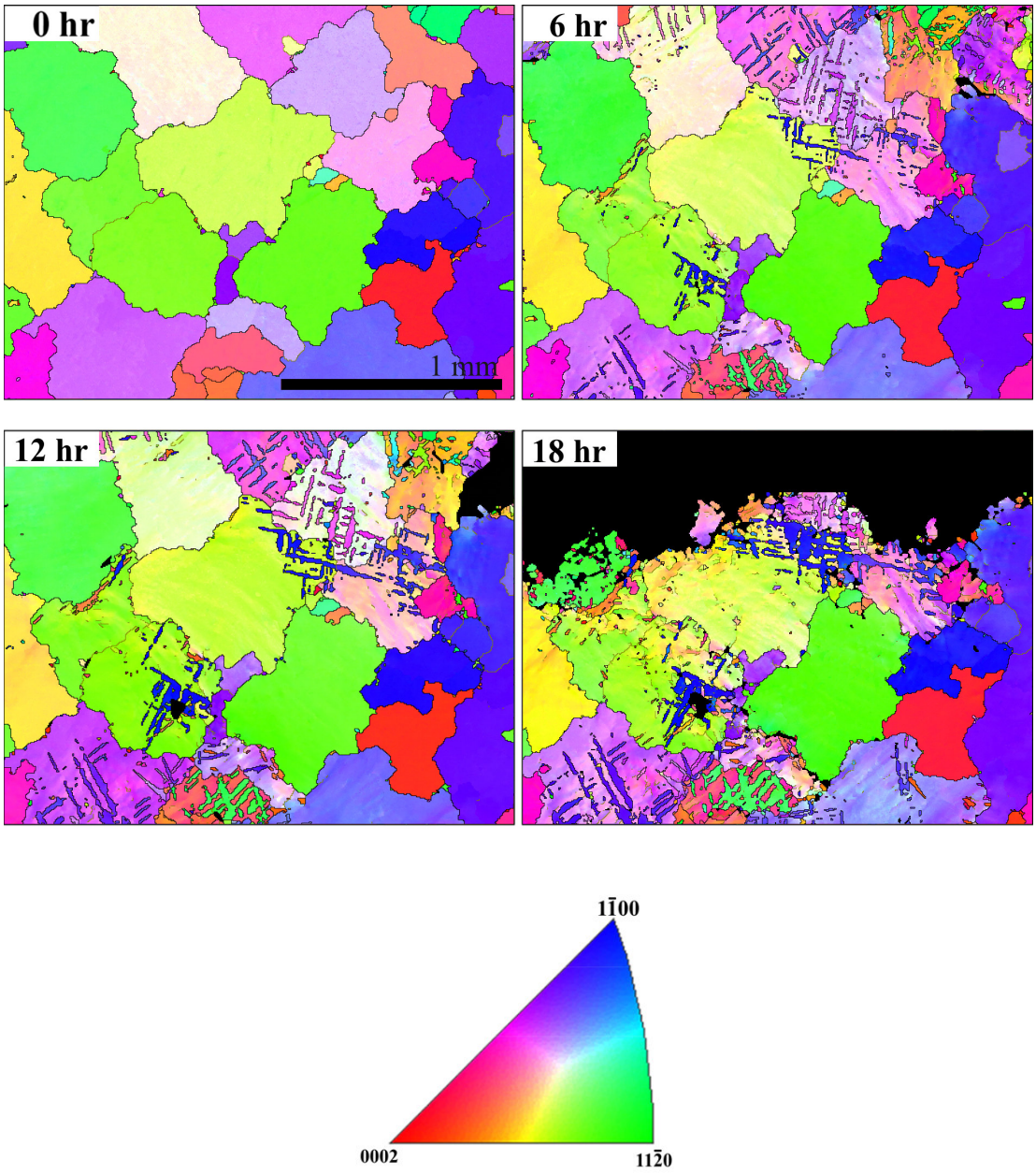

Figure 8.6. EBSD texture orientation map of Specimen D at each interruption stages. The inverse pole figure represents the surface normal direction.

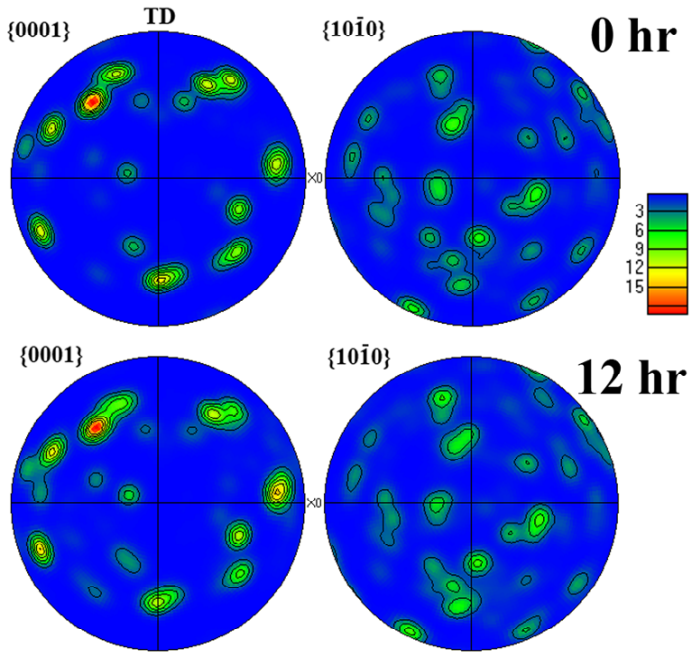

Figure 8.7. Pole figures of specimen D prior to and after 12 hours of creep

8.3.3 Specimen E (200 ºC, 50 MPa)

Since Specimen D (75 MPa) failed very quickly, the subsequent Specimen E was tested at a lower stress level of 50 MPa but now at a longer interruption intervals of 24 hours. The EBSD maps were acquired on a same map size as Specimen D (2500 x 1850 micron at 5 micron step intervals).

The creep strain-time plot of Specimen E is shown on Figure 8.8, which exhibits a secondary creep rate of 5.4×10^{-9} /s.

The key point to note about this specimen is that the test was terminated at 144 hours instead of carrying on until eventual failure. This decision was made because the secondary creep rate was very low, and appeared to be slowing down even further than originally anticipated. A simple assumption that the specimen will exhibit similar strain to failure as Speicmen D (3.4%) would suggest the test to carry on for more than 1500 hours until failure, and therefore the test had to be terminated due to the limited time available to conduct creep tests on other specimens.

One other reason for the termination of the test was the limitation of the minimum deformation resolution of the LVDT extensometer. The extensometer becomes unreliable in resolving the sub-micron level deformation experienced by this specimen. This explains the rough, fluctuating appearance of the creep curve.

The EBSD maps on Figure 8.9 also show very little texture changes, which agrees with the very little strain observed in the creep curve. One notable feature is the development of twinned grains as creep progressed.

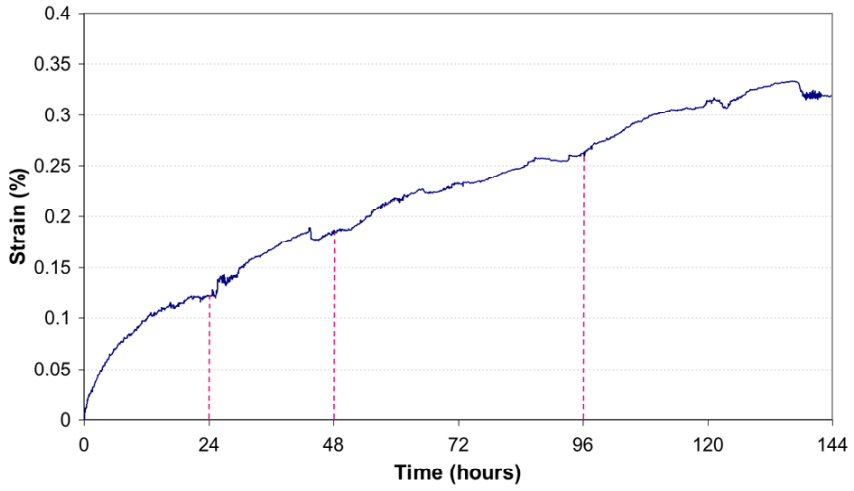

(a)

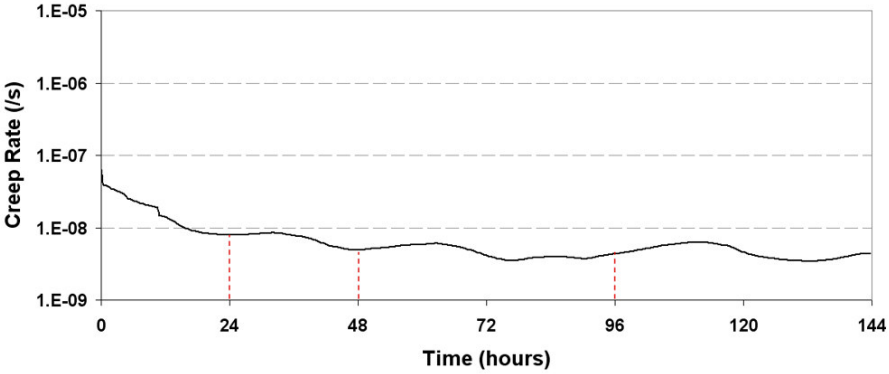

(b)

Figure 8.8. (a) Sequential creep time-strain graph and (b) creep rate graph of Specimen E (200°C, 50MPa). Red lines indicate the interruption stages

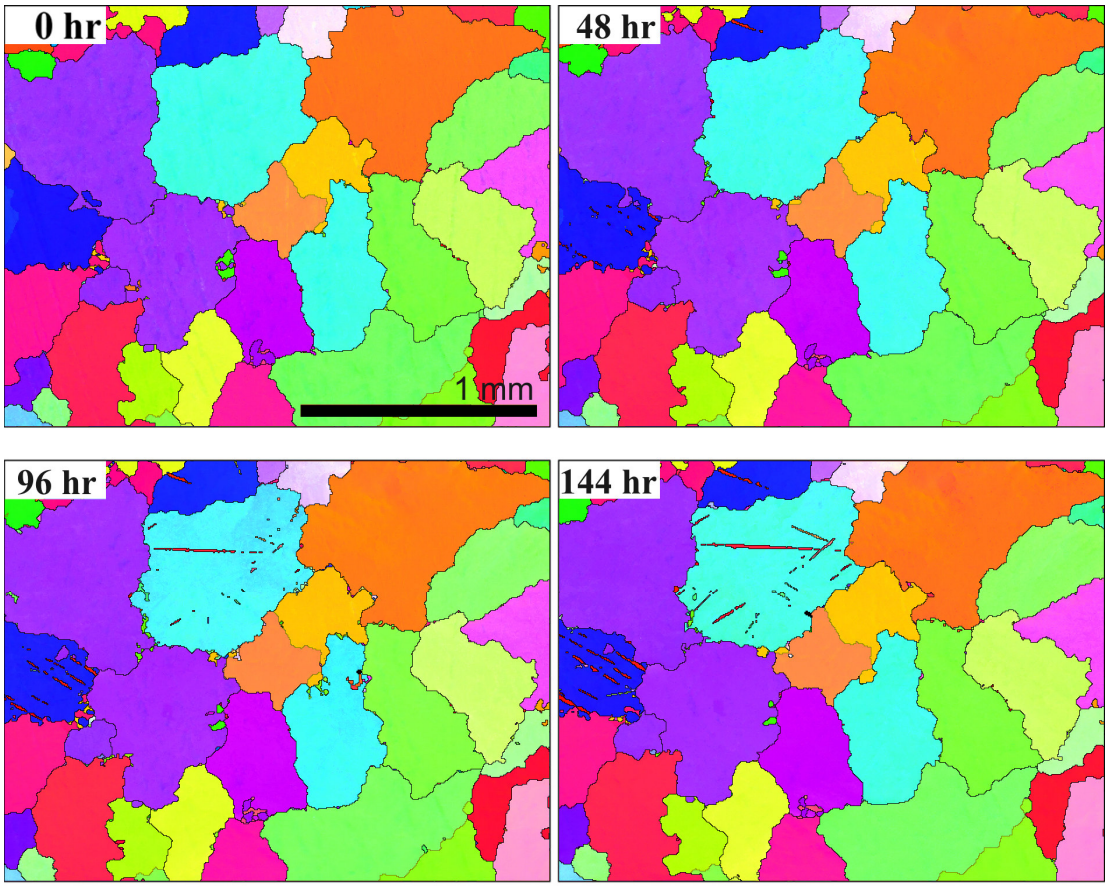

Figure 8.9. EBSD texture map of Specimen E at various interruption stages

8.3.4 Specimen F (200 ºC, 60 MPa)

Based on the two prior creep test conditions, Specimen F was tested at 60 MPa. The EBSD maps were acquired on the same map size as Specimens D and E.

The creep strain-time plot of Specimen F is shown on Figure 8.10. The specimen exhibits a secondary creep rate of 1.9×10^{-8} /s, which lies in between Specimens D and E, as expected.

Similar to Specimen E, this test was also terminated prior to achieving eventual failure. However, this was attributed to a very unique behaviour of this specimen under creep. The creep strain-time plot illustrates that the secondary creep rate slows down after approximately 220 hours, to the point where the creep deformation no longer takes place to any significant degree. Based on this observation, the creep test was terminated at 288 hours. The interruption process at 204 hours did not contribute to this slow-down of the creep rate, since the regular secondary creep deformation continues beyond this interruption point, and gradually reaching a plateau. The "secondary" creep rate was calculated based on the steady-state region of the graph prior to the slow-down, as illustrated on Figure 8.10(b).

A selection of EBSD maps taken at the interruption stages are summarized on Figure 8.11. The maps illustrate very little textural development within grains nor any substantial grain decomposition, even for a relatively large total strain of 1.3%. The development of twinned grains are observed, along with the formation of voids at some grain boundaries (black areas in the maps). Not all voids are necessarily due to creep cracks, but many of them are minor surface defects (e.g. dimples) that can be influenced by the degree of micropolishing performed prior to the each EBSD maps. These defect features can be

observed under the conventional SEM images, and illustrate the areas prone to the formation of such surface defects as creep progresses.

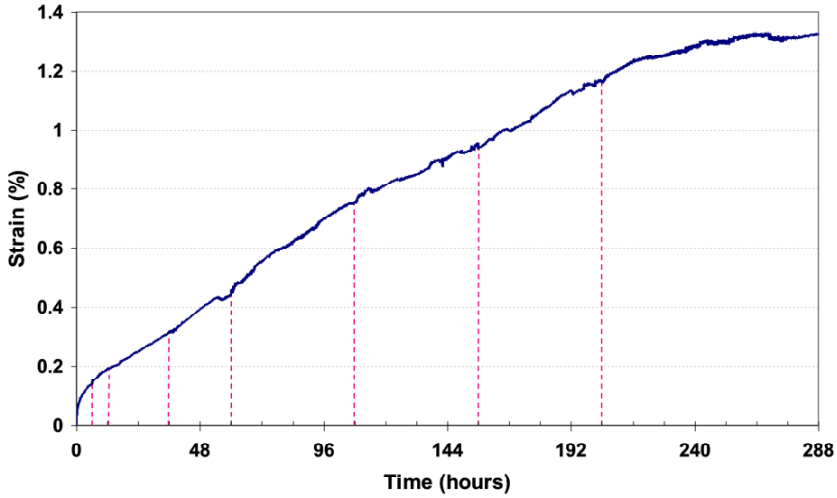

(a)

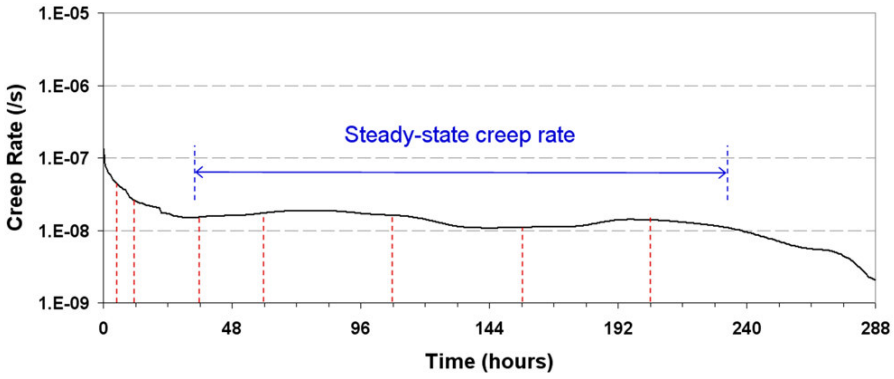

(b)

Figure 8.10. (a) Sequential creep time-strain graph and (b) creep rate graph of Specimen F (200ºC, 60MPa). Red lines indicate the interruption stages

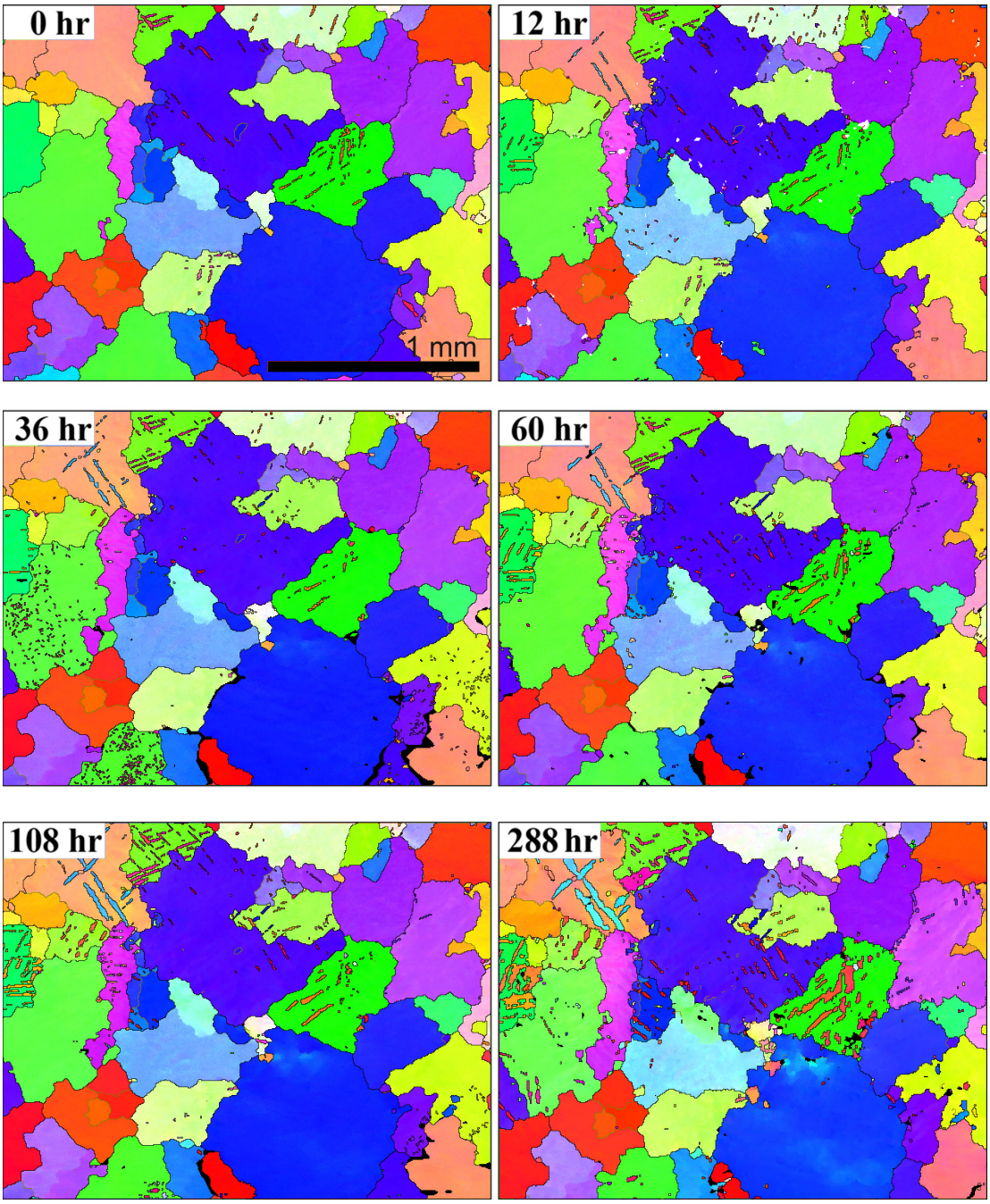

Figure 8.11. EBSD orientation map of Specimen F at interruption stages

8.4 DISCUSSION

In order to simplify the interpretation of the results, all subsequent analysis only deals with the three specimens successfully creep-tested at 200 °C, namely Specimens D, E, F, with applied loads of 75, 50, and 60 MPa respectively. This is to allow the analysis to focus on the isothermal (200 °C) creep condition at various stress levels. Therefore, all subsequent graphs label the three specimens by their stress levels only. Figure 8.12 summarizes the creep curves of the three isothermal specimens against time. The plots illustrate the increase in secondary creep rates as the applied stress is increased.

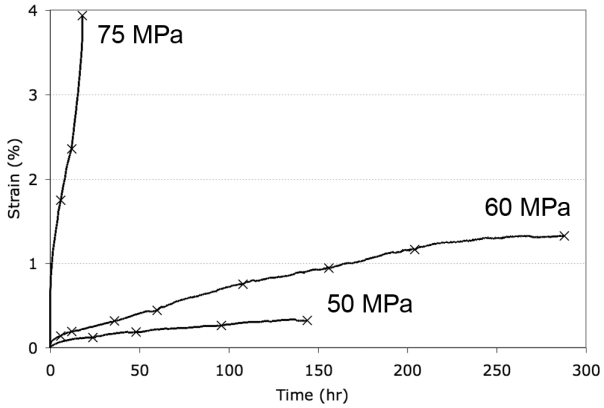

Figure 8.12. Combined time-strain curves of the interrupted specimens D (75 MPa), E (50 MPa), and F (60 MPa) at 200 °C. Markers (x) indicate the interruption stages

8.4.1 Contribution of grains and grain boundaries

A significant observation made from the sequential EBSD maps was that the formation of voids and the eventual onset of catastrophic failure was strongly related to the high angle misorientation (grain) boundaries, whereas the dendrite arm (intragranular) boundaries and their associated $(Mg,Al)_2(Ca,Sr)$ precipitate networks appear to remain unaffected by the creep deformation during steady-state creep. This suggests that the $(Mg,Al)_2(Ca,Sr)$

precipitate network was sufficiently stable and provided reinforcement to the primary α-Mg dendrite structure and minimized the onset of intragranular creep deformation mechanisms [3] [4]. Figure 8 shows high magnification images of the creep micro-cracks on the 75 MPa specimen near failure. Corresponding EBSD maps of the same areas reveal that these cracks always follow high angle misorientation boundaries, which are not clearly evident in the secondary electron images. A contrast can be made against the level of intragranular textural evolution observed in the studies of pure magnesium creep on Chapter 6, which was carried out at much lower temperature and stress levels.

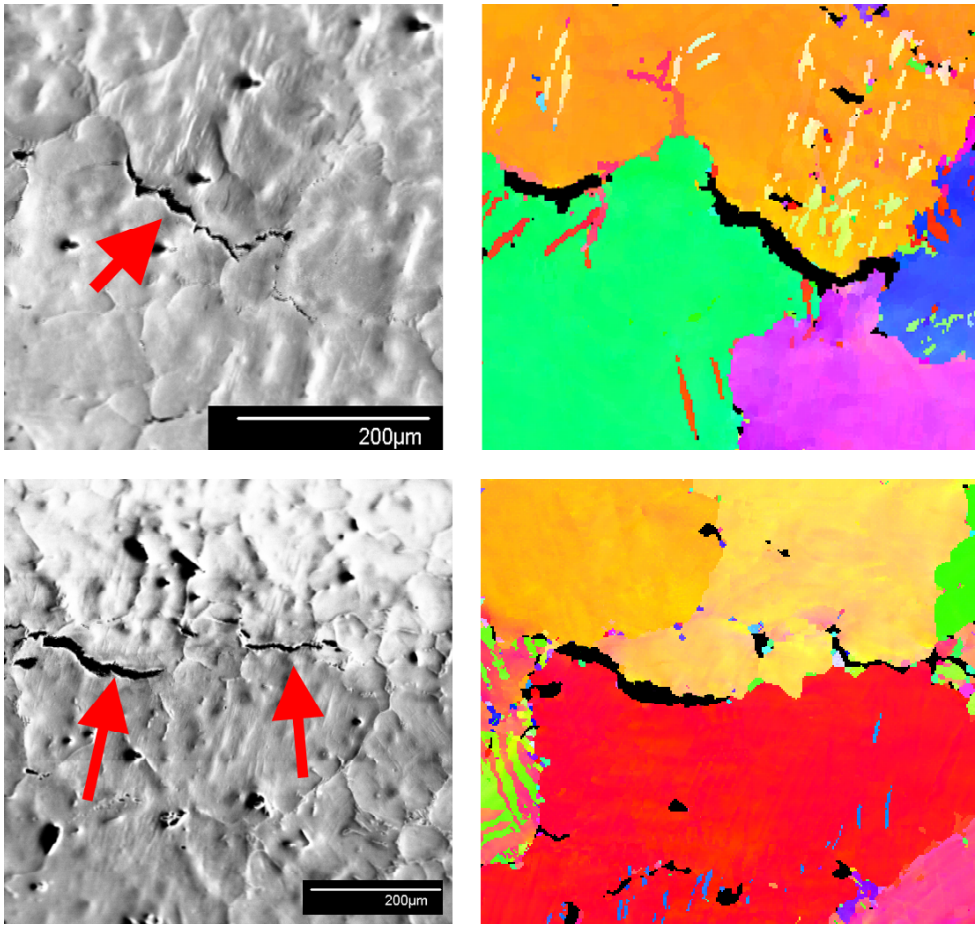

Figure 8.13. Some microcracks observed under the SEM and their corresponding EBSD orientation maps

The observation that the contribution of intragranular deformation was low can also be illustrated by Figure 8.14, which plots the average grain size at each interruption stages. The "average grain size" was measured by the average diameter of 150 largest grains within the EBSD map, where a "grain" is defined as an area enclosed by a misorientation angle of more than 15°. The 86° $\{10\bar{1}2\}$ twin boundaries were not treated as grain boundaries. The number of grains was limited to 150 since this was an approximate limit of the resolution of the EBSD maps in visualizing a "grain" as a cluster of at least 3x3 pixels.

The average grain sizes of the three specimens are in a range of 130-150 μm, and remain unchanged throughout the creep deformation. This is in contrast to the pure magnesium case, where in some cases the original grains decomposed into smaller grains due to the activity of intragranular deformation mechanisms.

Figure 8.15 is a plot of the average intragranular misorientation angles within the 150 grains measured above. These misorientation values exclude the 86° twin boundaries within the grains. The plot illustrate that the intragranular misorientation (i.e. texturing of the grains) increases steadily as creep strain increases but not to any significant degree (< 3%) until eventual failure of Specimen D (75MPa). These intragranular texture evolutions can be observed in the orientation texture maps of Specimen D on Figure 8.6, particularly in highly deformed areas near the fracture surface. Specimen E (50MPa) did not show an increase in the intragranular misorientation, because it experienced very little strain, and exhibits a comparable behavior to the early stage of the plot of Specimen F.

The significance of high angle misorientation interfaces suggests the merit of improving the alloy fabrication process to reduce the number of such interfaces (i.e. large "grain" structure) to improve the creep properties. However, it can also be speculated that at higher stress levels, the dendrite arm boundaries (where the precipitates lie) will also become the sites for localized void formation. This observation agrees with the power-law creep rate calculations in Chapter 5, which shows that at low stress levels (50, 60 MPa), the experimental creep rates agree with the "large" grain size model based on the high angle misorientation boundaries (375 µm), whereas at high stress level (75 MPa), the creep rates tend towards the "small" grain size model based on the dendrite arm spacings (58 µm).

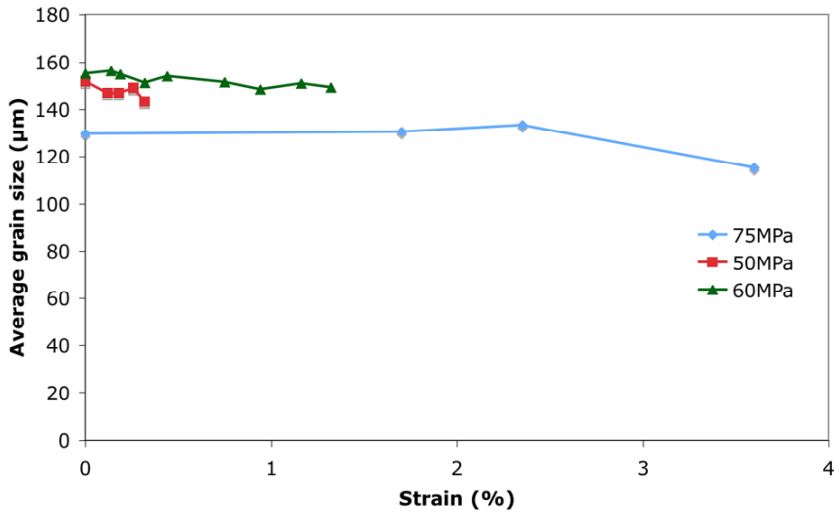

Figure 8.14. Average grain sizes of specimens D (75 MPa), E (50 MPa), and F (60 MPa) at 200 ºC normalized for total strain. Markers indicate the interruption stages

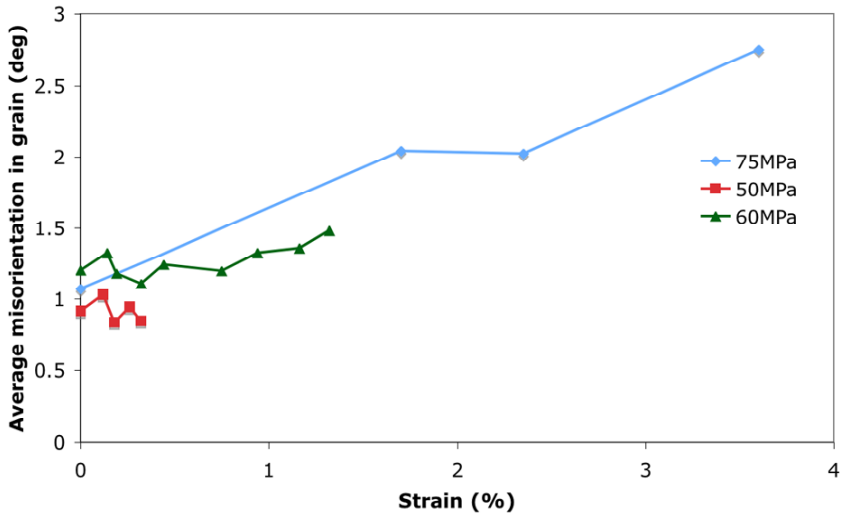

Figure 8.15. Average misorientation within grains of specimens D (75 MPa), E (50 MPa), and F (60 MPa) at 200 ºC normalized for total strain. Markers indicate the interruption stages

In addition to the sequential creep test specimens, another specimen was tested at a higher stress level (90 MPa) as a comparison. The test resulted in failure within 30 minutes of the commencement of the creep test, and therefore a steady-state creep rate was not recorded for this specimen. The post-failure EBSD map is shown on Figure 8.16.

The rapid failure of the 90MPa specimen is attributed to power-law breakdown, where the stress level is sufficient for creep deformation to take place with less dependence on temperature-activated dislocation mechanisms [5]. A study by Zhu *et al.* on a similar alloy [6] identified power-law breakdown from σ/G (stress normalized by shear modulus) value of greater than 6×10^{-3}, which corresponds to 92 MPa at 200 ºC. Figure 8.17 compares a post-failure secondary electron image of the 90 MPa specimen with an EBSD orientation map of the same area. In this sample, the formation of micro-cracks at the intermetallic phase interfaces of the low-angle dendrite arm boundaries did not necessarily correspond with the high angle grain boundaries.

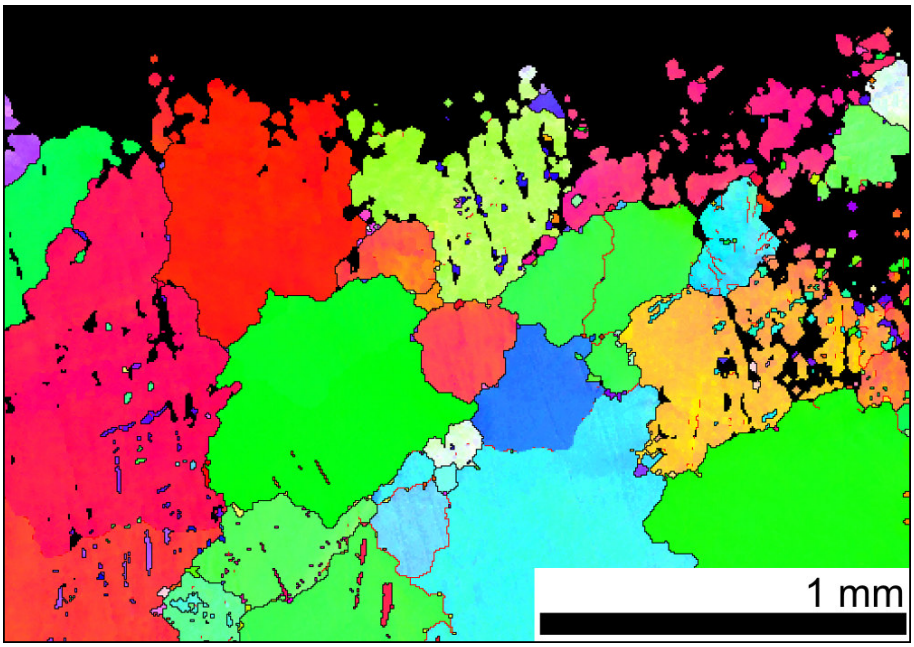

Figure 8.16. EBSD orientation map of 90 MPa specimen after failure

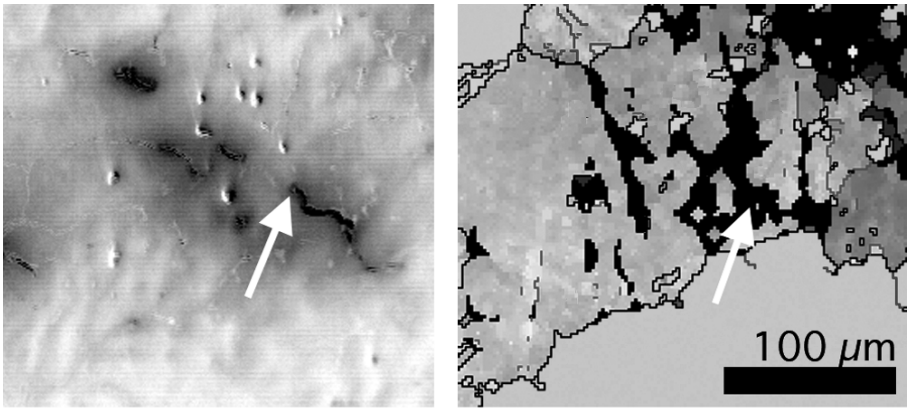

Figure 8.17. (a) SEM (SE) image and (b) EBSD orientation map of a same area of 90 MPa specimen, highlighting the intragranular cracks

8.4.2 Contribution of twins

The EBSD orientation maps of the specimens at each interruption stages illustrated the formation of heavily twinned grains as creep progressed. The twinned grains were observed in all specimens to a varying degree. The twins were identified as a $\{10\bar{1}2\}$ HCP tension twins with 86° relationship with the parent matrix, with a $\langle 2\bar{1}\bar{1}0\rangle$ rotation axis [11, 12]. Figure 8.18 separates an EBSD orientation map of Specimen F after 288 hours of creep (which corresponds to Figure 8.11) into grains with twins (highlighted in colour), and grains without twins (only shown by their outlines). The corresponding pole figures of these two types of grains illustrate that the grains with twins have their basal axis inclined towards the tensile direction, compared to grains without twins, which shows a clear tendency for the basal axis clustered perpendicular to the tensile direction. This agrees with the relationship between the applied stress (CRSS/*m*) and the inclination of the basal axis from the tensile axis(Φ) illustrated on Figure 2.3b, which shows that twinning is most favourable when the basal axis is aligned closer to the tensile axis, and is unlikely to occur when the basal axis deviates beyond about 60° from the tensile axis.

The number of twins appears to increase as creep deformation progressed, and this is illustrated in Figure 8.19, which plots the level of 86° misorientation interfaces (twins) in the EBSD map area at each interruption stages. The graph x-axis is normalized to the total creep strain instead of time or T/Tr. This is to illustrate the contribution of twin formation to the overall deformation of the material. The misorientation interface fractions were quantified by taking the angle of misorientation between pairs of adjacent EBSD patterns (i.e. adjacent pixels in the map) and the twins were evaluated as the fraction of such pairs that have a misorientation between 85-87° from all misorientation pairs greater than 15°.

The same technique was used for the study of pure magnesium creep in Chapter 6, and this agreed with the physical number of twins counted manually.

Figure 8.19 shows that the number of twins increased consistently as creep strain increased, and all three specimens at different stress levels exhibited similar amounts of twins corresponding to the amount of strain experienced. This suggests that the twins act as a major source of secondary creep deformation mechanism in the alloy MRI-153M at the prevailing creep test conditions. One exception may be the Specimen E (50 MPa), which shows a rate of twin formation much faster than the other two specimens. However, this may be attributed to the fact that the specimen E did not originally have as many twinned grains as the other two specimens (as illustrated in Figure 8.19 at strain of zero), and therefore rapidly reached the level of twins similar the other two specimens as creep progressed. The twin formation was a secondary creep phenomenon (i.e. thermally activated), since the number of twins increased gradually through the secondary creep stage, rather than at the initial primary transient creep.

Plot of the Specimen D (75MPa) shows a plateau in the rate of twin formation from after the first interruption (1.5% strain). This suggests that the amount of grains able to twin has been exhausted at this level of strain. Unfortunately, similar plateaus could not be observed on the other two specimens, since the creep tests were stopped prior to reaching this level of strain. It must be reminded that the graph is normalized to the unit of strain, rather than time, where in fact a time-interval of 132 hours lie between the last two interruption markers of Specimen F (60MPa).

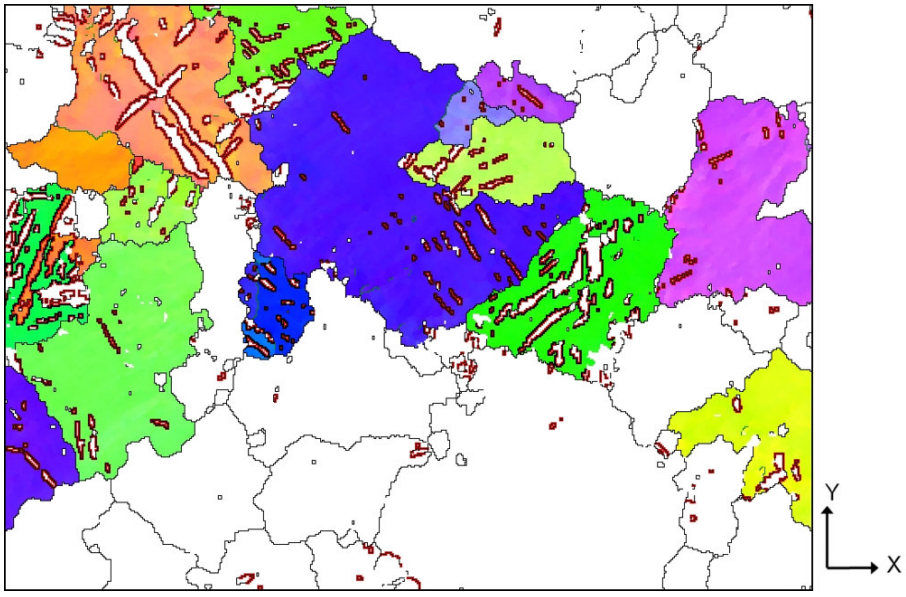

(a)

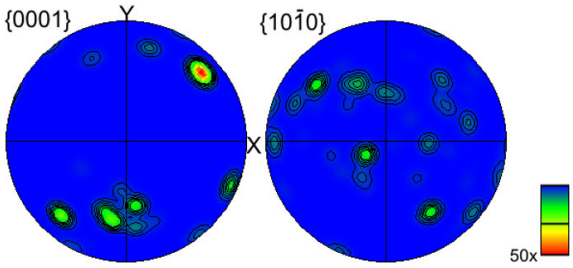

(b)

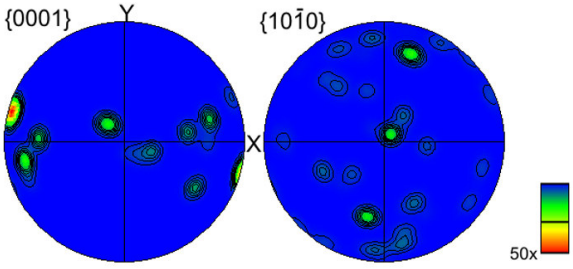

(c)

Figure 8.18. (a) EBSD orientation map of specimen F (60 MPa) at 288 hours with twinned grains highlighted in colour, (b) pole figure of only the twinned grains and (c) of grains without twins. Tensile direction corresponds to the y-axis on the figures.

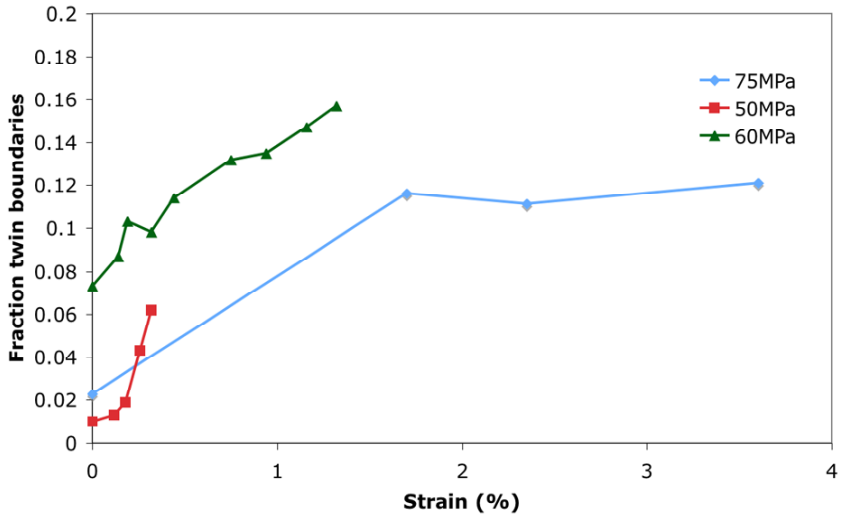

Figure 8.19. Fraction of misorientation angles that corresponds to a twin (86 ± 1º) for specimens D (75 MPa), E (50 MPa), and F (60 MPa) at 200 ºC normalized for total strain. Markers indicate the interruption stages

Figure 8.20 shows an EBSD map of Specimen D, which is identical to Figure 8.6, except only the high angle (>15°) misorientation boundaries are shown. The figure also highlights the 86° special boundaries in red, which corresponds to the twin boundaries. The eventual fracture surface at 18 hours illustrates that the crack path follows the high angle misorientation boundaries at highly twinned region of the map.

These high angle misorientation boundaries and the gradual development of the localized twinned regions cannot easily be observed or quantified under the conventional SEM studies. Figure 8.21 is a conventional SEM image of Specimen D after fracture, corresponding to the same EBSD map location at 18 hours on Figure 8.20. Although high angle misorientation boundaries or twins cannot be distinguished from the other dendrite arm boundaries on the SEM image, it is apparent that the highly twinned grains shown in Figure 8.20 corresponds to heavily deformed areas as indicated by red arrows in Figure 8.21.

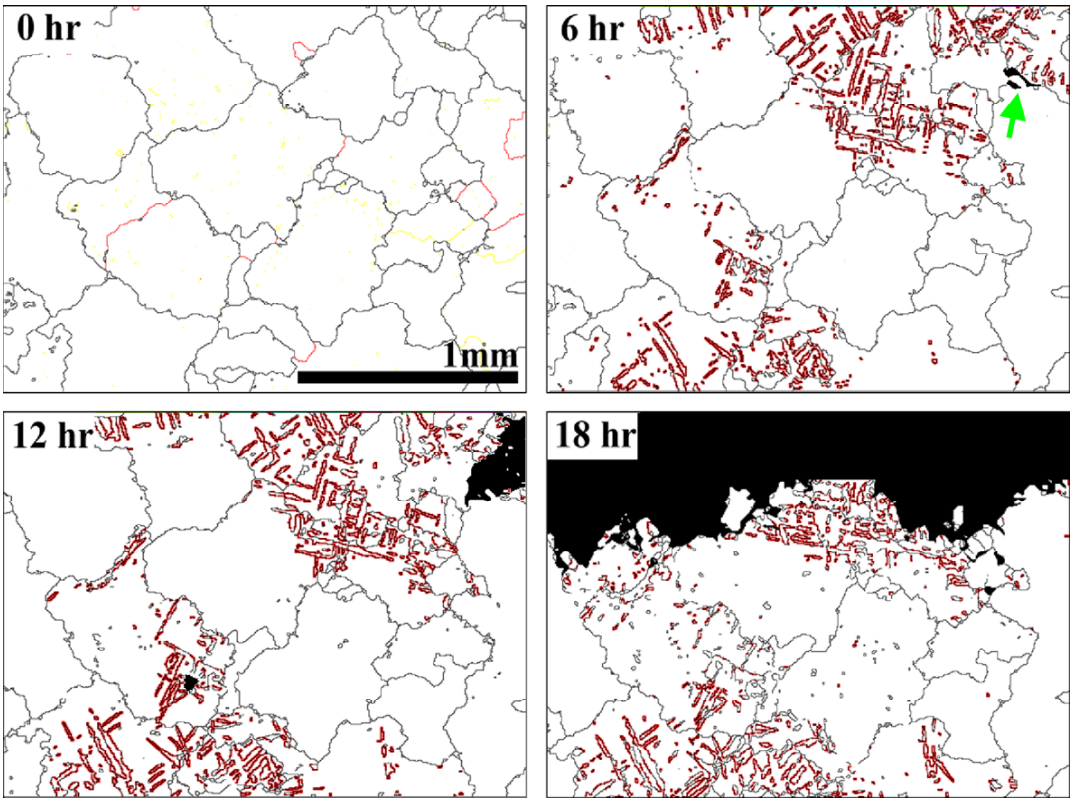

Figure 8.20. EBSD maps of Specimen D at each interruption stages, with only the high angle (>15°) boundaries (black) and twin boundaries (red). Initial onset of crack formation is indicated by an arrow (green)

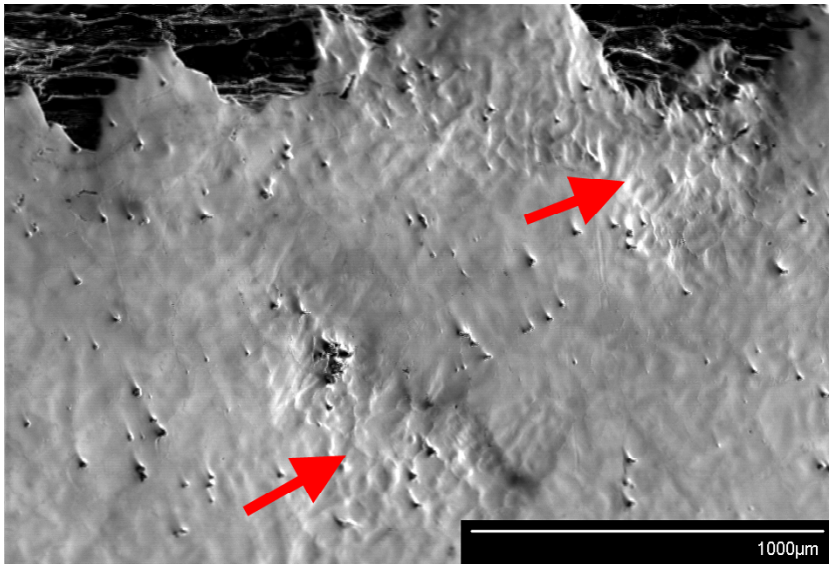

Figure 8.21. Fracture region of Specimen D observed under SEM. Red arrows indicate the dimpled regions

8.4.3 Sequence of the creep deformation process

In light of the above observations, the dominant deformation mechanism for the alloy MRI-153M in the current test conditions (200 °C, 50-75 MPa) can be summarized as follows:

Stage 1: First, significant twinning in specific grains takes place after the initial creep rate transient. The onset of twin formation is determined by the original crystallographic orientation texture of the microstructure [7], produced by the prior casting or forming processes experienced by the alloy [14, 15]. This results in a localized strain of the twinned regions, creating stress concentration zones, further assisting the development of stress-induced twinning of the nearby grains. The formation of new twins decreases as the potential sites for their formation is exhausted.

Stage 2: Subsequent to twinning, the creep strain rate may decrease due to the exhaustion of available twinning sites. Given sufficient stress (e.g. 75 MPa), formation and growth of creep voids takes place from high angle grain boundaries, and creep continues in a steady-state manner until failure. When stress is raised higher (e.g., 90 MPa), voids are also created from the intermetallic particle interface of the low angle, secondary dendrite arm boundaries, and result in rapid failure.

As shown earlier on Figure 8.10(b), an unexpected result from the current study was the observation of a gradual reduction of creep rate observed in Specimen E (60 MPa) after approximately 1.3% strain. Figure 8.19 shows that the steady-state creep was linearly related to the formation of twins. Therefore, it is possible that the initial twinning-assisted power-law creep rate was reduced by the lack of new twinning sites, and any subsequent

creep deformation process occurs at a slower rate. Further research, such as creep rupture testing and additional creep rate measurements, is required to investigate this phenomenon. This result also illustrates that the traditional classification of a "secondary" creep stage may be insufficient for understanding the creep of a complex alloy system when several deformation mechanisms are taking place, as has been pointed out by Blum et al. [8].

It must be noted that these creep tests were conducted exclusively at 200 °C and the observed creep deformation mechanisms may not take place under other conditions. At higher temperatures (> 200 °C), stability of the Mg-Al solid solution matrix may be compromised, and the corresponding mechanisms such as the formation of unstable β-phase precipitates may dominate the creep deformation. In a similar alloy (Mg-9Al-0.7Zn-1Ca-0.1Sr), Zhu et al observed a gradual increase in the creep rate due to the microstructural changes induced by the precipitation of the β-phase during creep [6]. Incomplete suppression of the β-phase is dependent on the Al/Ca ratio of the alloy [9].

8.5 CONCLUSION

The sequential creep/EBSD studies of the alloy MRI-153M was carried out to visualize the underlying deformation mechanisms at various stages of creep.

The studies carried out in isothermal condition at three stress levels (200 °C, 50, 60, 75 MPa) identified the following:

- All specimens deformed in a similar manner, indicating that they lie under the same mode of creep deformation. Secondary creep rates of all test specimens agreed with the basic power-law creep rate model from Chapter 5.

- The interdendritic $(Mg,Al)_2(Ca,Sr)$ precipitates were stable and provided resistance against dislocation climb-based creep deformation mechanisms of the α-Mg lattice.

- Crack formation and growth took place at high angle misorientation boundaries. This agrees with the power-law creep model in Chapter 5, which was based on the grain size values as high angle misorientation boundaries rather than the dendrite arm spacing.

- All specimens exhibited the gradual formation of $\{10\bar{1}2\}$ twins during secondary creep stage, resulting in a dimpled appearance of the surface. The failure took place on Specimen D (75MPa) from a heavily twinned region.

- Specimens tested at lower stress levels (50, 60MPa) exhibited slowing down and eventual halt of the secondary creep deformation.

These observations were made only on a small handful of test conditions, and two of the

creep tests (Specimens E, F) had to be terminated prior to the eventual failure. This was due to the time constraints imposed on the research.

The creep tests were conducted at 200 °C. Therefore, the observed deformation mechanisms only apply to the current test conditions, and similar creep deformation mechanisms may not take place under other test conditions.

At even higher stress levels (e.g. > 100 MPa), it is anticipated that the applied stress approaches the yield point and therefore the creep deformation will be more strictly dependent on the localized plasticity and the presence of defects rather than the underlying thermally activated dislocation mechanisms.

On the other hand, at higher temperature levels (e.g. > 250 °C), the stability of the Mg-Al solid solution matrix will likely be compromised, and the corresponding mechanisms such as the formation of unstable β-phase precipitates may dominate the creep deformation. This was not verified in the current study due to the limitation imposed on the upper temperature threshold of the specimen immersion oil.

Further creep tests at such elevated temperature or stress levels may be able to identify the dominance of other deformation mechanisms (e.g. grain boundary sliding [10], dislocation climb assisted lattice diffusion [5] or subgrain formation [11]). However, the test conditions selected for the current study (200 °C, 50-75 MPa) are those most likely to be of interest in the actual application of the alloy MRI-153M, and therefore of significant industrial as well as academic interest. In particular, the identification of the presence of threshold creep condition that results in catastrophic failure or slowing of the secondary creep can be pursued further to determine the practical limits of the alloy applications.

Chapter References

[1] M. O. Pekguleryuz, Mat. Sci. Forum 350 (2000) 131.

[2] F. J. Humphreys, Scripta Mater. 51 (2004) 771.

[3] A. Suzuki, N. D. Saddock, J. W. Jones, T. M. Pollock, Acta Mater. 53 (2005) 2823.

[4] R. Raj, M. F. Ashby, Met. Trans. 3 (1972) 1937.

[5] H. J. Frost, Ashby, M.F., Deformation-Mechanism Maps, Pergamon Press, 1982.

[6] S. M. Zhu, B. L. Mordike, J. F. Nie, Metall. Mat. Trans. A 37 (2006) 1221.

[7] M. R. Barnett, Z. Keshavarz, X. Ma, Metall. Mat. Trans. A 37A (2006) 2283.

[8] W. Blum, P. Eisenlohr, F. Breutinger, Metall. Mat. Trans. A 33 (2002) 291.

[9] S. M. Liang, R. S. Chen, J. J. Blandin, M. Suery, E. H. Han, Mater. Sci. Eng. A 480 (2008) 365.

[10] R. Raj, M. F. Ashby, Met. Trans. 2 (1971) 1113.

[11] O. D. Sherby, R. H. Klundt, A. K. Miller, Met. Trans. A 8A (1977) 843.

CHAPTER 9 - SUMMARY AND CONCLUDING REMARKS

9.1 SUMMARY OF ACHIEVEMENTS

9.1.1 Microstructural studies of MRI series creep resistant magnesium alloys

- A combination of EBSD and TEM enabled the identification of the eutectic appearing at the primary grain boundaries as having Mg_2Ca phase structure.

- SEM analysis showed that, compared to AZ-type alloys, the detrimental $Al_{12}Mg_{17}$ β-phase was reduced in MRI-153 alloy and completely suppressed in MRI-153M alloy.

- SEM/EDS analysis identified aluminum as a substitutional component in the $(Mg,Al)_2Ca$ structure, which suggests a reason behind the reduction in β-phase mentioned above.

- In addition, EDS/EBSD also identified strontium appearing in the $(Mg,Al)_2(Ca,Sr)$ structure at primary grain corners in the MRI-153M alloy.

- Deep etching was successfully applied to the MRI alloys to preserve and illustrate the nature of the 3-dimensional grain boundary precipitate network, and allowed observation of the bulky strontium-rich regions.

9.1.2 Sequential creep/EBSD study of pure magnesium

- The interrupted creep tests of pure magnesium measured secondary creep rates that agree well with the power-law rate equation predictions.

- Sequential EBSD studies on the two pure magnesium specimens verified and clearly isolated the contrasting mechanisms of high temperature and low temperature power-law creep exhibiting differences in dislocation motion and resultant texture development. The results were further verified by TEM study of the same specimens after failure.

- Sequential EBSD maps illustrated the gradual alignment of the hcp basal plane to the tensile axis, and the elimination of preexisting tension twins during the early stages of creep.

- The low temperature-high stress (100ºC, 50MPa) creep specimen exhibited the formation of subgrain cell structures, which subsequently developed into a network of fine grains near the original grain boundaries. This observation suggests a localized movement of dislocations toward the nearest high-energy interfaces such as grain boundaries.

- The high temperature-low stress (200ºC, 18MPa) creep specimen exhibited very little subgrain formation, which suggests the activation of lattice diffusion with climb assisted dislocation glide. Some low angle boundaries were observed that were aligned into straight parallel lines corresponding to prismatic slip.

9.1.3 Sequential creep/EBSD study of creep resistant alloy MRI-153M

- Interrupted creep tests of MRI-153M alloy measured secondary creep rates that agree with the theoretical predictions based on a modified power-law creep model.
- The secondary creep rates agree with a model using the grain size based on high angle misorientation boundaries.
- EBSD maps of the 75 MPa specimen identified that the crack formation and growth took place at high angle misorientation boundaries. This suggests that the interdendritic $(Mg,Al)_2(Ca,Sr)$ precipitates were stable and provided resistance against deformation in other low angle interdendritic boundaries.
- At higher stress level (90 MPa), creep cracks formed intragranularly, following low angle interdendritic boundaries, resulting in fast catastrophic failure.
- All specimens exhibited the gradual formation of $\{10\bar{1}2\}$ twins during secondary creep stage, resulting in the formation of surface textures. The failure took place on the 75MPa specimen from a heavily twinned region.
- Specimens tested at lower stress levels (50, 60MPa) exhibited slowing down and eventual halt of the secondary creep deformation. This corresponded with the slowing of the twin boundary formation.

9.2 CONCLUDING REMARKS

The primary objective of this research program was to perform fundamental studies of creep mechanisms in pure magnesium and the industrially relevant MRI-153M alloy using the newly developed sequential creep/EBSD analysis technique.

One of the most significant benefits realized from this research program was the identification of contribution by special boundaries such as the tension twins, clarification in the roles of high and low angle boundaries, crystallographic orientation, and the development of crystallographic texture during creep.

In the case of pure magnesium, the EBSD technique was successfully used to identify the two contrasting deformation mechanisms that were both in agreement with the predictions based on the power-law creep model. This observation has reaffirmed the importance of understanding the creep deformation mechanisms, rather than simply measuring and tabulating the secondary creep rates, because one must be aware of the transitions in the underlying deformation mechanism regimes in order to fully appreciate their implications on the creep properties. For example, the difference in creep deformation texture from high-temperature, lattice diffusion oriented creep to low-temperature, dislocation cell structure oriented creep was clearly distinguished in the current study of pure magnesium.

The study of the MRI-153M alloy has identified three key areas of interest that will benefit the improvement in creep properties of the current alloy.

Firstly, the dependence of secondary creep rates and the formation of creep cracks on the high angle grain boundaries implies that the creep properties can be improved by alloy

design and process techniques that is aimed at reducing the total grain boundary area. This may seem trivial but was only confirmed by the use of EBSD orientation maps to visualize the "actual" grain boundaries (i.e. high angle misorientation boundaries) from the other low angle secondary dendrite arm boundaries. This is in contrast to the traditional method of counting the average dendrite arm spacing to characterize dendritic microstructures.

Secondly, the catastrophic creep void formation and growth in the 75 MPa specimen took place on a heavily twinned region of the specimen, which suggests that the material's susceptibility to twinning plays an important role in improving its creep properties. This is particularly important for magnesium alloys since the HCP crystal structure of α-Mg has little alternative potential slip systems other than basal slip and tension twinning in order to accomodate deformation. This means that some design considerations can be introduced, or the alloy texture may be controlled (e.g. by the alignment of the basal axis to be perpendicular to the tensile axis) in order to enhance the creep properties.

Thirdly, the creep properties may benefit from further study on the strength and stability of the interdendritic intermetallic phase $(Mg,Al)_2(Ca,Sr)$. The improved creep resistance of the MRI-153M was found to be partly due to the stability of this precipitate phase at the secondary dendrite arm boundaries, and the maximum creep stress in the current experiments (90 MPa) was limited by the breakdown at these precipitate interfaces.

The study of creep in pure magnesium and the alloy MRI-153M has successfully integrated and reconciled the three key areas of research; theoretical prediction, mechanical testing and microscopy, to provide a solid foundation for the future studies in the development of creep resistant magnesium alloys.

CHAPTER 10 - FUTURE WORK

10.1 ADDITIONAL WORK ON THE PURE MAGNESIUM AND THE MRI-153M

10.1.1 Evaluation of the twin formation and disappearance

The sequential creep/EBSD studies have shown that the creep in both the pure magnesium and the alloy MRI-153M were related to the twinning of the primary α-Mg. In particular, the disappearance of the preexisting twins on pure magnesium and the growth of new twins on the MRI-153M were observed by the sequential EBSD maps. The twinning mechanism, as with the other HCP slip systems, can be evaluated by their CRSS and Schmid factor of the specimen texture, and further studies can be conducted to determine the exact contribution to the overall creep deformation mechanism.

10.1.2 Slowing secondary creep rate of the MRI-153M specimen

The 200 °C, 60 MPa creep test specimen of the MRI-153M alloy exhibited an unexpected behaviour in which the supposed "secondary" creep stage was found to slow down over a period of time (over many interruptions), instead of exhibiting the typical tertiary creep and failure. Unfortunately, the creep test had to be stopped after 288 hours, since further creep strain to failure was not realistic due to the slowing creep rate. This behavior puts into question the exact nature of the term "secondary" creep stage, since it is impossible to identify what stage of the creep curve represents a steady-state or a minimum creep rate. The sequential EBSD maps have shown that this slowing creep rate corresponded with a

similarly slowing twin formation, illustrating the lack of deformation in the microstructure, but the exact nature of the slowing behavior is unclear. One of the reasons for such variations in the creep rate can be attributed to the competing nature of more than one active deformation mechanisms, and further study such as a prolonged creep test in this creep regime, along with more detailed microscopy, is required to identify the cause of this phenomenon.

10.2 STUDIES BEYOND THE CURRENT ALLOY SYSTEM

10.2.1 Advanced analysis in conjunction with behavioral modeling

The advantage of the sequential creep/EBSD analysis is its ability to visualize the significance of special boundaries and orientation texture during creep deformation. These observations can be utilized in conjunction with advanced computational techniques such as phase formation thermodynamics or modeling of dislocation motions.

The current study acquired the sequential EBSD maps at a low magnification (45~100x) since it was important to capture as many grains as possible. The same technique can be implemented at high magnification to visualize more localized phenomena such as fine precipitate formation. The technique can also be applied to advanced areas of grain boundary engineering or alloy designs, in which the presence of special boundaries are known to play significant roles in the overall mechanical properties.

The maximum creep testing temperature in the current experiments system was 220ºC due to the use of silicone oil. Other bath fluids, or a different furnace with a similar control of

temperature, will have to be used in order to carry out a similar analysis on other metals such as those described on Table 10.1. New designs must also take into account the maximum safe operating temperature of the LVDT extensometer (85ºC).

Table 10.1. Creep testing temperature range of common metals

Material	Temperature
Magnesium alloys	50 – 300 ºC
Aluminum alloys	200 – 400 ºC
Steels	350 – 600 ºC
High temperature superalloys	> 1000 ºC

10.2.2 Study of multi-phased systems

Interrupted creep/EBSD studies of multi-phase alloy systems would be of great interest. In the present work, EBSD maps ignored the grain boundary intermetallic precipitate phases. This posed little significance in the current studies since the precipitate phase was assumed to be a stable, rigid, incoherent solid. The complication was that the main intermetallic phase $(Mg, Al)_2(Ca, Sr)$ had almost exactly twice the lattice parameter of primary α-Mg lattice. Therefore, the frequency of false identification between the two phases was very high within the tolerance limit imposed on the maximum mean angle deviation for positive pattern matching. These obstacles could be overcome by integrating EBSD and EDS systems to cross-verify the phase identification.

10.2.3 In-situ creep/EBSD analysis

In pursuing the concept of texture analysis during creep deformation, it may be possible to perform creep deformation *in-situ* inside the SEM specimen chamber, so that the specimen can be heated and stressed whilst the EBSD collects the surface texture data. If texture

data can be acquired continuously without interruption, the technique can be applied to specimens that are sensitive to shock loading or with significant primary transient creep. Another benefit is that an extensometer may not be required, since the amount of elongation could be directly observed in the SEM image, provided fiducial markers were used.

The in-situ creep/EBSD testing is technically feasible for the scope of future research, but there are three key obstacles that have to be overcome:

- The time taken to acquire one complete EBSD map must be significantly faster than the rate of creep deformation. For example, for a current case of 16 hours per complete map, the magnesium specimen at 100 ºC, 50 MPa would have elongated by over 5%.

- There are in-situ tensile loading and heating equipment already commercially available. However, an issue particularly for ductile specimens is the formation of surface faceting due to localized plastic deformation. This reduces the quality of EBSD pattern identification since the proper geometry must be maintained to capture the backscattered beam.

- There are dangers associated with the eventual catastrophic specimen failure or heating of the SEM chamber, which may damage the EBSD detector.

These effects must be carefully evaluated prior to considering undertaking an in-situ creep EBSD experiment.

10.3 CONCLUSION

Modern alloy development is a multi-faceted exercise that relies on a vast amount of experimental data and predictions based on theoretical and computational models. The difficulty arises when such studies must be verified against physical microstructural observations, since it may be difficult to visualize many of the complex deformation mechanisms using conventional microscopy techniques alone.

The most desired outcome to derive out of this research program is for the findings to contribute to the realization of the significance of the various underling creep deformation mechanisms on the creep properties, and to provide greater insight into the development of advanced creep resistant magnesium alloys in the future.

APPENDIX A - SEQUENTIAL CREEP/EBSD TEST SYSTEM

A.1 OVERVIEW

Following the detailed study of magnesium and its alloys, it was found that the conventional creep testing methods conducted by many of the industrial and academic researches are lacking in their ability to correlate the observed creep deformation with the underlying microstructural developments until after the ultimate failure had occurred. A new testing method called "sequential creep/EBSD testing" was proposed, in which a tensile creep test can be interrupted at various stages of creep deformation and the specimen surface microstructure is repeatedly analyzed by automated EBSD orientation map at identical locations for each interruption stage. The ultimate aim is such that the cumulative EBSD images can be viewed sequentially to illustrate the gradual changes in the microstructure and texture throughout the process of creep deformation. This technique required specific design objectives that cannot be achieved by using conventional creep testing facilities. It was also found that many of the commercially available creep test machines were expensive (> US$50,000) and laden with features that were not essential for the studies of creep in light alloys, and therefore a proposal was made for a new low-cost design that can achieve high accuracy sequential creep/EBSD test of magnesium alloys at less than one third of the cost of commercial alternatives. One of the major undertakings of this research program was the design and building of this new creep testing system that can carry out such a task. This chapter summarizes the work undertaken in the preliminary design process of this new sequential creep/EBSD system, followed by the detailed descriptions of the actual constructed unit.

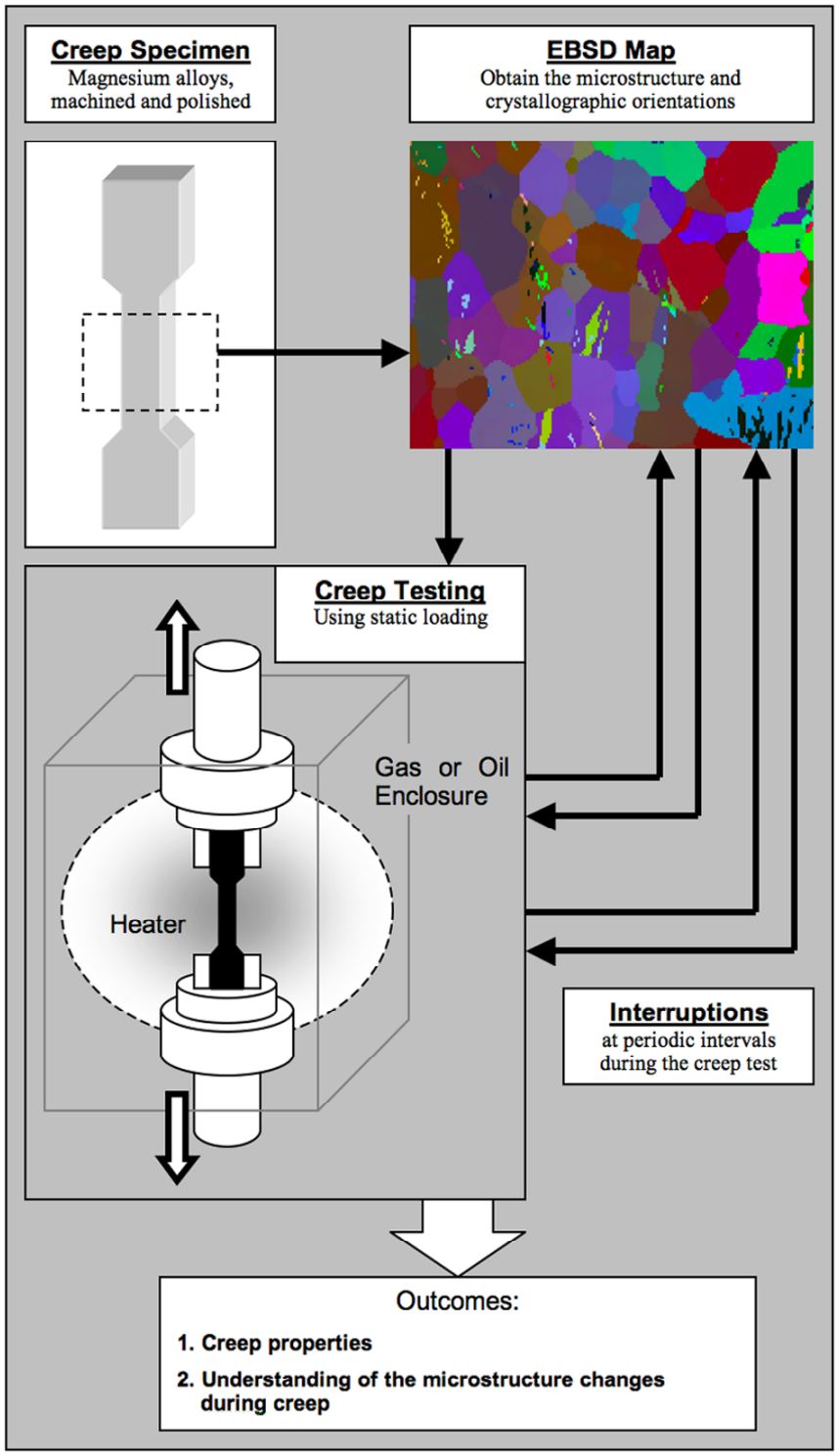

Figure A.1. Workflow diagram of the proposed sequential creep/EBSD technique

A.2 CONCEPTUAL DEVELOPMENT OF SEQUENTIAL CREEP/EBSD TEST SYSTEM

A.2.1 Design requirements

The basic parameters of the sequential creep/EBSD test system were decided to be as follows. Detailed explanations of the reasons behind each parameter are discussed in the subsequent sections.

Table A.1. Initial design parameters for the sequential creep/EBSD test system

Material	Pure magnesium and MRI-153M
Specimen shape	Rectangular (4 × 3 mm) miniature ASTM E-139
Test duration	Up to 300 hours continuous
Load	Up to 100 MPa
Temperature	Up to 220 ºC

A.2.2 Creep test specimen

A.2.2.1 Material

The objective of this research program was narrowed down to the study of creep characteristics of pure wrought magnesium and the alloy MRI-153M studied in Chapter 4. Pure wrought magnesium was chosen because past literatures of its creep properties were readily available, and had low levels of macroscopic defects that may affect the creep test results. MRI-153M was chosen because it was industrially relevant and complementary to

the research carried out on a similar alloy MRI-153 at Monash University [1].

A.2.2.2 Tensile test piece shape

The creep test piece shape was decided to be rectangular rather than a tapered cylinder cross-section primarily because the surface of a rectangular specimen can be directly polished and analyzed by SEM/EBSD without destruction as illustrated on Figure A.2. This design choice was essential in satisfying the objective of carrying out nondestructive analysis at each interrupted stage of creep.

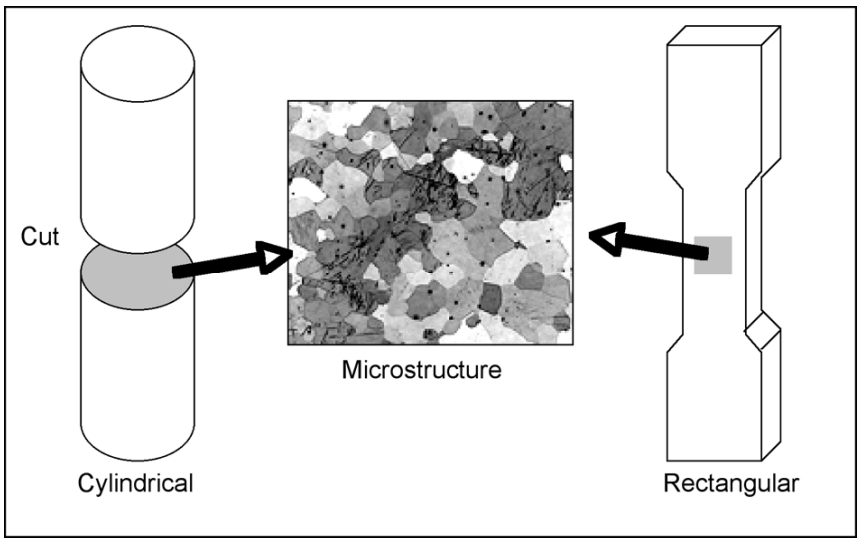

Figure A.2. Advantage of rectangular over cylindrical specimens

One disadvantage of a specimen with rectangular cross section is that the stress distribution is more complex due to surface interactions at the corners (corner stresses) that may reduce the specimen creep life compared to a smooth cylindrical cross section. However, this was not treated as a significant issue as long as such corner areas were avoided in the EBSD maps, since the primary interest in these experiments was the study of microstructural development rather than developing creep life data.

Specimen dimensions were based loosely on ASTM E-139 and E-466 for conventional rectangular tensile test specimens as illustrated on Figure A.3. The specimen dimensions were scaled down from the full-size ASTM E-139 size to a rectangular cross section of 4 mm × 3mm for several reasons.

1. A small specimen was desirable since the loading conditions (up to 100 MPa) could be accommodated without excessively heavy weights or hydraulic loading systems.

2. The minimum dimensions must be at least 3 mm if TEM studies are to be carried out on the post-creep specimens. A conventional TEM foil is a 3 mm disc, hence the minimum specimen width of 4 mm was chosen to accommodate for anticipated reduction in width of post-creep specimens due to necking.

3. The specimen length (25 mm) and fillet radii (4 mm) were kept proportional to the ASTM E-139 to avoid failure due to stress concentrations. This created a physical dimensional limit for the test piece to fit inside the SEM chamber fixture for EBSD analysis. The dimensions of 4 mm × 3mm cross section was found to be the most appropriate for the SEM fixture.

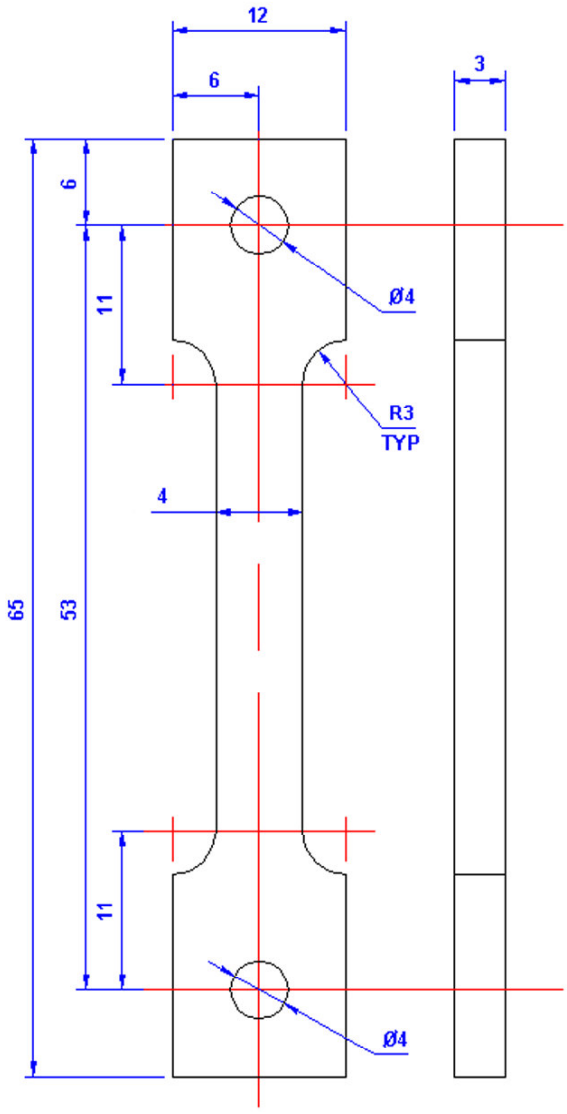

Figure A.3. Final dimensions for the miniature ASTM E-139 specimen

With the use of such a small tensile creep specimen, a question arises whether the size factor alters the results of the creep experiments to any significant degree compared to using a full sized tensile test specimen. Some of the key concerns are summarized below.

1. The most interesting factor was the relationship between average grain sizes of the microstructure compared to the specimen dimensions. One of the assumptions of the sequential creep/EBSD test is that the specimen surface microstructure is a fair representation of the bulk microstructure. The idea was to consider a sheet metal microstructure as illustrated on Figure A.4, whereby the specimen thickness is thin enough to only consist of a few grains. Therefore, in this respect, the grain size is preferred to be as large as possible. (The extreme case is single crystal creep, where the surface microstructure truly represents the bulk.)

2. In contrast to the above statement, in terms of statistical significance, there should be as many grains as possible in one EBSD surface map. Therefore, smaller grains and large specimen size is preferable in this respect. A rough guideline was set so that a typical EBSD map should contain at least 20 grains.

3. Variation in specimen dimensions would have more effect on the applied tensile stress on smaller specimens. Closer dimensional tolerances must be maintained during the fabrication and in measurement of the tensile cross section. Fortunately, the specimen geometry could be easily manipulated since the surface was processed through polishing procedures for EBSD analysis at every interruption stages. The specimens' cross sectional dimensions were measured to micron accuracy for every creep experiment conducted in this research.

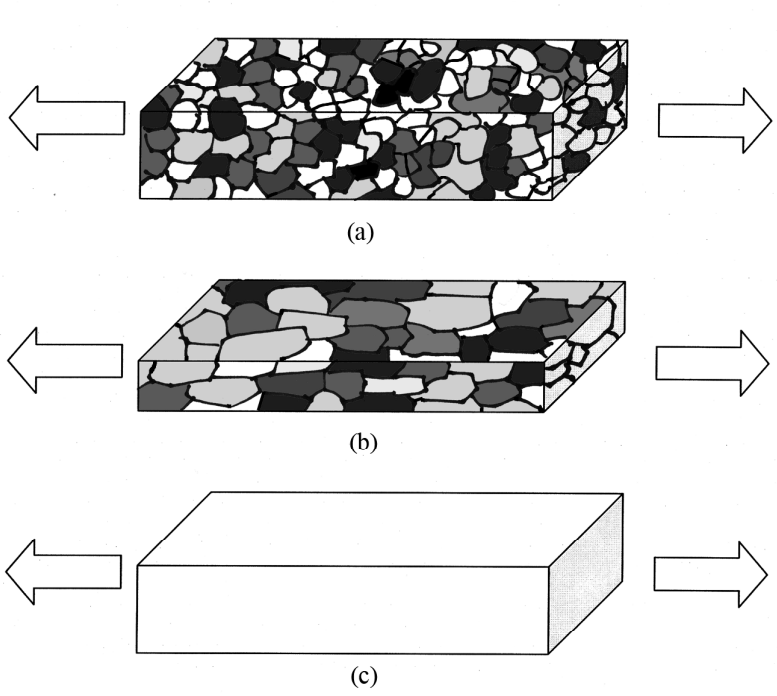

Figure A.4. Illustration of grain size vs. thickness on a typical (a) bulk metal, (b) sheet metal, and (c) single crystal

Ultimately, the size of a typical EBSD map (point 2 above) turned out to be the most limiting factor in determining how small the specimen size should be. This was because the minimum magnification of the SEM in order to achieve a reasonable EBSD map without significant image skew was 45× magnification, which creates a scan area of approximately 2.5 mm width. Therefore, any excess test piece width over 2.5 mm would be pointless in terms of the size of achievable EBSD map for statistical benefit, as illustrated on Figure A.5. For this reason the specimen width of 4 mm was deemed sufficient.

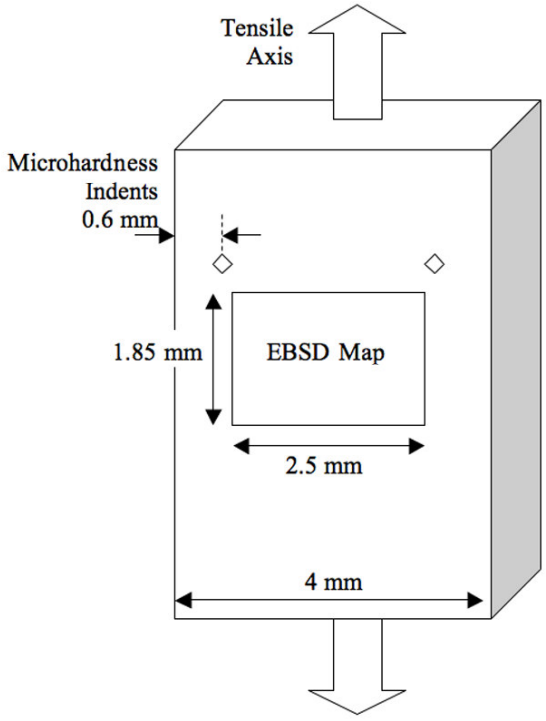

Figure A.5. Maximum EBSD window size in relation to the tensile specimen dimensions

A.2.3 Test Duration

As mentioned previously in Chapter 2, typical tensile creep tests can take as long as several hundred hours to complete. The system design must be able to provide stable test conditions and data acquisition for the entire duration of the test. It could be argued that increasing the applied temperature or load can shorten test duration. However, changing the temperature and load may alter the underlying creep mechanisms as illustrated in Figure A.6, and therefore contradicts the original intention of conducting the sequential creep/EBSD tests in order to identify the mechanisms of creep deformation that is relevant to real life applications. This is the fundamental reason why accelerated creep tests may not represent behavior in actual service conditions.

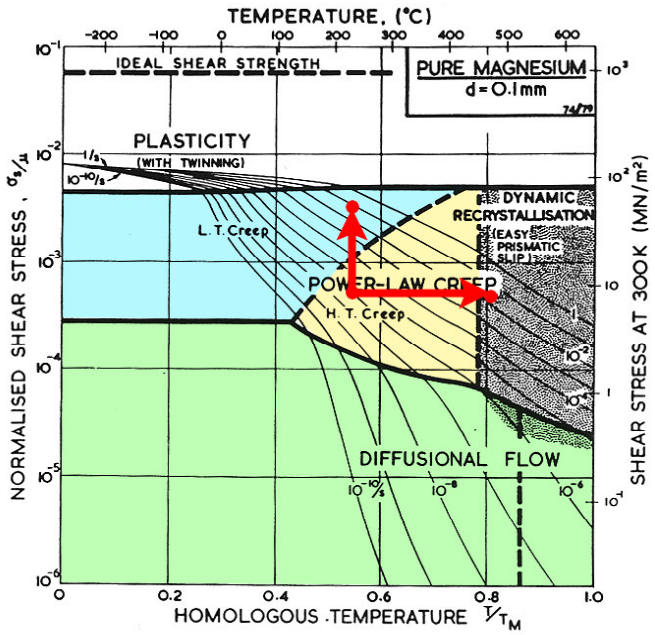

Pure magnesium with a grain size of 0·1 mm.

Figure A.6. Example deformation mechanism map illustrating the effects of accelerating the creep test conditions

Creep tests in excess of several hundred hours could introduce problems that are not present in simple tensile tests. Some of these are summarized below:

- Data acquisition is most likely be operated by a computer system. The system must be sufficiently robust enough to continue acquiring the data for several hundred hours without interruption, and handle large quantities of data without error. Most data acquisition systems on tensile test machines are not designed to handle such a long operation time.

- If a servo-hydraulic system was chosen for applying tensile load to the specimen, providing a continuous hydraulic pressure for several hundred hours would be uneconomical and unreliable.

- There is a potential risk of drift error of extensometer data due to thermal, mechanical, or electrical variations during the process. This factor was verified prior to conducting the creep tests and discussed further later in this Chapter.

- The designed temperature and environmental control system must be able to operate for the entire duration of the test. For example, if an inert gas hood was used to prevent oxidation of the specimen, the quantity of gas supply must be large.

A.2.4 Loading

The tensile loading was decided to be adjustable to produce up to 100 MPa using static hanging weight loading. It is understood that the creep rate will increase as the stress level increases due to reduction in area. Creep of magnesium alloys require very low applied load compared to similar experiments on steel or aluminum. Creep tests on conventional alloys such as the AZ series are carried out in the range of 20 to 80 MPa, and even the

specialized creep resistant alloys do not necessarily require higher loading levels, because there is little difference in the yield point of creep resistant alloys compared to conventional alloys, therefore the testing temperature may need to be higher but the applied loads do not change greatly.

The drawback of using a static hanging weight is that the load cannot easily be adjusted during the test in order to compensate for the necking of the specimen and provide constant stress condition. However, this issue was not considered significant for the current experiments due to several reasons outlined below:

- The objective of this research was to observe the microstructural changes at a given range of creep parameters, instead of collecting a comprehensive database of material creep curves.

- The primary interest of this experiment takes place in the secondary creep deformation, at which point the amount of deformation is still small. The majority of the deformation and necking takes place in the final tertiary creep stage.

- Past research shows that the MRI series magnesium alloys exhibit very small creep deformation to failure (< 2 %). Therefore, the deviation in stress is very small unlike creep tests of other superplastic materials that deform in excess of 100%.

A.2.5 Environmental control

A.2.5.1 Summary

Immersion in silicone oil bath was chosen as the best solution to avoid corrosion and improve temperature stability of the specimen during the creep experiment.

In typical creep experiments of light metals, inert gas hood (e.g. nitrogen or argon) or oil immersion is used to avoid corrosion of the specimen during the prolonged exposure to high temperature environment. In particular, magnesium alloys are prone to corrosion by humidity in the atmosphere. Although the level of corrosion is not of a significant level to rapidly destroy the specimen, it is still essential to reduce the amount of surface corrosion in order to minimize the depth of polishing required at each interruption stages prior to the EBSD analysis. Less surface corrosion will mean less thickness of surface layer needs to be removed, therefore each consecutive interruption stages can be retain a more consistent microstructure.

The decision between selecting a gas hood or oil immersion was carried out by considering their benefits and tradeoffs.

Benefits of oil immersion compared to gas circulation

- Oil immersion can be a static bathtub design that does not require constant feeding of the gas agent during the duration of the experiment
- Oil has the benefit of stabilizing the temperature due to its high thermal capacity, whereas gas cycling will have the reverse effect of disturbing the heated chamber, and will be more sensitive to the atmospheric temperature

- Creep of magnesium can be carried out at relatively low temperatures (< 220ºC), which is below the flash point of many oils

Benefits of gas circulation compared to oil immersion

- Gas hood requires no sealed container whereas oil immersion has a risk of leakages
- Design of gas circulation system can be more easily accommodated within the dimensions of the creep furnace, whereas the oil bath would interfere with the furnace, extensometer and the tensile loading mechanisms
- Inert gas circulation is relatively safe compared to oils that can be a potential fire hazard
- Gas hood is cleaner than oil when handling the specimen after each interruption stages in the experiment

An initial test observed temperature stability of ± 2 ºC under oil immersion bath without any glass wool insulation, whereas the temperature varied as much as ± 8 ºC without the oil bath. A quick-release hook system was developed for the specimen holder in which the specimen could be inserted and removed from the oil bath without draining the hot oil at each interruption stages.

A.2.5.2 Selection of immersion oil

Selection process for the immersion oil was carried out with consideration of following aspects.The immersion oil must;

- be chemically compatible and inert against magnesium and its alloys
- not absorb moisture and should minimize oxidation of the specimen
- easily be washed off the specimen without requiring strong chemical agents
- not have any risk of flammability within the maximum furnace temperatures of up to 300 ºC. (in case the temperature controller malfunctions)
- not chemically alter its properties within the operating temperatures
- be readily available and affordable

Two candidates emerged as potentially applicable for the above conditions.

- Heat treatment/quenching oil
- Liquid silicone

A.2.5.3 Heat treatment/quenching oil

Quenching oil is readily available in metallurgical foundry facilities, and is relatively affordable (< $10/L). Its properties are similar to mineral based automotive engine oil. However, standard engine oils cannot be used for specimen immersion since they contain chemical additives such as zinc, molybdenum and phosphates to reduce mechanical friction, as well as cleaning agents such as detergents that prevents carbon build-up in the engine. These additives could affect the microstructure of magnesium alloys, and therefore are not suitable. Mineral based machine oils can be acquired free of additives, but they have high rate of evaporation and are more prone to deterioration due to atmospheric contamination when exposed to elevated temperatures.

Quenching oils are typically free of additives, and are able to provide sufficient thermal capacity to stabilize the temperature. Key specifications of typical quenching oil (Fuchs Alloyquench 1921) are summarized below.

Fuchs Alloyquench 1921	
Kinematic viscosity at 40ºC	20 cSt
Density	0.865
Oxidation stability	2000 hr
Flash point	200 ºC (min)
Fire point	210 ºC (min)

One critical drawback of any of the mineral or synthetic based oils is their relatively low recommended operating temperatures (typically up to 150 ºC) with minimum flash point of 200 ºC. When such oils are exposed to temperatures above their recommended range, some constituents of the oil tend to "burn" away, creating toxic fumes and rapid deterioration of the remaining liquid component. Experiments identified that such "burning" residues become embedded to the magnesium specimen and is difficult to remove, as shown on Figure A.7.

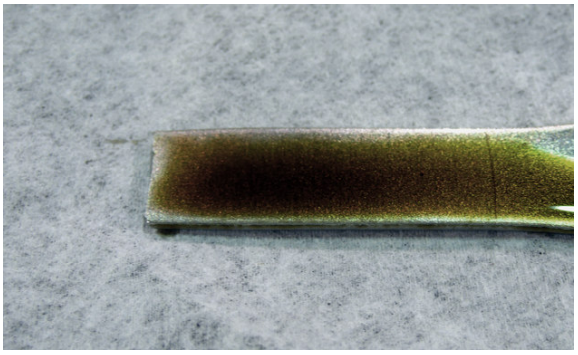

Figure A.7. Burnt quenching oil on specimen surface

A.2.5.4 Liquid silicone

Liquid silicone, more commonly known as silicone oil, is an inert, alternative lubrication fluid that is used for sealing and lubrication of metals and polymers that must be resistant to oxidation (e.g. vacuum circuits). Silicone itself has high resistance to oxidation, and therefore is suitable for specimen immersion in terms of corrosion prevention. However, silicone oils do have some issues, and this is largely attributed to the tradeoff between the oil's chemical stability against price. Cheaper silicone oils (e.g. Dow Corning 200) tend to have poor thermal and oxidation resistance compared to expensive variants that are fabricated from more sophisticated polymer chains (e.g. Dow Corning 550, 210H). Although the proposed creep experiments required very little quantities of these oils, their minimum purchase quantity requirements and high price (> US$1500) due to the lack of existing stock in New Zealand made it difficult to justify the risk of selecting these products. Specifications of high quality silicone oil (Dow Corning 550) are summarized below.

Dow Corning 550

Kinematic viscosity at 25ºC	125 cSt
Density	1.07
Volatile content	2.1% /hr at 250 ºC
Flash point	308 ºC
Fire point	343 ºC

A.2.5.5 DOT5 brake fluid (selected solution)

During the evaluation of various immersion oils mentioned above, a discovery was made that a conventional automotive DOT5 brake fluid is extremely suitable for the immersion

bath. After several trial experiments, this fluid was chosen to be the most appropriate fluid for the proposed creep testing of magnesium alloys. A typical DOT5 is a viscous silicone fluid with purple dye addition, compared to glycol based DOT4 with green dye addition. The product specification sheet of a certain DOT5 states as follows.

- Dry boiling point (0% H_2O) 265 ºC
- Wet boiling point (3.7% H_2O) 180 ºC
- Max operation temperature 150 ºC

Clearly the above specifications barely meet the criteria for the suggested magnesium creep test temperature of 200 ºC. However, due to their low cost and availability, several preliminary experiments were conducted, with results indicating that it can be used at up to 220 ºC if certain precautions are taken. Details of the experiments are discussed later in this chapter.

A.2.6 Temperature range / Furnace selection

A.2.6.1 Summary

Temperature range for the creep test was decided to be 50 ~ 220 °C with tolerance of up to ± 5 °C (nominal target ± 2 °C), using a wrap-around type ceramic resistance heater. This temperature range was selected based on the following reasons.

- Literature reviews suggest that the creep testing of Mg-Al alloys is typically performed in the range of 50 to 200 °C.
- The prior creep studies of the MRI alloys conducted by the Monash University group was carried out at 100 ~ 200 ºC using the same alloys.

- Typical operation temperatures of automotive components rarely go beyond 200 ºC. Therefore, the MRI alloys were designed to be used below this temperature.

- Above 250 ºC, pure magnesium enters recrystallization temperature range. Therefore, conventional low temperature creep theories no longer apply.

To achieve the specified temperature range of 50 ~ 220 ºC, a small wrap-around type ceramic resistance heater shown on Figure A.8 was selected. It has a cylindrical heated region of 200 mm diameter and height, and is capable of temperatures up to 300 ºC using standard 240V mains power with a digital PID controller.

Figure A.8. Compact wrap-around ceramic resistance heater

The heater surrounds the steel bath in which the specimen is immersed in an oil bath. Although the heater can easily achieve higher temperatures, creep testing of magnesium was not feasible above 250 ºC. Temperature stability of the heater arrangement was evaluated later in this chapter as ± 2 ºC. In addition to the properties of the heater, the limiting factor to the attainable temperature range and stability was due to the properties of the immersion oil. This is discussed in later sections of this chapter.

A.2.7 Extensometer

A.2.7.1 Summary

An extensometer is a device that measures the specimen elongation during the tensile creep test. It is typically connected to some form of data recorder to monitor and log the changes in elongation throughout the duration of the experiment. Typically an extensometer is a variable resistance device, where a current is applied from a power source, and the output voltage is proportional to the amount of extension experienced by the extensometer. A typical extensometer system consists of five key components.

- Extensometer (typically variable resistor)
- Electrical power source / Amplifier
- Signal acquisition hardware (typically a PC interface)
- Voltage/displacement filter and translator software
- Data acquisition software

Resolution of an extensometer is governed by the relative stability and noise floor of the entire signal path, and the robustness and reliability of the data acquisition software is also a large contributing factor. There are many commercial companies that specialize in manufacturing high precision extensometer packages for tensile testing. However, there are surprisingly few extensometers that can withstand temperatures in excess of 100 ºC. This is because many components within a typical extensometer are fabricated from thermoplastics to reduce the overall weight. In addition, thermal expansion also affects the strain data since extensometers are comprised of various mechanically moving components.

A Linear variable differential transducer (LVDT) type extensometer with a custom built

fixture was selected for this research. An LVDT is a type of transformer used to measure small levels of linear displacement. They are widely used in CAM/design applications to measure the object surface topography, or in manufacturing to perform automatic measurements of the dimensional tolerances. A simple LVDT consists of a magnetic pushrod surrounded by a cylindrical sheath with mirrored pair of AC excited solenoid coils and a centre coil as illustrated on Figure A.9. A small displacement of the pushrod away from the centre coil position causes a difference in inductance across the pair of solenoids that varies the output voltage. Because the underlying mechanism of the LVDT is electromagnetism induced in a transformer circuit, the pushrod and the coils require no physical contact, and therefore immune to mechanical problems of wear or thermal expansion.

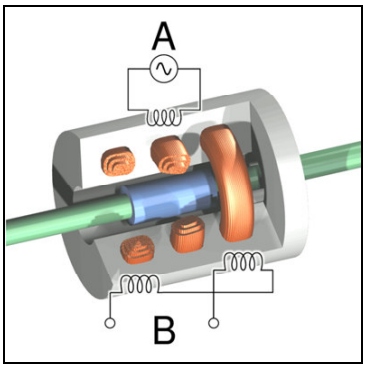

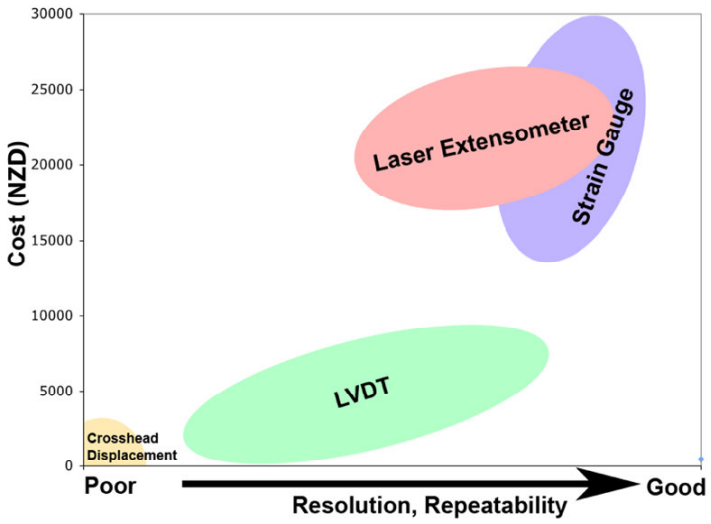

(a) (b)

Figure A.9. (a) Internal mechanism of a typical LVDT and (b) relative costs of the extensometer types

The greatest advantage of LVDT is the cost, in which a typical LVDT can be purchased at less than 1/10 of the cost of conventional strain gauge type extensometer of comparable resolution (~ 1 μm). The resolution could be further improved by using a pair of LVDT to act in differential array, which will still be cheaper than the cost of a conventional strain gauge extensometer. However, this paired approach was not used since it adds additional weight on the specimen, and the resolution obtained from a single LVDT was sufficient for the objectives of this research project.

Although LVDT appears to be the most ideal solution for the linear extensometer application, it does have several problems that must be addressed:

- LVDT requires constant supply of high frequency (~10 Hz) AC energizing voltage, and the resultant displacement signal must be demodulated into DC prior to interpretation. This adds extra electrical signal path that contributes to higher cost and unreliability over conventional strain gauge type DC resistance extensometers. The accuracy and reliability of the entire LVDT system is dependent on selecting a satisfactory demodulator unit, and many problems were encountered in dealing with the demodulator unit during this research program.

- Because LVDT utilizes electromagnetism, it is vulnerable to environmental electromagnetic interference and must be properly shielded against nearby electrical equipment such as computer monitors. The interference issue may worsen in a typical thermo-mechanical testing laboratory that is equipped with many furnaces with resistance coils that are sources of high power electromagnetic emission.

- The maximum specified operating temperature of a standard model LVDT was 85

ºC. This meant that the unit must be as kept far away as possible from the creep test furnace.

- Output of the LVDT varies with temperature at approximately 0.005% per ºC within its operation temperature range of -40 to 85 ºC. However, this did not cause a significant issue since the creep tests were conducted fairly constant temperatures.

Although bound with above potential issues, a suitable LVDT was purchased for evaluation due to its low cost. A series of experiments were conducted to verify whether the LVDT system would be an appropriate solution for the proposed sequential creep/EBSD experiments. Results of these studies are discussed further in the subsequent sections of this chapter.

These evaluation studies confirmed LVDT to be the most favorable for the intended application, and detailed design process of the associated extensometer configuration was initiated.

A.2.8 Conclusion

The selection process for an ideal sequential creep/EBSD testing machine proved to be a difficult task, since many critical requirement factors were associated in interdependent relationships.

To summarize the key points, the overall design was narrowed down to three separate system configurations as listed on Table A.2, with some degree of interchangeability amongst the various components. The cells colored in yellow are the components that are not available at the research facility, and therefore requires to be purchased.

As a result of the preliminary evaluation studies discussed in this chapter, the decision was made to go ahead with detailed design stage based on Option 4. The decision to select Option 4 was not purely based on cost, since both Options 2 and 3 would have provided cheaper alternatives. However the main deciding factor was the flexibility in design to incorporate all the desired features (such as the specimen immersion bath) without being bound by the preexisting system configurations. The drawback of selecting Option 4 was that the entire creep test system had to be designed and built from scratch, which would inevitably consume more of the total allocated research period, and would be more susceptible to delays, problems and design flaws encountered in the process. However, these obstacles had to be overcome in order to fabricate a system that is most appropriate for conducting the proposed sequential creep/EBSD experiments.

Table A.2. Summary of potential configurations

	Option 1	**Option 2**	**Option 3**	**Option 4**
Loading	Servohydraulic (MTS 858)	DMA (Perkin Elmer)	Direct hanging weight	Lever hanging weight
Temperature control	Commercial furnace attachment (Instron 1615)	Provided with DMA	Vertical tube furnace	Wrap-around ceramic resistance heater
Environment	Gas circulation	Gas circulation	Gas circulation	Silicone oil immersion
Extensometer	MTS high temperature (633.11F-14)	Provided with DMA	LVDT	LVDT
Estimated cost	$60,000 US	$0 US	$1,000 US	$6,000 US

A.3 DETAILED DESIGN OF THE SEQUENTIAL CREEP/EBSD TEST SYSTEM

Conceptual design and equipment selection process was carried out in the previous section. This section discusses the process of detailed design and construction of the sequential creep/EBSD test system.

A.3.1 Finalized design requirements

Based on the preliminary studies in the previous section, final design requirements for the system configuration were determined to be as summarized in Table A.3.

Table A.3. Final design requirements for the sequential creep/EBSD test system

Material	**Pure magnesium and MRI-153M alloy**
Specimen shape	Rectangular (4 × 3 mm) miniature ASTM E-139
Tensile loading	Static hanging weight with lever mechanism
Furnace	Wrap-around type ceramic resistance heater
Temperature control	240V digital PID system
Environment	DOT-5 silicone oil immersion bath
Extensometer	Custom built LVDT type

A.3.2 Detailed CAD design

All production blueprints and 3D models were constructed on AutoCAD 2002. Various design modifications were made after the completion of the initial creep test system, based on the feedback from the actual test results. The details described in this section refer to the final system design used in the later stages of the experiments. The changes made during the experimental stage were conducted purely for improvements towards specimen handling and convenience, thus in no way compromised the consistency of data collected from the experiments.

This section describes the final design process by dividing the critical design features into four categories

- Specimen design and fabrication
- Tensile load beam
- Load linkage mechanism with heater and silicone bath
- Extensometer

A.3.3 Specimen design and fabrication

Rectangular tensile test specimens based on ASTM E139 were fabricated from wrought extruded magnesium ingot. The design of the miniature ASTM E139 specimen geometry was revised after first three creep test sessions, since failure were initiating from the 2.5 mm radius shoulder fillets. Therefore, subsequent specimen batches were modified to have a larger 3 mm radius shoulder fillet to reduce stress concentration of the region. The final design and the actual test piece is shown on Figure A.3.

Wire cutting was used to produce the accurate outline of the specimen shape, followed by manual 1200 grit sandpaper polish on all surfaces to remove any microstructural artifacts caused by the wire cutting procedure. Prior to the micropolishing of the EBSD target surface, all other sides were polished by 9µm diamond compound paste to remove any surface defects. Shoulder fillet regions were polished by an electric rotary hand-tool.

A pair of 100gf microhardness indents was used as markers to locate the same EBSD map area for each creep interruption stages. The markers were placed 0.6 mm from each specimen edges and aligned perpendicular to the tensile axis as illustrated on Figure A.5, such that when the two markers were positioned at the top corners of a SEM image, the resultant EBSD orientation map (corrected for image tilt and rotation) would have its vertical axis correspond with the specimen tensile axis. Furthermore, the microhardness indents were used to determine the depth of surface layer removed during the polishing process as discussed in Chapter 3.

A.3.4 Tensile load beam

A simple lever type loading mechanism was designed and built as a primary structure for the creep testing system. CAD design drawing and the actual constructed unit are shown on Figure A.10. Static weights are hung on the longer lever side, and are supported by an automotive jack to assist the raising and lowering of the weight. The lever beam applies a five-fold load magnification factor onto the specimen. This value was chosen purely for convenience, since it enables the applied stress ranges of 10~100 MPa by the use of preexisting lead discs that were previously used for other experiments at the research laboratory. All vertical tensile beams are connected with plain bearing tie-rods to achieve self-alignment, which in turn generates pure tensile loading of the specimen.

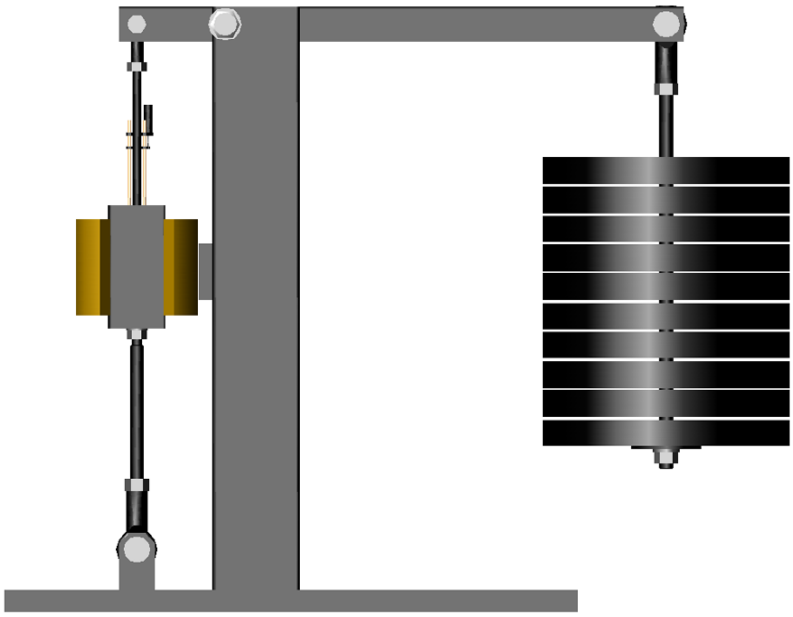

(a)

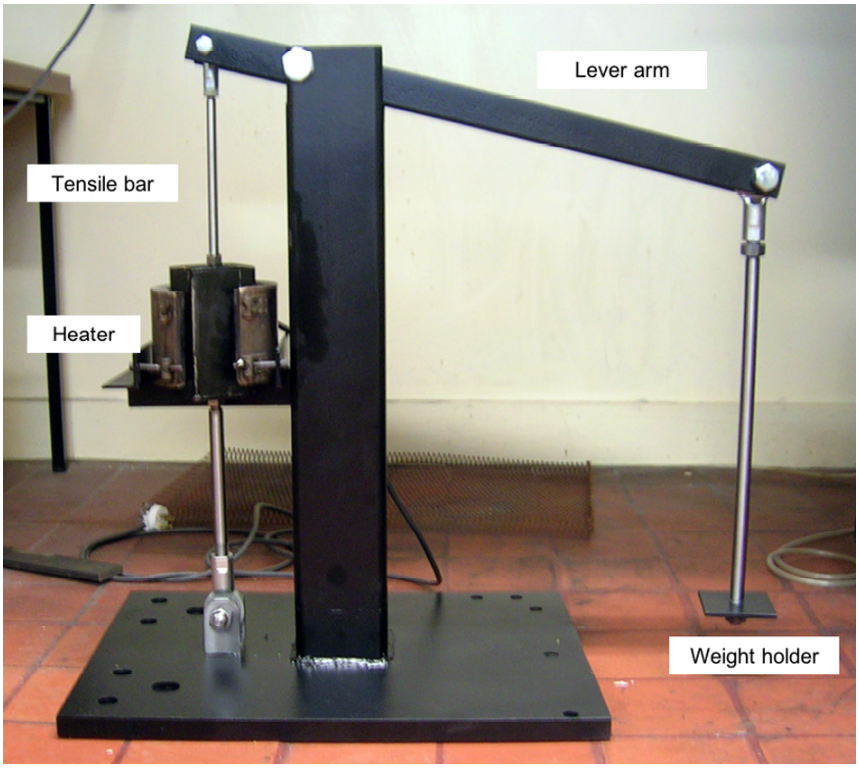

(b)

Figure A.10. Tensile load beam (a) CAD design and (b) constructed unit

A.3.5 Load linkage mechanism with heater and silicone bath

Vertical tensile load beam and the silicone bath were designed as an integrated system as illustrated on Figure A.11. The silicone bath was built from a mild steel square channel section of 3 mm thickness, with a welded plate steel bottom. The loading beam penetrates through the bottom of the bath and screws onto the lower specimen linkage system. High temperature resistant RTV (room-temperature vulcanizing) silicone seal was used to seal this interface against silicone oil leakage. The ceramic heater was wrapped around the silicone bath but was mounted on the central structural column instead of being part of the tensile load bearing components. This allows easy removal of the lower half of the tensile beam and the silicone bath as one integrated unit, without removal of the heater.

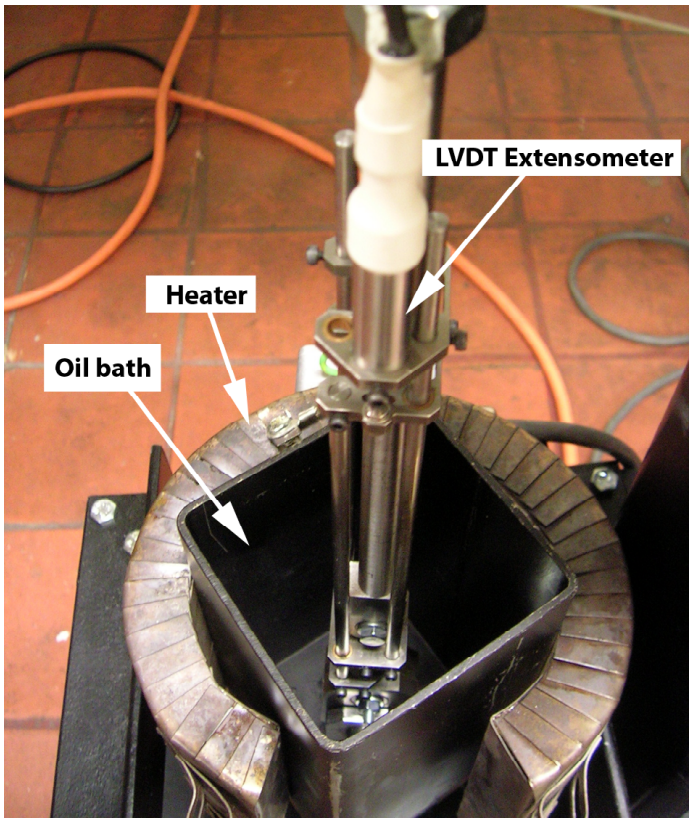

Figure A.11. Integrated loading and silicone bath

A.3.6 Extensometer

A limitation of the LVDT type extensometer is that the maximum operating temperature of the selected LVDT unit was 80ºC, compared to the maximum furnace operating temperature of 220 ºC. A conceptual design sketch of the extensometer system is shown on Figure A.12a. LVDT temperature is reduced by placing it above the furnace using extension beams with forced air cooling. With this design, the specimen at its gauge length must support the whole extensometer system, therefore the attachment must be secured against the specimen, instead of single sided blade attachment typically seen in commercial extensometers. In such a design, it is best to have the extensometer mass center close to loading axis to avoid any bending force to act on the specimen, as illustrated on Figure A.12b. Final outcome of the extensometer design is illustrated on Figure A.13 along with the actual production unit on Figure A.14.

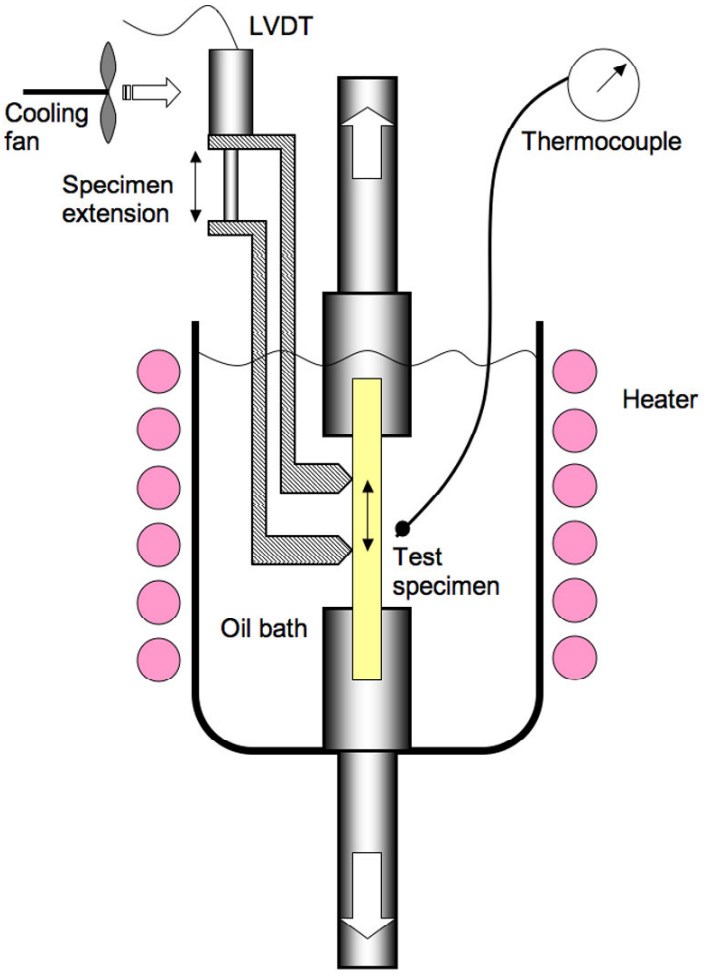
LVDT
Cooling fan
Specimen extension
Thermocouple
Heater
Test specimen
Oil bath

(a)

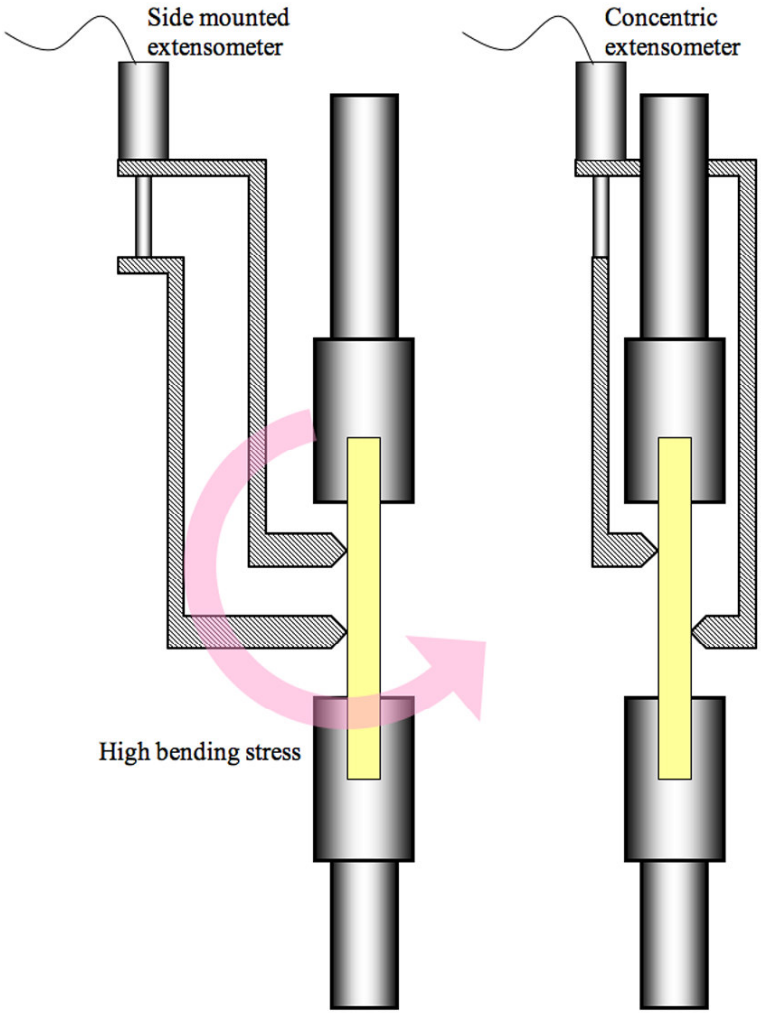

(b)

Figure A.12. Extensometer (a) design concept and (b) issue of bending stress

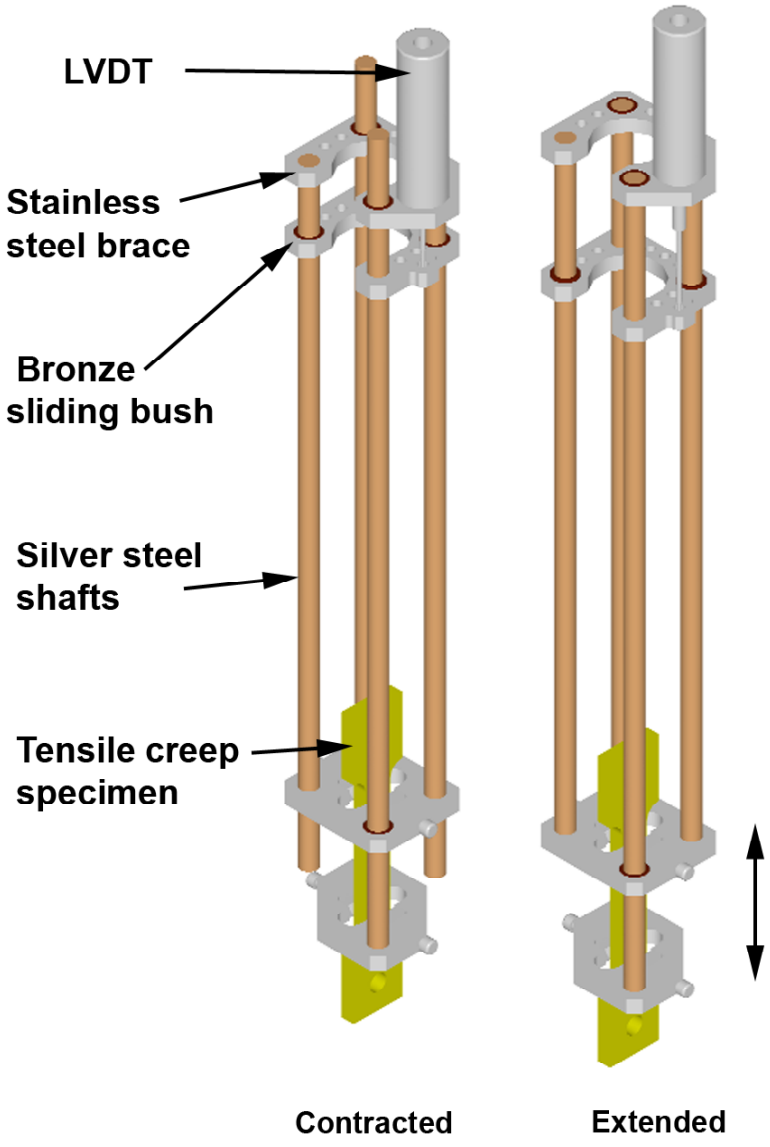

Figure A.13. Extensometer CAD design

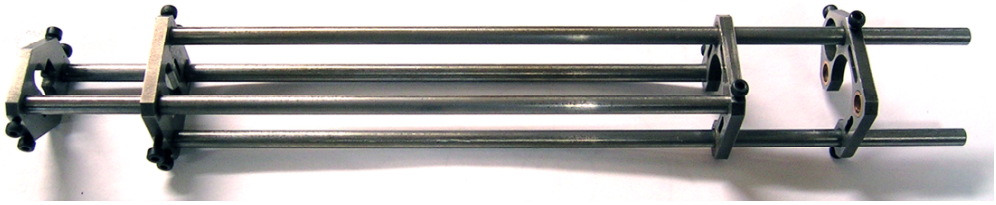

Figure A.14. Fabricated extensometer system

Material selection for the various components was purely based on thermal expansion and stability point of view, since the furnace temperature (up to 220 ºC) was well below the transformation temperatures for common steels. Particular focus was placed on the material selection for the beams and their sliding surfaces, since friction between the two translating members had to be minimized in order to avoid static friction hindering the specimen extension. The beams were selected to be made from BS1407 silver steel (1.0C, 0.3Si, 0.4Cr, 0.35Mn) since this tool steel achieves high thermal stability and hardness suitable for wear surfaces, and are commercially available in pre-machined high precision rods, thereby saving the cost of machining the friction surfaces that would have been required if rolled stainless steel were chosen instead. The beam braces were wire cut and machined from plate 410 stainless steel, and bronze bushes were chosen for the beam sliding surfaces.

A key design feature was the four concentric beams that are supported by four rigid stainless steel braces that allow the tensile load beam to be removed from one side. The overall tensile load beam and extensometer unit is illustrated on Figure A.15a. The overall unit length can be adjusted by the tie-rods at the ends of the upper and lower load beams, in order to adjust the load lever to be perfectly horizontal for a given specimen length. This design allows the load induced by the extensometer to be as central as possible, except for the LVDT itself that weighs 10 grams. The stainless steel braces have cutouts for further weight reduction, resulting in the overall weight of the extensometer system of 200 grams.

The specimen gripping mechanism utilizes a pair of blade edges that are screwed in with M2 cap screws, as illustrated on Figure A.15. The edges are tightened against the specimen surface with hand tightening force only until it is sufficient for the extensometer to not slip with its self-weight. The largest concern with this type of grip mechanism is the amount of

stress concentration induced by the marks created by the blade edges. Care was taken not to place the blade edges on the same location for each consecutive sequential creep/EBSD stage. Fortunately, these stress concentrations were found to only produce minor consequences, since all of the specimens tested during the course of this research program exhibited reasonable level of secondary creep stage and failed at regions other than the marks generated by these stress concentration regions.

One further design technique used in this extensometer was the management of close tolerances of the four beams and the linear friction surfaces. This was one of the critical flaws identified in similar systems used elsewhere, in which typically the sliding surfaces were deliberately made loose fit in order to accommodate the misalignment of the four parallel beams. In this extensometer design, the four beams were initially inserted in a relatively firm transitional fit against the bronze sliding bushes, and the non-sliding ends of the beams were press fit into the stainless steel braces and securely tightened further using M2 cap screws. Once this rigid structure was assembled, it was heated up to 250 ºC to remove and thermally induced stresses that may occur during the experiments. Following this heating procedure, a small amount of 3 µm diamond polishing compound paste was applied to the bronze sliding bushes and the sliding surfaces were worked by hand until the interface was sufficiently loosened by the diamond compound. The process was stopped once the lower half of the sliding pair was able to naturally slide with its own self weight without any sticking within the usable range of the LVDT.

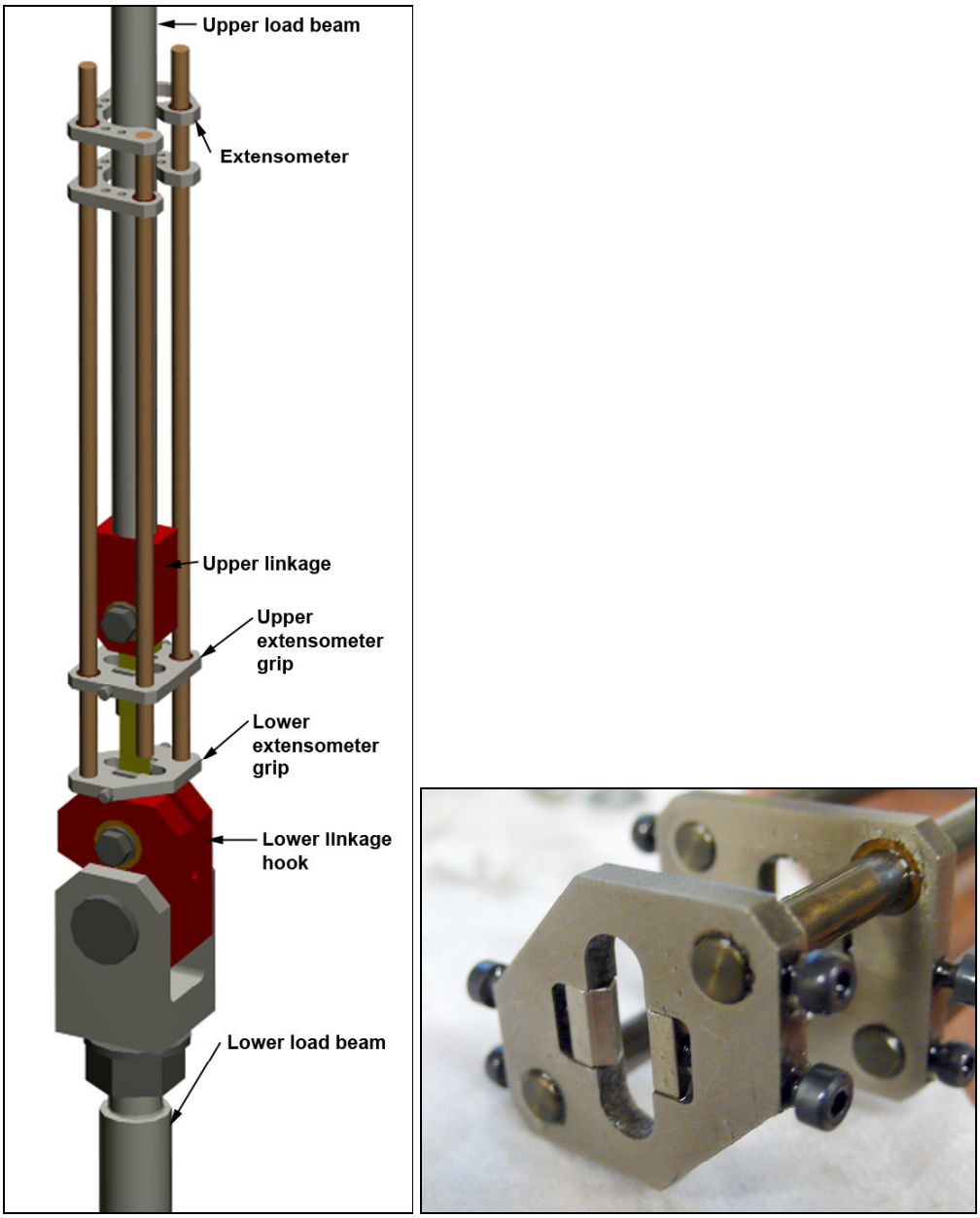

(a) (b)

Figure A.15. (a) Overall tensile beam and LVDT extensometer unit, and the (b) lower extensometer grip mechanism

A.3.7 Specimen exchange procedure

A specimen release system was designed so that the tensile test piece could be removed at each interruption stage without shock-loading the specimen or having to move or drain the hot silicone oil bath. The specimen exchange procedure is conducted as follows:

- The lower half of the tensile specimen is attached to the lower linkage hook with a grip that can be rotated in one axis as illustrated on Figure A.16a.

- The upper half of the tensile specimen is attached to the rigid upper load bearing beam with a similar rotating specimen grip, and this entire unit along with the extensometer is considered a single integrated unit, also illustrated on Figure A.16a.

- The extensometer and the tensile load beam is self-aligned by placing them horizontal against a flat surface, as illustrated on Figure A.16b. The two M2 cap screws are tightened to grip the extensometer on the specimen.

- The unit is lowered into the silicone bath and is hooked on to the aforementioned lower linkage pin fixed to the lower tensile beam at the bottom of the bath, as illustrated on Figure A.17.

- Once a secure lower link is established, the horizontal lever beam is lowered towards the upper tensile beam pivot point by a jack, and is connected by a bolt.

- By lowering the jack slowly, the tensile load can be applied gradually without significant shock to the specimen

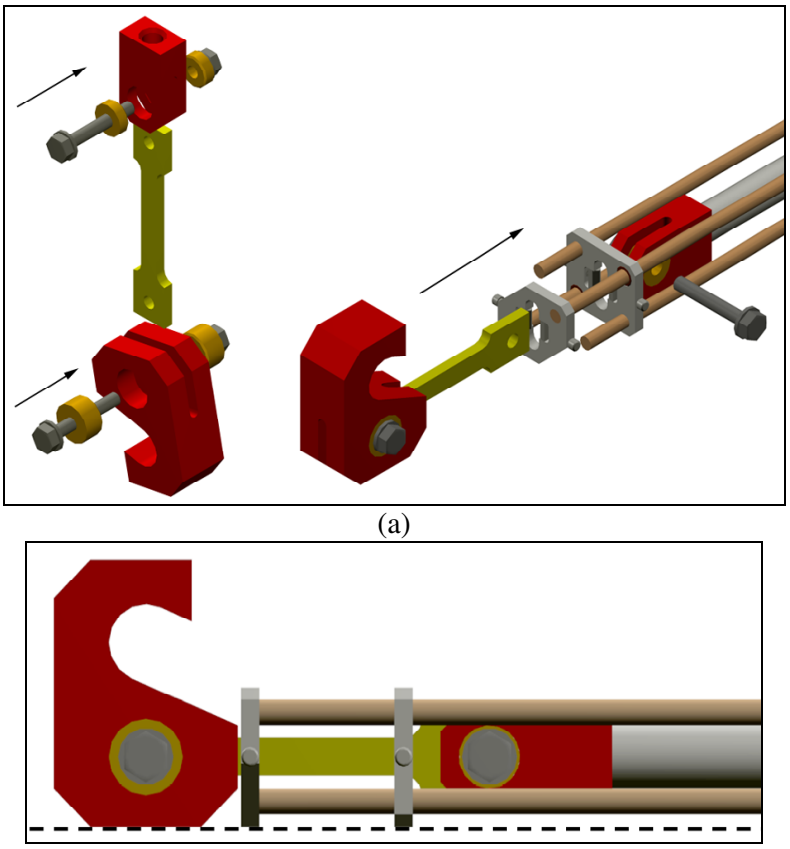

(a)

(b)

Figure A.16. (a) Specimen mounting procedure for the load beam and the LVDT, and (b) the self-alignment of the LVDT and load beam on a flat surface (dashed line)

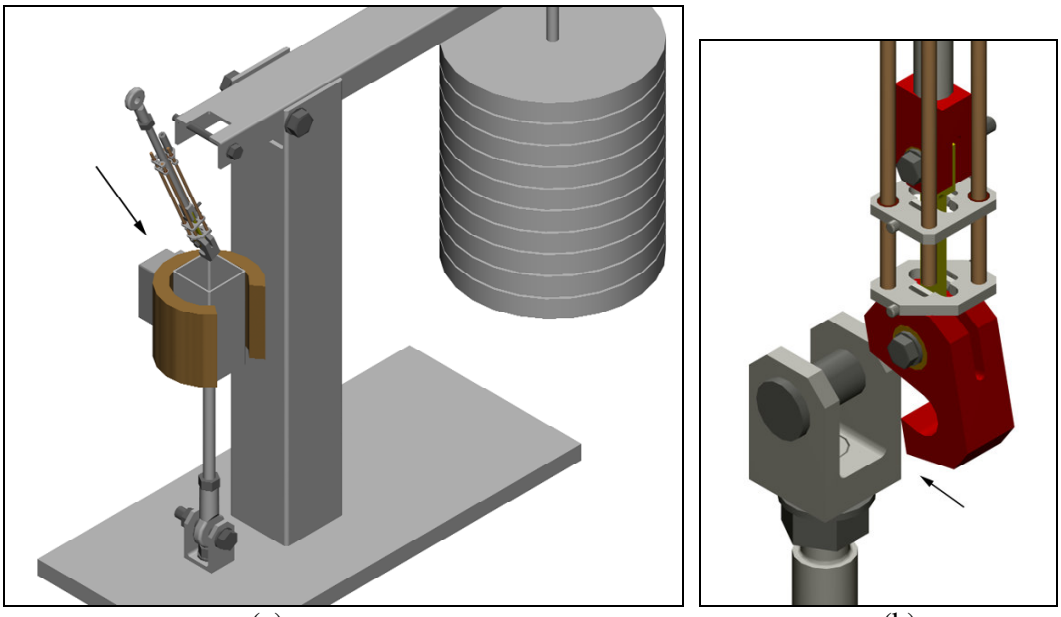

(a) (b)

Figure A.17. (a) Specimen linkage connection and loading procedures and (b) close-up of the lower linkage hook

The specimen removal process is conducted in reverse of the attaching process, except for one important difference. For the attachment process, the lower specimen linkage was secured to the tensile beam pin by the hook mechanism. However, the reverse of this process is difficult since the hook is now submerged in hot, viscous silicone oil. A design solution was introduced, in which the linkage pin is allowed to easily slide out to one side with the use of a long screwdriver, as illustrated on Figure A.18. The linkage section was designed such that the pin would slide out sufficiently to release the linkage hook, but will hit the silicone bath wall before the pin drops out of the linkage base. This design allows the entire top half of the load beam, specimen, and the extensometer to be removed quickly and smoothly as one complete unit whilst the lower load beam and the silicone bath can remain attached to the main structure.

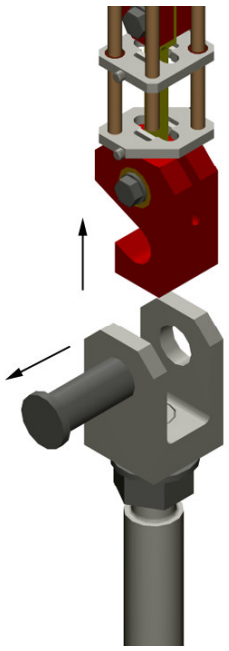

Figure A.18. Specimen removal process by sliding out the lower linkage pin

A.3.8 Conclusion

Several innovative design features were introduced to construct a creep test system that is particularly suitable for the proposed sequential creep/EBSD experiments. Some of the key features were:

- Integrated tensile load beam and silicone bath
- Hook and sliding pin attachment for the lower load beam
- LVDT extensometer with low bending load on the specimen and easy alignment

Emphasis was placed on the ease of specimen handling to minimize accidental shock loading or extensometer misalignment. These design features were made possible since the testing temperature was relatively low (< 220 ºC) hence the constraints placed on the choice of material and design was relaxed.

A.4 EVALUATION OF TEMPERATURE STABILITY AND RELIABILITY OF RESISTANCE HEATER AND IMMERSION OIL

A.4.1 Introduction

Based on the final design process discussed in the previous section, the heating and environmental control systems of the sequential creep/EBSD test system was decided to be as follows:

- Wrap-around type ceramic resistance furnace operating at up to 220 ºC
- Specimen immersion bath of DOT-5 silicone oil

Several evaluations were carried out to confirm the effectiveness of this system during the design stage of the creep test system.

A.4.2 Experimental procedure

DOT-5 silicone oil is a standardized formula for automotive brake fluids used in a small number of antique vehicles made prior to the 1970's. Small quantities of this silicone oil can be purchased from automotive supplies outlet for moderate cost (< US$80 /liter). To evaluate the variety of manufacturers available in the market, two products were selected for initial trials.

- Shell Advance DOT-5 (US$27/500ml)
- Spectro Golden American DOT-5 (US$25/300ml)

A steel bath with capacity of 300 ml was filled to 80% level with the oil and was heated to various temperatures to observe the behavior. The wrap-around type ceramic heater was controlled via digital PID controller with a feedback thermocouple located at the center of the oil bath. This steel bath is identical to the type used in the actual creep experiments, and the thermocouple location corresponds to the location of the specimen undergoing creep.

The PID controller was initially calibrated for the thermal capacity of the fluid bath prior to this experiment, in order to achieve a stable temperature without significant overshoot.

A.4.3 Results and discussion

A.4.3.1 Performance of the heating system

Both brands of silicone oils evaluated in this experiment showed no notable difference in their performance characteristics. At a constant holding temperature of 150ºC, the temperature fluctuation was measured for the period of 5 hours. Figure A.19 shows that there is no notable overshoot or fluctuation in the temperature, which is common in PID type temperature controllers when the furnace triggers on and off to adjust the temperature. The observed error in temperature was ± 2 ºC, which is sufficiently within the initial target of ± 5 ºC. These results clearly illustrate the effectiveness of silicone oil bath to provide sufficient thermal capacity to stabilize the temperature. The figure also shows that the time required to preheat the furnace to 150 ºC is approximately one hour.

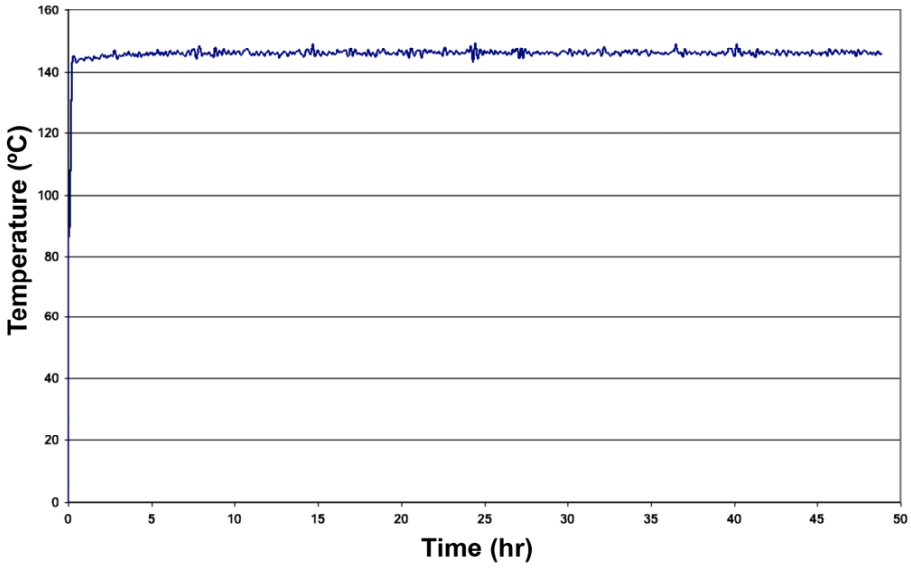

Figure A.19. Constant target temperature of 150ºC for 5 hours

A.4.3.2 Observations on the behavior of the silicone oil

Aside from the basic properties obtained from the main experiments conducted above, the DOT-5 silicone oils evaluated in this experiment exhibited four characteristic properties that needed to be taken into consideration for their use in creep experiments. These characteristics are discussed in detail below.

- Maximum temperature threshold
- Safety dye
- Solidification problem

A.4.3.3 Maximum temperature threshold

A simple test was conducted in order to evaluate the maximum temperature the silicone oil can endure, and to observe its behavior towards this critical temperature.

The oil was stable to the temperature of up to 240 ºC, but beyond this, strong toxic fume was emitted from the oil and part of the oil congealed into rubbery texture. Therefore, by taking into account the initial temperature overshoot that may potentially be caused by the PID temperature controller, the upper limit of creep experiment temperature was decided to be 220 ªC.

A.4.3.4 Removal of safety color dye

Due to the specifications enforced under the DOT-5 standard, the silicone oil was intentionally colored by purple dye to assist the visual identification of the liquid. This dye may stain the test piece surface microstructure or potentially chemically react with the metal at elevated temperatures. In order to avoid such concerns, the silicone oil was heated for approximately 10 hours at 200 ºC prior to the creep experiments. By performing this

preheating process, the impregnated purple dye was evaporated out of the solution along with any absorbed moisture, leaving the silicone oil colorless and transparent. The difference in appearance of the oil prior to and after the heating process is shown on Figure A.20.

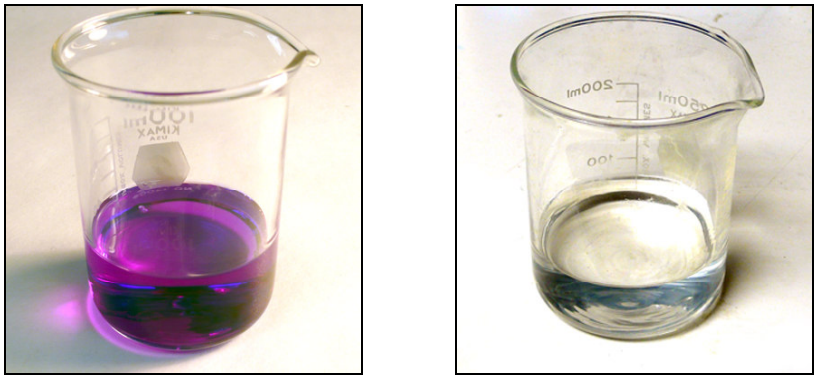

(a) (b)

Figure A.20. Appearance of silicone oil (a) as received and (b) after heating

A.4.3.5 Solidification problem

A serious problem on the use of DOT-5 silicone oil was identified sometime after the commencement of main creep experiments on the magnesium specimens. When creep tests are conducted at temperatures near 200 ºC, silicone oil becomes of viscosity similar to that of water. However, in rare occasions after prolonged thermal exposure, the oil suddenly solidified into clear, hard rubber-like texture without any prior indication, fully solidifying within a short period of approximately 2 hours. To suggest that this was not a random occurrence, this incidence occurred three times during the course of the research, all at exposure of up to 200 ºC, and in all cases solidifying after approximately 400 hours of usage. This solidified silicone is shown on Figure A.21.

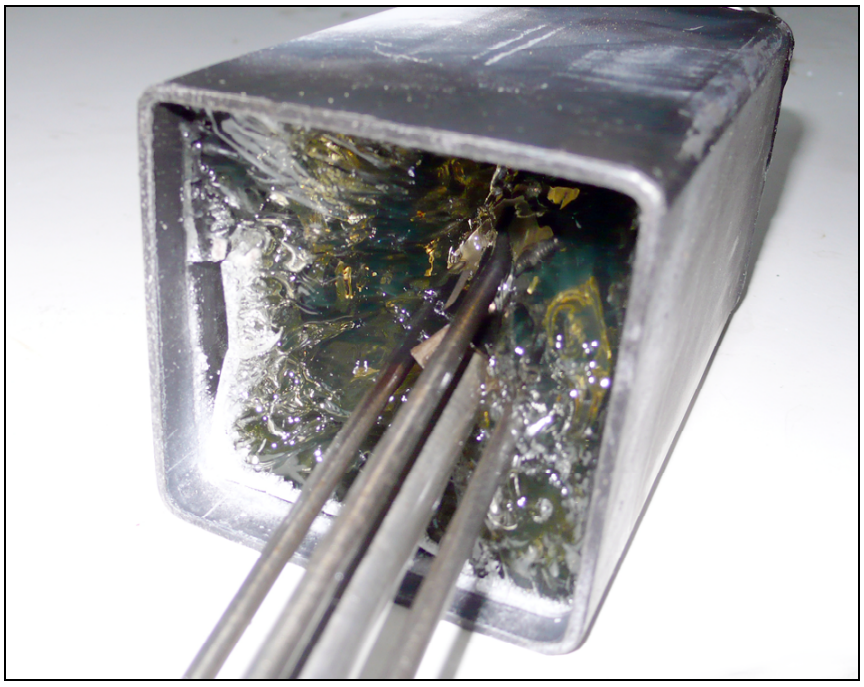

(a)

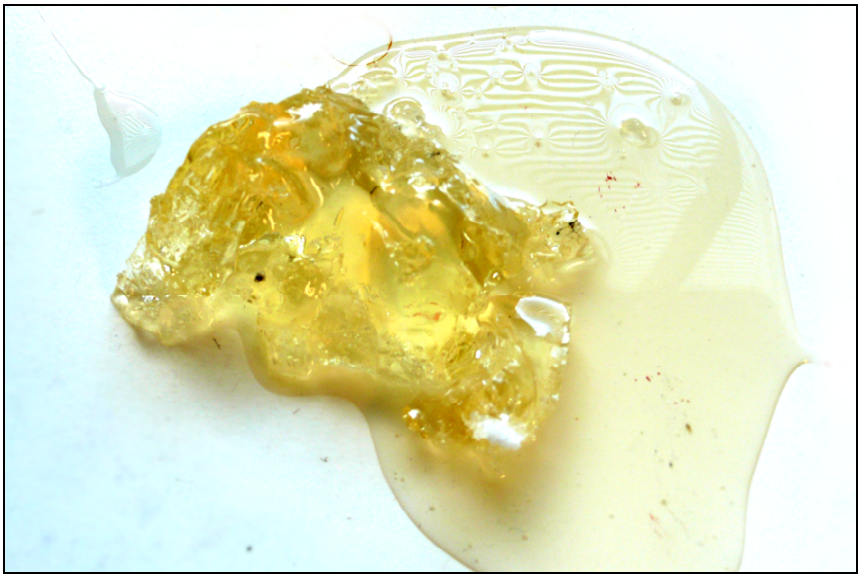

(b)

Figure A.21. (a) Viscosity of the solidified silicone oil and (b) comparison between solid and liquid silicone oil

A.5 CALIBRATION OF THE LVDT EXTENSOMETER

A.5.1 Introduction

LVDT is a simple, robust yet effective instrument to perform accurate measurements of small linear displacements such as in the current experiments dealing with tensile creep deformation of a magnesium alloy specimen. Specifications of the LVDT selected for the creep experiments (Solartron SM3) are summarized in Table A.4. The basic geometry is a non-contact case and rod without any stroke-end stops, as shown in Figure A.22.

Table A.4. LVDT extensometer specification

Model	Solartron SM3 miniature LVDT
Calibration stroke	± 3 mm
Nonlinearity	0.3%
Energizing voltage	1 ~ 10 V rms @ 1 ~ 20 kHz
Operating temperature range	-40 ~ 85 ªC (0.005%/ºC)
Material	440 stainless steel (case), titanium (rod)
Price	SM3 US$260 + Demodulator US$620

Figure A.22. Solartron SM3 miniature LVDT

The output of the LVDT is obtained through a custom-built demodulator unit from the LVDT energizing (AC) voltage as a proportion of the demodulated (DC) voltage, which in the current setup is ±5V. Therefore, the output reads +5V and -5V at each extreme of 3mm linear stroke of the LVDT. One of the problems with the LVDT is that the nonlinearity in

the output voltage worsens as the LVDT reaches towards its stroke limits. In this research, LVDT was calibrated by using a micrometer to generate a series of known displacements as illustrated on Figure A.23.

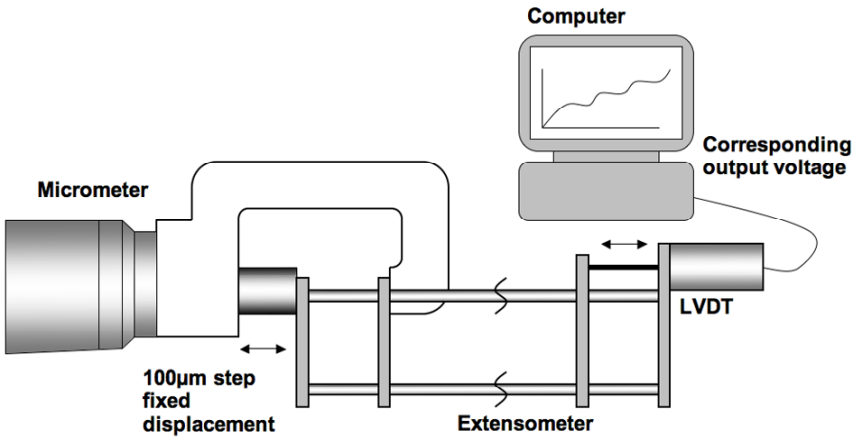

Figure A.23. Arrangement of the LVDT calibration

A.5.2 Results

A.5.2.1 Raw data resolution

Figure A.24 shows the LVDT output voltage as the micrometer was translated at 100 µm increments. The thickness of the output voltage graph indicates the amount of inherent noise present in the LVDT signal path, and this corresponds to the smallest amount of displacement that this LVDT can measure. With the raw LVDT output signal, this linear resolution limit was approximately ± 5 µm. This signal noise band is illustrated on Figure A.24 (b) at a higher magnification.

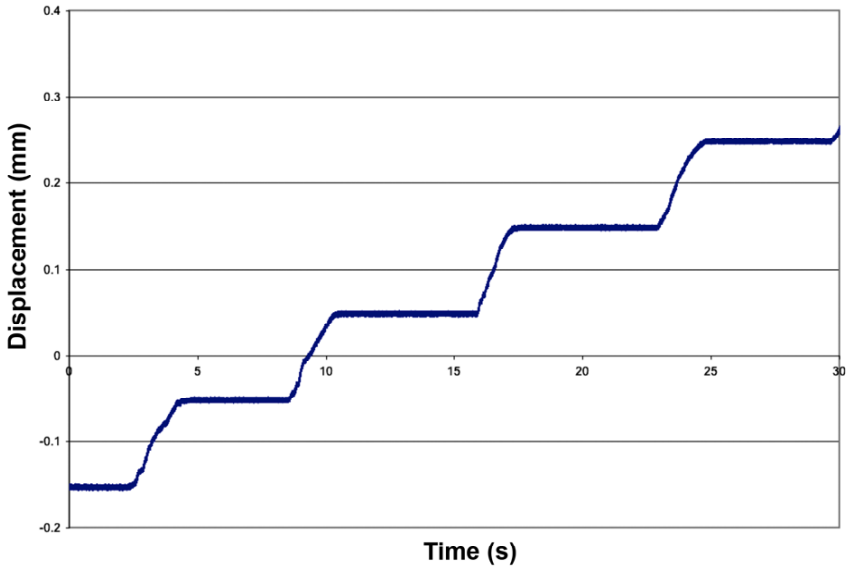

(a)

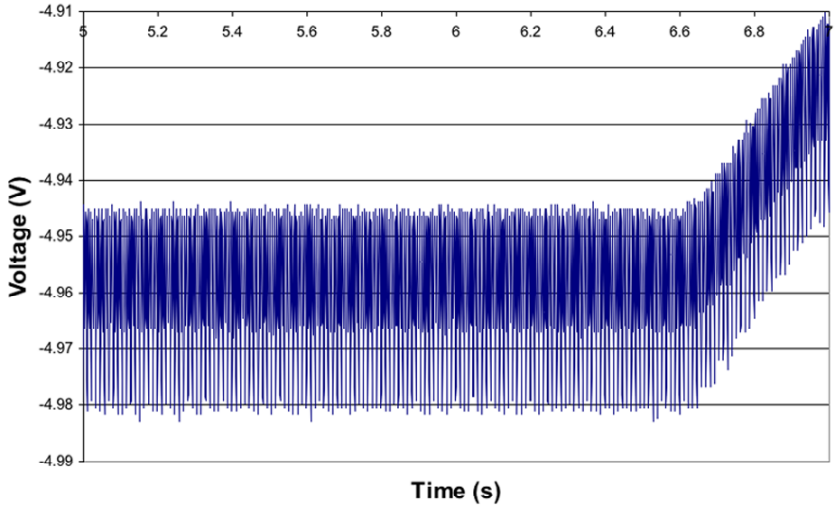

(b)

Figure A.24. (a) LVDT output voltages at every 100 µm steps, and (b) higher magnification graph of the LVDT signal noise band

The relationship between the displacement and output voltage was evaluated close to the centre (0V), and at the extremes (±4.5~5V) of the stroke range. The results are as follows:

- 4.5 ~ 5V: 1.35V/mm
- -0.5 ~ +0.5V: 1.39 V/mm

This indicates the nonlinear nature of the LVDT output vs. displacement. Furthermore, one observation made during the experiment was that the level of noise on the signal worsens as the LVDT approaches the stroke limits. This is because the signal amplitude is higher at the stroke limits (±5V), and the noise is proportionally higher. The difference between signal noises at stroke centre (0V) compared to at the extremes (5V) is illustrated on Figure A.25. The level of signal noise equates to ± 4 μm at best (0V) and ± 16 μm at its worst (5V) position. Since all of the creep test specimens exhibited no more than 1 mm displacement during the tests, these issues could be avoided as long as the creep test was always started at the LVDT stroke center.

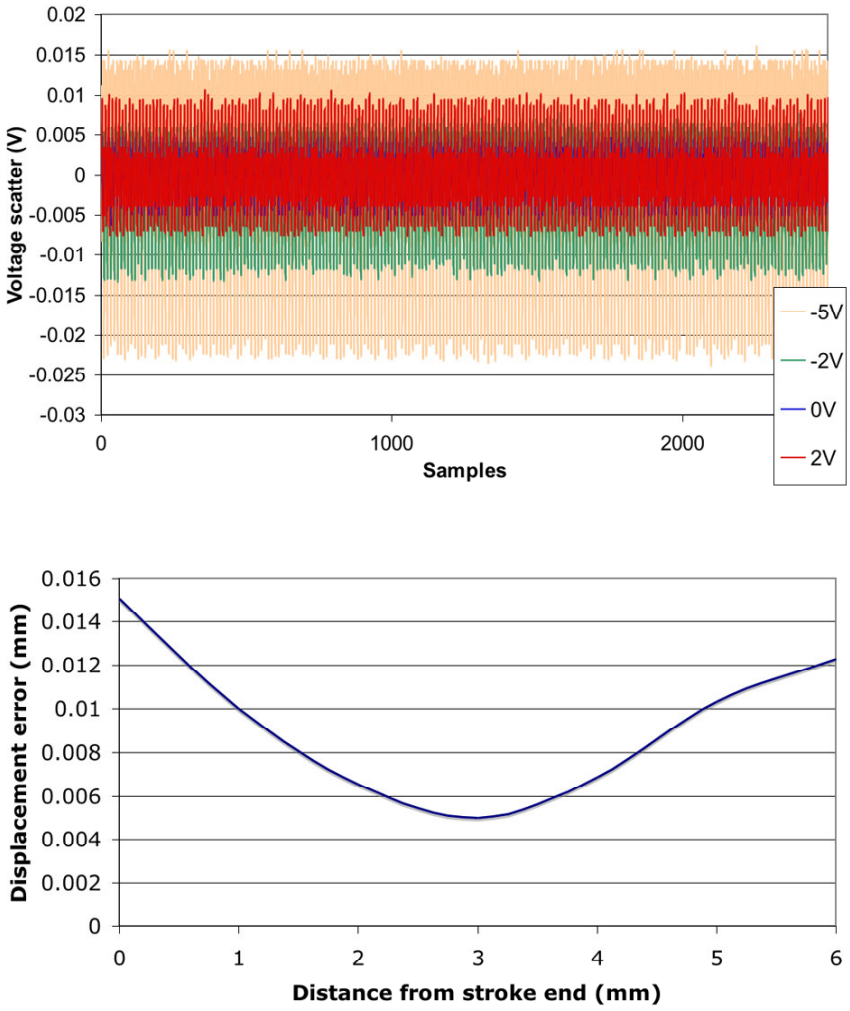

Figure A.25. Difference in signal noise at various stroke positions

A.5.2.2 Improved resolution through data processing

Although the linear resolution of ± 4 µm was sufficient for the current research objectives as stated in the initial proposal, it was still possible to obtain further improvements in the displacement resolution by performing a software filtering process. This process involves oversampling the raw data acquisition rate from 1 Hz (1 data point per second), to 100 Hz (100 data per second) whereby this dataset is averaged for every 100 data points, thus effectively reducing the dataset back to 1 Hz but at a much higher linear resolution compared to the raw 1 Hz data. This technique was made feasible because the signal error observed in the raw dataset exhibits a clear limit in its fluctuation amplitude, and therefore can be treated as a broad "band" of signal with a stable mean signal level.

It must also be noted that although data averaging was performed, it does in no way reduce the sensitivity of the data, since no averaging was performed beyond the original intended data acquisition rate of 1 Hz. Although this process increases the computer process overhead one hundredfold, it has the effect of minimizing the contribution of signal noise errors of the individual 1 Hz data points so that the linear resolution was improved to approximately 1 µm. The outcome of this filtering process on the data from Figure A.24a is shown on Figure A.26.

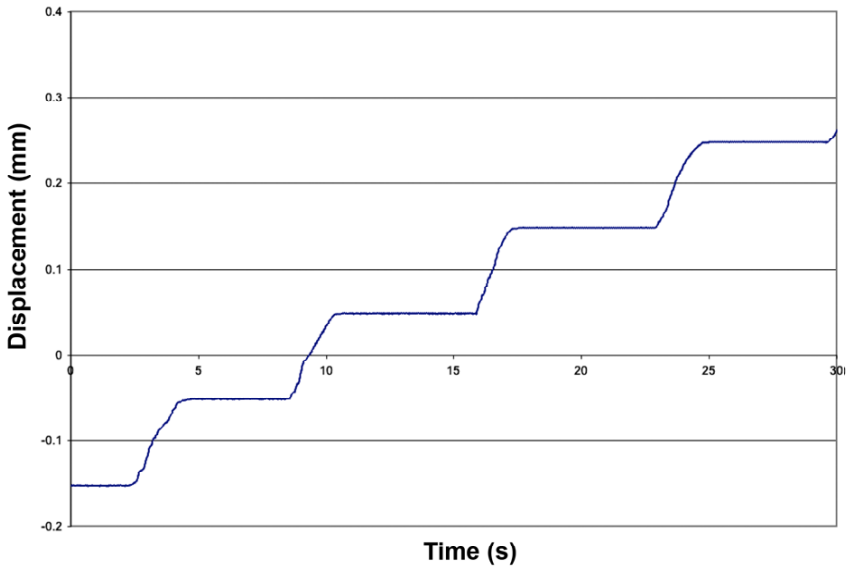

Figure A.26. Improved LVDT signal resolution after the post-processing filter

A.5.3 Conclusion

The LVDT nonlinearity and minimum resolution was evaluated prior to conducting the proposed creep experiments. The results indicated that a linear relationship of 1.35V/mm could be applied as long as the measurement is taken near the stroke centre (0V) and the amount of specimen deformation is sufficiently small compared to the LVDT stroke limits of 5V (± 3 mm). This linearity assumption was maintained in every creep experiments conducted in this research program, since the LVDT was never used beyond ± 1.5V. Along with the nonlinearity, the signal error band also worsened towards the LVDT stroke limits, ranging from ± 4 ~16 µm. This signal error was reduced to below 1 µm by applying 100-fold signal oversampling and averaging filter.

A.6 LVDT ELECTROMAGNETIC NOISE INTERFERENCE

A.6.1 Appearance of the signal noise

In early attempts to calibrate the LVDT and data acquisition software for creep tests, some of the acquired data illustrated unexpected data spikes. An example of these data spikes is shown on Figure A.27.

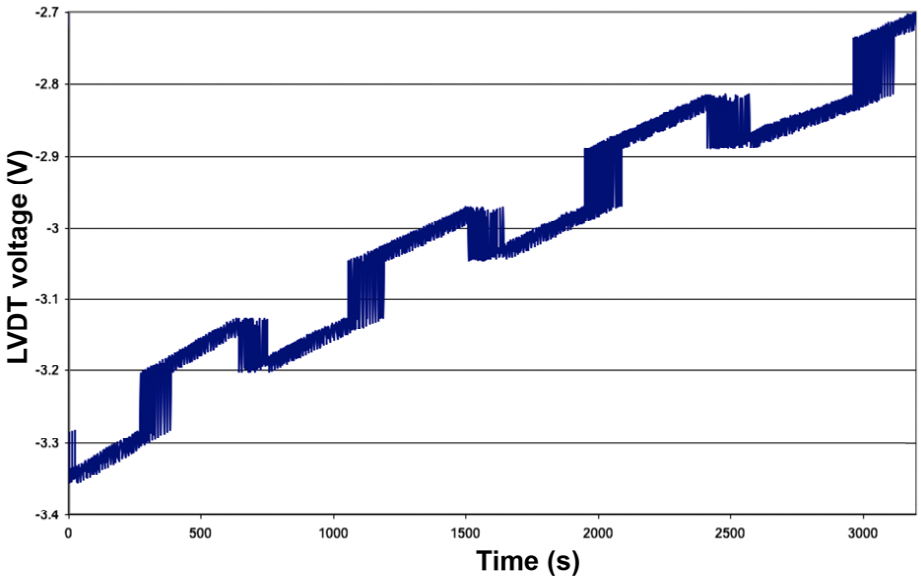

Figure A.27. Creep deformation graph with periodic noise

A.6.2 Identification and solution

When some erroneous data is observed during a creep test, it is typically caused by a physical slip of the extensometer from the specimen, which occurs when the extensometer grips are not wedged into the specimen with sufficient force. This generally shows a large jump in the acquired data as shown on Figure A.28.

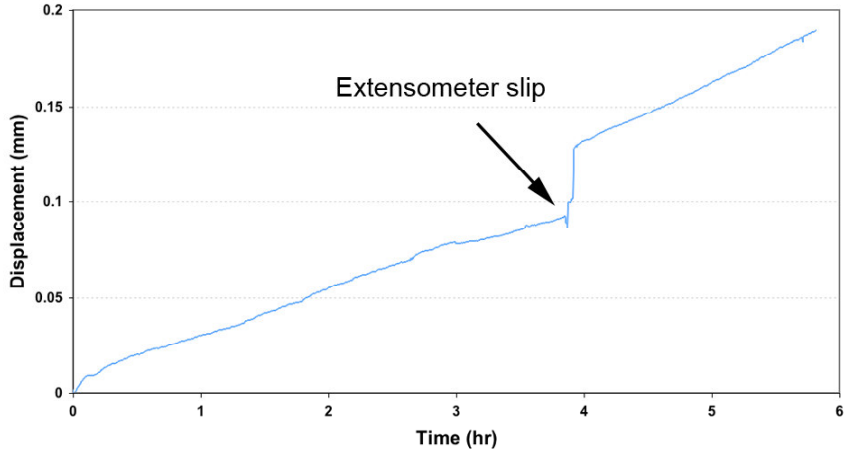

Figure A.28. A LVDT error caused by extensometer slip

However, in the case of Figure A.27, the sudden jumps in the data do not appear to be extensometer slip. Firstly, the graph shows the data jumps taking place in more than one occasion, in some form of periodic intervals, in which the jumps are always of the same magnitude. This is unlikely to occur on a mechanical slip condition. Secondly, after the first data jump, it is followed by a symmetrical backward data jump. This is also very unlikely in a mechanical slip situation, since this suggests the specimen to "contract" during the tensile creep test. In fact, such periodic, symmetrical data errors are typically associated with errors in the digital domain, rather than physical mechanical errors. If the error was in the analog domain (i.e. LVDT excitation voltage) then the error will not appear as discrete jumps, but rather more chaotic noise (such as a badly tuned radio). On

the other hand, errors in the digital data can take place as bit reversals where certain digits that is supposed to show "1" becomes misrepresented as "0" due to some external influence, resulting in particular digits to jump by a fixed amount. This agrees well with what has been observed so far.

Upon further evaluation and experimentation with the wiring and arrangement of the LVDT data acquisition components, the cause of the data jump was identified as electromagnetic interference on the LVDT demodulator IC chip by the data acquisition computer positioned nearby.

When the demodulator box was moved close to the signal-USB converter unit, the data jump occurred instantly, whereas when the demodulator box was placed far away, the jump did not occur even after 6 hours of data acquisition. The solution was to keep all the critical electronic devices as far away as possible, but as an extra precaution, the demodulator unit was placed inside a steel shielding cage for the subsequent creep tests as shown on Figure A.29.

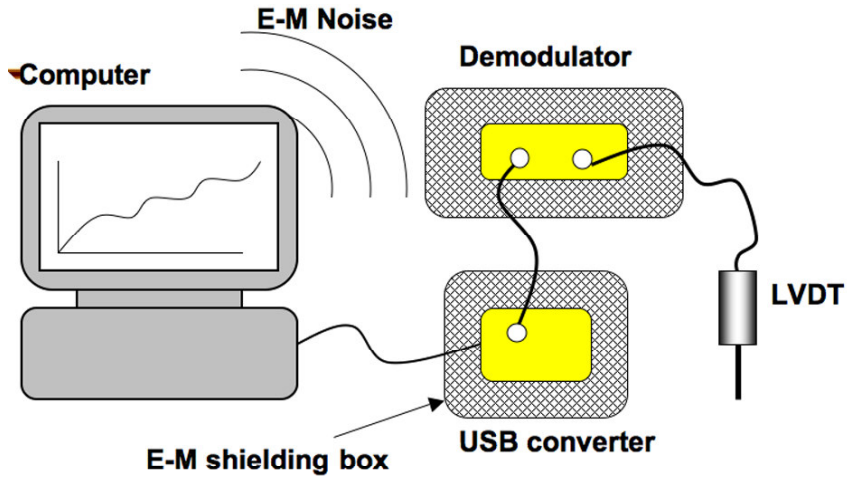

Figure A.29. Arrangement of the LVDT system components to prevent EM interference

As a supplementary note, if there were any incidences of EM interference errors taking place during the critical experiments, it was fairly simple to correct this error and reconstruct the original extensometer data, provided that the data spikes did not exceed the measurable range of the data acquisition software. This is because the digital error caused by the electromagnetic interference always raises the data by a fixed magnitude and eventually return the signal by the same magnitude, therefore it is easy to select that particular range of erroneous data and subtract the raised magnitude from the LVDT output data. This is possible because the error has in no way altered the real LVDT data other than the simple constant addition to the data in the digital domain.

A.6.3 Conclusion

The cause of unexpected errors in the LVDT signals was due to the electromagnetic (EM) interference of electronic devices affecting the LVDT demodulator IC chip. This issue did not cause a significant compromise in the research progress, since the improved shielding of the relevant devices could eliminate the EM interference, and a technique to reconstruct the erroneous data was established.

A.7 LVDT STATIC DRIFT OVER A LONG DATA ACQUISITION PERIOD

A.7.1 Introduction

One of the technical obstacles in performing tensile creep tests of long duration (e.g. over 24 hours) is the stability of measurement equipment used to record the specimen strain during creep. It is impossible to measure the creep strain of a specimen over the duration of the test if the data acquisition instrument itself carries a large amount of drift error in the measurement.

It is technically difficult to design a strain measuring device that does not carry any inherent measurement errors at high precision (e.g. < 1 μm) for extended period of time, since even a theoretically perfect strain gauge can be affected by variety of external environmental factors such as vibration, humidity and temperature.

Some of the major contributions to this drift error are the changes in ambient atmospheric temperature and humidity over the duration of the creep test, since the test may be carried out throughout one 24 hour day cycle, that will have its natural change in environment from night to day. Therefore it is ideal to carry out the creep experiments in a controlled, insulated atmosphere that can minimize these changes. However, due to the large size of the creep testing facility, it was not possible to accommodate such solutions within the available time and budget restrictions. To evaluate such effects of temperature changes throughout a hypothetical creep experiment, the LVDT strain gauge system was exposed to the atmosphere for 20 hours whilst recording the strain data in a static environment.

A.7.2 Experimental procedure

The LVDT strain gauge and its full set of electronic systems were placed in an open room to carry out the subsequent creep experiments. The room was not equipped with air conditioning and is exposed to incoming sunlight from the windows. The LVDT strain gauge was placed on a workbench and the data acquisition software was engaged to record the displacement data for the period of 20 hours. The duration of 20 hours was chosen for convenience because this generates a displacement data of approximately 100 MB, which was deemed to be sufficient to evaluate whether static drift in fact takes place. After the test was completed, the acquired LVDT output voltage data was converted to displacement data using the standard 1.39V/mm conversion factor. The result was plotted on a conventional time vs. displacement graph.

A.7.3 Results and discussion

The result from the static drift experiment is shown on Figure A.30. The graph shows that the LVDT does in fact carry some form of inherent displacement measurement drift, even in a static environment.

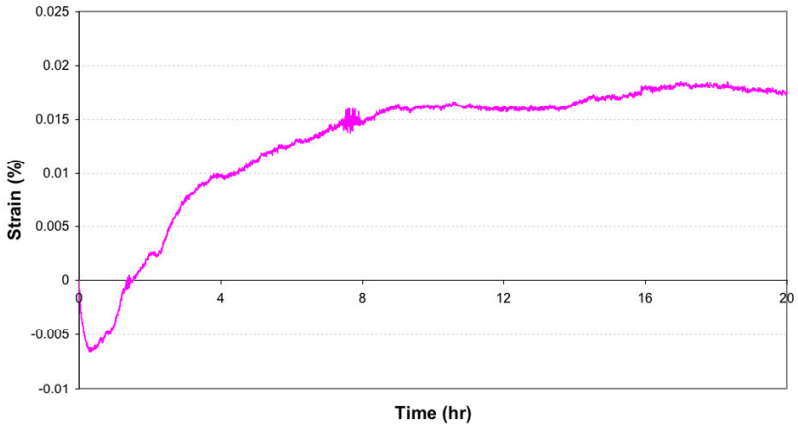

Figure A.30. Static LVDT data acquisition for 20 hours

Upon closer inspection, majority of displacement drift occurred approximately in the first 6 hours of the test, whereas the remaining 14 hours showed very little changes in the displacement measurement. The amount of drift in the initial 6 hours was evaluated to be approximately 3 µm, which although is not large compared to the intended range of deformation carried out in the actual creep tests (up to few mm), it is nonetheless too significant to be ignored. On the other hand, the level of drift after the initial 6 hours fits within a range of 1 µm, and therefore can be considered nonexistent within the requirements of the current research project.

Upon further investigation and tests, the underlying cause of this static drift was identified as the heating up of the LVDT demodulation IC chipset that converts the LVDT AC signal to the DC signal recognized by the computer. This IC circuit is shown on Figure A.31.

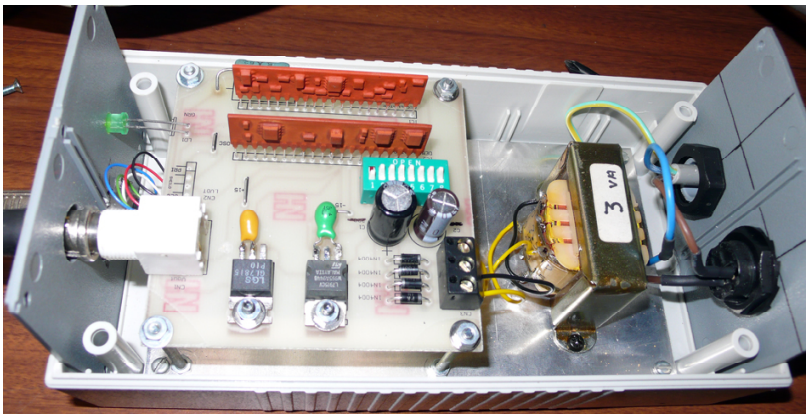

Figure A.31. The demodulator IC chip that was found to be the cause of thermal drift

It appears that when the LVDT system is initially switched on and data acquisition commenced, the chipset heats up due to heavy processing loads, and until this stabilized to the IC's equilibrium operating temperature, the LVDT demodulator produces unstable output dataset to the computer. Once the normal operating temperature was reached, the LVDT demodulator chip no longer appeared to be influenced by any changes in the

ambient temperature, since the subsequent 14 hours of the experiment did not record any significant changes in the displacement readout.

Assuming that the initial "preheating" stage of the LVDT demodulator is 6 hours, there are several proposed methods to overcome this drift error issue. It must be noted at this stage that the actual drift error is up to 3 μm, therefore it does not cause any significant contribution to the actual creep test data in most cases. However, it is important to eliminate every known recognized sources of error.

One of the potential solutions is to enclose the LVDT demodulator chipset in a thermally conductive casing with an appropriate heat sink to regulate the chipset temperature. Alternatively, forced fan cooling can be carried out, or the operation voltage may be lowered to regulate the heating, although this may compromise the overall resolution.

Instead of pursuing any of the above methods, decision was made that the best possible solution to this issue is to leave the LVDT demodulator chipset always in operation, or for at least 6 hours prior to the experiment, so that the optimal operation temperature is already reached and the drift is minimized during the actual creep test.

A.7.4 Conclusion

The major contribution to the static drift in LVDT extensometer data was due to the errors induced by thermal fluctuations of the demodulator IC chip. By allowing sufficient preheating to minimize this, the overall drift in the extensometer data was evaluated to be less than 1 μm, which is sufficiently low for the current experimental objective.

Chapter References

1. Zhu, S. M., Mordike, B. L., et al., Magnesium Technology 2005, 2005, 429

APPENDIX B - METHODOLOGY FOR EBSD ANALYSIS AND MAPPING

B.1 INTRODUCTION

Electron backscatter diffraction (EBSD) is a modern analysis technique that has become popular in the last decade. The basic operation of a typical EBSD system is illustrated on Figure B.1. The EBSD detector acquires electron backscatter diffraction pattern (EBSP) from a spot on the sample surface. These patterns are unique to the target material's atomic arrangement (Figure B.1b). The EBSD analysis system can process the acquired EBSP through an automated pattern-matching algorithm to relate the acquired pattern against known structures to identify the phase (Figure B.1c) and the crystallographic orientation of the target material.

The fundamental concepts and academic interests in EBSD have existed since the 1980's, but only in the late 1990's has the technology and technique become readily available to wider non-specialized research applications, as part of supplementary analysis tool in the suite of SEM studies of crystalline materials. This was primarily due to the development of accurate and reliable detectors that can be retrofit onto conventional SEMs, and the availability of commercial analysis software packages that enables the analysis of crystallographic parameters without requiring extensive knowledge or effort in the calculation of the underlying vector matrices.

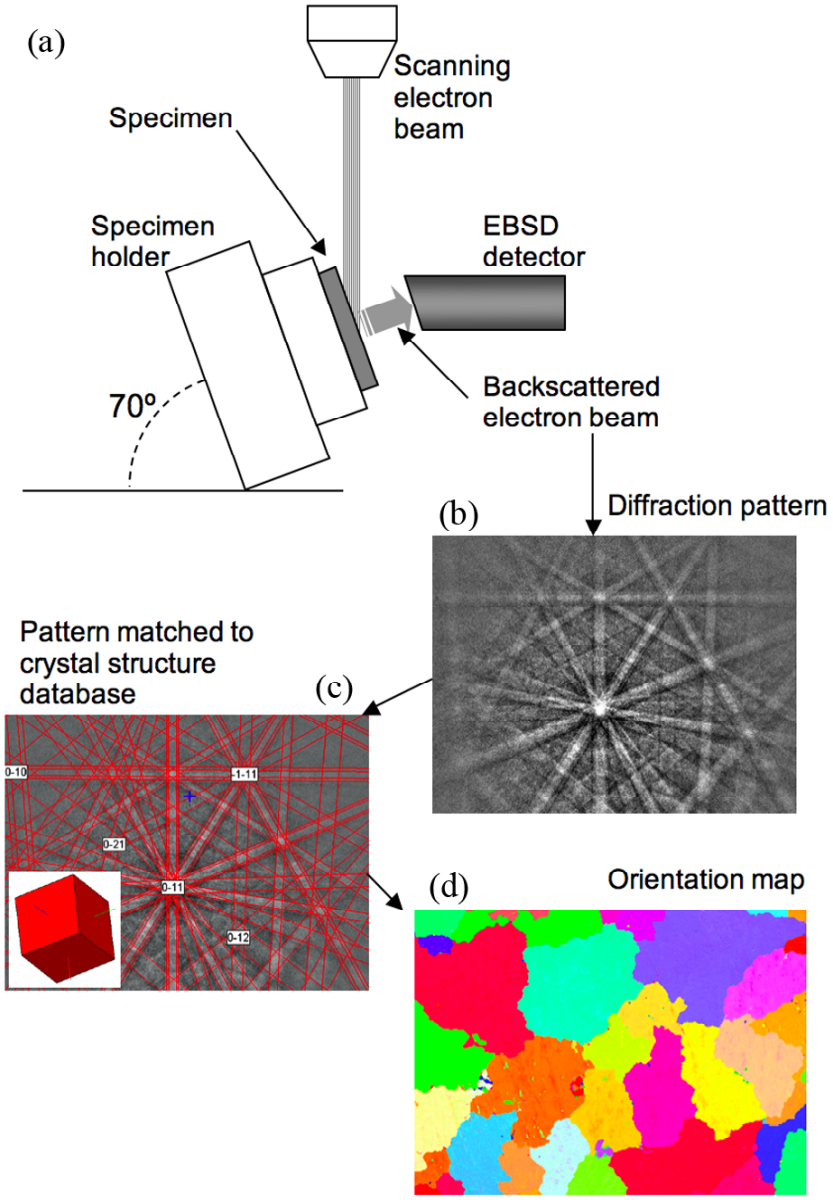

Figure B.1. Schematic illustration of a typical EBSD system, (b) an EBSP, (c) pattern matching process, and (d) automated orientation map

This section provides a brief discussion of the EBSD analysis techniques and methodology used in this research. At the start of this research program in 2002, there was little or no documentation available in the use of EBSD for the study of light alloys such as aluminum or magnesium. This was because although it was known to be feasible to obtain satisfactory EBSD patterns from light alloy specimens, its potentials in specific research objectives were only just starting to become realized. However, during the course of this research, various publications begun emerging from other research institutes with the use of EBSD for such applications.

Unfortunately, at the time of writing, there is still a large knowledge gap between research publications that specializes in advanced applications of EBSD for crystallographic studies [1, 2, 3, 4, 5, 6] compared to more primitive use of EBSD for phase/texture visualization, which seems to suggest that the general industrial level material studies have yet to fully utilize the benefits of EBSD, and its capabilities is still only appreciated in purely academic studies by a select number of experts in the field of crystallography.

Although it may now appear redundant to discuss the basic operational techniques of EBSD due to the recent widespread popularity in its use, it would nonetheless be a valuable aid for the future researches in the study of magnesium alloys in particular.

B.2 BASIC OPERATIONS OF THE EBSD SYSTEM

For this research, EBSD studies were carried out on JEOL 6100 SEM with HKL Nordlys 2 EBSD detector and HKL Channel 5 software package. SEM was operated at 20kV and the specimen surface was tilted 70º against the incident electron beam, with image rotation corrected to have 0º rotational relationship with the specimen orientation along the x-y coordinates.

B.2.1 Specimen preparation

In this research, two types of specimen shapes were studied under the EBSD. Standard microscopy specimens mounted in cylindrical resin were used during the initial stages of the research, whereas the later stages of the research required the analysis of miniature tensile test specimens. In either case the specimen was mounted in a special SEM holder to obtain a certain height from the SEM workbench calibrated for correct EBSD working distance. Examples of such specimen holders are shown on Figure B.2.

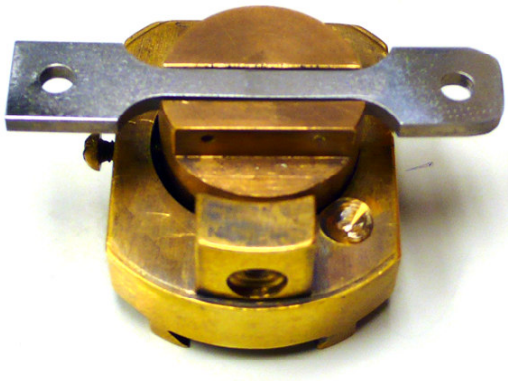

Figure B.2. SEM specimen holders used for the EBSD analysis

The most immediate operational precaution of the EBSD analysis is that the physical distance between the specimen surface and the phosphor screen of the EBSD detector is very close (few mm), therefore extreme care was required when positioning the specimen at the correct working distance. The SEM workbench is a motorized turret that can translate in x-y plane axis and also provide rotation of the specimen. Special attention must be paid to the rotation axis, since if the area of interest on the specimen is not located at the absolute centre of rotation axis, any specimen rotation will result in a proportional change in specimen distance against the EBSD detector screen. Therefore, the specimen had to be placed in the SEM specimen holder in such a way to have the area of interest coincide with the initialized central coordinate of the SEM workbench. This was especially important for irregular specimen shapes such as the rectangular tensile specimen used in this research.

Although the specimen height could easily be corrected by adjusting the specimen holder, the angle of tilt against the horizontal plane causes problems that are more difficult to manage. The EBSD relies on detecting the backscattered beam diffracted at a fixed angle from the incident electron beam as shown on Figure B.3.Therefore even a small error (< 1º) in the tilt of the specimen surface results in a change in diffraction angle and the detector would no longer intercept the backscattered beam. For this reason, etching was especially forbidden on the EBSD specimens since the surface roughening and grain boundary rounding due to the etching creates random scatter of the backscattered beam, resulting in weakening of the EBSP. The etching process also creates a thin chemically altered film layer on the surface further diffusing the EBSP.

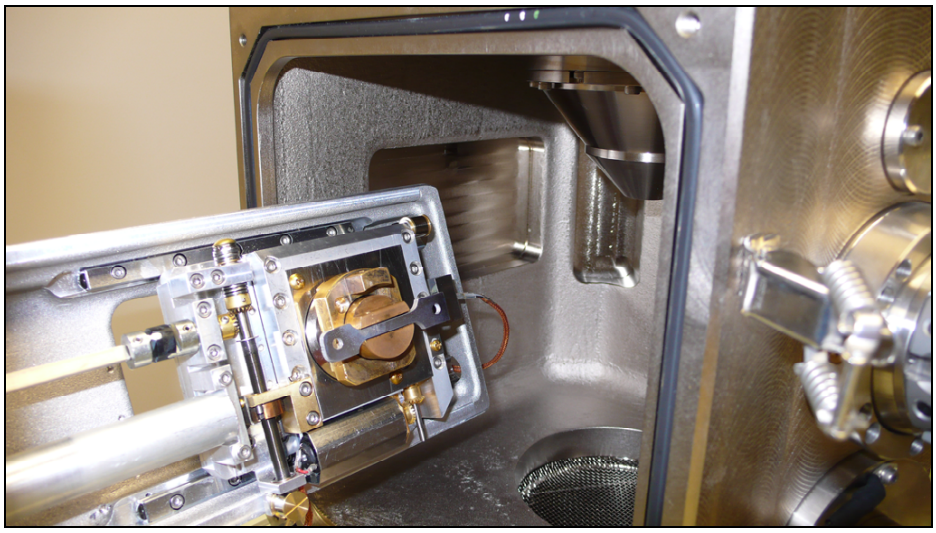

Figure B.3. Specimen orientation in relation to the SEM chamber

B.3 AUTOMATED MAPPING

By correctly setting up the various parameters in automated phase-orientation identification of magnesium alloy specimens, maximum acquisition rate of 0.23 seconds per pattern was achieved. This implies that approximately 15000 patterns can be analyzed per hour, hence a typical automated map size of 500 × 300 points (total of 150000 points) would require ten hours to complete.

The maximum acquisition rate was determined by interrelated contributions of four key parameters:

B.3.1 Computer processing power

When the EBSD detector captures a pattern, the computer must process the pattern for orientation and phase candidate match based on the lattice parameters from the database. The speed is determined by the overall process speed of the computer, and therefore a fast computer would achieve increase in analysis speeds. In this research program, this was carried out on an Intel Xeon 2GHz personal computer with Windows 2000 operating system.

When the captured pattern is matched to the phases listed in the database, the computer must perform a comparison with each of the registered candidate phases. Therefore, large number of potential phase solutions would result in slower process results. In order to increase the speed of pattern matching, unnecessary phases must be removed from the candidate list. For example, when performing automated map of AZ91D magnesium alloy, which consists of primary α-Mg grains surrounded by $Mg_{17}Al_{12}$ β precipitates, these

precipitate phases should not be included in the candidate phases list, since their phase identification would not be necessary if they are clearly visible on the SEM image, but it will add extra load on the computer if it must compare every α-Mg patterns with potential match against the precipitate phase parameters. An exception to this guideline would be when the crystallographic orientation of the precipitate phases is required. However, this was generally unfeasible on a typical automated map performed in this research program, since the resolution of the step interval (~1 μm) and the large spot size of the incident beam was insufficient to acquire a discrete pattern from small precipitate phases unless the beam was targeted on an ideally bulky precipitate formations. This is illustrated on Figure B.4.

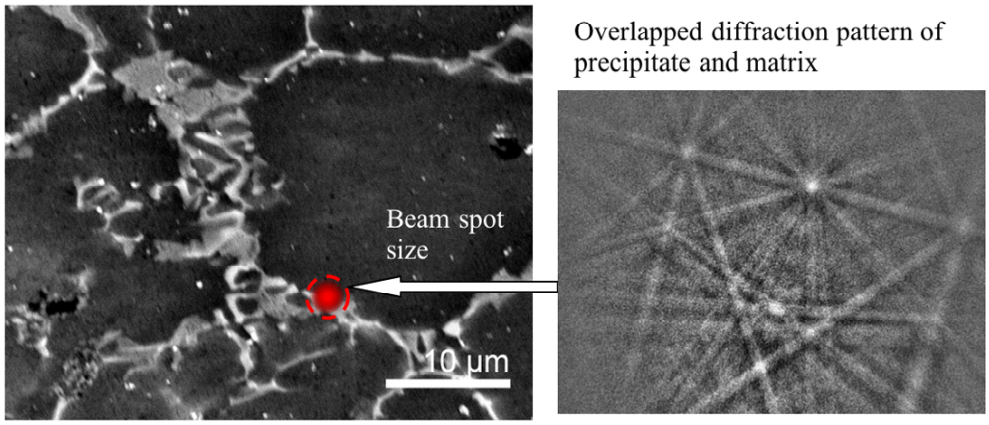

Figure B.4. Point analysis of a precipitate phase limited by the beam spot size

B.3.2 Maximum physical size of an automated orientation map

In many analysis cases where a large coverage of the specimen surface area is required. However, the attempt to increase the sample size by lowering the magnification would inherently encounter two issues:

Firstly, a larger target area would result in reduction in resolution, since the EBSD map is constructed as a grid array of analysis points with fixed distance between each step intervals proportional to the magnification of the observed image. Therefore, carrying out a same physical resolution map (e.g. 1µm step intervals) on a target area twice the size would require four-fold increase in analysis time. In this research program with each map construction requiring up to 16 hours, any further refinement of step size was unachievable, either due to the limitation imposed by the life of SEM filament (~100 hr), or due to the image drift caused by charging of the specimen during long exposure to the electron beam, as illustrated on Figure B.5. Furthermore, any further reduction in resolution was unacceptable, since the step interval of 1µm was barely enough to capture many of the fine subgrain formations.

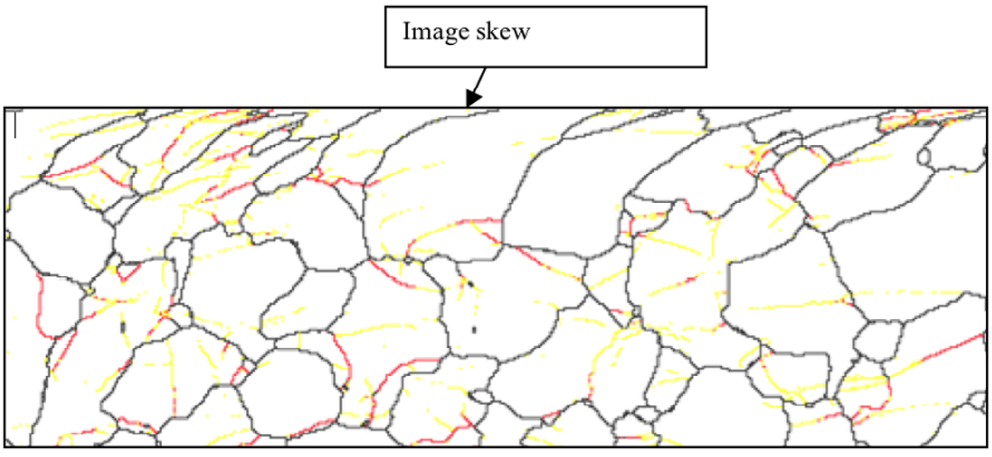

Figure B.5. Image drift causing a skew in the automated orientation map

Secondly, observation of a larger target area would lead to inaccuracies in EBSD data, since the deviation from the ideal 70º incident beam-specimen tilt relationship would be more pronounced at the extremes of a larger target area. This would result in a map of poor acquisition rate or inaccurate orientation solution further away from the center of the map. A large deviation in specimen height also exceeds the depth of field of the SEM, resulting in loss of focus and significant skewing of the image.

In the current configuration of GEOL 6100 SEM and HKL Nordlys II detector, the maximum physical size of the automated mapping procedure was achieved at 45× magnification of the microscope, generating an orientation map for a specimen surface area of 2.50 × 1.85 mm.

B.3.3 Parameter 2. Signal strength

In any material, the critical criterion in conducting an EBSD analysis is the available signal strength of the electron backscatter pattern (EBSP). A strong backscatter beam would result in faster and more defined EBSP, which would require less exposure time, and also will be faster in finding a correct database match with greater orientation accuracy. The largest obstacle to the study of magnesium alloys is their low signal strength compared to other alloys such as steels. In this research, optimal camera exposure time was evaluated to be 60 ms. In a single point analysis, exposure times of greater than 2 seconds could be used to acquire a pattern from a weak signal. However, this was unreasonable for automated analysis of many thousands of points. Typically, a specimen surface that failed to generate a satisfactory pattern in less than 60ms was found to be too poor to generate a reliable pattern at any exposure.

Raising the SEM beam current could increase the signal strength to some degree.

However, 80% peak beam current was used for all automated maps carried out in this research, in order to avoid the risk of over-saturation reducing the life of the SEM filament.

In magnesium alloy specimens, poor signal strength was attributed to surface contamination or oxidation due to the poor polishing process. When the surface was contaminated with silica polishing agent or water, the nonconductive surface layer would brightly charge under electron beam exposure. These charged surfaces would "burn", leaving a trace of exposed regions. As a rough indication, satisfactory signal strength could not be obtained if the surface becomes "burnt" under optimal beam current condition. In such case, automated mapping was not carried out since burning also leaves permanent damage on the subsurface microstructure.

B.3.4 Parameter 3. Pattern stability and averaging

When the apparent EBSP appears unstable due to the instabilities in the electron beam source, vacuum condition or specimen charging, the pattern must be averaged in time-domain in order to obtain a sufficient accuracy for determining the crystallographic parameters. Time-domain averaging of 4 frames was used for all automated analysis in this research, where 3~10 frames are typically used in most cases. The implication of the time-domain averaging is such that a sequence of multiple image frames is required to construct one time-averaged image frame. Therefore, EBSP acquired at 60 ms exposure time and 4 frame averaging would require 240 ms to construct one pattern image for analysis. This illustrates that doubling the time-domain averaging would result in doubling of the time taken to complete the automated map construction. Although reducing the number of averaging frames would speed up the pattern acquisition process, it will inevitably result in inaccurate identification of the EBSP.

B.3.5 Pattern matching calibration

When the pattern matching software generates a simulated pattern to match the real pattern, the size of intersected projection sphere is preconfigured at default values based on the distance between the specimen surface and the EBSD detector, its rotation, and the beam center. However, the actual values of these parameters differ depending on each specimen, positioning, and beam alignment. Therefore, calibration must be performed for each event of EBSD analysis in order to achieve the best accuracy. Although phase identification and pattern matching can be performed with relative ease even with poorly calibrated pattern matching, the accuracy of crystallographic orientation is more severely affected. This is because poor calibration typically does not affect the central region of the pattern that is required for lattice parameter matching, but the fringes would be more deviated from its simulated solution as illustrated on Figure B.6. Poor calibration also slows down the acquisition speed, since the acquired pattern would have more difficulty in matching against a simulated pattern. In this research, all EBSD patterns were calibrated prior to each automated mapping process based on four EBSP at each corners of the map area.

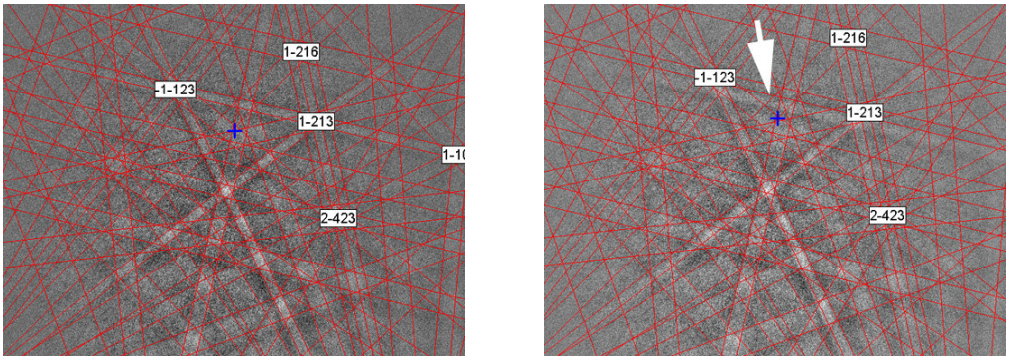

(a) (b)

Figure B.6. Comparison between an EBSP with (a) good calibration, and (b) poor calibration

Other than the four parameters mentioned above, the specimen topography also affects the EBSP accuracy, although not necessary affecting the acquisition rate. When applying an electron beam spot of finite diameter on a rough or bumpy surface, the resultant Kikuchi-band on the EBSP would broaden. Being aware that the accuracy of orientation is purely dependent on the sharpness of the Kikuchi-bands on the EBSP, introduction of such instabilities would be detrimental when accuracies of $< 1^{\circ}$ is essential in the current analysis case of low angle boundaries in magnesium alloys.

Summarizing the key points, in order to achieve a satisfactory automated EBSD map, one needs to aim for:

- Contamination and corrosion free specimen surface
- Smooth specimen surface without scratches or pits
- Flat specimen surface with minimal deviation from the 70° to the incident beam
- Stable vacuum level and low specimen charging to avoid thermal instabilities
- Stable beam current and alignment to avoid drift
- Optimized EBSD exposure and pattern averaging parameters
- Optimized phase candidate list and pattern fitting calibration

Failure to meet any of the above criteria would result in inadequate EBSD pattern quality or slowness of the automated map generation.

B.4 TREATMENT OF LOW ANGLE BOUNDARIES

Automated orientation maps created by EBSD have a significant benefit of being able to "see" the crystallographic orientation boundaries and quantify the misorientation angle between the adjacent crystals. This is especially helpful in the case of magnesium alloys, since majority of diecast alloys have a complex dendritic microstructure that is difficult

to distinguish the real high angle boundaries from other dendrite arm boundaries. As a common practice, grain boundaries are defined as incoherent boundaries with greater than 15º of orientation mismatch [6]. The 15º comes about due to convenience but with no particular reason, except to say that boundaries with greater than this angle can usually be seen under polarized light or orientation contrast electron microscopy, and also because misorientations below this angle could retain their coherency as a kink boundary [7]. Boundaries with 10º~15º are ambiguous in that sense, but are not treated as grain boundaries in the current study.

With such criteria, boundaries with special orientation relationships such as twin boundaries are usually not considered a grain boundary, since the required activation energies for defects to migrate across these special boundaries would be different to those of purely incoherent interfaces. For this reason, special boundaries representing hcp tension twins with orientation relationship of 86º was automatically excluded from the grain boundary analysis.

Below the grain boundary criteria of 15º, the treatment of low angle boundaries becomes one of the most significant interests in this research. The presence of such low angle boundaries plays an important role in defect transport kinetics under power-law creep, but has historically been difficult to visualize or quantify under traditional optical microscopy techniques, and also under TEM due to the lack of large represented grain area, and bucking of the thin foil making the determination of precise orientation relationships difficult.

EBSD enables the determination of low angle boundaries as low as 0.5º. However, it becomes questionable whether such misorientations between adjacent regions are due to

genuine boundaries or merely artifacts introduced by aforementioned pattern matching errors. An example is shown in Figure B.7, in which the boundaries greater than 5º have a definite subgrain arrangement, whereas those in the region of 2º ~ 5º also highlighted some of the surface defects such as a scratch. Therefore, in this study, only the boundaries greater than 5º was accounted for in statistical analysis, whereas those in 2~5º range were used for visual interpretations, and those below 2º were rejected. This assumption is physically reasonable, since boundaries as low as 1~2º, irrespective of whether they are genuine or not, would contribute very little to the overall creep behavior of the bulk material.

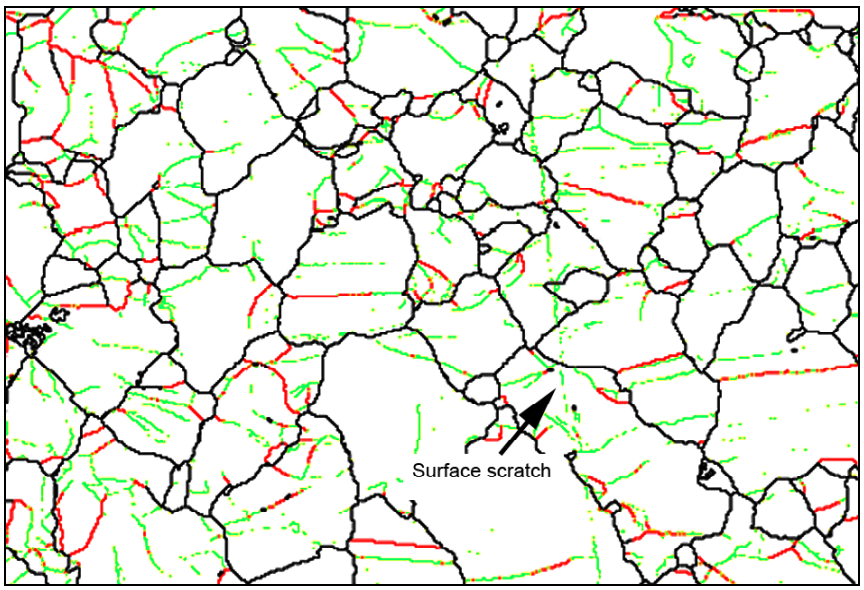

Figure B.7. Low angle boundaries illustrated by: Green: 2~5º, red: 5~15º and black: 15º and above

B.5 PRESENTATION OF THE ORIENTATION MAP

The advantage of automated orientation map of EBSD is in its diverse ways to exhibit the output data in order to produce a variety of color maps that is visually informative about some textural features of the material. Some of the key output methods used in this research are summarized below.

B.5.1.1 Pattern quality map

When a single EBSP is acquired, the data about its accuracy is also recorded. This indicates whether the pattern was acquired with high confidence, suggesting a flat, consistent crystal, or of a poor confidence, suggesting some irregularities in the target surface region. By constructing a map based on this information, it becomes evident that the ambiguous regions such as grain boundaries or scratches are clearly illustrated, as shown on Figure B.8. In this research, pattern quality maps were used to identify the areas of zero solution, such as fine scratches or grain boundaries.

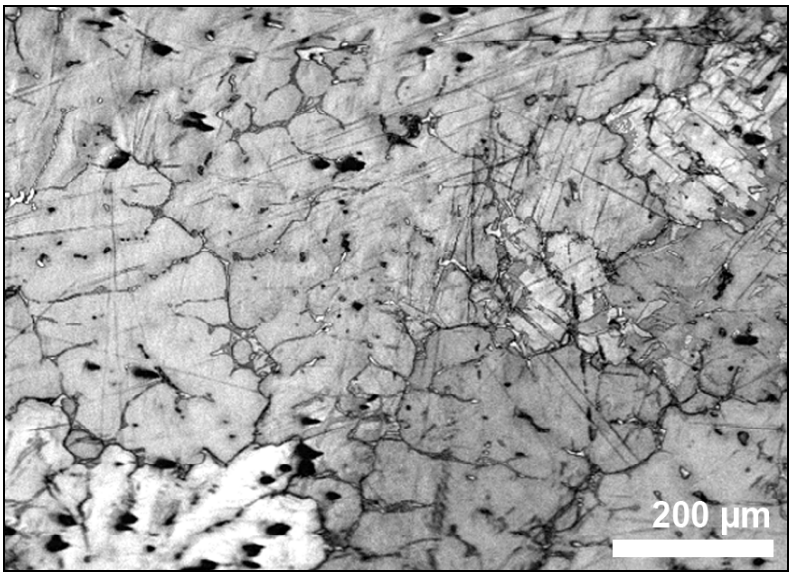

(a)

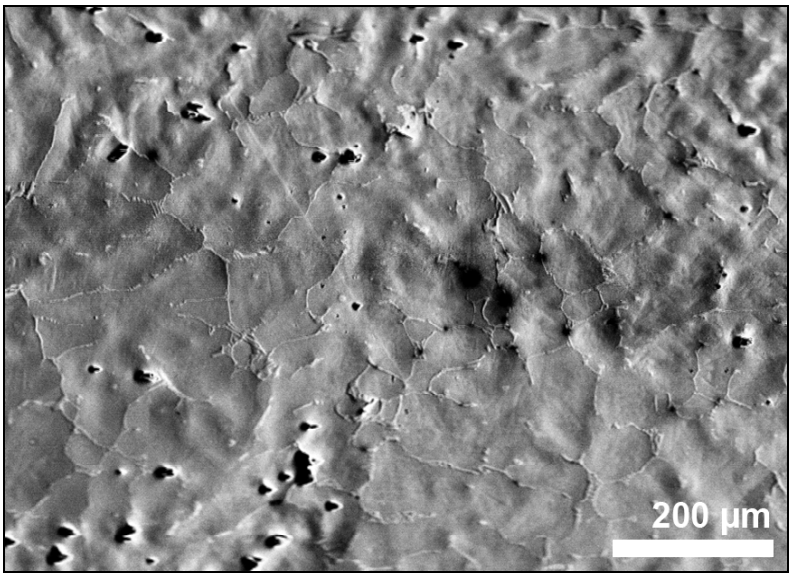

(b)

Figure B.8. An example of a (a) pattern quality map compared to the standard SEM image of the same area

B.5.1.2 IPF contrast

IPF contrast colors the nodes based on the crystallographic orientation, using the coloring convention illustrated by the inverse pole figure as shown on Figure B.9

Since the IPF projection is dependent on the specimen orientation, the IPF contrast must be colored based on a particular projection axis, such as the specimen surface normal.

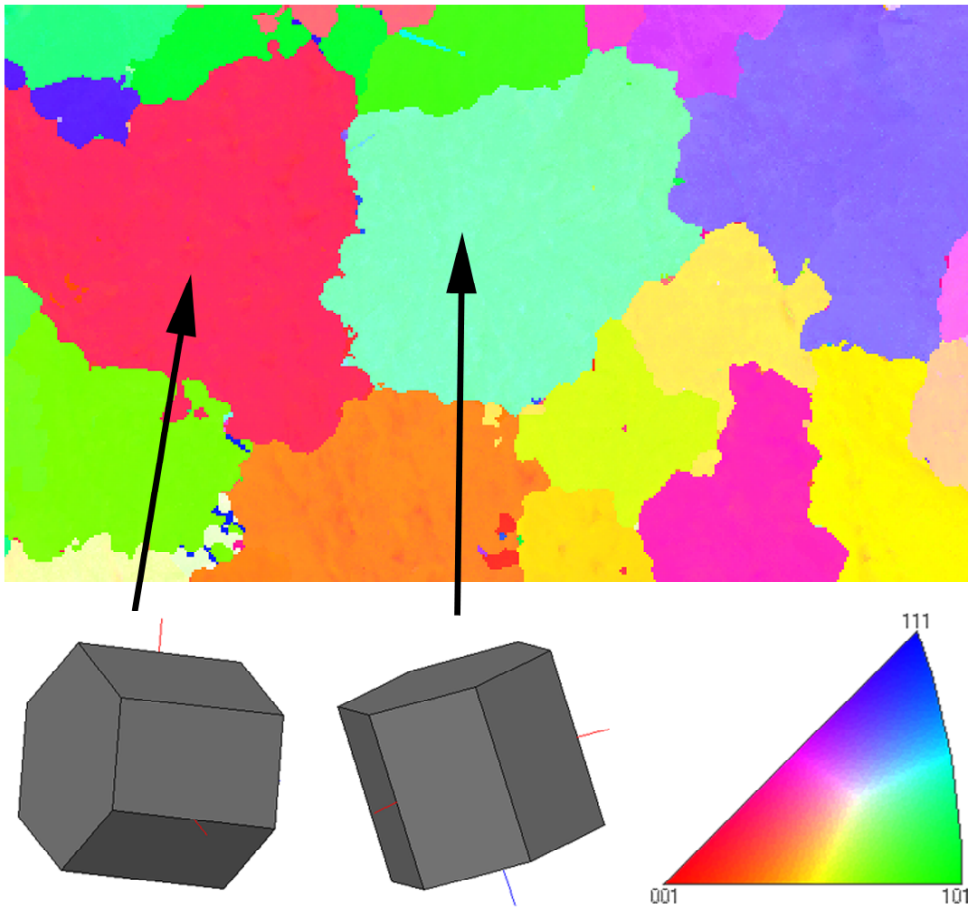

Figure B.9. An example of IPF contrast map and the corresponding color key

B.5.1.3 Euler contrast

Euler contrast is similar to the IPF contrast, but generates contrast based on one of the three fundamental Euler angles (φ_1, φ_2, ϕ) that defines the rotation of a crystal [5, 8] as illustrated on Figure B.10a. It is effective for example in highlighting all the grains that have their basal axis perpendicular to the surface normal.

B.5.1.4 Misorientation boundary by angle or orientation

The map can illustrate boundaries between a pair of nodes with a misorientation angle beyond a specified minimum. In this research, the high angle grain boundaries (>15°) were shown in black, low angle 5° ~ 15° boundaries were red, and 3° ~ 5° boundaries were in yellow, as shown on Figure B.10b. The boundary map can also be applied to highlight boundaries that possess a certain orientation relationship between the adjacent pair of nodes. In the current research, this technique was used to identify the twin boundaries as shown on Figure B.10c.

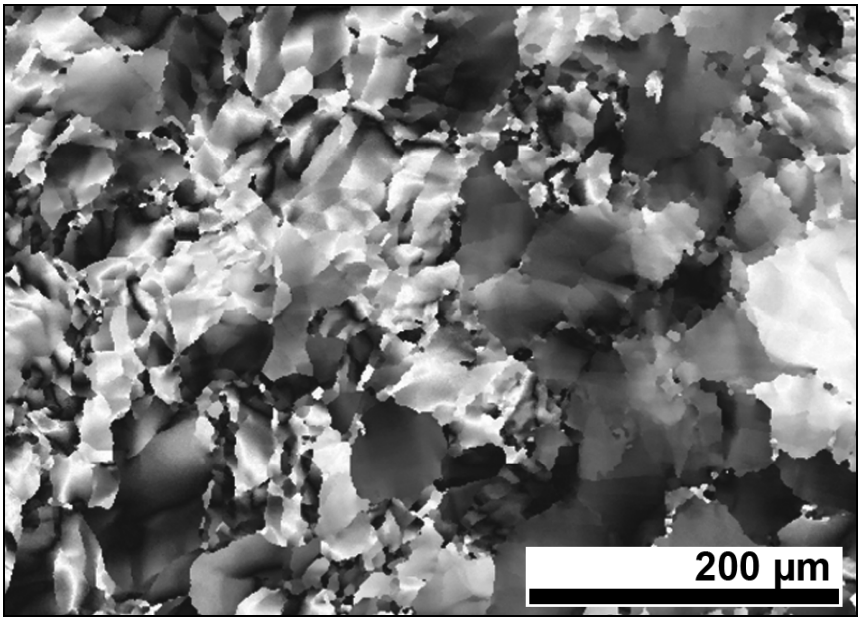

(a)

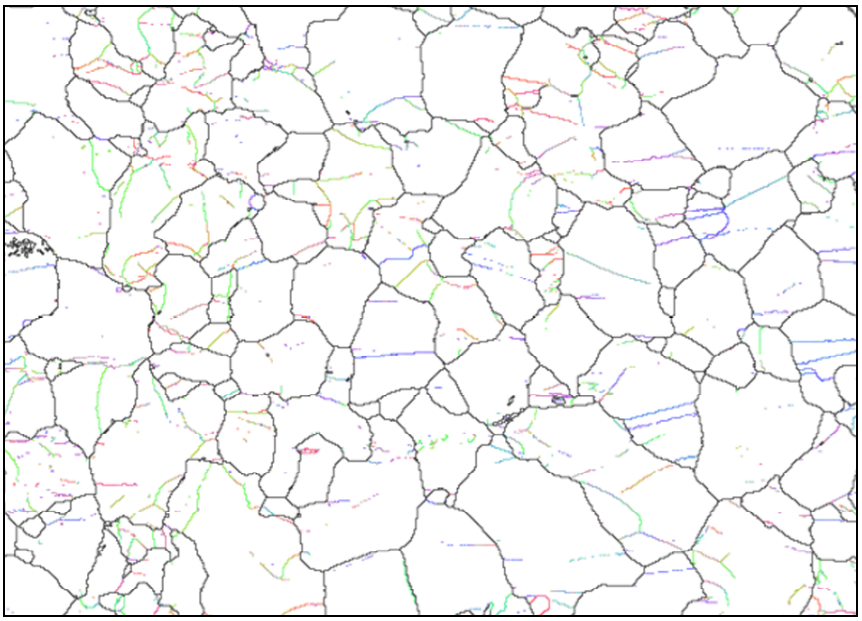

(b)

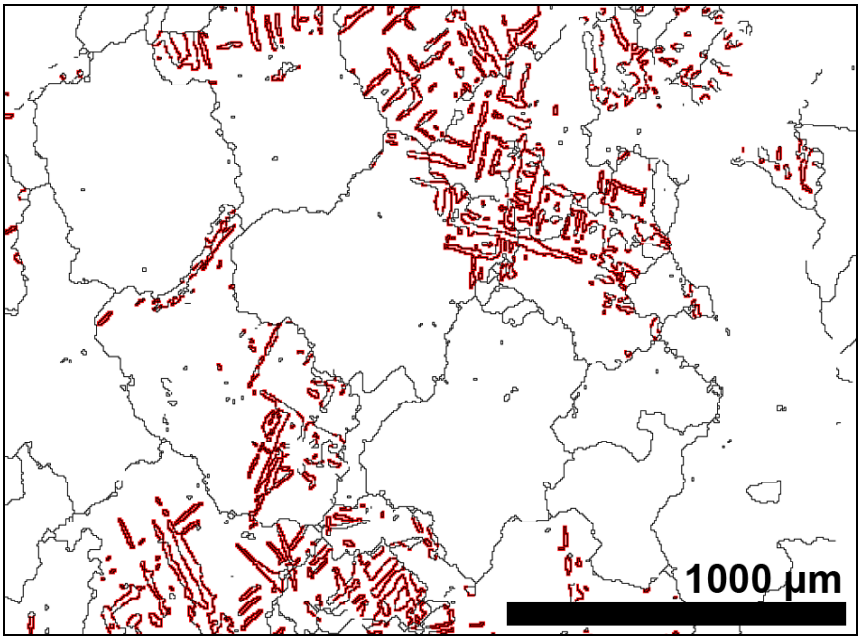

(c)

Figure B.10. Examples of (a) Euler contrast on ϕ_2, (b) Misorientation by angle, and (b) only highlighting twin boundaries

B.5.1.5 Summary

Various ways of illustrating the orientation map output can provide further understanding and visualization of some of the material features that were not possible previously. However, one must pay special attention in order to understand the underlying systems of data interpretation, since many of the techniques (e.g. IPF, Euler) could be interpreted in a totally contradictory way if they were represented on a wrong axis with respect to the specimen, beam, or detector orientation. To understand the definitions of pole figures and Euler angles, an excellent textbook "*The Measurement of Grain Boundary Geometry*" by V. Randle [8] is highly recommended.

B.6 POST PROCESSING AND PATTERN CLEANING

B.6.1 Limitations of automatic and manual cleaning

A raw EBSD orientation map contains a small percentage of blank data points generated when EBSD failed to provide a solution. In addition to these, typical maps would have a small number of irregular, inconsistent solutions that must be removed prior to performing the subsequent statistical analysis.

Blank solutions occur when the acquired EBSP fails to match within a threshold mean angle deviation (MAD) against the simulated pattern from the list of possible crystals. In this research, the automated map construction was considered a success when the amount of blank solutions was limited to less than 20%. When the map contained more than 20% blank solution, the specimen was re-polished and the map was constructed again until the blank solution was suppressed to a satisfactory level.

Blank solutions were typically attributed to grain boundaries or surface scratches where a clear EBSP could not be generated. These defects could easily be detected under the EBSD pattern quality map, and therefore re-polishing usually results in a satisfactory solution. However, the re-polishing could not be performed frequently since the interrupted creep experiments require repeated observation of identical surface region, whereas each re-polishing process may remove up to 5 μm of surface microstructure.

Typical blank solutions such as those caused by a surface scratch shown on Figure B.11 could be eliminated by automated post processing algorithms that fills the blank solution pixel by the taking an average from surrounding pixels. This technique should not alter the overall statistical data significantly unless performed excessively, since the surface scratches are represented simply as a row of blank solutions within a grain structure of a consistent orientation.

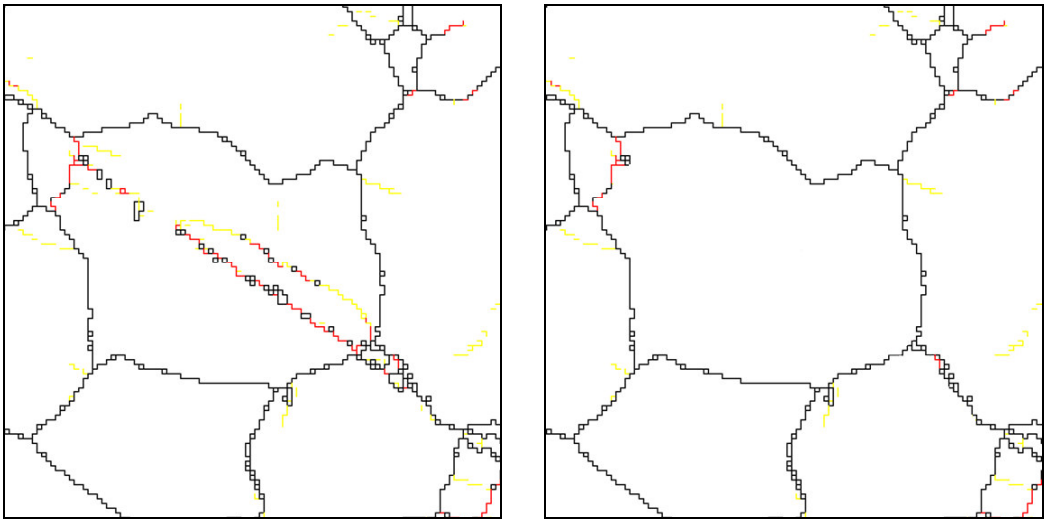

(a) (b)

Figure B.11. (a) A row of blank solutions caused by a scratch, (b) removed by automatic and manual cleaning process

Irregular, inconsistent non-blank data points were also present in a typical map. However, the amount of these errors could not be quantified since there is no clear distinction between which solution is genuine or false. These inconsistent data points typically appeared as a single pixel within otherwise consistent grain structure.

Although these inconsistent data points existed in such a low level that they had very little contribution to the overall statistical trend, they did introduce visually distinctive artifacts that had to be eliminated. This is because these inconsistent data points did not usually occur at random, but were generated by the pattern-matching algorithm due to the misinterpretation of a particular pattern as its crystallographically similar orientation. A common case is a misinterpretation of a crystal as its 86º twin orientation. When such irregular data point occurs, they are represented as a single pixel surrounded by a high angle boundary, as illustrated on Figure B.12, and visually distracts from the real distribution of low and high angle boundaries.

HKL Channel 5 software suite provides a "Wild Spike" reduction algorithm that identifies such single irregular pixel and replaces this pixel with the average orientation of the adjacent pixels. This algorithm is effective in most cases, but fails to remove artifacts that are 2 or more pixels wide, found in rare occasions. In such cases, the irregular pixels were manually erased without the aid of automated systems, as illustrated on Figure B.13.

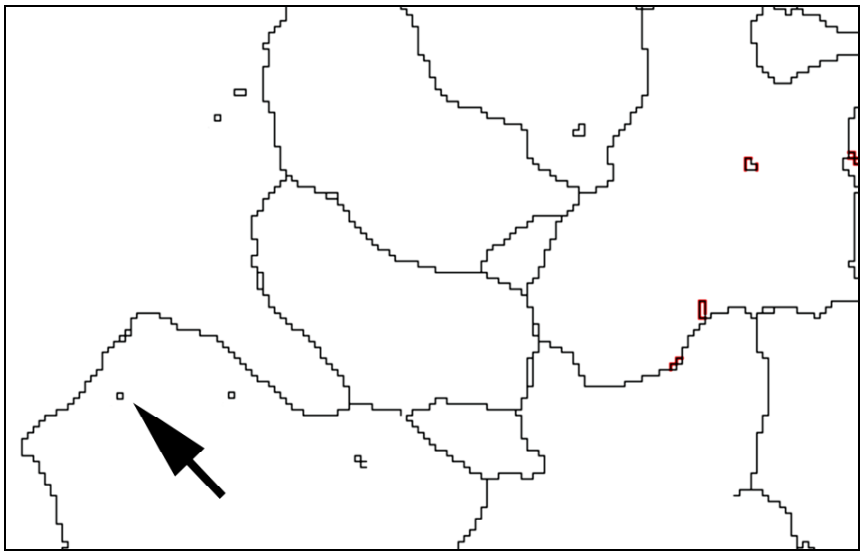

Figure B.12. A single misindexed pixel represented by a high angle boundary

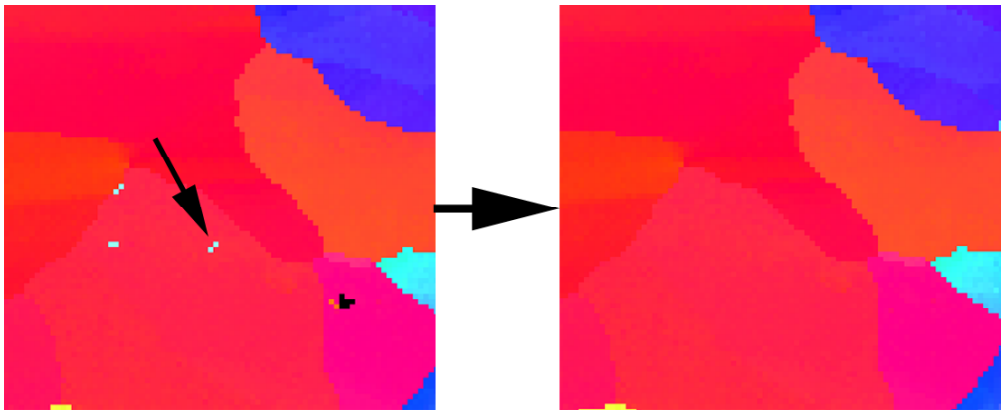

Figure B.13. Manual removal of 2-pixel wide irregular solution artifact

B.6.2 Kuwahara filter

Later versions of the HKL Channel 5 software suite (received towards the end of the research program) also provided an additional filter known as Kuwahara filter, which can be used for further artifact cleaning. This filter analyze blocks of pixels (e.g. 4×4 pixels) to evaluate the presence of any wild spikes surrounded by otherwise consistent orientation pixels, and fills the wild spikes with the surrounding orientation average. This filter was designed to be effective in removing multiple pixel clusters of irregular data that could not be automatically eliminated by the single pixel wild spike reduction algorithm mentioned previously.

However, the Kuwahara filter was not used in any of the orientation maps acquired in this research program, because the excessive automated data averaging resulted in data monotony and loss of fine details in intragranular texture, as illustrated on Figure B.14.

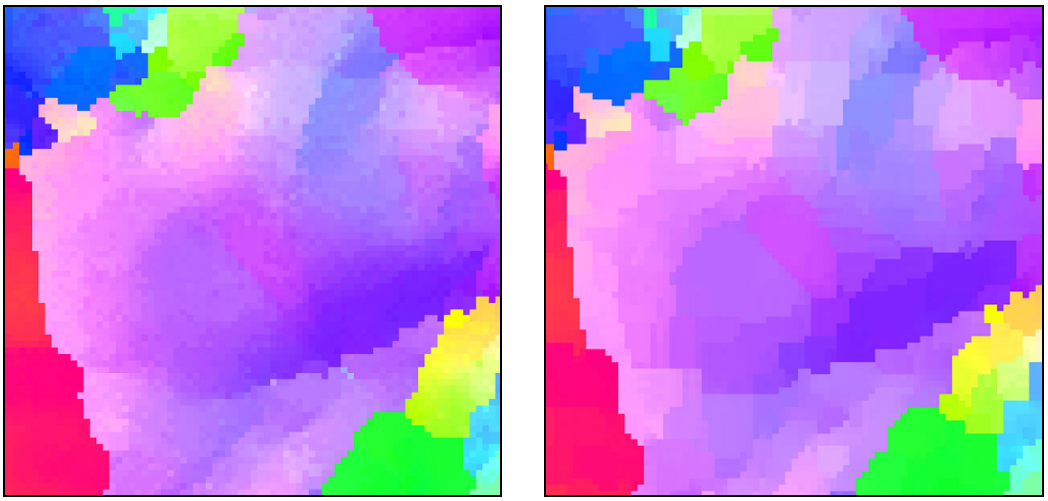

(a) (b)

Figure B.14. IPF map (a) before filtering, and (b) block pixelation of low angle grain boundaries introduced by the use of automatic Kuwahara filter

B.6.3 Summary of orientation map cleaning techniques

Based on the observations made above, the standard sequence for EBSD orientation map cleaning procedure was established as follows:

- The completed raw map was checked for sufficient solution count. The map was rejected if the proportion of blank solution was greater than 20%
- Automatic "Wild spike" correction was applied to remove single pixel irregular solutions
- Blank solution regions due to minor surface scratches and grain boundaries were automatically filled in by adjacent pixels
- Other noticeable multi-pixel artifacts were removed manually until they no longer interfered with the visual inspection of the map

Figure B.15 summarizes the degree of cleaning performed for all the maps used in this research. The critical concern with the automated EBSD orientation maps is such that the cleaning algorithms can be detrimental if used excessively, since many critical information such as low angle boundaries, twins, and fine precipitate phases can be lost during the cleaning process. Therefore, the operator discretion is the most important factor in obtaining a satisfactory map that is a good representation of the actual microstructure, but free of incidental, random artifacts at the same time.

Although it may seem obvious, the most critical factor in obtaining an accurate orientation map is to spend as much effort as possible in the specimen surface preparation and EBSD calibration stages prior to the map acquisition, so that only a minimal amount of subsequent post-processing is required.

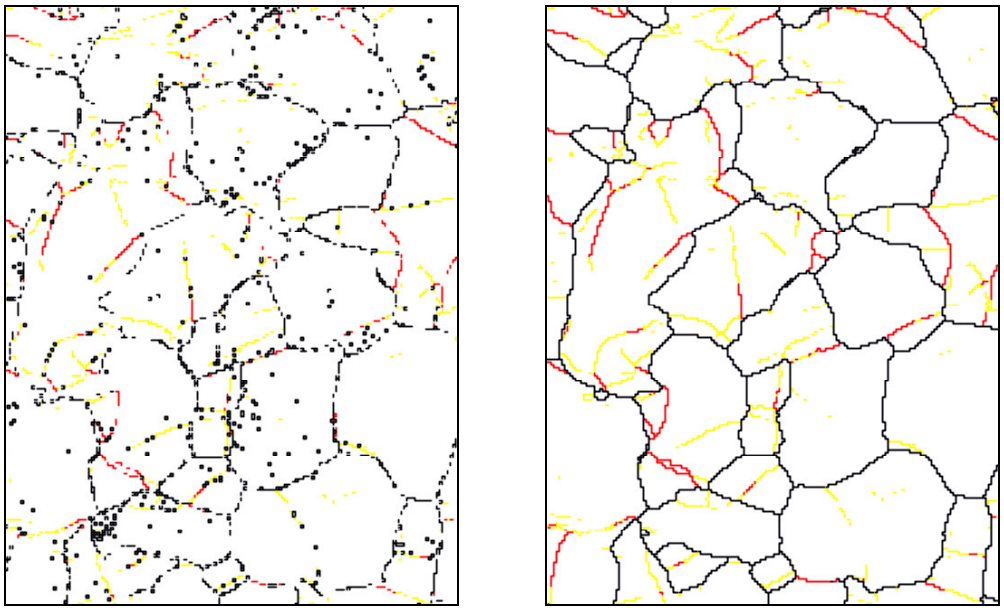

(a) (b)

Figure B.15. Level of manual cleaning used in this research (a) before cleaning and (b) after cleaning

B.7 CONCLUSION

Automated orientation maps generated by EBSD differs from majority of other metallurgical analysis tools in a way that the resultant dataset consists of a two-fold benefits of:

- Visually informative images of the surface phase and orientation texture
- Crystallographic orientation parameters of each generated pixel

The visual image aspect is similar in style to interpretation of polarized light microscopy, whereas the crystallographic parameters aspect can be treated as an extension of TEM-SAD and XRD. The significance of this two-fold data interpretation is that a cross-reference can be made whereby a visually poor map would indicate a poor representation of the crystallographic parameters, which adds a further confidence over other techniques

such as XRD in which the acquired diffraction characteristics of a phase can only have indirect correlation with the actual specimen microstructure.

The largest obstacle in the EBSD orientation mapping is that the process is strongly dependent on the operator skill level and the knowledge in interpretation of issues encountered in the process of:

- Specialized specimen surface preparation techniques for EBSD
- Calibration and optimization of the EBSP pattern matching process
- Selection of an appropriate automated mapping resolution and window size
- Subsequent post-processing such as data cleaning and statistical analysis

Chapter References

1. Humphreys, F. J., Jnl. Mater. Sci., 2001, 36, 3833

2. Humphreys, F. J., Scripta Mater., 2004, 51, 771

3. Jazaeri, H. and Humphreys, F. J., Jnl. Microscopy, 2004, 213, 241

4. Humphreys, F. J., Jnl. Microscopy, 2004, 213, 247

5. Cho, J.-H., Rollett, A. D., et al., Metall. Mat. Trans. A, 2005, 36, 3427

6. Sonnweber-Ribic, P., Gruber, P., et al., Acta Mater., 2006, 54, 3863

7. Honeycombe, R. W. K., The Plastic Deformation of Metals, Edward Arnold Publishers, 1984

8. Randle, V., The Measurement of Grain Boundary Geometry, Institute of Physics Publishing, 1993

APPENDIX C – PUBLICATIONS

The following articles were published during the course of this research:

- **T, Sato, B.L. Mordike, J-F. Nie, and M.V. Kral,** *An Electron Microscope Study of Intermetallic Phases in AZ91 Alloy Variants*, Magnesium Technology 2005, Ed. N.R. Neelmeggham, H.I. Kaplan, and B.R. Powell, TMS, pp. 435 - 440 (2005).

- **T. Sato, M.V. Kral,** *Electron Backscatter Diffraction Mapping of Microstructural Evolution of Pure Magnesium during Creep*, Metall. Mat. Trans. A, Vol. 39, pp. 688 – 695 (2008).

- **T. Sato, M.V. Kral,** *Microstructural Evolution of Mg-Al-Ca-Sr Alloy During Creep*, Mater. Sci. Eng. A, (currently awaiting publication)

Magnesium Technology 2005
Edited by N.R. Neelameggham, H.I. Kaplan, and B.R. Powell
TMS (The Minerals, Metals & Materials Society), 2005

An Electron Microscope Study Of Intermetallic Phases In AZ91 Alloy Variants

T. Sato[1], B. L. Mordike[2], J.-F. Nie[3], M. V. Kral[1]

[1]University of Canterbury, Mechanical Engineering, PO Box 4800, Christchurch New Zealand
[2]Institut für Werkstoffkunde und Werkstoftechnik, TU Clausthal, Agricolastrasse 6, D-38678, Clausthal-Zellerfeld Germany
[3]Monash University, School of Physics & Materials Engineering, PO Box 69M, Clayton, Victoria 3800 Australia

Keywords: magnesium, intermetallic, electron microscopy

Abstract

The magnesium alloy AZ91D has been employed extensively in the automotive and electronics industry due to its superior castability and mechanical properties at room temperature. New alloys, MRI-153 and MRI-153M, based on AZ91D have been developed to improve creep properties by forming grain boundary and intragranular intermetallic phases via additions of elements such as calcium and strontium. Intermetallic phase stability and distribution are not well understood in these new alloys. In the present work, the various intermetallic phases present in two high pressure die cast AZ91-type alloys were characterized using a combination of transmission electron microscopy, selected area diffraction, scanning electron microscopy, electron backscatter diffraction pattern analysis and energy dispersive x-ray spectroscopy.

Introduction

Conventional AZ91D die-casting alloy has relatively poor high temperature mechanical properties due to its susceptibility to creep failure. It has been suggested that that this is primarily caused by the formation of grain boundary α-Mg + $Al_{12}Mg_{17}$ eutectic, that is thermally unstable and prone to aging [1]. Since reduction of aluminum content is not favorable from castability and room temperature strength points of view, it is of a great interest to suppress the formation of $Al_{12}Mg_{17}$ phase whilst maintaining an appropriate aluminum content.

High pressure die casting can achieve faster solidification rates than conventional casting, thus supersaturating aluminum in the α-Mg matrix, achieving finer grain structure [2] and reducing shrinkage voids during solidification [3]. However, for any magnesium alloys with aluminum supersaturated in the primary Mg matrix, precipitation of $Al_{12}Mg_{17}$ phase is unavoidable upon aging at elevated temperatures [4], resulting in the rapid deterioration of creep resistance.

Modern creep resistant alloys rely on the formation of aluminum rich precipitates that are stable at elevated temperatures, in order to reduce the formation of $Al_{12}Mg_{17}$, and to act as stable barriers against dislocation motion [5]. In recent developments, such precipitates are typically binary compounds of (Mg, Al) and (rare earths, Ca, Sr). Modern creep resistant alloys containing up to 2% rare earths (RE) or strontium achieved dramatic improvements in mechanical properties up to 150°C due to a fine distribution of Al_4RE or Al_4Sr precipitates, but problems with poor castablility, hot tearing and high oxidation rate, along with the significant cost of the alloying elements are also of concern [1, 5].

Currently, an addition of up to 3% calcium has gained attention, in which the formation of thermally stable Al_2Ca precipitate achieved similar creep resistance compared to rare earth alloys at significantly lower cost [6]. Calcium additions may introduce problems with castability and hot tearing although these effects can be mitigated with proper casting conditions and additions of zinc to similar levels as AZ91D [7, 8]. As the creep resistance of some magnesium alloys has reached the levels comparable to some aluminum alloys [9], some interests in current developments lie in the areas of reducing alloying costs (e.g., reducing the use of expensive elements such as RE and Sr) and improving castability (reducing process control costs).

Two patented high-pressure die cast alloys, designated MRI-153 and MRI-153M (Dead Sea Magnesium Ltd.), were studied in the present work. These are modified AZ91D type magnesium alloys, based on a combination alloying with Ca and Zn for MRI-153 and Ca and Sr for MRI-153M, designed to improve high temperature properties with less expensive alloying elements. Room temperature and elevated temperature properties of these alloys in comparison with other commercial alloys can be found elsewhere [10]. The purpose of the present work was to reveal the major phases present, their morphologies and distributions in order to provide more information regarding the reasons behind their improved high-temperature properties.

Experimental Procedures

The specimens prepared for this study were high pressure die cast patented Mg-Al-Ca-Sr alloys MR-153 and MRI-153M. The relative compositions of each alloy are shown in Table 1. Rods of high pressure die cast specimens 180 mm length, 20 mm diameter, were obtained in the as cast condition.

Table 1. Composition of MRI-153 and MRI-153M alloys

Element	MRI-153	MRI-153M
Mg	89.00	91.00
Al	8.60	8.40
Si	< 0.01	< 0.01
Fe	< 0.0005	< 0.0005
Cu	0.01	0.001
Ca	0.94	0.99
Mn	0.29	0.28
Ni	0.0006	0.001
Zn	0.63	0.01
Sr	0.1	0.27

Specimens for optical microscopy and scanning electron microscopy/energy dispersive x-ray spectroscopy (SEM/EDS) were mounted in a conductive copper/diallyl pthalate mixture and polished to 0.05 μm alumina suspension. Some optical microscopy specimens were etched in 2% picric acid in ethanol solution but most were studied in the unetched condition.

Some specimens were deep etched in 2% HNO_3 in ethanol solution to remove the primary α-Mg grains and isolate the precipitates. Observations between timed etching steps were made to ensure that the grain boundary phases were not being attacked by the etchant. In general, this technique revealed the three-dimensional arrangement of grain boundary precipitates but some of the more delicate branches of the lamellar grain boundary constituent appeared to break away.

Specimens for electron backscatter diffraction analysis (EBSD) were not etched. For transmission electron microscopy (TEM) studies, 3-mm diameter samples were punched from 0.3-mm thick cross sections and then ground to approximately 0.1-mm thickness. Some samples were thinned using a Fischione twin jet electropolishing unit in solution of 7% magnesium perchlorate, 3% lithium chloride, 75% methanol, 15% butoxyethanol at nominal condition of –45°C, 12 mA. Other samples were prepared using a Gatan Model 656 Dimple Grinder and a Model 691 Precision Ion Polishing System.

SEM-EBSD observations were carried out on JEOL JSM-6100 equipped with HKL Nordlys II with HKL Channel 5 acquisition software and an Oxford eXL EDS system. The database for identification of possible phases comprised of all compounds listed in Pearson's Handbook [11] containing combinations of Mg, Al, Ca, Mn, Zn, and Sr. TEM observations were carried out on a Hitachi H-600 operated at 100kV and a Philips CM20 operated at 160 kV and 200 kV.

Results and Discussion

MRI-153

The optical micrograph in Figure 1 shows the typical appearance of the MRI-153 alloy in the as-cast condition. The main feature is the interconnected grain boundary network of intermetallic phases. Compared to typical micrographs of AZ91 alloys found elsewhere [12], the grain boundary phases appear more continuous and primary α-Mg grains generally larger and dendritic, although with large variations in grain size.

Observation of the MRI153 microstructure revealed two distinct precipitate phases, as shown in Figure 1. The most abundant (labeled '1' in Figure 1) was the nearly continuous lamellar intergranular phase as shown in Figures 2a and 2c. This phase was identified as hexagonal Mg_2Ca [13] by EBSD and SAD (Figures 2b and d). However, the presence of varying amounts of aluminum in the EDS spectra within various precipitates suggests that this phase may be more accurately described as $(Mg, Al)_2Ca$. Note that the cubic Al_2Ca phase [14] was not observed in the present work, which is in agreement with a report by Ozturk et al. [4] who suggest that the formation of cubic Al_2Ca phase was suppressed due to the relatively rapid solidification rate in high pressure die cast materials.

The $Al_{12}Mg_{17}$ phase [15] (labeled '2' in Figure 1a) was also observed in moderate quantity, as shown in Figure 3, typically surrounded by the $(Mg, Al)_2Ca$ phase. Although this phase is easily distinguished in optical microscopy, there is very little difference in contrast in the SEM, either in SE or BSE mode. The only way to be certain of identification of this phase was to employ EBSD in the SEM (Figure 3b) or CBED/SAD in the TEM.

A bulky and faceted but comparatively minor constituent containing aluminum and manganese was identified by EBSD as Al_8Mn_5 [16] as shown on Figure 4. This identification was confirmed by selected area diffraction in TEM. It is reported that manganese is often added to suppress the formation of detrimental Fe-containing intermetallics [17] and excess Mn will form large blocky precipitates in the alloy.

Occasional instances of $Al_{46}Ca_{25}Mn_4$ [18] were identified in this alloy in both EBSD and TEM/SAD, where the relatively large lattice parameter of this phase (a=0.5723 and c=1.826 nm) were observed.

Although the MRI-153 alloy contains 0.63% zinc, there were no observations of zinc rich precipitates such as $Mg_{32}(Al, Zn)_{49}$ reported elsewhere [7]. Isolated examples of $Al_6Mg_{11}Zn_{11}$ were found in very small quantity but most of the zinc is either in solution in the various phases or as discrete but relatively small Zn-rich precipitates in the α-Mg matrix [19].

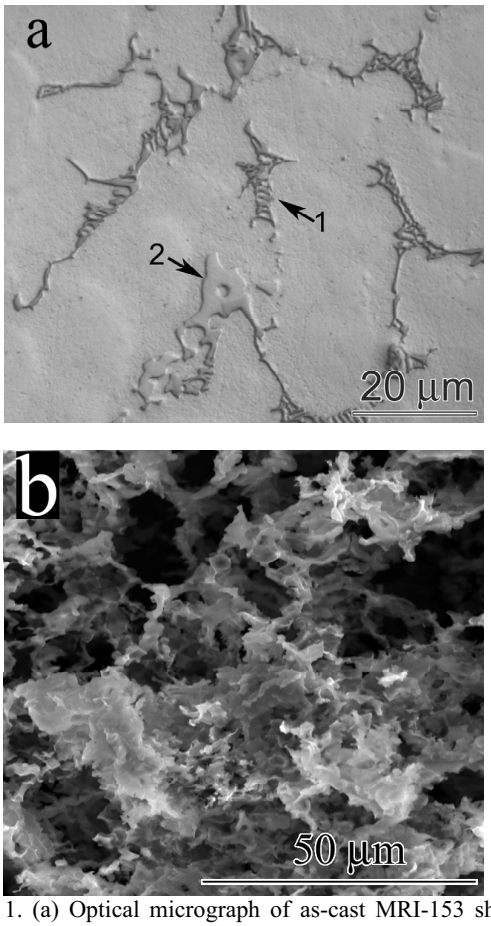

Figure 1. (a) Optical micrograph of as-cast MRI-153 showing intergranular phases surrounding the primary α-Mg grains (unetched) and (b) after 1 hour of deep etching to show the interconnected nature of the grain boundary phases.

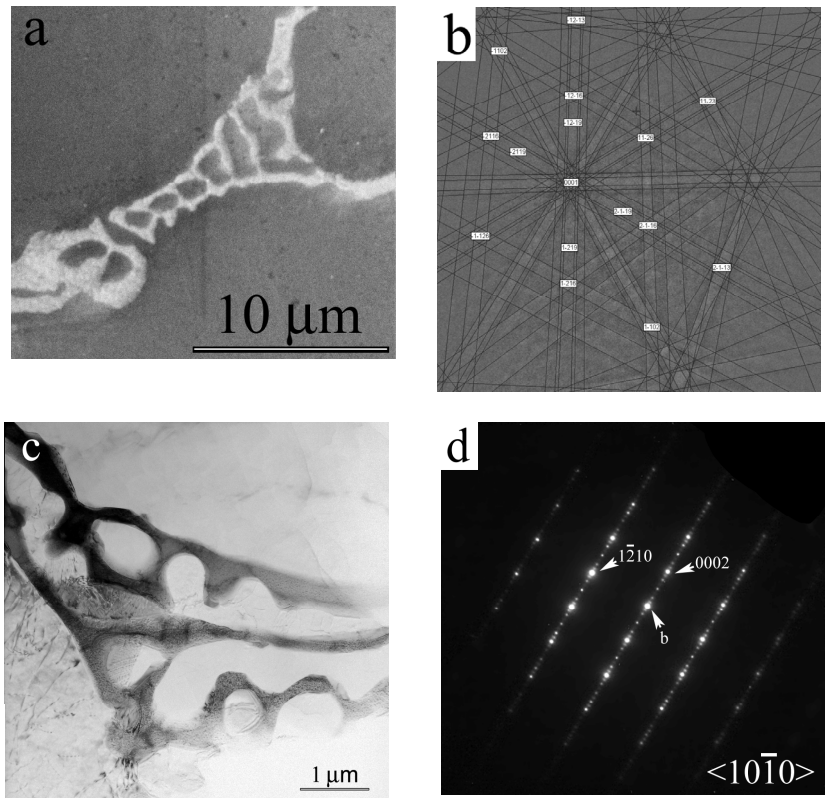

Figure 2. Intergranular $(Mg, Al)_2Ca$ phase shown by (a) SEM and identified by (b) an indexed EBSD pattern; also shown by (c) bright field TEM and (d) SAD pattern from the particle in (c).

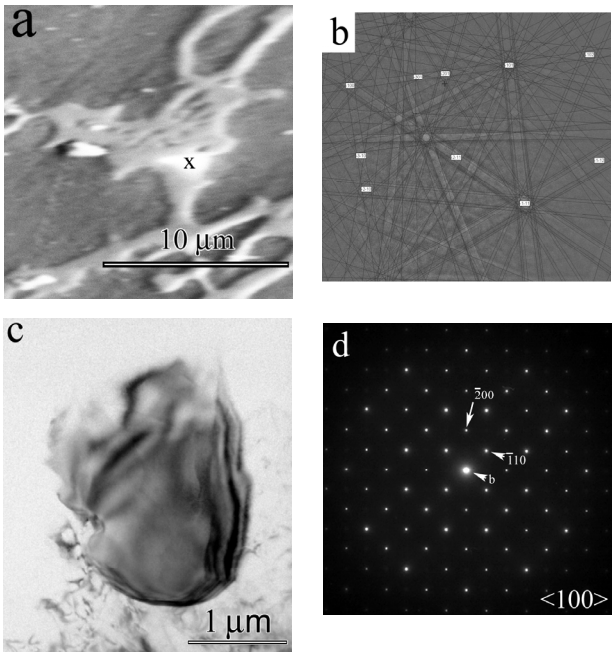

Figure 3. $Al_{12}Mg_{17}$ precipitate (a) surrounded in $(Al\ Mg)_2Ca$, shown in SEM and identified by (b) an indexed EBSD pattern of the same particle; shown in (c) bright field TEM and identified by (d) am indexed SAD pattern from the same particle in (c).

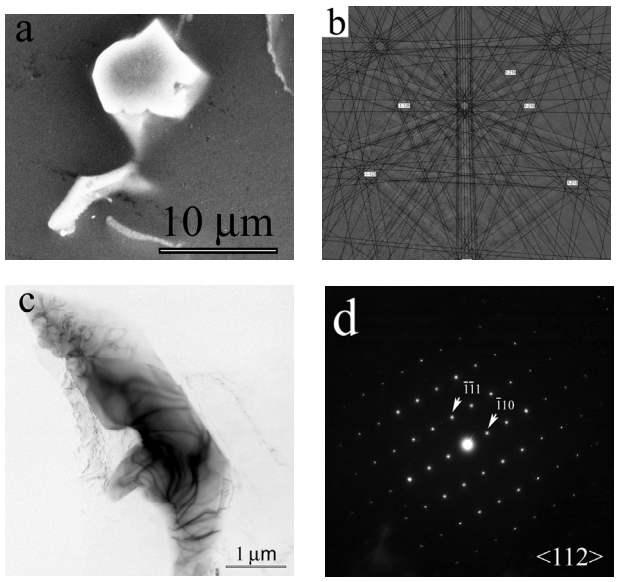

Figure 4. Al_8Mn_5 shown b (a) SEM and identified by (b) an indexed EBSD pattern; also shown by (c) bright field TEM and (d) SAD pattern from the particle in (c).

MRI-153M

Optical microscopy of MRI-153M such as shown in Figure 5a illustrates the basic microstructure of primary α-Mg surrounded by intergranular precipitates. Again, SEM images of deep etched microstructures are helpful for understanding the three-dimensional morphology and arrangement of intermetallic phases (Figure 5b). The grain boundary phases appear to be coarser and less interconnected in comparison to the MRI-153 alloy shown in Figures 1 – 4.

Although the overall as-cast microstructures of MRI-153 and MRI-153M appear similar, the phases present in the grain boundary network are different. As in MRI-153, the majority intermetallic phase was $(Mg, Al)_2Ca$, indicated as '1' in Figure 5c. SEM and TEM observations of this phase are documented in Figure 6.

Another abundant intermetallic phase, indicated as '2' in Figure 5c, was shown by EDS to contain significant amounts of Sr. These Sr-rich precipitates were typically found at grain boundaries, especially at grain corners, surrounded by the $(Mg, Al)_2Ca$ precipitates. EDS results showed varying proportions of Mg, Al and Ca and EBSD patterns (Figure 7) were indexed as Mg_2Sr [20], suggesting that this phase is most accurately described as hexagonal $(Mg, Al)_2(Sr, Ca)$. Note that the space groups for Mg_2Sr and Mg_2Ca are the same (194) and that their lattice parameters are very similar (Mg_2Sr: a=0.6426, c=1.0473 nm; Mg_2Ca: a=0.6225, c=1.018 nm) but this difference is within the resolution of the HKL EBSD system when care is taken to obtain the highest resolution patterns.

No other Sr-rich phases, such as orthorhombic Al_2Sr or tetragonal Al_4Sr phases that have been reported in earlier work [21], were observed in this alloy. Only one example of the $Al_{12}Mg_{17}$ phase was identified.

The suppression of $Al_{12}Mg_{17}$ in MRI-153M should have a positive influence upon this alloy's creep resistance. Current understanding of creep resistance in similar alloys attributes poor performance to the formation of $Al_{12}Mg_{17}$ [19].

Annealing

Figures 8a and 8b, respectively, show the microstructures of MRI-153 and MRI-153M specimens annealed at 200°C for 48 hours. Examination of the annealed MRI-153 alloy in TEM showed that there was another type of precipitate found within the α-Mg matrix, evident only with TEM. This phase, shown in Figure 9a, may be the orthorhombic $Mg_{21}(Zn,Al)_{17}$ phase identified previously [19].

The most obvious microstructural change in both alloys upon annealing treatment was the development of sub-micron aluminum-rich precipitates in the vicinity of the coarse grain boundary phases. Larger examples of the precipitates shown in Figure 9b were identified as $Al_{12}Mg_{17}$ using EBSD. The evolution of this phase may influence the creep performance in several ways. Unlike the coarse lamellar $Al_{12}Mg_{17}$ precipitates found in AZ91D, precipitation such as observed in Figure 9b is reported to lead to a reduction in creep rate due to a precipitation hardening mechanism [22]. However, thermal instabilities in microstructure are also reported to be unfavorable for interrupted creep conditions that more closely represent the real-life service conditions, in which case, pre-aging the alloys may be favorable for some applications [23].

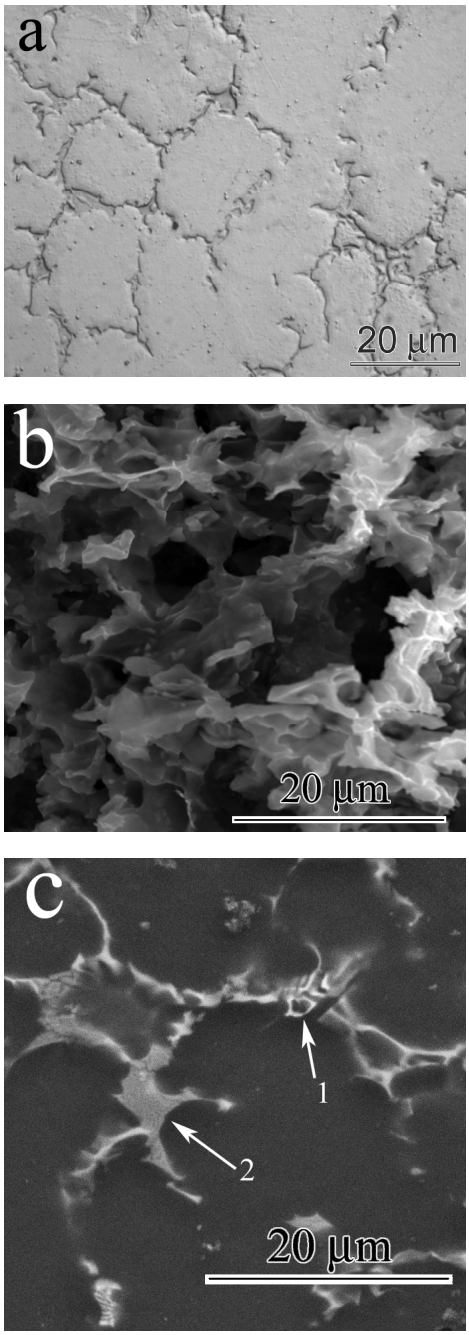

Figure 5. (a) Optical micrograph of as-cast MRI-153M showing grain boundary phases surrounding primary α-Mg grains (unetched) and (b) after 1 hour of deep etching to show the interconnected nature of the grain boundary phases (c) backscatter electron image with arrows indicating the (1) Ca-rich and (2) Sr-rich phases.

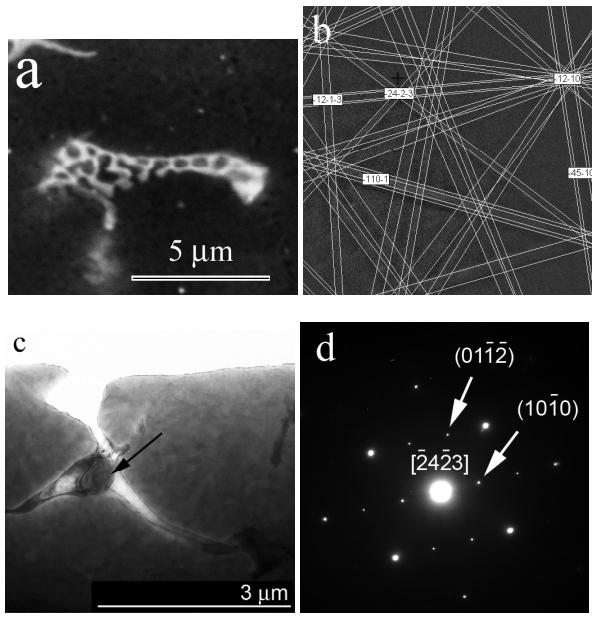

Figure 6. Intergranular (Mg, Al)$_2$Ca phase shown in SEM and identified by (b) an indexed EBSD pattern; also shown in (c) bright field TEM and identified by (d) SAD pattern from the particle in (c).

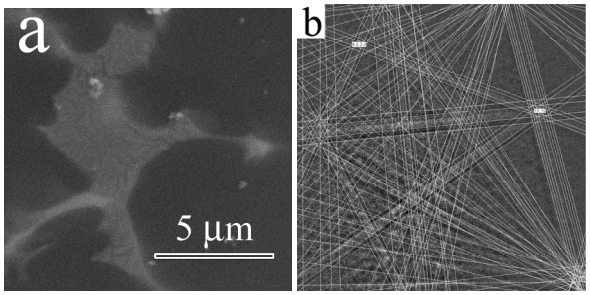

Figure 7. Intergranular (Mg, Al)$_2$(Sr, Ca) phase, shown by SEM and identified by (b) an indexed EBSD pattern.

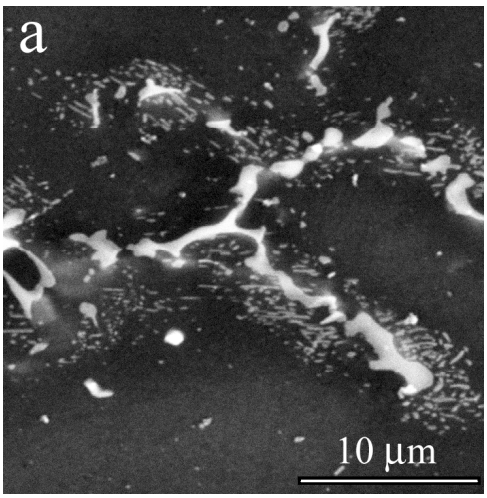

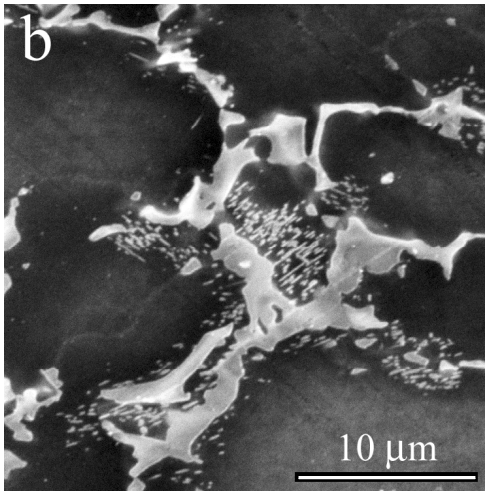

Figure 8. SEM images of (a) MRI-153, and (b) MRI-153M alloy annealed at 200 ^{o} C for 48 hours, showing the formation of $Al_{12}Mg_{17}$ precipitates in the α-Mg matrix near grain boundary regions.

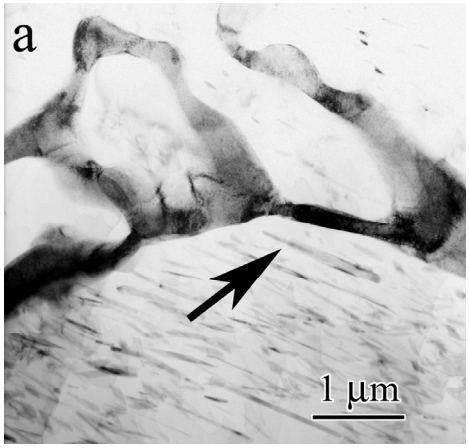

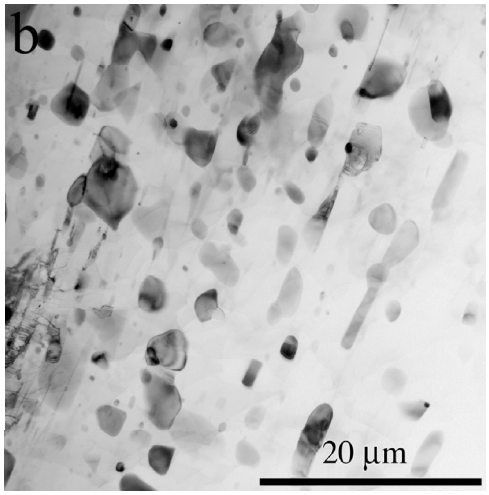

Figure 9. Bright field TEM images showing (a) fine intragranular precipitates and (b) relatively coarse $Al_{12}Mg_{17}$ precipitates in annealed MRI-153 alloy.

Conclusions

The microstructures of MRI-153 and MRI-153M high pressure die cast alloys were investigated in as-cast and annealed conditions. The microstructures of both alloys contained a calcium-rich grain boundary intermetallic phase described as $(Mg,Al)_2Ca$. Compared to AZ91D, the presence of $Al_{12}Mg_{17}$ was reduced in the MRI-153 alloy and appeared to be nearly completely suppressed in the MRI-153M alloy. The MRI-153M phase contained a hexagonal strontium-rich phase described here as $(Mg,Al)_2(Sr,Ca)$. Upon annealing, both alloys exhibited a distribution of relatively coarse $Al_{12}Mg_{17}$ precipitates in the vicinity of the grain boundary intermetallic phase network.

Acknowledgements

MVK gratefully acknowledges the financial support Monash University School of Physics and Materials Engineering and access to their electron microscopy center. TS is supported by a Technology New Zealand TIF project with ION Automotive, Auckland New Zealand.

References

1. M. O. Pekguleryuz, "Development of creep resistant magnesium diecasting alloys," *Materials Science Forum Proceedings of the 1st Nagaoka International Workshop on Magnesium Platform Science and Technology 2000*, 350 (2000), 131-40.

2. E. Cerri, et al., "A comparison of aging kinetics between a die cast and a thixocast magnesium alloy", *Magnesium Technology 2002*, ed. H. I. Kaplan (Warrendale, PA.: Minerals, Metals and Materials Society, 2002), 221-26.

3. S. Kleiner, O. Beffort and P. J. Uggowitzer, "Microstructure evolution during reheating of an extruded Mg-Al-Zn alloy into the semisolid state," *Scripta Mater*, 51 (5) (2004), 405-10.

4. K. Ozturk, et al., "Creep Resistant Mg-Al-Ca Alloys: Computational Thermodynamics and Experimental Investigation," *JOM*, 55 (11) (2003), 40-44.

5. F. von Buch and B. L. Mordike, "High-Temperature Properties of Magnesium Alloys", *Magnesium Alloys and Technology*, ed. K. U. Kainer (Weinheim: Wiley-VCH GmbH & Co. KGaA, 2003), 106-29.

6. R. Ninomiya, T. Ojiro and K. Kubota, "Improved heat resistance of Mg-Al alloys by the Ca addition," *Acta Metall Mater*, 43 (2) (1995), 669-74.

7. M. Vogel, O. Kraft and E. Arzt, "Creep behavior of magnesium die-cast alloy ZA85," *Scripta Mater*, 48 (8) (2003), 985-90.

8. M. Vogel, et al., "Microstructure of die-cast alloys Mg-Zn-Al(-Ca): A study by electron microscopy and small-angle neutron scattering," *Z Metallkd*, 94 (5) (2003), 564-71.

9. E. Baril, P. Labelle and M. O. Pekguleryuz, "Elevated Temperature Mg-Al-Sr: Creep Resistance, Mechanical Properties, and Microstructure," *JOM*, 55 (11) (2003), 34-39.

10. E. Aghion, et al., "Newly Developed Magnesium Alloys for Power-train Applications," *JOM*, 55 (11) (2003), 30-33.

11. P. Villars and L. D. Calvert, *Pearson's handbook of crystallographic data for intermetallic phases* (Materials Park, OH: ASM International, 1991).

12. A. Maltais, et al., "Improvements in the metallography of as-cast AZ91 alloy," *Mater Charact*, 52 (2) (2004), 103-19.

13. H. Nowotny, "Die Kristallstrukturen von Zn9Th und (Ag,Mg)2Ca," *Z Metallkd*, 37 (1946), 31-34.

14. A. Iandelli, "Crystallographic studies of the systems MAl2 - MGa2 (M=Yb, Ca, Eu, Sr)," *J Less-Common Metals*, 135 (1987), 195-98.

15. P. Schobinger-Papamantellos and P. Fischer, "Neutronenbeugungsuntersuchung der Atomverteilung von Mg17Al12," *Naturwissenschaften*, 57 (3) (1970), 128-29.

16. K. Schubert, et al., "Einige strukturelle ergebnisse an metallischen phasen," *Naturwissenschaften*, 47 (13) (1960), 303.

17. E. Ghali, "Corrosion and protection of magnesium alloys," *Materials Science Forum Proceedings of the 1st Nagaoka International Workshop on Magnesium Platform Science and Technology 2000*, 350 (2000), 261-72.

18. E. Czech, G. Cordier and H. Schafer, "CaMnxAl2-x und CaMn4Al8 Ternare Verbindungen der MgNi2 - Beziehungsweise ThMn12 Struktur," *J Less-Common Metals*, 90 (1983), 109-19.

19. L. Bourgeois, B. C. Muddle and J. F. Nie, "The Crystal Structure of the Equilibrium Phi Phase in Mg-Zn-Al Casting Alloys," *Acta Mater*, 49 (2001), 2701-11.

20. M. M. Makhumudov, et al., "Phase Equilibria in the Mg-Al-Sr System," *Russian Metallurgy*, 6 (1981), 209-12.

21. A. Prince and N. I. Nikitina, "Aluminum-Magnesium-Strontium", *Ternary Alloys A Comprehensive Compendium of Evaluated Constitutional Data and Phase Diagrams*, ed. G. Effenberg 1999), 413-25.

22. W. Blum, B. Watzinger and P. Zhang, "Creep of die-cast light-weight Mg-Al-base alloy AZ91hp," *Advanced Engineering Materials*, 2 (6) (2000), 349-55.

23. M. Regev, et al., "Continous versus interrupted creep in AZ91D magnesium alloy," *Mat Sci Eng*, 302 (1) (2001), 51-55.

Electron Backscatter Diffraction Mapping of Microstructural Evolution of Pure Magnesium during Creep

TAKANORI SATO and MILO V. KRAL

To provide new insight into microstructural development during creep, sequential electron backscatter diffraction (EBSD) orientation maps were obtained from fixed surface areas during interrupted creep tests of extruded pure magnesium. Samples were tested under two distinctly different conditions, *i.e.*, low-temperature power-law creep and high-temperature power-law creep. Three aspects of microstructural evolution during creep were observed. In both specimens, transient creep was marked by the elimination of tension twins formed during the extrusion process. As steady-state creep rates were obtained, both specimens exhibited an ever-decreasing contribution by basal slip accompanied by an ever-increasing contribution by prismatic slip. In the low-temperature specimen, prismatic slip was manifested by the formation of a network of new fine subgrains along original grain boundaries, resulting in a bimodal grain size distribution. However, the high-temperature specimen developed linear prismatic slip lines while maintaining its original grain size.

DOI: 10.1007/s11661-007-9360-x

I. INTRODUCTION

IN pure magnesium and some Mg-Al alloys, creep can be a significant factor from temperatures as low as 100 °C, which severely limits their possible automotive and aerospace applications.[1–3] In its common maximum operating temperature range of approximately 0 °C to 200 °C, the creep of magnesium is known to fit into the power-law-creep regime, governed by the ability for dislocation climb to take place.[1] Within the power-law-creep regime, as illustrated by the deformation mechanism map compiled by Frost and Ashby,[4] there is an inflection in the isostrain rate curves as the underlying creep mechanism shifts from "low-temperature power-law creep" to "high-temperature power-law creep." Mathematically, this is expressed as a low-temperature power-law creep exponent term of $n + 2$ (Eq. [1]) and a high-temperature power-law-creep exponent of n, with all other material property parameters held constant (Eq. [2]).

$$\dot{\gamma} \propto \left(\frac{\sigma_s}{\mu}\right)^{n+2} \quad [1]$$

$$\dot{\gamma} \propto \left(\frac{\sigma_s}{\mu}\right)^{n} \quad [2]$$

High-temperature power-law creep can take place *via* a lattice diffusion dominant mechanism, since there is enough thermal energy to permit significant self-diffusion.[4–6] In order to achieve a given creep rate at a lower temperature, a material within the low-temperature power-law-creep regime, with little thermal energy, would consequently require a higher stress. The material would thus undergo deformation primarily by a core diffusion dominant mechanism with dislocation short-circuiting, which is strongly dependent on dislocation density and the applied stress.

Although it has little industrial relevance, pure wrought magnesium has the experimental advantage of reduced macroscopic problems such as porosity, segregation, and grain size, and orientation variations that can be found in cast alloys. Furthermore, comprehensive creep data is readily available for pure magnesium,[4] enabling the comparison between the data obtained by past conventional creep tests and the present interrupted creep tests. One of the characteristics of the wrought magnesium is its inevitable tendency to form nonrandom texture as a result of the orientation of the extrusion direction with respect to the specimen geometry.[7,8] The creep deformation of magnesium is primarily dependent on the crystallographic orientation of the grains, because there are limited numbers of potential slip systems available for the hexagonal close packed (hcp) lattice. In particular, the orientation for the activation of basal slip becomes an important factor.[1,9] Therefore, in wrought magnesium where the prevailing texture can be oriented in a way to make basal slip difficult, such as in the case of a rolled sheet in tension, the activation of other high energy slip modes such as prismatic, pyramidal, or twinning becomes of interest.

Although the pioneering studies of creep by Roberts, Gibbs, Sherby, and others[10–15] provide good understanding of the underlying mechanisms of creep in polycrystalline magnesium, there is surprisingly little

TAKANORI SATO, PhD Student, and MILO V. KRAL, Associate Professor, are with the Department of Mechanical Engineering, University of Canterbury, Christchurch 8140, New Zealand. Contact e-mail: milo.kral@canterbury.ac.nz

Manuscript submitted January 31, 2007.
Article published online January 15, 2008

information available on microstructural development during creep, perhaps due to the greater industrial interest in Mg-Al alloys. Microstructurally, the high-temperature low-stress power-law creep is believed to exhibit an ordered arrangement of dislocation substructures resulting in the formation of subgrains that resemble slip lines.[6,11,16] On the other hand, low-temperature high-stress creep has been shown to be dominated by more localized clustering of dislocation cells or subgrains,[17] which eventually break down into fine grains. In this article, adjacent grain misorientations of 5 to 15 deg are considered subgrains and misorientations greater than 15 deg are considered grain boundaries.[18] The relationship between flow stress and subgrain size and its contribution to the creep rate is summarized by Sherby *et al.*[6] and remains an area of interest in the study of creep mechanisms.[17,19] Examples of low-temperature power-law creep microstructure can be observed in the compilation by Gandhi and Ashby[20] of creep at high-stress levels, and more recently a similar microstructure is also exhibited in the work by Liu and Wu[21] on creep of AZ31 at a very fast strain rate.

There has always been an interest in observing the sequential development of microstructure to elucidate mechanisms of change, rather than characterizing "before and after" cases. A case in point is the recent real-time synchrotron study of a copper alloy undergoing creep.[22] Electron backscatter diffraction (EBSD) enables the simultaneous observation of microstructure and analysis of crystallographic orientations that was previously only possible in transmission electron microscopy (TEM) and high energy diffraction techniques.[18,21,23–26] A significant advantage of EBSD is that it is a scanning electron microscopy (SEM)–based surface analysis technique that does not require destructive specimen preparation. Therefore, in the present study, a unique attempt was made to track and characterize the contrasting microstructure evolution of pure magnesium during both low-temperature and high-temperature power-law creep using a sequential EBSD technique, rather than conventional postfailure microstructure study. Creep tests were conducted on extruded 99.6 pct pure magnesium specimens and two sets of temperature-stress conditions were selected in order to represent the different power-law creep mechanisms.[4] The same selected regions were mapped at specific intervals during these tests using EBSD for orientation texture data in order to track microstructure, texture, and intragranular misorientations throughout the creep deformation process. It is envisioned that the same methods will be applied to more industrially relevant materials once the technique is developed and validated.

It must be noted that a surface analysis technique such as EBSD may reveal a microstructural development that differs from the bulk of the material. However, in many industrial applications of magnesium, such as sheet or intricate die-cast components, the specimen thickness is relatively small in relation to the grain size and thus the present EBSD analysis should still provide a relevant representation of the overall creep mechanisms.

II. EXPERIMENTAL PROCEDURES

An extruded ingot of 99.6 pct high-purity Mg with an average grain diameter of 40 μm was wirecut into miniature ASTM E8 rectangular tensile test specimen shapes with 3 × 4-mm cross section and 15-mm gage length. The specimens were not annealed prior to creep testing. The surfaces were polished with 0.05-μm colloidal silica and microhardness indents were placed as reference markers for EBSD mapping. Creep tests were conducted in a heated pure silicone oil bath to reduce the temperature fluctuations and surface oxidation. The specimen extension was measured by a linear variable displacement transducer (LVDT) extensometer with a resolution of 1 μm.

Two creep tests were conducted, with specimen 1 at 373 K and 50.2 MPa, and specimen 2 at 473 K and 17.7 MPa. These conditions were selected to achieve a minimum creep strain rate of 2.5 to 5×10^{-7}/s for both specimens, based on the available data for pure magnesium[4] and consideration of the grain size (approximately 40 μm).[27] The samples were removed from the creep test every 6 hours and the same predetermined surface locations were repeatedly mapped by EBSD. The surface was lightly polished prior to each EBSD map with 0.05-μm colloidal silica to remove the oxide layer formed during the creep test. The polishing step removed up to 5 μm of thickness and therefore the procedure is not strictly nondestructive. However, this effect was considered negligible, since the general microstructure showed minimal variations. The automated EBSD maps were constructed on a 560 × 410-μm window with 1-μm step intervals using an HKL Channel 5 EBSD system (Oxford Instruments HKL, Hobro, Denmark) on a JEOL JSM-6100 SEM (Tokyo, Japan). A schematic of the specimen geometry is shown in Figure 1.

III. RESULTS

Figure 2 shows a plot of creep-strain *vs* time for the interrupted creep tests. The data exhibits the expected transient in the first 20 hours, with up to 4 pct deformation, which is the primary transient creep stage.

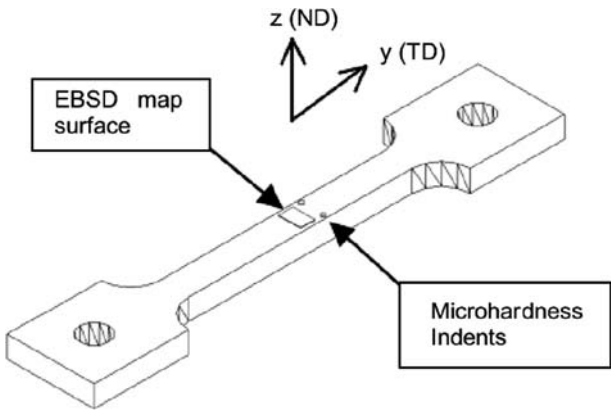

Fig. 1—Geometry of creep specimen indicating the tensile direction (TD) and EBSD scan normal direction (ND).

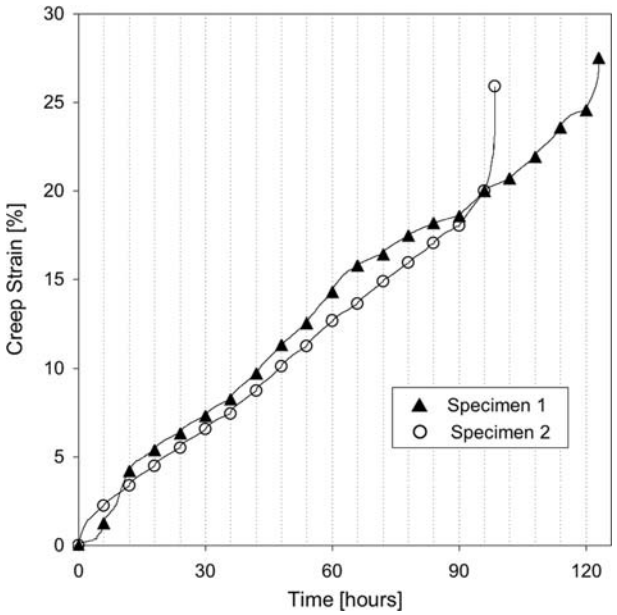

Fig. 2—Combined creep-strain graphs of specimens 1 and 2. Each marker represents an interruption.

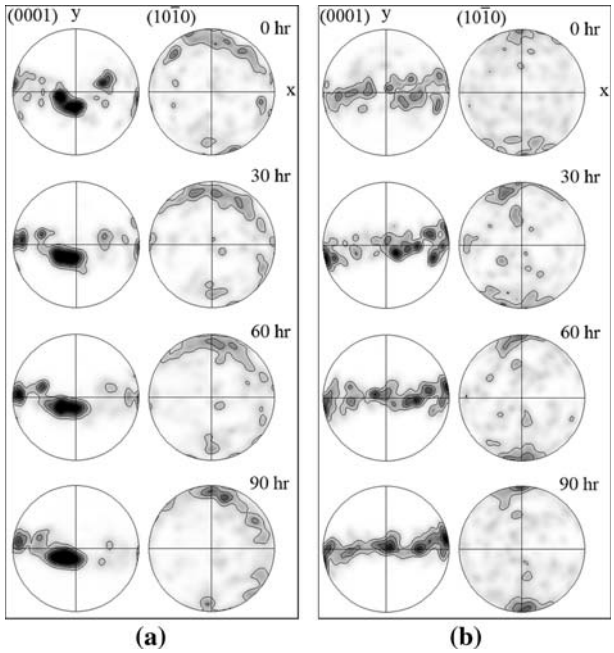

Fig. 3—Sequence of pole figures for (*a*) specimen 1 and (*b*) specimen 2 before creep and after 30, 60, and 90 h of creep. Each contour line is at 2 MUD apart. The *z*-axis is specimen surface normal, *y*-axis is tensile axis, and *x*-axis is specimen transverse direction.

Secondary creep then produced a consistent creep-strain rate even after each interruption, which suggests that the periodic removal of the creep specimen did not lead to any significant shock or cyclic loading issues. The secondary creep rates of specimen 1 and 2 were 5.31×10^{-7} and 5.26×10^{-7}/s, respectively. This agrees very well with the creep rate initially predicted (2.5 to 5×10^{-7}/s).

Since the texture data were collected at 6-hour intervals on the same area, the deformation process is best illustrated as a time-sequence animation of pole figures and orientation maps. Since animation is not possible in printed publication, Figure 3 offers a compromise by showing selected pole figures from the specimens at much larger time intervals. The axes in Figure 3 refer to the coordinate system identified on Figure 1, where the *z*-axis is the specimen surface normal, *y*-axis is the tensile axis, and the *x*-axis is the specimen transverse direction. The initial specimen texture showed characteristics typical of extruded wrought magnesium, where the specimens were cut in an orientation with a strong (0001) texture facing the specimen surface.[28,29] The initial texture is similar to a rolled sheet texture, but without significant grain elongation in the rolling direction since the material would have experienced recrystallization during the extrusion process.[30] Although the two specimens originated from the same source material, the difference in initial texture between them was unavoidable due to the inhomogeneity in the specimen and the limitation in the size of surface area covered by the EBSD mapping technique.

The original texture contained tension twins and deformed grains caused by the compressive stress of the extrusion process. As creep progressed, both specimens showed the typical tendency for the (0001) plane normals to gradually rotate perpendicular to the *y*-axis (the tensile axis).[29] This effect appears subtle in Figure 3, but can be observed as a reduction in scatter of (0001) planes and a slight migration of the (0001) plane normal toward the equator. This behavior is typical of tensile creep in hcp material.[31] Basal slip, with the most easily activated slip system in hcp magnesium, contributes to the specimen strain until the basal planes align parallel to the tensile axis. Through this process, basal slip gradually becomes less favorable as the resolved shear stress upon the (0001) planes tends toward zero.[29] The data shown in Figure 3 appears similar to pole figures that can be generated in X-ray diffraction experiments, but it should be noted that these pole figures were obtained from the exact same local regions on the specimens' surface, after each interruption. The contour lines are drawn at intervals of two multiples of uniform distribution (MUD), which shows the strength of the clustering of poles relative to that of a random distribution.

Figure 4 shows the sequence of EBSD orientation maps obtained from both specimens as creep progressed. These maps were created by contrast based on the crystallographic orientation, where darker areas represent (0001) facing the *x*-axis, and the lighter areas having (0001) facing the *z*-axis. Grain boundaries have also been superimposed. It must be noted that there is a significant difference in microstructural appearance between the 0- and 30-hour maps. This is attributed to the fact that the actual interruption intervals were in fact 6 hours, hence a significant amount of initial transient creep deformation and up to 25 μm of material was removed by surface polishing during each 30-hour interval. However, the pole figures in Figure 3 suggest that such changes in appearance did not significantly alter the overall texture. It can be seen that both specimens exhibit $\{10\bar{1}2\}\langle\bar{1}011\rangle$ tension twin boundaries created by the extrusion process.

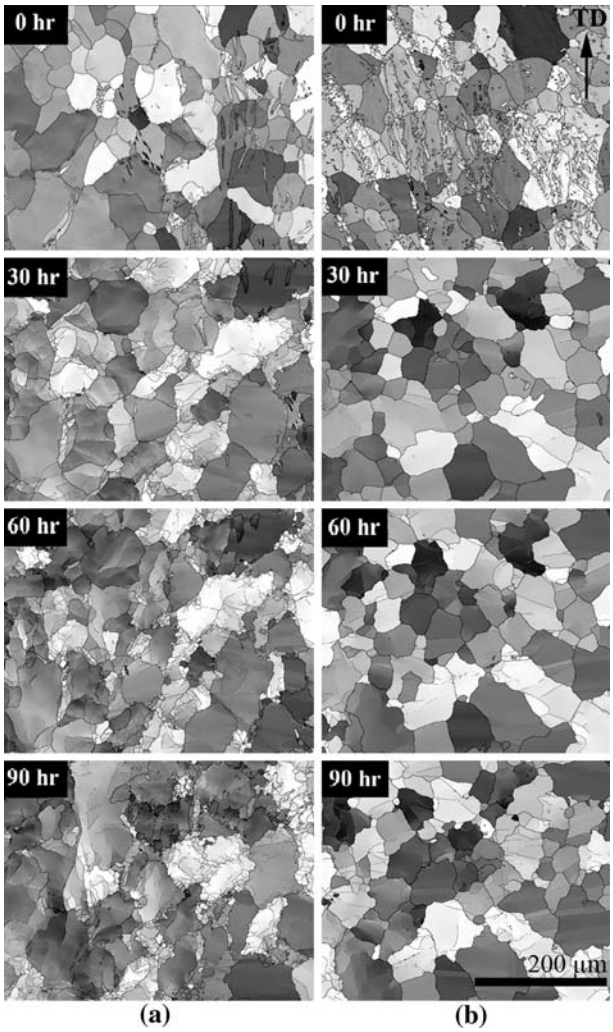

Fig. 4—EBSD orientation maps of (*a*) specimen 1 and (*b*) specimen 2 as creep progresses.

A typical twin is shown at higher magnification in Figure 5(a), where the $\{10\bar{1}2\}$ boundary indices and the misorientation angle of 86.5 deg were determined by the EBSD software. In the early stages of creep, both specimens exhibited a reduction in the number of tension twin boundaries. No development of $\{10\bar{1}1\}\langle\bar{1}210\rangle$ compression twins[32–34] was observed, which is not surprising since the specimens texture did not favor the formation of compression twins.[35,36] The proportion of tension twins was quantified by the HKL software by the relative frequency of 86 deg misorientation boundaries between adjacent EBSD pattern pairs, as shown in Figure 5(b). (The automated measurement of twin frequency was confirmed by manual counting.) After testing commenced, the relative frequency of twins dropped rapidly until approximately 30 hours of testing and then remained at a steady, relatively low value.

After the initial transient stage, both specimens developed relatively high frequencies of low-angle subgrain boundaries. This is quantified in Figure 6, which shows the relative frequency of 5 to 15 deg misorientation boundaries at each creep interruption stage. Boundaries misoriented less than 5 deg were not displayed in the figures so that the significant (5 to 15 deg misorientation) low-angle boundaries are clearly visible. A high-angle grain boundary misorientation was defined as 15 deg, according to established convention.[37,38] Specimen 1 exhibited a rapid development of low-angle boundaries during the early stages of creep compared to specimen 2, but after approximately 70 hours both specimens settled to a similar frequency occurrence of low-angle boundaries.

The characteristic difference between the specimens was that specimen 1 exhibited a clustering of low-angle boundaries near the original high-angle boundaries to a point where, after approximately 96 hours (16 pct deformation), subgrains had evolved into a network of fine grains as illustrated in Figure 7(a). This observation is quantified in Figure 8, where the average grain size of specimen 1 increased during the initial transient stage due to the elimination of twins, followed by a reduction in average grain size after 48 hours of creep. There is a large scatter in specimen 1 average grain size data beyond 48 hours, since some fine subgrains lie in the borderline range for EBSD grain detection criteria and are also easily affected by the surface polishing process. In contrast, specimen 2 formed parallel lines of

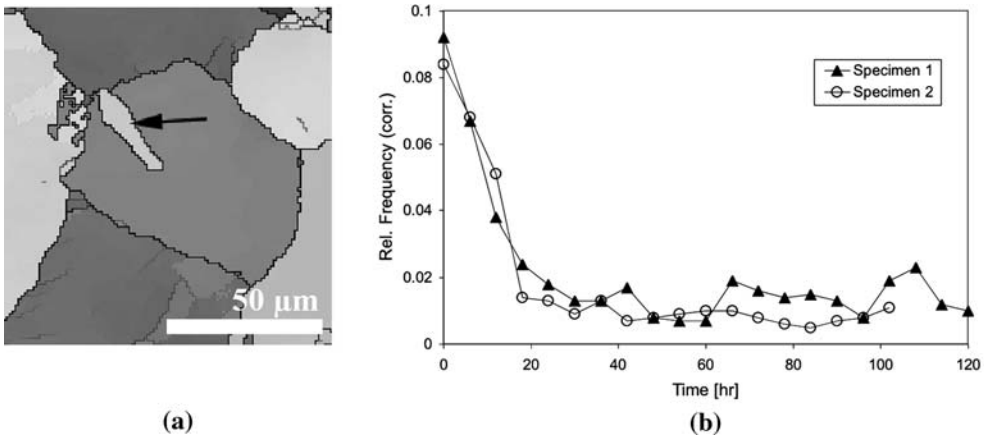

Fig. 5—Typical tension twin boundary identified on (*a*) EBSD map of specimen 1 with 86.5 deg misorientation on $\{10\bar{1}2\}$ and (*b*) frequency of 86 deg twin misorientation pairs relative to total number of boundaries with misorientation greater than 3 deg.

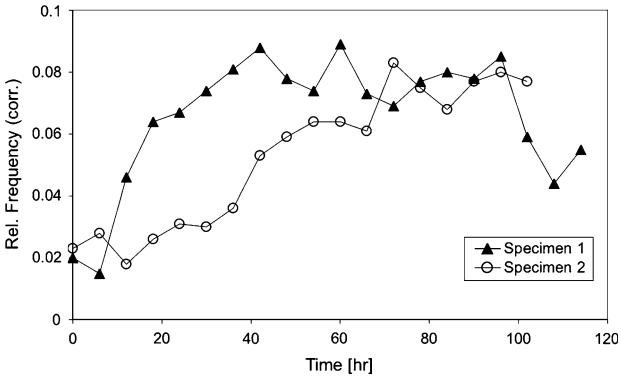

Fig. 6—Frequency of misorientation pairs with 5 deg low-angle boundary relationships in each EBSD map relative to the total number of boundaries with misorientation greater than 3 deg.

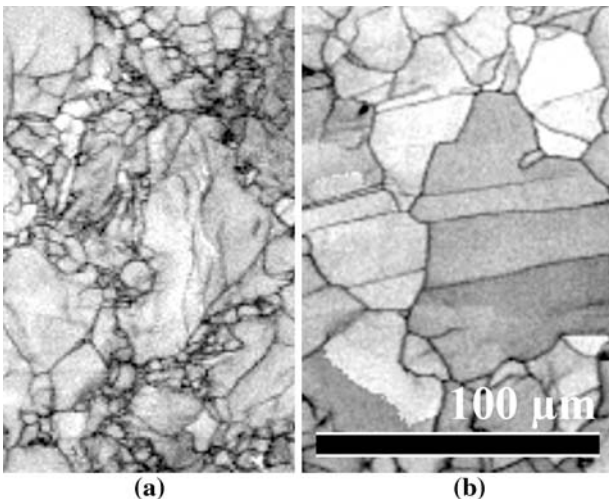

Fig. 7—Pattern quality maps of (*a*) specimen 1 and (*b*) specimen 2 at 96 h of creep.

low-angle boundaries in certain grains as shown in Figure 7(b) and, after the transient stage, the grain size of specimen 2 maintained a steady value until failure finally occurred (Figure 8).

Figure 9 shows the final grain size distributions in both specimens, in terms of both frequency of occurrence and total area for a range of grain size categories. Specimen 1 had few very large grains and a relatively large number of small grains after 96 hours of creep. Conversely, specimen 2 shows a near-Gaussian distribution of grain size after 96 hours of creep, which is basically unchanged from the original distribution.

IV. DISCUSSION

The time-sequence crystallographic orientation maps from the sequential EBSD technique provide new insight to the study of creep. The present work showed three important aspects of microstructural development during creep of pure wrought magnesium. The first aspect consists of the statistical reduction of the number of tension twins. Second, strain also occurs *via* a simple

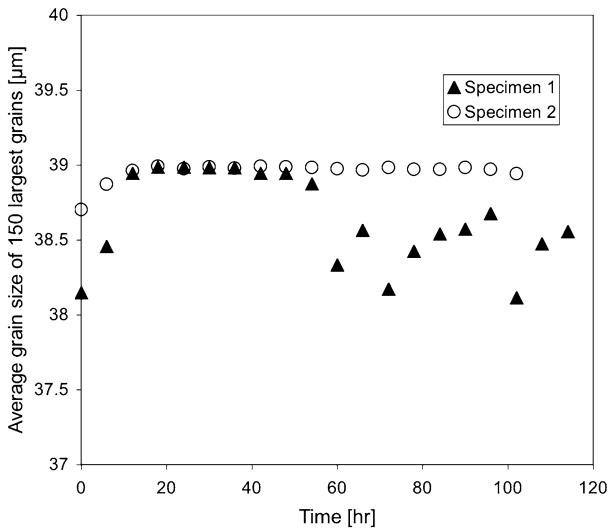

Fig. 8—Average grain size *vs* time. Criteria for "grain" is a region fully surrounded by high-angle (> 15 deg) boundaries.

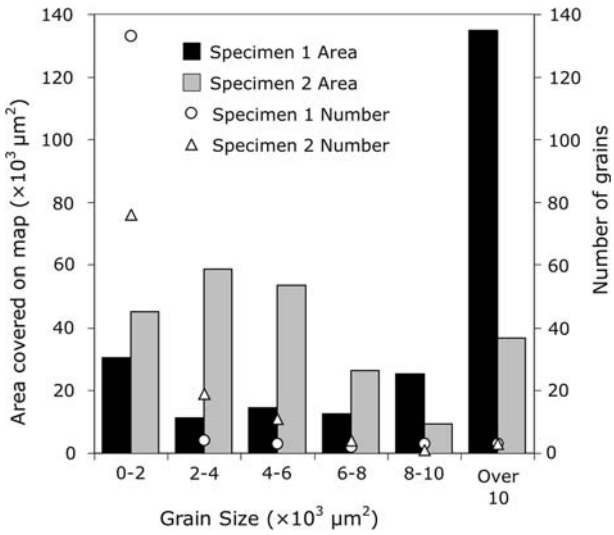

Fig. 9—Grain size distributions after 96 h of creep for both specimens as measured automatically *via* EBSD.

hcp *a*-axis basal slip until the supply of the available "crystallographically soft" grains gradually dwindles, which is illustrated by the rotation of (0001) poles toward the equator in the pole figures of Figure 3.

The first two aspects of microstructural development are similar in mechanism and magnitude in both the low-temperature and high-temperature power-law creep regimes. However, there is a departure in behavior of the two regimes at approximately 60 hours of creep, which is marked by a change in average grain size (Figure 8) for the low-temperature power-law-creep regime.

In the third aspect of microstructural development, which distinguished the two different creep regimes, subgrain boundaries gradually become more evident as illustrated in Figures 7(a) and (b). In low-temperature power-law creep, low-angle boundaries form and subsequently develop into fine grain networks near the

original grain boundaries. This observation suggests a localized short-circuiting of dislocations toward the nearest grain boundaries, and is consistent with (1) insufficient thermal energy to activate creep deformation by lattice diffusion alone,[39] and (2) an increase in dislocation density due to the relatively high applied stress. In contrast, high-temperature power-law creep, although experiencing a similar level of strain, displays no noticeable fine grain formation near the original grain boundaries. Instead, low-angle boundaries tend to align themselves into what can be observed as straight parallel lines, as shown on Figures 4 and 7.

For pure magnesium, the only other microstructural characterization of creep near the current test conditions (to the authors' knowledge) was provided by Roberts,[11] who illustrated a combination of both fine grain networks and slip line formation due to ambiguous test conditions. The work performed in the current research intentionally separated the two regimes of microstructural development, by firmly choosing test conditions in low-temperature power-law creep and high-temperature power-law creep for specimens 1 and 2, respectively.

The pattern quality map in Figure 7 reveals low-angle boundaries and damaged regions (*i.e.*, poor pattern quality) more clearly than the equivalent Euler orientation maps, but does not provide any information about the orientation and significance of each of the observed boundaries, since both low and high-angle boundaries appear as dark regions. One benefit of EBSD mapping is the diverse method of expressing the map data, which is especially useful in the present case to further elucidate the microstructural evolution of high-temperature power-law creep (specimen 2). Figure 10 highlights the significant low-angle (~5 to 15 deg) boundaries in red, and the grains are colored based on the orientation of the (0001) planes with (0001) normal alignment to the specimen *x*-axis, *y*-axis, and *z*-axis colored green, yellow, and blue, respectively, as illustrated in the accompanying pole figure. Figure 10(b) clearly shows that, in specimen 2, the green grains exhibit parallel lines of low-angle boundaries, whereas the low-angle boundaries appear broken and disordered in the blue grains. It is also noted that there are no yellow grains, since there are no grains with (0001) plane normals oriented parallel to the specimen *y*-axis (tensile axis). In contrast to the observations in high-temperature power-law creep (specimen 2), low-temperature power-law creep (specimen 1) showed little ordered deformation by lattice slip, as shown on Figure 10(a). Both blue and green grains showed less development of ordered low-angle boundaries, and the accumulation of low-angle boundaries and breakup near the original grain boundaries is apparent, while the original grain interiors remain relatively undamaged.

By tracking the same area as creep progressed, inverse pole figures can be utilized to illustrate the texture development within specific grains of interest at a given point in time.[37] Typical examples of grains of significantly different orientations in specimen 2 are shown in Figure 11. The respective pole figures show that these grains have their basal plane normals oriented nearly perpendicular to the tensile axis (the *y*-axis), hence deformation by basal slip is restricted due to the low

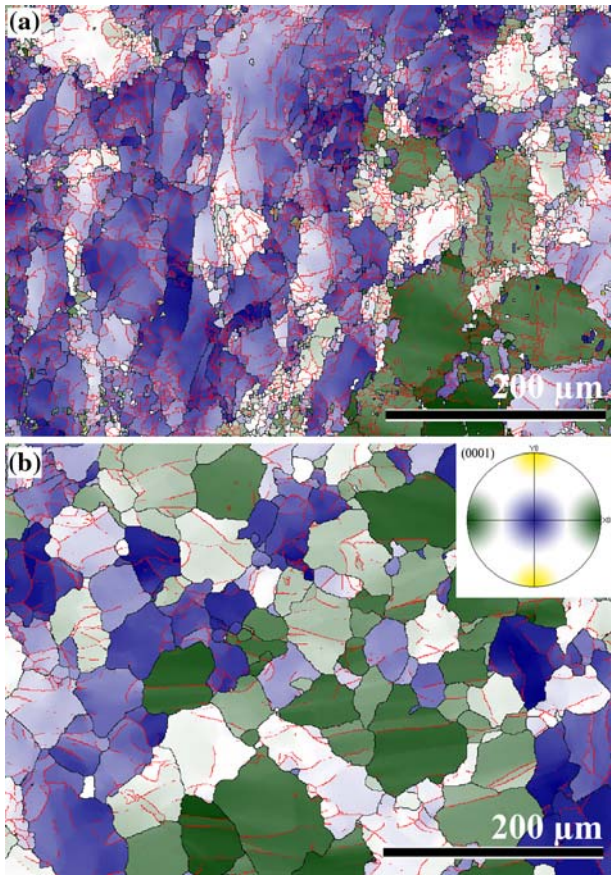

Fig. 10—Grain orientation map of (*a*) specimen 1 and (*b*) specimen 2 at 90 h of creep.

Schmid factor.[35] As mentioned previously, due to the high temperature, this orientation could allow the activation of $\{10\bar{1}0\}\langle 11\bar{2}0\rangle$ prismatic slip,[10,35] where low-angle boundaries observed on the map of Figures 10 and 11 (at higher magnification) correspond with the prismatic slip planes. The green grains such as grains "a" and "b" in Figure 11 have their (0001) oriented toward the *x*-axis, and parallel slip lines are visible. In comparison, the blue grains such as grains "c" and "d" have their (0001) oriented toward the *z*-axis and the slip lines of the three possible prismatic slip systems will be 60 deg apart. This is consistent with the general disorder and breakup in the blue grains. The third aspect is thus characterized by prismatic slip, which increases as basal slip decreases. There is no distinct point at which basal or prismatic slip will stop or start. Instead, a crossover will occur, as basal slip becomes less dominant and prismatic slip more so.

The parallel observation of two different creep deformation regimes in sequence has successfully linked classical diffusion-based creep theories with microstructural observations, and holds the potential to provide useful data toward the texture and deformation modeling and simulations. Recent computer-based texture simulation techniques can predict the likely overall texture development of a polycrystalline structure, but have difficulty in modeling the subgrain formation and breakup into high-angle boundaries due to the

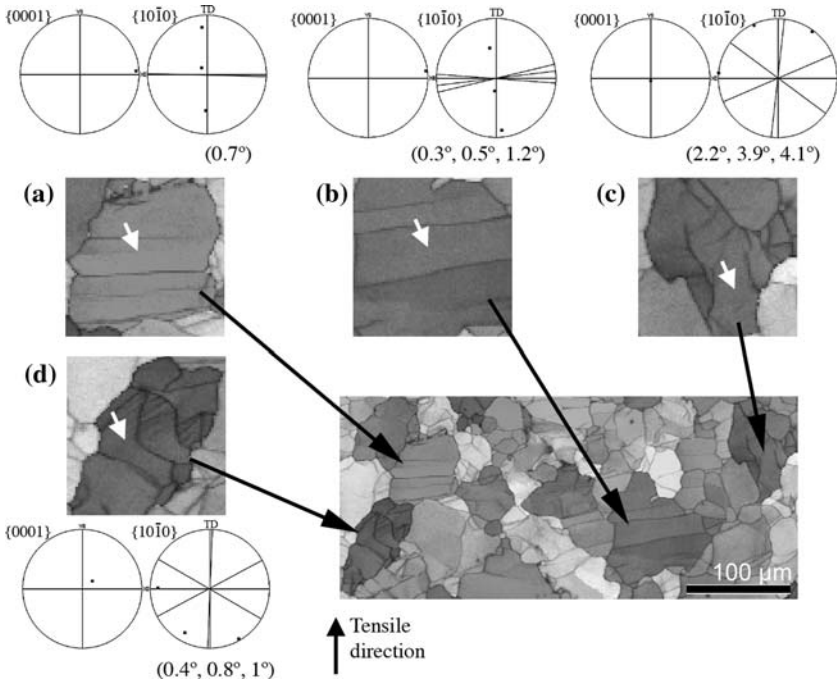

Fig. 11—Pole figures with trace lines corresponding to likely prismatic low-angle boundaries. Pole figures were taken from the locations indicated by white arrows. Angles indicate the difference in measurement between the pole figure and observed slip traces.

complexity of the transitions in contributing mechanisms. Although TEM could provide higher resolution information regarding the activity of individual dislocations in specific grains, sequential EBSD analysis could be used to illustrate the effects of various creep deformation regimes with the advantages of greater statistical robustness and relative ease in specimen preparation, while avoiding complete specimen destruction.

V. CONCLUSIONS

Sequential orientation mapping of creep specimen surfaces was found to be an effective method for analyzing the evolution of microstructure during creep. In the present experiments in pure magnesium, two creep regimes, low-temperature and high-temperature power-law creep, were studied. In each regime, three aspects of microstructural evolution were shown to occur. The first two aspects: (1) the elimination of compressive twins and (2) the rotation of (0001) plane normals in ''soft'' grains to be perpendicular to the tensile axis (*i.e.*, a hardening process), were shared in both creep regimes. The regimes differed in the third aspect. Low-temperature power-law creep exhibited the formation of fine grains (specimen 1) while high-temperature power-law creep developed slip lines (specimen 2) induced by the prismatic slip.

REFERENCES

1. K.U. Kainer: *Magnesium Alloys and Technology*, Wiley-VCH, New York, NY, 2003, pp. 1–22.
2. B.L. Mordike: *Mater. Sci. Eng. A*, 2002, vol. 324, p. 103.
3. M.O. Pekguleryuz: *Materials Science Forum Proc. 1st Nagaoka Int. Workshop on Magnesium Platform Science and Technology*, Trans Tech Publications Inc., Switzerland, 2000, vol. 350, p. 131.
4. H.J. Frost and M.F. Ashby: *Deformation-Mechanism Maps*, Pergamon Press, Oxford, 1982, pp. 43–52.
5. F.R.N. Nabarro: *Acta Mater.*, 2006, vol. 54, p. 263.
6. O.D. Sherby, R.H. Klundt, and A.K. Miller: *Metall. Trans. A*, 1977, vol. 8A, p. 843.
7. G.S. Rao and Y.V.R.K. Prasad: *Metall. Trans. A*, 1982, vol. 13A, p. 2219.
8. S.R. Agnew and O. Duygulu: *Int. J. Plast.*, 2005, vol. 21, p. 1161.
9. D.J. Bacon and V. Vitek: *Metall. Mater. Trans. A*, 2002, vol. 33A, p. 721.
10. C.S. Roberts: *Magnesium and Its Alloys*, John Wiley & Sons, Inc., New York, NY, 1960, pp. 81–125.
11. C.S. Roberts: *JOM*, 1953, vol. 5, p. 1121.
12. G.B. Gibbs: *Phil. Mag.*, 1966, vol. 13, p. 317.
13. O.D. Sherby and J. Weertman: *Acta Metall.*, 1979, vol. 27, p. 387.
14. H.E. Evans and G. Knowles: *Acta Metall.*, 1977, vol. 25, p. 963.
15. J. Weertman: *Trans. ASM*, 1968, vol. 61, p. 681.
16. W.J.M. Tegart: *Acta Metall.*, 1961, vol. 9, p. 614.
17. H. Brehm and G.S. Daehn: *Metall. Mater. Trans. A*, 2002, vol. 33A, p. 363.
18. F.J. Humphreys and P.S. Bate: *Acta Mater.*, 2006, vol. 54, p. 817.
19. W. Blum, P. Eisenlohr, and F. Breutinger: *Metall. Mater. Trans. A*, 2002, vol. 33A, p. 291.
20. C. Gandhi and M.F. Ashby: *Acta Metall.*, 1979, vol. 27, p. 1565.
21. Y. Liu and X. Wu: *Metall. Mater. Trans. A*, 2006, vol. 37A, p. 7.
22. A. Pyzalla, B. Camin, T. Buslaps, M. Di Michiel, H. Kaminski, A. Kottar, A. Pernack, and W. Reimers: *Science*, 2005, vol. 308, p. 92.
23. F.J. Humphreys: *J. Mater. Sci.*, 2001, vol. 36, p. 3833.
24. S.B. Yi, S. Zaefferer, and H.G. Brokmeier: *Mater. Sci. Eng. A*, 2006, vol. 424, p. 275.
25. L. Helis, K. Okayasu, and H. Fukutomi: *Mater. Sci. Eng. A*, 2006, vol. 430, p. 98.
26. M.D. Nave and M.R. Barnett: *Scripta Mater.*, 2004, vol. 51, p. 881.
27. C.R. Barrett, J.L. Lytton, and O.D. Sherby: *Trans. AIME*, 1967, vol. 239, p. 170.

28. A. Beck: *The Technology of Magnesium and Its Alloys*, F.A. Hughes & Co. Ltd., London, 1941, pp. 166–77.
29. R.W.K. Honeycombe: *The Plastic Deformation of Metals*, Edward Arnold Publishers, London, 1984, pp. 200–20.
30. W. Bulian and E. Fahrenhorst: *Metallography of Magnesium and Its Alloys*, F.A. Hughes & Co. Ltd., London, 1944, p. 38.
31. G.E. Dieter: *Mechanical Metallurgy*, McGraw-Hill, New York, NY, 1961.
32. S.R. Agnew, M.H. Yoo, and C.N. Tome: *Acta Mater.*, 2001, vol. 49, p. 4277.
33. M.R. Barnett: *Mater. Sci. Eng. A*, 2007, vol. 464, pp. 1–7.
34. M.R. Barnett: *Mater. Sci. Eng. A*, 2007, vol. 464, pp. 8–16.
35. M.R. Barnett, Z. Keshavarz, and X. Ma: *Metall. Mater. Trans. A*, 2006, vol. 37A, p. 2283.
36. Z. Keshavarz and M.R. Barnett: *Scripta Mater.*, 2006, vol. 55, p. 915.
37. V. Randle: *The Measurement of Grain Boundary Geometry*, Institute of Physics Publishing, Bristol, 1993, pp. 112–41.
38. F.J. Humphreys: *Scripta Mater.*, 2004, vol. 51, p. 771.
39. L. Shi and D.O. Northwood: *Acta Metall. Mater.*, 1994, vol. 42, p. 871.

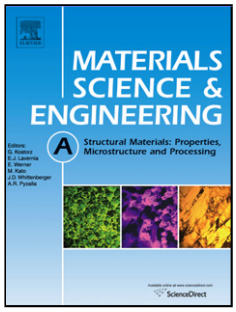

Title: Microstructural Evolution of Mg-Al-Ca-Sr Alloy During Creep

Authors: T. Sato, M.V. Kral

PII: S0921-5093(08)00980-5
DOI: doi:10.1016/j.msea.2008.08.006
Reference: MSA 24468

To appear in: *Materials Science and Engineering A*

Received date: 30-6-2008
Revised date: 11-8-2008
Accepted date: 11-8-2008

Please cite this article as: T. Sato, M.V. Kral, Microstructural Evolution of Mg-Al-Ca-Sr Alloy During Creep, *Materials Science & Engineering A* (2007), doi:10.1016/j.msea.2008.08.006

Microstructural Evolution of Mg-Al-Ca-Sr Alloy During Creep

T. Sato and M. V. Kral

Department of Mechanical Engineering, University of Canterbury

Private Bag 4800, Christchurch New Zealand

Keywords: Creep, Magnesium, Mg-Al-Ca, EBSD, texture, deformation

To provide new insight into microstructural development during creep, sequential EBSD (electron backscatter diffraction) orientation maps were obtained from fixed surface areas at intervals in creep tests of a high-pressure die-cast Mg-8.5Al-1Ca-0.3Sr alloy. Samples were tested at 200 ºC at various stress levels to achieve power-law creep behavior. In all specimens, steady-state creep was marked by the formation of tension twins. At intermediate stress levels, specimen failure was initiated by the formation of defects at boundaries with high crystallographic misorientation. However, at high stress levels, the failure mechanism was assisted by the crack formation at interdendritic boundaries with low crystallographic misorientation.

Introduction

In many Mg-Al alloys, creep can be a significant factor from temperatures as low as 100 ºC, which severely limits their possible automotive and aerospace applications [1, 2]. It has been suggested that this is primarily caused by the formation of grain boundary α-Mg + $Al_{12}Mg_{17}$ eutectic, which is thermally unstable and prone to aging [3]. In alloy design, it is therefore of great interest to suppress the formation of $Al_{12}Mg_{17}$, while retaining aluminum content of up to 9% in order to maintain castability and room temperature strength comparable to the conventional AZ91 alloy [1]. Recent creep resistant alloys rely on the formation of aluminum-rich precipitates (other than $Al_{12}Mg_{17}$) that are stable at elevated temperatures to act as stable barriers against dislocation motion [1]. In recent developments, such precipitates are typically intermetallic compounds of magnesium or aluminum with rare earths, calcium, and/or strontium.

As the creep resistance of some magnesium alloys has reached the levels comparable to some aluminum alloys [4], interests in current developments tend toward reducing alloying costs (e.g., reducing the use of expensive additions such as rare earths and strontium). In the last decade, an addition of up to 3% calcium has gained attention, in which the formation of thermally stable Al_2Ca achieves a similar creep resistance compared to Mg-RE alloys at significantly lower cost [5]. The present work is a fundamental study of microstructural evolution during creep of high-pressure die cast alloy Mg-8.5Al-1Ca-0.3Sr.

In its typical intended operating temperature range of up to 200ºC, pure magnesium is known to fit into the power-law creep regime, governed by the ability for dislocation climb to take place [6], and has been confirmed in recent experimental work [7]. For a complex alloy such as the Mg-Al-Ca-Sr in the current study, a simple power-law creep model is inadequate. This deviation from the conventional power-law relationship can be broadly attributed to three aspects.

1. Supersaturated aluminum in the primary α-Mg matrix may increase the resistance to lattice diffusion creep.
2. If lattice diffusion creep is inhibited so that the contribution of grain boundary creep becomes significant, the interdendritic network of the stable intermetallic phase may act as barriers against grain boundary creep.
3. A complex dendritic microstructure may behave differently to the predictions based on homogeneous equiaxed grain structure.

Obviously, compared to single phase wrought materials, the present cast Mg-Al-(Ca,Sr) alloys are relatively complex since they are dendritic. With dendritic structures, it is critical to distinguish between secondary dendrite arm boundaries and random, high angle grain boundaries between dendrites. It has been suggested that high angle grain boundaries are more susceptible to diffusional creep and grain boundary sliding [8, 9], thus it is likely that creep damage will occur at high angle grain boundaries rather than secondary dendrite arm boundaries. Confusion arises because many of the past studies on the creep of magnesium alloys have simply referred to any dendrite arm boundary with intermetallic particles as grain boundaries, irrespective of their crystallographic misorientation e.g. [10-12]. The present study will distinguish boundaries between individual dendrites and secondary dendrite arms.

However, the distinction between dendrite arm boundaries and random, high-angle grain boundaries is particularly difficult with the usual metallographic methods. An illustration of this difficulty is shown in Figure 1(a), which is a secondary electron image of a polished section of the present Mg-8.5Al-1Ca-0.3Sr alloy. In the present study, a high angle boundary is

defined as a boundary with crystallographic misorientation of greater than 15º [13]. The electron backscatter diffraction (EBSD) orientation map of the same area in Figure 1(b) clearly reveals the high angle misorientation boundaries with a calculated average grain diameter of 375 µm. Figure 1(c) is secondary electron image of a grain labeled 'A' and shows the secondary dendrite arm boundaries in that grain with a measured spacing of 58 µm.

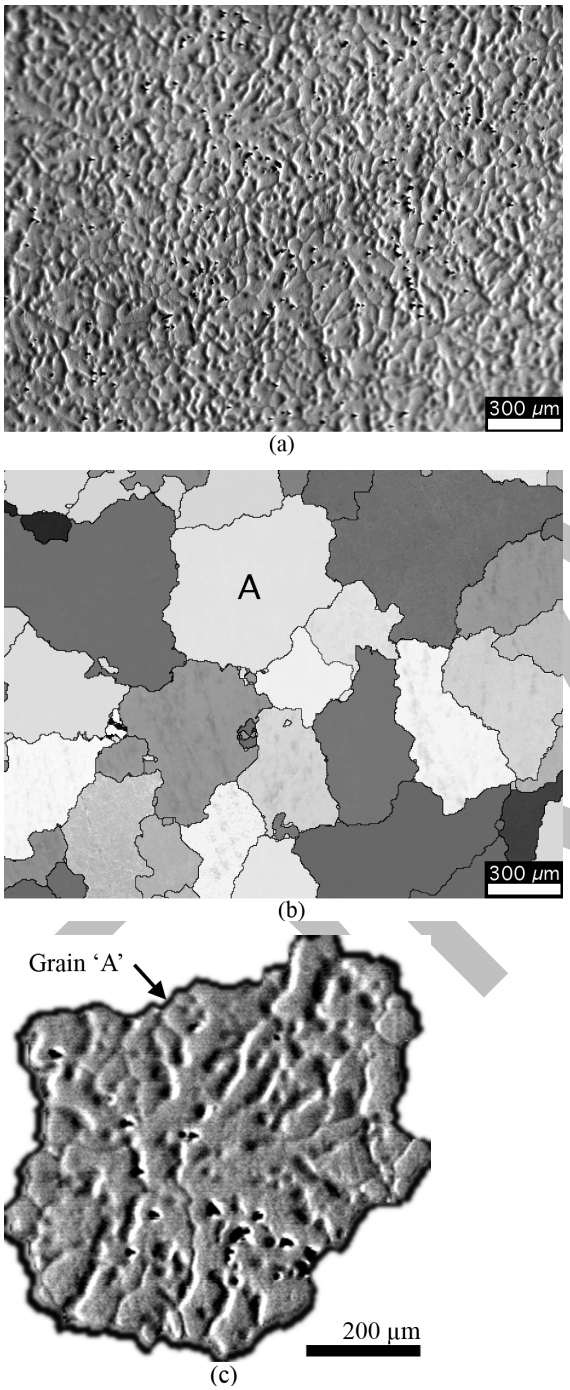

Figure 1. (a) Secondary electron image of the Mg-8.5Al-1Ca-0.3Sr alloy, (b) EBSD orientation map of the same area, and (c) a higher magnification secondary electron image of grain 'A' illustrating the secondary dendrite arm boundaries within the grain.

A further complexity to the present alloy is that intermetallic phases are distributed on both primary and secondary dendrite arm boundaries. The prevalent Mg_2Ca-type interdendritic phase has been reported to have a rational orientation relationship with the parent, primary α-Mg dendrites [10]. Post-creep microstructure studies on a Mg-4Al-2Sr alloy by Bai *et al.* [11] showed that creep cracks follow intermetallic precipitate interfaces, and concluded that both lattice diffusion and grain boundary sliding contribute to creep. The study further reported that creep resistance was compromised when the interdendritic, intermetallic phase network was made discontinuous upon annealing [14]. Thermodynamic calculations by Han *et al.* [15] indicate that creep in magnesium alloys is dependent on the existence of non-uniform stress distributions near intermetallic precipitate interfaces, and the stability of the α-Mg and the intermetallic phase will determine the effective contribution of the precipitate interfaces on the creep rate. The influence of the morphology, distribution and crystallography of the intermetallic phases in the present alloy was not specifically studied here, and is the subject of ongoing work.

A detailed microstructural analysis of the current alloy in as-cast condition was carried out previously and is reported elsewhere [16]. Essentially, the alloy consists of a dendritic primary α-Mg structure with a network of interdendritic Mg_2Ca-type precipitates with varying degrees of Al and Sr substitution, therefore more accurately described as $(Mg, Al)_2(Ca, Sr)$. These precipitates are most likely the dihexagonal (C36) $(Mg,Al)_2Ca$ phase identified on a recent detailed study of a similar structure by Suzuki et al. [17]. An optical microscope image of the alloy microstructure is shown in Figure 2. It is important to note that no $Al_{12}Mg_{17}$ β-phase was observed in that study.

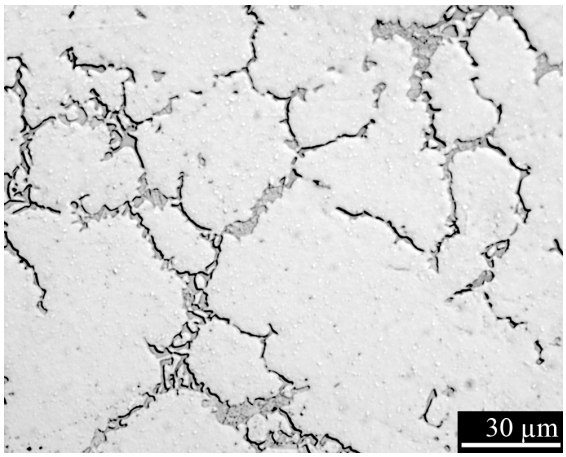

Figure 2. Optical microscope image of the present alloy with the interdendritic $(Mg,Al)_2(Ca,Sr)$ precipitates at dendrite arm boundaries

In this research, a sequential creep-EBSD technique was used to study the creep behavior of the alloy Mg-8.5Al-1Ca-0.3Sr [7]. This technique involves performing a tensile creep test on a miniature specimen with rectangular cross-section, and interrupting the creep process at periodic intervals. Mapping the crystallographic orientation on fixed surface area using EBSD reveals the gradual development of microstructure during creep. This technique has been successfully applied to the study of power-law creep behavior in pure magnesium [7]. It must be noted that a surface analysis technique such as EBSD may reveal a microstructural development that differs from the bulk of the material. However, in many industrial applications of magnesium alloys, such as sheet or intricate die-cast components, the thickness is relatively small in relation to the grain size and thus the present EBSD analysis should still provide a relevant representation of the overall creep behavior.

The main purpose of this study was to describe the microstructural evolution of a Mg-8.5Al-1Ca-0.3Sr alloy under a range of creep conditions. Particular interest was held in identifying underlying dominant creep deformation mechanisms, and describing any changes in mechanism that might occur as conditions were changed. As implied earlier, it was also important to account for how the different types of boundaries may affect the creep behavior.

Experimental Procedures

The specimens prepared for this study were high-pressure die cast Mg-8.5Al-1Ca-0.3Sr alloy. The cast blocks were cut into miniature ASTM E8 rectangular tensile test specimen shapes with 3 × 4 mm cross-section and 15 mm gauge length. Material was removed from each face of the cast block to a depth of 10 mm to reduce the influence of microstructural anomalies. All test pieces were obtained from the same orientation in the cast block. The test pieces were polished to 0.05µm colloidal silica and microhardness indents were placed as reference markers for EBSD mapping. Creep tests were conducted in a heated silicone oil bath to reduce temperature fluctuations and surface oxidation. The specimen extension was measured by a linear variable displacement transducer (LVDT) extensometer with a resolution of up to 1µm.

The creep tests were conducted at 200ºC at 50, 55, 60, 75, and 90 MPa. The samples were periodically removed from the creep test at intervals of 6~24 hours depending on the strain rate, and the same pre-determined surface locations were repeatedly orientation mapped by EBSD. The surface was lightly polished prior to each EBSD map with 0.05 µm colloidal silica to remove the oxide layer formed during the creep test. The polishing step removed up to 5 µm of thickness, and therefore the procedure is not strictly non-destructive, but this effect was considered negligible, since the general microstructure showed minimal variations. The orientation maps were constructed on a 2500 × 1850 µm window with 5 µm step intervals using an HKL Channel5 EBSD system on a JEOL JSM-6100 SEM.

Results

Figure 3 summarizes the interrupted creep test results of the specimens tested at 50, 60, and 75 MPa. The 50 and 60 MPa tests were not carried out to failure but were stopped after at least four interruption EBSD maps were acquired. The circle markers indicate the intervals at which EBSD maps were acquired. The absence of discontinuities in these plots at interruptions indicates that the test interruption procedure did not affect the creep rate to a significant degree.

The 60 MPa specimen exhibited a steady creep rate of 1.1×10^{-8} /s up to total strain of approximately 1.3%, followed by an unexpected gradual reduction to a creep rate of 10^{-9} /s at the test conclusion. This result can be seen in Figure 3 but also more clearly in Figure 4, which shows the creep rate of the 60 MPa specimen for the duration of the test. There was no variation in temperature, stress, or external influence such as an interruption/EBSD mapping process. It must be noted that the initial 'steady-state' creep rate of 1.1×10^{-8} /s was treated as the steady-state creep rate for the subsequent analysis, since this rate was consistent with other research in similar alloys [12]. This phenomenon will be discussed later in this paper.

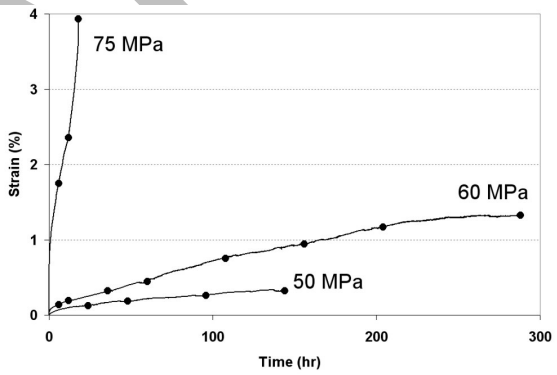

Figure 3. Creep time-strain graphs of specimens tested at 50, 60, and 75 MPa. Circle markers indicate each interruption. Steady-state creep rates (/s) for the 50, 60 and 75 MPa samples were 3.4×10^{-9}, 1.1×10^{-8} and 2.3×10^{-7}, respectively.

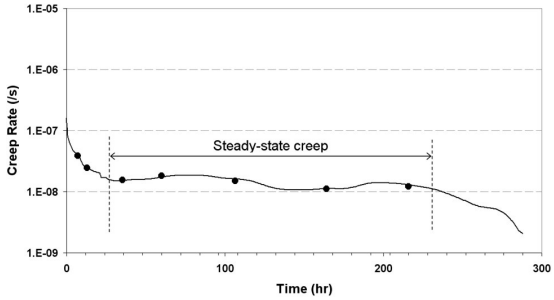

Figure 4. Time vs. creep rate graph of specimens tested at 60 MPa, illustrating the reduction of creep rate from the "steady-state" creep condition. Circle markers indicate each interruption.

Figure 5 highlights sequential EBSD orientation maps of the 50 and 60 MPa specimens at three of the interruptions. The average grain sizes of the three test specimens measured by EBSD remained unchanged throughout the creep test duration. However, some of the grains exhibited twinning as creep progressed. The twins were identified as HCP $\{10\bar{1}2\}$ tension twins [18, 19]. Figure 6a shows a sequential EBSD orientation map of the 75 MPa specimen at 6-hour intervals until failure. A gradual crack growth and failure process can be observed within the EBSD map window, initiated by a crack on the map first observed at 6 hours indicated by an arrow on the upper right area of the map. Note that the final fracture occurred along high angle grain boundaries.

In addition to the sequential creep test specimens, another specimen was tested at a higher stress level (90 MPa) as a comparison. The test resulted in failure within 30 minutes of the commencement of the creep test, and therefore a reliable steady-state creep rate was not obtained. The post-failure EBSD map is shown on Figure 7.

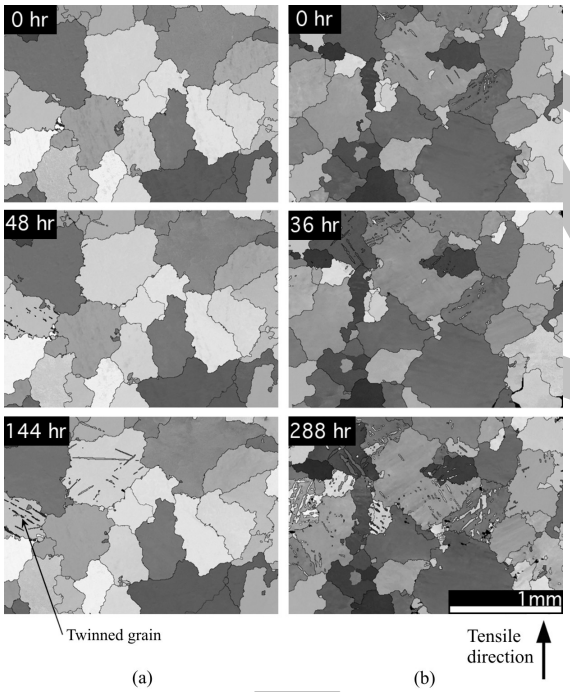

Figure 5. Series of sequential EBSD orientation maps for the (a) 50 MPa and (b) 60 MPa specimens. The tensile direction is vertical. An example of a twinned grain is shown by an arrow.

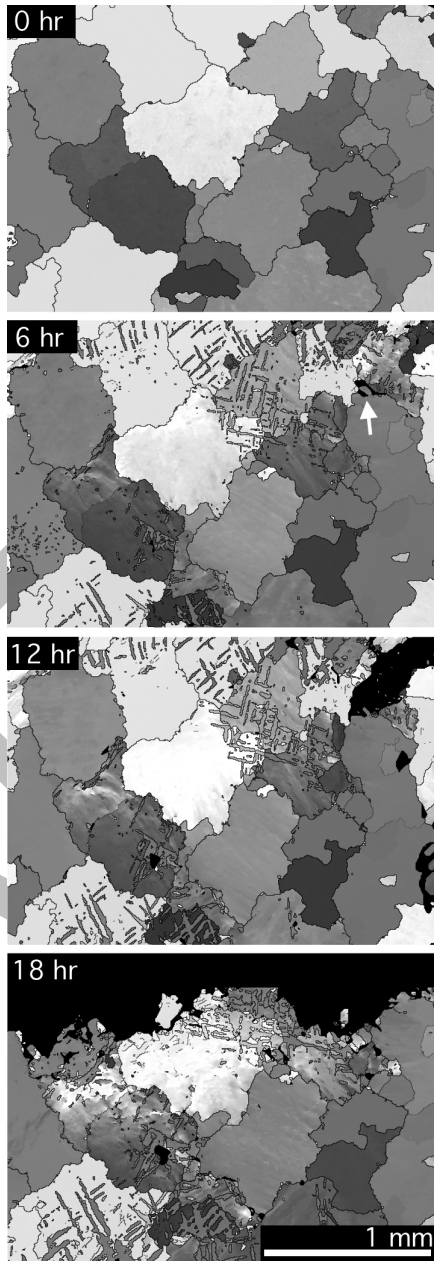

Figure 6. Series of sequential EBSD orientation maps for the 75 MPa specimen. The arrow on the 6 hr image indicates a creep crack initiation site that led to the subsequent failure. The tensile direction is vertical.

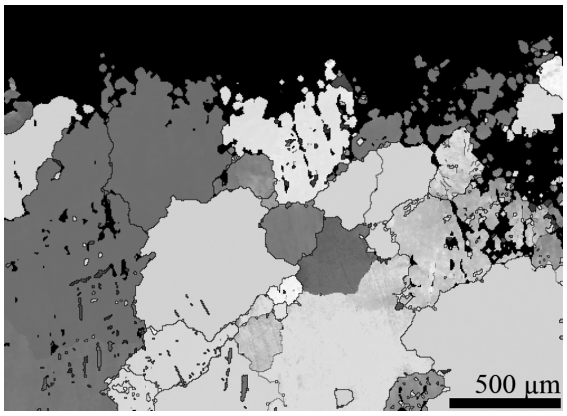

Figure 7. EBSD orientation map of the 90 MPa specimen after failure. The tensile direction is vertical.

Discussion

Grain boundary effects

A significant observation made from the sequential EBSD maps was that the formation of voids and the eventual onset of catastrophic failure was strongly related to the high angle misorientation (grain) boundaries, whereas the dendrite arm (intragranular) boundaries and their associated $(Mg,Al)_2(Ca,Sr)$ precipitate networks appear to remain unaffected by the creep deformation during steady-state creep. This suggests that the $(Mg,Al)_2(Ca,Sr)$ precipitate network was sufficiently stable and provided reinforcement to the primary α-Mg dendrite structure and minimized the onset of intragranular creep deformation mechanisms, which is consistent with previous findings [10, 20]. Figure 8 shows high magnification images of the creep micro-cracks on the 75 MPa specimen near failure. Corresponding EBSD maps of the same areas reveal that these cracks always follow high angle misorientation boundaries, which are not clearly evident in the secondary electron images.

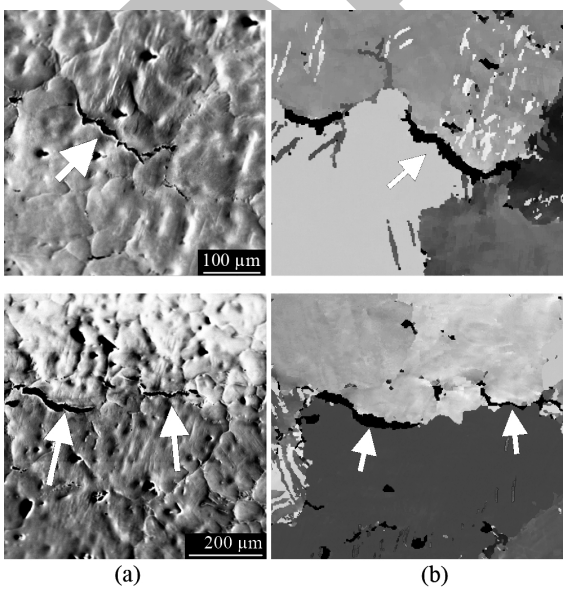

Figure 8. (a) Secondary electron images and (b) EBSD orientation maps of the 75 MPa specimen highlighting the creep micro-cracks at high angle misorientation boundaries.

A power-law creep model for the current Mg-Al-Ca-Sr alloy was constructed by combining the creep rate models for power-law creep ($\dot{\gamma}_{PL}$) and grain boundary creep ($\dot{\gamma}_{GB}$) presented by Frost and Ashby [6] as illustrated on Equation (1).

$$\dot{\gamma}_{total} = \dot{\gamma}_{PL} + \dot{\gamma}_{GB} \quad \text{.....(1)}$$

Equation (2) models the creep rate for lattice/core diffusion creep within the primary dendrites, with applied shear stress σ_s, Boltzmann's constant k, temperature T = 473 K, shear modulus of magnesium μ = 15 GPa, Dorn constant $A_2 = 3.2 \times 10^{-7}$, Burger's vector for HCP magnesium $b = 3.2 \times 10^{-10}$ m, and the power-law stress exponent n = 5. The constant ΔF is material specific, and was determined experimentally to fit at $\Delta F = 7 \times 10^{-20}$. The effective diffusivity D_{Leff} is dependent on both the temperature and stress, but was calculated to fall within 7~13 $\times 10^{-9}$ m^2/s, following Frost and Ashby [6].

$$\dot{\gamma}_{PL} = \frac{A_2 D_{Leff} \mu b}{kT} \left(\frac{\sigma_s}{\mu} \right)^n \exp\left[-\frac{\Delta F}{kT} \right] \quad \text{.....(2)}$$

Equation (3) models the grain boundary creep, and considers the effect of grain size on the power-law creep rate. This equation suggests that grain boundary creep is inversely related to the square of the grain size d. The atomic volume of magnesium $\Omega = 2.33 \times 10^{-28}$ m^3. The effective grain boundary diffusivity D_{Beff} is dependent on temperature and was calculated to be 3×10^{-18} m^2/s at 200 ºC, again following Frost and Ashby [6].

$$\dot{\gamma}_{GB} = \left(\frac{42 \sigma_s \Omega}{kTd^2} D_{Beff} \right) \quad \text{.....(3)}$$

Figure 9 illustrates the experimentally determined minimum creep rates obtained from the sequential creep tests, compared with the two power-law creep models generated using (1) the average grain size based on high angle grain boundary (d = 375 μm), and (2) the model based on dendrite arm spacing (d = 58 μm). The figure illustrates that the steady-state creep rates of the low stress specimens (50~60 MPa) agrees with the model based on high angle grain boundary, but the creep rate tends toward the dendrite arm spacing model as the stress level is increased. Note that the steady-state creep rate for the 60 MPa specimen is based on the rate exhibited up to 1.3% strain (prior to the unexpected reduction in creep rate).

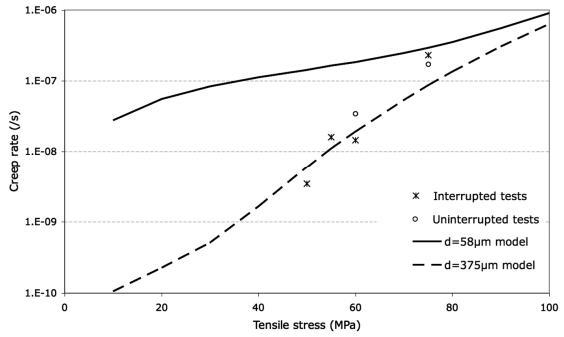

Figure 9. Steady-state creep rates vs. applied load at 200ºC, with power-law predictions based on two different grain sizes (d = 58μm, 375μm)

The rapid failure of the 90MPa specimen is attributed to power-law breakdown, where the stress level is sufficient for creep deformation to take place with less dependence on temperature-activated dislocation mechanisms [6]. A study by Zhu *et al.* on a similar alloy [12] identified power-law breakdown from σ/G (stress normalized by shear modulus) value of greater than 6×10^{-3}, which corresponds to 92 MPa at 200 ºC. Figure 10 compares a post-failure secondary electron image of the 90 MPa specimen with an EBSD orientation map of the same area. In this sample, the formation of micro-cracks at the intermetallic phase interfaces of the low-angle dendrite arm boundaries did not necessarily correspond with the high angle grain boundaries indicated by black lines in Figure 10(b). This is in contrast to the 75 MPa specimen (shown in Figure 8), in which cracks were only observed at high-angle grain boundaries.

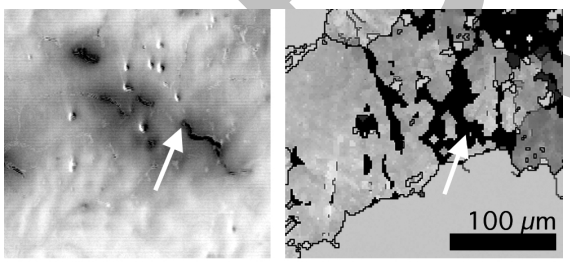

(a) (b)

Figure 10. (a) Secondary electron image of the 90 MPa specimen after failure and (b) EBSD orientation map of the same area, indicating cracks at low-angle boundaries.

Twin formation

The EBSD orientation maps of the specimens at each interruption illustrate the formation of heavily twinned grains as creep progressed (see Figure 5b). Twinned grains were observed in all specimens to varying degrees, and the failure of the 75 MPa specimen initiated from a region with a high density of twins. The degree of twinning (measured by EBSD at each interruption) is illustrated on Figure 11 as the fraction of interfaces on an orientation map possessing misorientation of 86 ± 1º about $\langle 2\bar{1}\bar{1}0 \rangle$ rotation axis.

The 75 MPa specimen exhibited a plateau in the rate of twin formation from after 1.5% strain, which suggests that the grains able to twin were exhausted beyond this level of strain. Post-failure secondary electron images of the 75 MPa specimen in Figure 12a illustrate areas with surface relief. Regions with surface relief correspond to the heavily twinned regions in the EBSD map on Figure 12b, which shows only the twins and high angle grain boundaries.

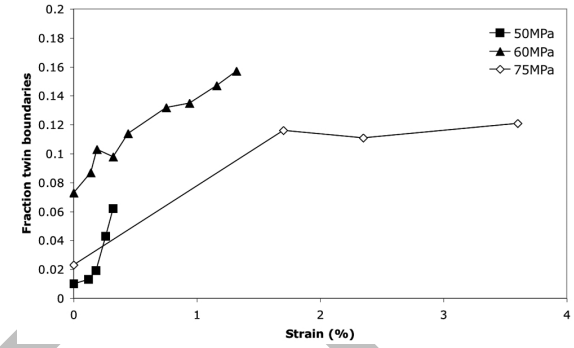

Figure 11. Plot of creep strain vs. twins as a fraction of the misorientation boundaries in the EBSD maps. A twin is defined as a misorientation with 87º $\langle 2\bar{1}\bar{1}0 \rangle$ relationship.

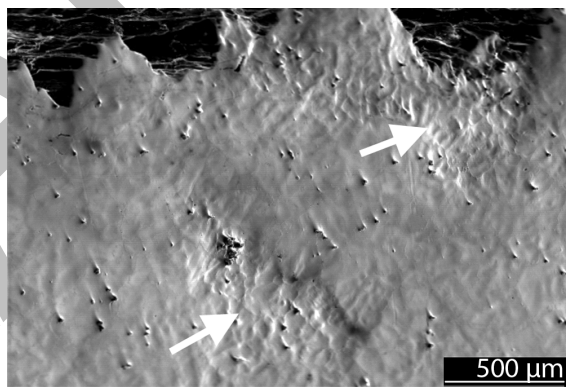

(a)

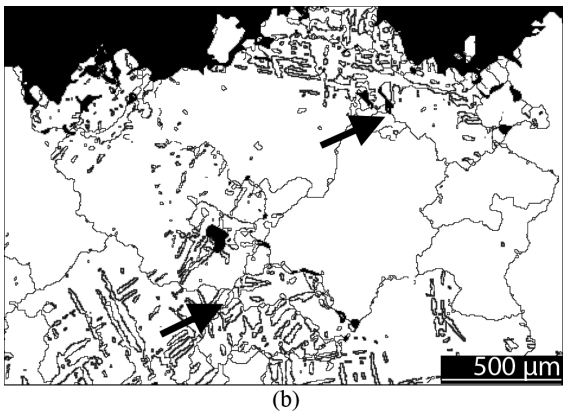

(b)

Figure 12. (a) Secondary electron image of the 75MPa specimen near the fracture surface. Arrows highlight regions exhibiting surface relief. (b) EBSD maps highlighting the twin boundaries and grain boundaries with misorientation of greater than 15º. Surface relief in the SE image corresponds to twins in the orientation map at 18 hours.

Sequence of the deformation process

In light of the above observations, the deformation sequence for the alloy under the current creep test conditions (200 °C, 50~75 MPa) can be summarized as follows:

Stage 1: First, significant twinning in specific grains takes place after the initial creep rate transient. The onset of twin formation is determined by the original crystallographic orientation texture of the microstructure [21] produced by the prior casting or forming processes experienced by the alloy [22, 23]. This results in a localized strain of the twinned regions, creating stress concentration zones, further assisting the development of stress-induced twinning of the nearby grains. The formation of new twins decreases as the potential sites for their formation is exhausted.

Stage 2: Subsequent to twinning, the creep strain rate may decrease due to the exhaustion of available twinning sites. Given sufficient stress (e.g. 75 MPa), formation and growth of creep voids takes place from high angle grain boundaries, and creep continues in a steady-state manner until failure. When stress is raised higher (e.g., 90 MPa), voids are also created from the intermetallic particle interface of the low angle, secondary dendrite arm boundaries, and result in rapid failure.

As explained earlier, an unexpected result from the current study was the observation of a gradual reduction of creep rate observed in the 60 MPa sample after approximately 1.3% strain (see Figure 4). Figure 11 shows that the steady-state creep was linearly related to the formation of twins. Therefore, it is possible that the initial twinning-assisted power-law creep rate was reduced by the lack of new twinning sites, and any subsequent creep deformation process (not identified here) occurs at a slower rate. Further research, such as creep rupture testing and additional creep rate measurements, is required to investigate this phenomenon. This result also illustrates that the traditional classification of a "secondary" creep stage may be insufficient for understanding the creep of a complex alloy system when several deformation mechanisms are taking place, as has been pointed out by Blum *et al.* [24].

It must be noted that these creep tests were conducted exclusively at 200 °C and the observed creep deformation mechanisms may not take place under other conditions. At higher temperatures (> 200 °C), stability of the Mg-Al solid solution matrix may be compromised, and the corresponding mechanisms such as the formation of unstable β-phase precipitates may dominate the creep deformation. In a similar alloy (Mg-9Al-0.7Zn-1Ca-0.1Sr), Zhu et al observed a gradual increase in the creep rate due to the microstructural changes induced by the precipitation of the β-phase during creep [12]. Incomplete suppression of the β-phase is dependent on the Al/Ca ratio of the alloy [25].

Conclusions

The sequential creep/EBSD studies of the Mg-8.5Al-1Ca-0.3Sr alloy were carried out to visualize the underlying deformation mechanisms at various stages of creep, with the following outcomes.

- All specimens exhibited the gradual formation of twins during the steady-state creep stage.
- The interdendritic $(Mg,Al)_2(Ca,Sr)$ precipitates in this alloy were stable and provided resistance against lattice diffusion creep.
- Creep crack formation and growth took place at high angle grain boundaries.
- Steady-state creep rates of all test specimens at stress between 50~75 MPa agreed with the power-law creep rate model, whereas the 90 MPa specimen failed at a rate faster than predicted (power-law breakdown).
- Experimental creep rates agreed with a creep model based on the high angle grain size rather than secondary dendrite arm spacing. This agrees with the observation of preferential void formation and growth at high angle grain boundaries.
- A specimen tested at 60 MPa exhibited a constantly decreasing creep rate, which is attributed to the exhaustion of twinning sites resulting in a strain-hardened state.

References

[1] K. U. Kainer, Magnesium Alloys and Technology, Wiley-VCH, 2003.

[2] B. L. Mordike, Mater. Sci. Eng. A 324 (2002) 103.

[3] M. O. Pekguleryuz, Mat. Sci. Forum 350 (2000) 131.

[4] E. Baril, P. Labelle, M. O. Pekguleryuz, JOM 55 (2003) 34.

[5] R. Ninomiya, T. Ojiro, K. Kubota, Acta Metall. Mater. 43 (1995) 669.

[6] H. J. Frost, Ashby, M.F., Deformation-Mechanism Maps, Pergamon Press, 1982.

[7] T. Sato, M. V. Kral, Metall. Mat. Trans. A 39 A (2008) 688.

[8] P. A. Thorsen, J. B. Bilde-Sørensen, Mater. Sci. Eng. A 265 (1999) 140.

[9] R. S. Kottada, A. H. Chokshi, Metall. Mat. Trans. A 38 (2007) 1743.

[10] A. A. Luo, M. P. Balogh, B. R. Powell, Metall. Mat. Trans. A 33A (2002) 567.

[11] J. Bai, Y. S. Sun, S. Xun, F. Xue, T. B. Zhu, Mater. Sci. Eng. A 419 (2006) 181.

[12] S. M. Zhu, B. L. Mordike, J. F. Nie, Metall. Mat. Trans. A 37 (2006) 1221.

[13] F. J. Humphreys, P. S. Bate, Acta Mater. 54 (2006) 817.

[14] J. Bai, Y. S. Sun, F. Xue, S. Xue, J. Qiang, T. B. Zhu, Mat. Sci. and Tech. 22 (2006) 1208.

[15] Q. Han, B. K. Kad, S. Viswanathan, Phil. Mag. 84 (2004) 3843.

[16] T. Sato, B. L. Mordike, J.-F. Nie, M. V. Kral, Magnesium Technology 2005 (2005) 305.

[17] A. Suzuki, N. D. Saddock, J. W. Jones, T. M. Pollock, Scripta Mater. 51 (2004) 1005.

[18] M. R. Barnett, Mater. Sci. Eng. A 464 (2007) 1.

[19] M. D. Nave, M. R. Barnett, Scripta Mater. 51 (2004) 881.

[20] R. Raj, M. F. Ashby, Met. Trans. 3 (1972) 1937.

[21] M. R. Barnett, Z. Keshavarz, X. Ma, Metall. Mat. Trans. A 37A (2006) 2283.

[22] Y. N. Wang, J. C. Huang, Acta Mater. 55 (2007) 897.

[23] L. Jiang, J. J. Jonas, A. A. Luo, A. K. Sachdev, S. Godet, Mater. Sci. Eng. A 445 (2007) 302.

[24] W. Blum, P. Eisenlohr, F. Breutinger, Metall. Mat. Trans. A 33 (2002) 291.

[25] S. M. Liang, R. S. Chen, J. J. Blandin, M. Suery, E. H. Han, Mater. Sci. Eng. A 480 (2008) 365.